UNIVERSITY OF BELGRADE
FACULTY OF PHYSICS

Ivana B. Vidanović

NUMERICAL STUDY OF QUANTUM GASES AT LOW TEMPERATURES

Doctoral Dissertation

Belgrade, 2011

UNIVERZITET U BEOGRADU
FIZIČKI FAKULTET

Ivana B. Vidanović

NUMERIČKO PROUČAVANJE KVANTNIH GASOVA NA NISKIM TEMPERATURAMA

Doktorska disertacija

Beograd, 2011

Thesis advisor, Committee member:
Dr. Antun Balaž
Associate Research Professor
Institute of Physics Belgrade
University of Belgrade

Committee member:
Dr. Aleksandar Bogojević
Associate Research Professor
Institute of Physics Belgrade
University of Belgrade

Committee member:
Prof. Dr. Sunčica Elezović-Hadžić
Associate Professor
Faculty of Physics
University of Belgrade

Committee member:
Prof. Dr. Milan Knežević
Professor
Faculty of Physics
University of Belgrade

The doctoral dissertation of Ivana Vidanović was defended on December 23, 2011.

Dedicated to the memory of my father, Bora Vidanović.

Acknowledgements

This thesis is written under the guidance of Dr. Antun Balaž. A strong scientific input from his side and unwavering persistence in solving and understanding scientific problems helped me essentially in my graduate research. Antun always had time to answer my questions, but also had time to help me apply for summer schools and he also showed much care about the graduate students in general. I gratefully acknowledge Antun's support in all aspects of my work in the Scientific Computing Laboratory (SCL) at the Institute of Physics Belgrade. First part of the thesis was done in close collaboration with Dr. Aleksandar Bogojević and Dr. Aleksandar Belić from SCL. I thank both of them for many scientific discussions and for numerous things that I have learned from them, also during the graduate courses. Most of the results presented in the thesis were obtained in the collaboration with Dr. Axel Pelster from the Department of Physics, University Duisburg-Essen. I thank Dr. Pelster for learning many things on Bose-Einstein condensation from him and for guiding me through the unexplored topics of the physics of cold quantum gases. Within the graduate courses, Dr. Milica Milovanović gave me an opportunity to make a scientific excursion into the field of quantum Hall physics. This is a valuable experience and I acknowledge Prof. Milovanović effort in broadening my scientific horizon.

Years at the SCL office wouldn't be as nearly as interesting and inspiring without sitting next to other graduate students and senior members of SCL. Friendly atmosphere, bright comments and questions helped a lot in keeping positive attitude. I don't have enough space to mention all officemates, but they will recognize themselves.

I acknowledge financial support by the Ministry of Education and Science of the Republic of Serbia under projects No. ON141035, No. ON171017, PI-BEC and NAD-BEC, by DAAD - German Academic and Exchange Service under projects NAD-BEC and PI-BEC, and by the European Commission under EU FP6 project CX-CMCS (EU Centre of Excellence for Computer Modeling of Complex Systems). Numerical simulations were run on the AEGIS e-Infrastructure, supported in part by the European Commission under EU FP7 projects PRACE-1IP, HP-SEE and EGI-InSPIRE.

Finally, I am indebted to my mother, sister and Borislav for their unwavering support that goes far beyond my graduate studies.

Rezime doktorske disertacije

Numeričko proučavanje kvantnih gasova na niskim temperaturama

Koncept Boze-Ajnštajn kondenzacije je u fizici prisutan još od 1924. godine, kada je prvi put uvedena Boze-Ajnštajn statistika za identične čestice celobrojnog spina [1, 2]. Već prva teorijska kvantno-mehanička razmatranja sistema neinteragujućih čestica su ukazala na mogućnost postojanja ovog fenomena. Poznato je da fizičke osobine atomskih gasova jako zavise od temperature. Na sobnim temperaturama, osobine ovih sistema su dobro opisane zakonima klasične statističke fizike i kvantni fenomeni prolaze neopaženo. Snižavanjem temperature talasna dužina de Broljijevih talasa materije raste i dolazi do preklapanja talasa koji odgovaraju različitim česticama. U tom slučaju, kvantna statistika preuzima presudnu ulogu za fizičke osobine sistema. Česticama sa celobrojnim spinom, bozonima, zakoni kvantne statistike dozvoljavaju naseljavanje istog jednočestičnog kvantnog stanja. Kako snižavamo temperaturu, sistem teži konfiguraciji sa minimalnom energijom, a za bozone to je upravo makroskopski naseljeno osnovno kvantno stanje. Na taj način ovo kvantno stanje postaje dominantno, pa govorimo o makroskopskom kvantnom fenomenu i razlikujemo fazu sa makroskopskom naseljenošću osnovnog stanja (Boze-Ajnštajn kondenzat) i fazu bez ovog svojstava, koju nazivamo normalni gas. Fazni prelaz između ove dve faze naziva se Boze-Ajnštajn kondenzacija. I pored jake utemeljenosti teorijskog koncepta, do prve eksperimentalne realizacije ovog faznog prelaza je došlo tek 1995. godine, a rezultat je nagrađen Nobelovom nagradom za fiziku 2001.

Kao što smo ukratko objasnili, osnovni pojmovi o fenomenu Boze-Ajnštajn kondenzacije su uvedeni korišćenjem modela neinteragujućeg gasa. U realnim gasovima je naravno nemoguće zanemariti interakcije, zbog kojih oni na veoma niskim temperaturama prelaze u tečno ili čvrsto stanje. Zbog toga je za eksperimentalno postizanje Boze-Ajnštajn faznog prelaza neophodno koristiti slabo interagujuće gasove, kao što su su, na primer, razređeni gasovi koji interaguju kratkodometnom, Van-der-Valsovom interakcijom. U takvom sistemu, u kom je srednje rastojanje između čestica veliko zbog male gustine, kvantni fenomeni dolaze do izražaja tek na veoma niskim temperaturama. Zbog mogućnosti efikasnog hlađenja, za eksperimentalno dobijanje kondenzata odabrani su atomski gasovi alkalnih metala (Rb, Li, Na, ...), u kojima je fenomen Boze-Ajnštajn kondenzacije i ostvaren po prvi put [3, 4] za tipične gustine čestica u opsegu od $10^{18}\,\mathrm{m}^{-3}$ do $10^{21}\,\mathrm{m}^{-3}$ (što je šest redova veličine manje od tipične gustine vazduha) i temperature reda $100\,\mathrm{nK}$. Postizanje ovako niskih temperatura je zahtevalo razvijanje novih tehnika hlađenja i čuvanja atoma, koji su u eksperimentu zarobljeni u zamci napravljenoj od specijalno podešenog spoljašnjeg električnog ili magnetnog polja. Posle intenzivnih dugogodišnjih napora, proizvodnja kvantnih gasova sačinjenih od raznih vrsta alkalnih atoma je danas standardni proces u brojnim laboratorijama širom sveta.

Eksperimenti omogućavaju veoma detaljno testiranje fundamentalnih teorijskih koncepata - kolektivnih ekscitacija Boze-Ajnštajn kondenzata, superfluidnosti (prisustvo vorteksa kao odgovor sistema na spoljašnju rotaciju), osobina faznog dijagrama [5]. Veoma važna i interesantna osobina ultrahladnih kvantnih gasova je ekstremno velika mogućnost kontrole svih relevantnih parametara sistema - broja čestica, gustine, temperature, dimenzionalnosti (promenom oblika spoljašnje potencijalne zamke), a posebno je značajna mogućnost kontrolisanja jačine interakcija između atoma tehnikom koja se naziva Fešbah rezonanca [6]. Jednostavnom promenom spoljašnjeg magnetnog polja, efektivna interakcija između atoma se može menjati u rasponu od mnogo redova veličina, što čini ove sisteme zaista jedinstvenim. U novijim eksperimentima, atomi su zarobljeni u periodičnim potencijalima, tzv. optičkim rešetkama [7]. Zahvaljujući tome, sada je moguće na nov način realizovati i proučavati sisteme koji su analogni sistemima poznatim iz fizike čvrstog stanja, a koje još uvek ne razumemo u potpunosti (npr. visoko-temperaturna superprovodljivost). Upravo zato se kaže da ultrahladni kvantni gasovi predstavljaju Fajnmanove "kvantne simulatore" [8]. Intenzivan eksperimentalni razvoj i realizacija nove ultrahladne faze materije predstavljaju snažan podsticaj za nova, interdisciplinarna teorijska istraživanja.

Osnovni cilj ove teze je podrobno razumevanje dva zanimljiva fizička scenarija za manipulaciju hladnim bozonskim atomima, koja su predmet i nedavnih eksperimentalnih istraživanja. Prvo smo razmotrili fazni dijagram rotirajućeg idealnog bozonskog gasa u anharmonijskom potencijalu, dok se druga noseća tema teze bavi nelinearnim osobinama kolektivnih bozonskih moda, koje su pobuđene harmonijskom modulacijom interakcije.

Da bismo ostvarili ove ciljeve, najpre smo u Poglavlju 2 razradili detalje numeričkog metoda koji nam na efikasan način pruža informaciju o velikom broju svojstvenih stanja kvantnog sistema. Tačno poznavanje energetskih nivoa nam je neophodno radi preciznog određivanja faznog dijagrama Boze-Ajnštajn kondenzata. Metod koji smo koristili je zasnovan na egzaktnoj dijagonalizaciji evolucionog operatora [9], a da bi postigli njegovu optimalnu upotrebu, detaljno smo analizirali greške koje nastaju pri korišćenju ovog metoda iz dva razloga: greške nastale usled uvođenja prostorne diskretizacije, kao i greške pri računanju matričnih elemenata evolucionog operatora. Jedan od naših glavnih rezultata je mnogo optimalnije ponašanje diskretizacione greške ovog metoda u odnosu na standardni metod dijagonalizacije prostorno diskretizovanog Hamiltonijana. Detaljnim analitičkim i numeričkim razmatranjem, pokazali smo da dijagonalizacija diskretizovanog evolucionog operatora pokazuje neperturbativno malu diskretizacionu grešku, koja opada eksponencijalno sa $1/\Delta^2$, gde je Δ korak prostorne diskretizacije, dok standardni metodi imaju grešku koja polinomijalno zavisi od Δ. Ovo je osnovni razlog zbog kog je mnogo optimalnije koristiti dijagonalizaciju evolucionog operatora. Glavna teškoća u primeni ovog pristupa - precizno računanje matričnih elemanata evolucionog operatora, tj. amplituda prelaza, direktno se razrešava primenom ranije uvedenog metoda efektivnih dejstava [10, 11], koja nam daju razvoj amplitude prelaza po kratkom vremenu propagacije do veoma visokog nivoa. Veliku efikasnost ovog metoda smo demonstrirali na nekoliko jednodimenzionalnih i dvodimenzionalnih modela.

U poglavlju 3 primenili smo prethodno opisani metod na ispitivanje faznog dijagrama rotirajućih bozona u nestandardnom spoljašnjem potencijalu. Naime, najčešće korišćene potencijalne zamke su harmonijskog oblika, i o Boze-Ajnštajn kondenzaciji u ovakvim zamkama se već puno zna. Rotacija kvantnog gasa je jedan od načina da se ostvare jako korelisane faze materije [7] i od velikog je značaja. Međutim, jedna od posledica rotacije je pojava dekonfinirajuće centrifugalne komponente u potencijalu, koja za velike frekvencije rotacije (veće of frekvencije harmonijske potencijalne zamke) dovodi do razletanja čestica gasa i gubitka kondenzata. Da bi se to izbeglo, u nedavnom eksperimentu [12] je upotrebljen dodatni kvartični potencijal za formiranje potencijalne zamke. U zavisnosti od frekvencije rotacije, ukupan efektivni potencijal menja oblik od konveksnog potencijala sa jednim minimumom do potencijala koji ima oblik meksičkog šešira. Primenom egzaktne dijagonalizacije evolucionog operatora, proučavali smo kako promena spoljašnjeg potencijala utiče na temperaturu Boze-Ajnštajn kondenzacije, na raspodelu čestica u zamci i na rezultate eksperimentalnih merenja.

Uticaj slabih interakcija na fenomen Boze-Ajnštajn kondenzacije je predmet razmatranja Poglavlja 4. Ovo poglavlje je preglednog tipa, i u njemu smo predstavili Hartri-Fok opis bozonskog sistema. Hartri-Fok predstavlja jednu od aproksimacija u teoriji srednjeg polja, i u okviru nje smo opisali sistem ultrahladnih bozona na nultoj temperaturi, kao i u okolini Boze-Ajnštajn faznog prelaza. Za nultu temperaturu smo izveli čuvenu Gros-Pitaevski jednačinu [13, 14] - nelinearnu parcijalnu diferencijalnu jednačinu koja opisuje ponašanje makroskopse talasne funkcije kondnezata. Za konačne temperature predstavili smo nekoliko često korišćenih implementacija aproksimacije srednjeg polja i naveli njihove prednosti i nedostatke. Aproksimativni metodi ove vrste se veoma često koriste u interpretaciji eksperimentalnih merenja, što im daje veliki značaj. Nedavni eksperimentalni napredak u uočavanju efekata koji su izvan opisa teorije srednjeg polja zahteva popravke standardno korišćenih aproksimacija u najskorijoj budućnosti.

Jedan od osnovnih načina karaketrizacije faza materije, kako eksperimentalno tako i teorijski, su osobine njihovog ekscitaciong spektra, a posebno su interesantne i važne kolektivne mode. U sistemima hladnih gasova, kolektivne mode se obično pobuđuju modulacijom spoljašnjeg potencijala zamke, dok je u nedavnom eksperimentalnom radu [15] pobuđivanje kolektivnih moda ostvareno novim pristupom - harmonijskom modulacijom interakcije. U osnovi primenjenog eksperimentalnog metoda je tehnika Fešbah rezonance, kojom se jačina kratkodometne interakcije menja u vremenu usled modulacije spoljašnjeg magnetnog polja. Kao posledicu, imamo oscilacije veličine bozonskog oblaka, koje su u eksperimentu merene. U zavisnosti od vrednosti spoljašnje frekvencije upotrebljene za modulaciju interakcije, možemo da dobijemo linearni odgovor sistema ili rezonantno ponašanje karakterisano velikim amplitudama oscilacija. Kako je osnovna jednačina koja opisuje dinamiku ovakvog sistema nelinearna, u slučaju velikih oscilacija očekujemo izražene nelinearne efekte. U poglavlju 5 smo numerički simulirali dinamiku sistema i identifikovali nelinearne karakteristike dobijenih ekscitacionih spektara: pored osnovnih moda, pojavljuju se viši harmonici, kao i linearne kombinacije različitih moda, a najizraženiji nelinearni efekati su pomeraji u frekvencijama ekscitovanih moda u odnosu na vrednosti izračunate u linearnom režimu. Za kvantitativno objašnjenje nelinearnih efekata razvili smo perturbativi pristup u kom je mali parametar amplituda modulacije. Razvijeni perturbativni pristup je baziran na Poenkare-Lindštet metodu, i njegovom primenom smo našli analitičke izraze za nelinearne pomeraje svojstvenih frekvencija u blizini rezonanci.

Ključne reči: hladni kvantni gasovi, Boze-Ajnštajn kondenzacija, efektivno dejstvo, egzaktna dijagonalizacija, teorija perturbacija, nelinearna dinamika

Naučna oblast: Fizika

Uža naučna oblast: Fizika kondenzovanog stanja materije

UDK broj: 538.9

Abstract of the doctoral dissertation

Numerical study of quantum gases at low temperatures

The concept of Bose-Einstein condensation was introduced in 1924, at the same time as Bose-Einstein statistics, applicable to the integer-spin particles [1, 2]. Already first theoretical quantum-mechanical considerations pointed to the existence of this phenomenon. It is well known that physical properties of atomic gases strongly depend on the temperature. At room temperatures the properties of these systems can be described by the classical statistical physics, and quantum features are negligible. However, as the temperature decreases, the wavelengths of the de Broglie mater waves increase, leading to the overlap of waves corresponding to different particles. In this case, quantum statistics plays a dominant role. According to the rules of quantum statistics, integer-spin particles, bosons, are allowed to occupy the same single-particle quantum states. With the decrease in the temperature, the system seeks the minimal-energy configuration, and for bosons this is a macroscopically occupied single-particle ground state. Such a quantum state becomes dominant and the occurrence is designated as a macroscopic quantum phenomenon. Accordingly, we distinguish a phase with a macroscopic occupation of the ground state (Bose-Einstein condensate) and a phase without this feature, which is called a normal gas. The phase transition between the two phases is Bose-Einstein condensation. In spite of the firm theoretical foundation of the concept from the beginning, first direct experimental observation was achieved only in 1995, and the result was recognized by the Nobel prize for physics in 2001.

As briefly explained, the basic notion of Bose-Einstein condensation was introduced using a model of noninteracting gas. Of course, in realistic gases, interactions can not be neglected and only due to them the gas becomes liquid or solid at low temperatures. In order to remain close to the noninteracting gas description in experiments, it is essential to use weakly interacting gases, such as dilute gases interacting via short-range, van der Waals interaction. In this type of systems, with long interparticle distances due to diluteness, the quantum phenomena become relevant only at very low temperatures. Due to highly efficient cooling techniques,

the gases of alkali metals (Rb, Li, Na, ...) were selected as most suitable candidates and Bose-Einstein condensation was observed for the first time [3, 4] in such systems with the typical particle densities from $10^{18}\,\mathrm{m}^{-3}$ to $10^{21}\,\mathrm{m}^{-3}$ (six orders of magnitude lower than the density of air) and temperatures of the order of $100\,\mathrm{nK}$. In order to reach this extreme low-temperature regime, it was necessary to develop many new cooling and trapping techniques: in experiments, atoms are confined using specially designed configurations of external magnetic or electric fields. After many years of intensive experimental efforts, the achievement of Bose-Einstein condensation in cold alkali vapors is nowadays a common technique in laboratories all over the world.

The experiments make possible very detailed tests of fundamental theoretical concepts - collective excitations of a Bose-Einstein condensate, superfluidity (the appearance of vortices as a response to rotation), the properties of a phase diagram [5]. A very important and interesting feature of ultracold quantum gases is a possibility to control relevant parameters of the system over many orders of magnitude. Basically, all parameters can be tuned: number of particles, density, temperature, dimensionality (by changing the shape of the external trap), and even the strength of interactions between atoms using a technique called Feshbach resonance [6]. By a simple modification of the external magnetic field, the effective interatomic interaction can be tuned in the range of several orders of magnitude and this feature makes cold atomic systems really unique. In more recent experiments, atoms are trapped in periodic potentials, the so-called optical lattices [7]. In this way, it is now possible to study, in a very clean setup, systems which are highly relevant in condensed matter physics, and which are not yet completely understood (with a notable example of high-temperature superconductivity). For this reason, it is widely accepted that ultracold quantum gases represent Feynman's quantum simulators [8]. Intensive experimental progress and realization of the new ultracold phase of matter are strong stimuluses for further, interdisciplinary theoretical research.

The main subject of this thesis is a thorough understanding of two interesting physical scenarios for the manipulation of cold bosonic atoms, which were also the focus of recent experimental studies. First, we have explored the phase diagram of a rotating ideal bosonic gas in an anharmonic trap, while the second main topic deals with nonlinear features of collective modes excited by harmonic modulation of interaction strength.

On the way to accomplish this, after introductory Chapter 1, in Chapter 2 we have first worked out details of an efficient numerical method capable of providing highly accurate information on energy levels of quantum systems. The precise information on energy spectra is necessary for the characterization of the phase diagram of a Bose-Einstein condensate. Method that we have used is based on the exact diagonalization of the time-evolution operator [9]. In order to optimally apply it, we have carefully analyzed numerical errors which arise for two reasons: numerical errors which stem from the spatial discretization, as well as the errors due to the approximative calculation of matrix elements. One of our main results is highly superior behavior of the dicretization error of the discretized evolution operator compared to the common discretization error of the discretized Hamiltonian. Based on the analytical and numerical considerations, we have shown that the diagonalization of a time-evolution operator exhibits a non-perturbatively small discretization error, which vanishes exponentially with $1/\Delta^2$, where Δ is the discretization spacing, while standard discretization introduces errors polynomial in Δ. This is the main reason that makes the diagonalization of the time-evolution operator the preferred method. The main difficulty in the application of the method - precise calculation of the matrix elements of time-evolution operator (transition amplitudes) can be directly resolved using previously developed effective action approach [10, 11], which yields transition amplitudes as high-order expansions in the short time of propagation. The efficiency of this method has been demonstrated on several one- and two-dimensional models.

In Chapter 3 we have used the described numerical method to explore the phase diagram of rotating bosons in a non-standard external potential. Widely used confinements are harmonic traps and many details of Bose-Einstein condensation in such traps are already well understood. Rotation of a quantum gas is one way to reach strongly correlated phases [7] and is therefore highly relevant. One of the consequences of rotation is the appearance of the deconfining centrifugal component in the potential, which in the case of a very fast rotation frequency (exceeding the trapping frequency) leads to the deconfinement. In order to avoid this, recent experiment [12] introduced an additional quartic potential to enhance trapping. Depending on the value of the rotation frequency, the potential changes its shape from a simple convex one to the Mexican-hat-shaped potential. Using exact diagonalization of the time-evolution operator, we have studied how the modification of the external trap influences properties of a Bose-Einstein condensate, such as condensation temperature, equilibrium density distribution of atoms and the expansion time of the cloud after it is released from the trap.

The effects of weak interactions on the phenomenon of Bose-Einstein condensation are subject of Chapter 4. This chapter reviews the Hartree-Fock description of a bosonic system. Hartree-Fock is one of the mean-field approximations and within this framework we have described ultracold bosons at zero temperature, as well as in the vicinity of the Bose-Einstein phase transition. At zero temperature we have rederived famous Gross-Pitaevskii equation [13, 14] - nonlinear partial differential equation, which governs the dynamics of the macroscopic wave function of the condensate. For finite temperatures, we have scrutinized several widely used implementations of the mean-field approximation, with the emphasis on their benefits and their physical drawbacks. Approximations of this type are very often used in the interpretation of the experimental data, which makes them highly relevant. A very recent experimental progress in the observation of beyond-mean-field effects demands further improvements of these standard tools.

One of the basic methods to characterize phases of matter, both experimentally and theoretically, are properties of their excitation spectra, with collective modes being of special interest. In ultracold gases, collective modes are usually excited using modulation of the parameters of the external trap. In the recent experiment [15], however collective modes were excited using an alternative method - harmonic modulation of interaction. In its essence the experimental method relies on a Feshbach-resonance technique, which enables modulation of interaction via a modulation of the external magnetic field. As an outcome of this dynamical protocol, oscillations of the condensate size were induced and measured. Depending on the value of the external modulation frequency, either a linear response or resonant large-amplitude oscillations were obtained. Since the main underlying equation is nonlinear, in the case of large-amplitude oscillations strong nonlinear effects are expected. In Chapter 5 we have performed numerical simulations of the system dynamics and identified main nonlinear features of the obtained excitation spectra: beside the basic modes, higher harmonics appear together with their linear combinations. Most prominent nonlinear effects are nonlinearity-induced shifts in the frequencies of excited modes. In order to describe these results in an analytic way, we have developed perturbative approach where the small parameter is given by the modulation amplitude. The developed perturbative approach is based on the Poincaré-Lindstedt method, and gives analytical estimates for the shifts of the eigenfrequencies in the vicinity of resonances.

Keywords: cold quantum gases, Bose-Einstein condensation, effective action, exact diagonalization, perturbation theory, nonlinear dynamics

Field of Science: Physics

Research Area: Condensed matter physics

UDC number: 538.9

Contents

Nomenclature **xviii**

1 Introduction **1**

1.1 Foreword 1

1.2 Few basic facts on Bose-Einstein condensation 3

1.2.1 Noninteracting bosonic gas in the harmonic trap 3

1.2.2 Experimental realization 9

1.2.3 Interacting bosons at low temperatures 13

1.3 This thesis 16

2 Properties of quantum systems via diagonalization of transition amplitudes **19**

2.1 Space-discretized Schrödinger equation 22

2.2 Discretization effects 26

2.3 Effective actions 33

2.4 Numerical results for one-dimensional models 36

2.5 Numerical results for two-dimensional models 47

2.6 Conclusions and outlook 55

3 Thermodynamics of a rotating ideal BEC **57**

3.1 Numerical calculation of energy eigenvalues and eigenstates 62

3.2 Finite number of energy eigenvalues and semiclassical corrections . . 66

3.3 Global properties of rotating BECs 70

3.3.1 Condensation temperature 70

3.3.2 Ground-state occupancy 74

3.3.3 Comparison with semiclassical approximation 75

3.4 Local properties of rotating BECs 77

3.4.1 Density profiles 77

3.4.2 Time-of-flight graphs for BECs 79
3.4.3 Overcritical rotation 80
3.5 Conclusions and outlook 82

4 Mean-field description of an interacting BEC 84
4.1 Gross-Pitaevskii equation 88
4.2 Finite-temperature properties of a BEC 90
4.2.1 Almost-ideal model 91
4.2.2 Semi-ideal model 92
4.2.3 TFSC model 94
4.2.4 GPSC model 95
4.2.5 Calculation of the condensation temperature 97
4.3 Experimental assessment of different models 100
4.4 Conclusions and outlook 102

5 Nonlinear BEC dynamics by harmonic modulation of *s*-wave scattering length 104
5.1 Variational description of low-lying modes 107
5.2 Harmonic modulation of the *s*-wave scattering length: experiment . . 111
5.3 Harmonic modulation of the *s*-wave scattering length: theoretical framework 114
5.4 Spherically-symmetric BEC 117
5.4.1 Poincaré-Lindstedt method 121
5.4.2 Results and discussion 123
5.5 Axially-symmetric BEC 126
5.5.1 Poincaré-Lindstedt method 126
5.5.2 Results and discussion 129
5.6 Conclusions and outlook 132

6 Summary 134

A Numerical solution of the GP equation 137

B Time-dependent variational analysis 142

List of papers by Ivana Vidanović 144

References 146

CURRICULUM VITAE - Ivana Vidanović 158

Nomenclature

Roman Symbols

a	s-wave scattering length
g	interaction strength given by $4\pi\hbar^2 a/M$
k_B	Boltzmann constant
L	space cutoff
M	atomic mass
N	total number of particles
$n(\vec{r})$	total density of particles
N_0	number of particles in the condensate
$n_0(\vec{r})$	condensate density
N_{th}	number of thermal particles
$n_{\text{th}}(\vec{r})$	density of thermal particles
T	temperature
t	time
T_{c}^0	condensation temperature of ideal gas
$V(\vec{r})$	external trap potential

Greek Symbols

β	inverse temperature, $1/k_BT$

Δ	discretization spacing
λ_T	thermal de Broglie wavelength at temperature T
μ	chemical potential
$\omega_{x,y,z}$	trapping frequency
$\psi(\vec{r})$	condensate wavefunction

Other Symbols

$\hbar$	Planck constant divided by 2π
$\mathcal{B}_n(\mu, T)$	Bose-Einstein distribution
$\vec{p}$	momentum
$\vec{r}$	real-space coordinate

Acronyms

BEC	Bose-Einstein condensate
GP	Gross-Pitaevskii
HF	Hartree-Fock
TF	Thomas-Fermi
TOF	time-of-flight

Chapter 1 Introduction

1.1 Foreword

The essential ingredients of the quantum mechanical theory are dual particle-wave nature of the matter, and the notion of identical particles. The quantum indistinguishability of particles has a profound impact on the statistical properties. While particles with a half-integer spin (fermions) try to avoid each other due to the Pauli-exclusion principle, particles with an integer spin (bosons) do not exhibit such restrictions and are actually, as a consequence of the minimal energy principle, trying to occupy the same single-particle ground state. These effects are captured by two different probability distributions that describe the thermal equilibrium in the two types of physical systems. The Fermi-Dirac distribution for fermions was originally derived in 1926 by its two authors independently, while trying to introduce quantization concepts into an ideal gas of particles obeying the Pauli exclusion principle. The Bose-Einstein distribution for bosons was introduced in 1924 by the joint effort of Bose and Einstein [1, 2]. At the time, it was a missing piece of knowledge for the complete explanation of the Planck's law of black body radiation.

In the high-temperature limit, both distributions are well approximated by a common Maxwell-Boltzmann distribution. The condition necessary for the effects of the quantum statistics to become observable can be roughly estimated as follows. The noninteracting particles of the mass M affect each other if their thermal de Broglie wavelength λ_T at temperature T,

$$\lambda_T = \sqrt{\frac{2\pi\hbar^2}{k_B T M}}\,, \tag{1.1}$$

is comparable to the inter-particle distance given by $n^{-1/3}$, where n is a typical particle density. Naturally, the notion of the "high temperature" and "low temperature" depends on the features of the considered system. For example, electrons in a typical metal at room temperature (300K) are quite accurately described by the Fermi-Dirac distribution, making the Fermi-Dirac statistics widely present in our everyday experience. Originally, the Bose-Einstein statistics was developed for the photons. Immediately after it was derived it was suggested that in the low-temperature limit a macroscopic occupation of the single-particle ground state should emerge. A phase exhibiting the macroscopic quantum phenomenon is denoted as the Bose-Einstein condensate (BEC). An important necessity for the system to develop this type of behavior is the conservation of a number of particles, and as the photons can be spontaneously created and annihilated, a BEC doesn't appear in this type of a system. Although the concept of a BEC arises at the essential level of the theory, it managed to escape our clear observation until the first breakthrough experiments in 1995 [3, 4]. Between 1924 and 1995 a BEC was mainly discussed in the relation to the fascinating low-temperature phenomena of superfluidity and superconductivity that include macroscopic quantum effects. On the other hand, sometimes it was even considered as an artifact of a noninteracting description of a bosonic gas.

To explain why the concept of a BEC may seem elusive, we elaborate on stringent requirements which are prerequisites to experimentally accomplish Bose-Einstein condensation. As already discussed, two relevant length scales are the de Broglie wavelength and the inter-particle distance. For the first scale to be large enough, in experiments we need light particles at low temperatures. To make the second length scale comparable to λ_T, the system of particles should be dense enough. However, the upper limit of the density is set by a requirement to remain close to the noninteracting gas description. Strong interactions could spoil the observation of a BEC phenomena, by modifying the ground-state of the system significantly. It is well known that at low temperatures most of the elements are in the solid or liquid state, thus the noninteracting gas description loses its relevance. Eventually, experiments [3, 16] reached the regime of a dilute weakly interacting gas of alkali atoms, with typical densities of atomic clouds in the range $10^{18}\,\mathrm{m}^{-3} - 10^{21}\,\mathrm{m}^{-3}$ (six order of magnitudes lower than the density of air) and typical temperatures of the order of nanokelvin. The hallmarks of the Bose-Einstein condensation were unequivocally discerned in this range of parameters and the importance of the experimental realization was recognized by a Nobel prize for physics in 2001.

With these experimental achievements, the window into unexplored landscapes of the nature was opened. Since then, the subject has evolved into a more general research field of ultracold atoms and we will mention only some of the topics currently explored to illustrate the versatility of possibilities. Once that the properties of a weakly interacting quantum gas were understood and explored to some extent, more complex and interesting phases of matter came to the focus of experimental research. Progress in the last decade has led to the realization of optical lattices which practically allow simulations of condensed matter and other systems within ultracold atoms framework, in the sense of Feynman's quantum simulator [8]. Phase diagrams of strongly interacting quantum gases with long-range dipolar interaction are currently explored. Beside the equilibrium properties, non-equilibrium and dynamical phenomena in these systems are also major research topic. Most recent advances include the realization of non-Abelian gauge fields, as well as bosonic systems with the spin-orbit type of coupling. Beside bosonic atoms, experiments are now performed with ultracold fermionic atoms and even with ultracold molecules (emergent field of ultracold chemistry). Even a photonic BEC has been produced recently [17]. Of course, the exciting experimental developments are led and closely followed by theoretical studies. Some of those will be presented in this thesis.

1.2 Few basic facts on Bose-Einstein condensation

To set up the stage and to sharpen our intuition on the facets of cold bosonic gases, first we review a textbook knowledge on the Bose-Einstein condensation of a noninteracting gas. Initial ideas about this type of phase transition were based on the considerations of a homogenous gas of particles. However, as will be explained later in this Chapter, all experimental realizations include an external confining trap. Most widely used is a harmonic trap and hence here we consider thermodynamic properties of harmonically trapped noninteracting bosons [18, 19].

1.2.1 Noninteracting bosonic gas in the harmonic trap

The average occupation of a single-particle state of the energy E_n at temperature T in the gas of noninteracting particles is given by the Bose-Einstein distribution as

$$\mathcal{B}_n(\mu, T) = \frac{1}{e^{\beta(E_n-\mu)} - 1}\,, \tag{1.2}$$

where $\beta = 1/k_B T$ is the inverse temperature and μ stands for the chemical potential. Formally speaking, we use the grand canonical ensemble description and assume that the system can exchange both the energy and the particles with a reservoir. By adjusting the value of the chemical potential μ, the average total number of particles N can be tuned to the desired value, corresponding to the number of particles in the system

$$N = N(\mu, T) = \sum_{n=0}^{\infty} \frac{1}{e^{\beta(E_n-\mu)} - 1} \,. \tag{1.3}$$

From Eq. (1.3), by a careful inspection, we realize that μ increases as the temperature gets lower. Also, we notice that, in order to have a well defined probability distribution, the condition $\mu \leq E_0$ has to be satisfied. It is this limitation that leads to the conclusion that at the certain temperature, for which $\mu \approx E_0$, the number of thermally occupied states,

$$N_{\mathrm{th}} = \sum_{n=1}^{\infty} \frac{1}{e^{\beta(E_n-E_0)} - 1} \,, \tag{1.4}$$

becomes saturated. By lowering the temperature further, the number of atoms that can be accommodated in the higher energy states decreases, yielding a macroscopic occupation N_0 of the ground state, $N_0 \sim N$. For a finite number of particles, the condensation sets in once the saturation of a thermal states is reached and we formally define the condensation temperature T_{c}^0 from the condition $N = N_{\mathrm{th}}$ and $\mu = E_0$. This yields

$$N = \sum_{n=1}^{\infty} \frac{1}{e^{\beta_{\mathrm{c}}^0(E_n-E_0)} - 1} \,, \tag{1.5}$$

where $\beta_{\mathrm{c}}^0 = 1/k_B T_{\mathrm{c}}^0$. Let us now focus on the harmonic trapping potential

$$V(\vec{r}) = \frac{1}{2} M(\omega_x^2 x^2 + \omega_y^2 y^2 + \omega_z^2 z^2) \,, \tag{1.6}$$

with well known energy levels $E_{\vec{n}} = \hbar \left((n_x + \frac{1}{2})\omega_x + (n_y + \frac{1}{2})\omega_y + (n_z + \frac{1}{2})\omega_z \right)$, where $\vec{n} = (n_x, n_y, n_z)$, and indices n_x, n_y and n_z take the integer values $0, 1, 2, \ldots$ The condensation temperature can be found from Eq. (1.5), using $\mu = E_{\vec{0}} = \frac{\hbar}{2}(\omega_x + \omega_y + \omega_z)$, and we get the following implicit equation for T_{c}^0:

$$N = \sum_{n_x, n_y, n_z} \frac{1}{e^{\beta_{\mathrm{c}}^0 \hbar(\omega_x n_x + \omega_y n_y + \omega_z n_z)} - 1} \,. \tag{1.7}$$

Summations in the last expression can be exactly performed only numerically, so in order to proceed further in an analytic way, we use a semiclassical approximation [19, 5]. Practically, this means that we neglect the discretness of energy levels and replace summations by the integrals over now continuous n_x, n_y and n_z. Mathematically speaking, the approximation is justified if the values of the functions which we sum over do not vary significantly over the summation step. For the Eq. (1.7), the mentioned condition translates into the high-temperature limit $k_BT \gg (E_{n+1} - E_n)$, where the thermal energy is larger than the typical spacing of energy levels. With this simplification, we obtain:

$$\begin{aligned} N &\approx \int_0^\infty \int_0^\infty \int_0^\infty \frac{dn_x dn_y dn_z}{e^{\beta_c^0 \hbar(\omega_x n_x + \omega_y n_y + \omega_z n_z)} - 1} \\ &= \sum_{m=1}^{\infty} \prod_{j=x,y,z} \int_0^\infty dn_j e^{-\hbar \beta_c^0 m \omega_j n_j} \\ &= \frac{1}{(\beta_c^0 \hbar)^3 \omega_x \omega_y \omega_z} \sum_{m=1}^{\infty} \frac{1}{m^3} \\ &= \frac{1}{(\beta_c^0 \hbar)^3 \omega_x \omega_y \omega_z} \zeta_3 \,, \end{aligned} \tag{1.8}$$

where we introduce the Bose function (the polylogarithm function) $\zeta_\alpha(x) = \sum_{n=1}^{\infty} \frac{x^n}{n^\alpha}$ and the abbreviation $\zeta_\alpha \equiv \zeta_\alpha(1)$ for the Riemann zeta function. From the last expression, we find that the condensation sets in for:

$$k_B T_c^0 = \frac{\hbar \bar{\omega}}{\zeta_3^{1/3}} N^{1/3} \,, \tag{1.9}$$

where $\bar{\omega}$ is a geometric mean $\bar{\omega} = (\omega_x \omega_y \omega_z)^{1/3}$. Consequently, we distinguish the phase with a macroscopic occupation of the ground state and denote it as the condensate phase, and the phase without a macroscopic value of N_0 that is designated as the (normal) gas phase. However, the phase transition is well defined only in the thermodynamic limit [5, 20] and hence in the case of finite-size systems we refer to T_c^0 as the condensation temperature instead of the critical temperature.

The BEC phase transition is usually depicted in the phase diagram showing the condensate fraction N_0/N versus temperature. From Eq. (1.8), we infer that in the condensate phase, the number of atoms in the thermal component is proportional to T^3 and that the condensate fraction satisfies

$$\frac{N_0}{N} = 1 - \left(\frac{T}{T_{\rm c}^0}\right)^3 . \tag{1.10}$$

Next, we address the local properties of a BEC and analyze density profiles in two different phases. In the gas phase, the density profile is given by:

$$n(\vec{r}) = n_{\rm th}(\vec{r}) = \sum_{n=0}^{\infty} \mathcal{B}_n(\mu, T)|\psi_n(\vec{r})|^2 , \tag{1.11}$$

while in the condensate phase, using $\mu = E_0$, we have

$$n(\vec{r}) = n_0(\vec{r}) + n_{\rm th}(\vec{r}) = N_0|\psi_0(\vec{r})|^2 + \sum_{n=1}^{\infty} \mathcal{B}_n(E_0, T)|\psi_n(\vec{r})|^2 , \tag{1.12}$$

where $\psi_n(\vec{r})$ are the single-particle eigenstates of the external trap potential. Summations over the complete eigenspectrum of the harmonic trap potential cannot be performed analytically, even though we know the energy levels explicitely. Very often, for the purpose of an analytical consideration, the density profile of the gas phase is calculated within the semiclassical approximation where we use the classical Hamiltonian $\mathcal{H}(\vec{r}, \vec{p}) = \vec{p}^2/2M + V(\vec{r})$ and count the number of states in the phase space volume $d\vec{r}d\vec{p}$ as $d\vec{r}d\vec{p}/(2\pi\hbar^3)$. Within this approximation, we calculate

$$n_{\rm th}(\vec{r}) \quad = \quad \int \frac{d\vec{p}}{(2\pi\hbar)^3} \frac{1}{e^{\beta(\mathcal{H}(\vec{r},\vec{p})-\mu)} - 1} = \frac{1}{\lambda_T^3} \zeta_{3/2}(e^{\beta(\mu - V(\vec{r}))}) . \tag{1.13}$$

An important prerequisite, which guarantees the validity of this approximation, is that the de Broglie wavelength λ_T of particles has to be smaller than the characteristic length scale over which the external potential varies significantly [19]. The approximation cannot be used for the ground state, which has to be treated fully quantum mechanically. In addition, we emphasize that, in order for the Eq. (1.13) to be well defined, the value of the chemical potential has to satisfy the condition

$$\mu \leq \min_{\vec{r}} V(\vec{r}) . \tag{1.14}$$

The requirement for the achievement of a BEC can be rephrased in terms of characteristic length scales using Eq. (1.13). It is easy to show that, at the onset of

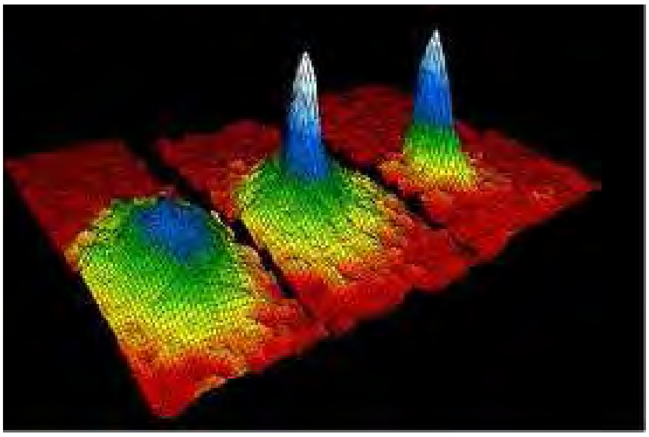

Figure 1.1: The hallmark of the Bose-Einstein condensation - a prominent density peak appears below the condensation temperature. Density profiles of the expanded cloud are shown at three different temperatures. From the left to the right we see bosonic cloud right above the condensation transition, just below the condensation transition and in the regime with almost a pure condensate. The experimental result is originally presented in Ref. [3] and this figure is taken from Ref. [5].

the BEC, the relation

$$n(0)\lambda_T^3 \approx \zeta(3/2) \approx 2.61238 \tag{1.15}$$

holds. Not surprisingly, this condition is very close to the intuitive argument given at the beginning of the Chapter.

The noticeable feature of the condensate phase in the harmonic trap, not present in the gas phase, is a prominent density peak located at the trap center that reflects macroscopically occupied ground state which has the symmetry of the trap potential, superimposed onto the broad thermal distribution. This is illustrated in Fig. 1.1. A bimodality of the density distribution is an important signature of the onset of Bose-Einstein condensation.

An important and convenient aspect of the harmonic trap is that the single-particle ground-state is localized both in the real and in the momentum space. Hence, beside static density profiles of the trapped atoms, another possibility for the experimental differentiation of the phases is free expansion of the gas from the trap. Initially, the gas is in the thermal equilibrium in the trap, and then suddenly the trap is switched off and the gas is allowed to expend freely. To describe the thermal gas we use the semiclassical approximation. The density profile after the expansion time t is given by [21]

$$\begin{aligned} n_{\mathrm{th}}(\vec{r},t) &= \frac{1}{(2\pi\hbar)^3}\int d\vec{p}\,d\vec{r}_0\frac{1}{e^{\beta(\mathcal{H}(\vec{r}_0,\vec{p})-\mu)}-1}\delta^3\left(\vec{r}-\vec{r}_0-\frac{\vec{p}}{M}t\right) \\ &= \frac{1}{\lambda_T^3}\prod_{\sigma=x,y,z}\left(\frac{1}{1+\omega_\sigma^2t^2}\right)^{1/2}\zeta_{3/2}\left(e^{\beta\mu-\frac{\beta M}{2}\left(\frac{\omega_x^2x^2}{1+\omega_x^2t^2}+\frac{\omega_y^2y^2}{1+\omega_y^2t^2}+\frac{\omega_z^2z^2}{1+\omega_z^2t^2}\right)}\right). \end{aligned}$$

For long expansion times we find an approximate expression for the density distribution of a thermal gas in the form [21]

$$n_{\mathrm{th}}(\vec{r},t) \sim \frac{1}{\lambda_T^3}\zeta_{3/2}\left(e^{\beta\mu-\frac{\beta Mr^2}{2t^2}}\right). \tag{1.16}$$

As we see, although the initial density distribution is anisotropic, after the expansion of the thermal cloud, we obtain an isotropic density profile. Another important thing that we learn from the result (1.16) is that expanded density profiles actually carry information on the initial velocity distribution of the cloud. This becomes obvious when we rewrite Eq. (1.16) as

$$n_{\mathrm{th}}(\vec{r},t) \sim \frac{1}{\lambda_T^3}\zeta_{3/2}\left(e^{-\frac{Mv^2}{2k_BT}}\right). \tag{1.17}$$

Now we compare this behavior with the expansion of a pure condensate ($N = N_0$) in the ground state of the trap (1.6). For the time evolution of a quantum mechanical state, we have

$$\begin{aligned} \psi_{\mathrm{HO}}(\vec{r},t) &= \langle\vec{r}|e^{-it\frac{\hat{\vec{p}}^2}{2M}}|\psi_{\mathrm{HO}}\rangle = \int d\vec{p}\,\langle\vec{r}|\vec{p}\rangle e^{-it\frac{\vec{p}^2}{2M}}\langle\vec{p}|\psi_{\mathrm{HO}}\rangle \\ &= \frac{1}{\pi^{3/4}}\prod_{\sigma=x,y,z}\left(\frac{\hbar}{M\omega_\sigma}\right)^{-\frac{1}{4}}(1+it\omega_\sigma)^{-\frac{1}{2}}e^{-\frac{\sigma^2M\omega_\sigma}{2\hbar}\frac{1-it\omega_\sigma}{1+t^2\omega_\sigma^2}}. \end{aligned} \tag{1.18}$$

From Eq. (1.18) we conclude that in the limit of long propagation times, the condensate widths are given by $(\hbar\omega_\sigma/M)^{\frac{1}{2}}t$ [19]. Obviously, the expansion of the ground state is spatially anisotropic and the aspect ratio of the cloud is inverted during the expansion. The behavior is substantially different from the isotropic expansion of the thermal cloud and can be used as a diagnostic tool for the presence of the condensate in the system.

Now that we have introduced the theoretical notations, in the next subsection we discuss in some detail the experimental realization of a BEC.

1.2.2 Experimental realization

As already mentioned, it was a pursuit of the clear physical realization of a very fundamental concept of a BEC that triggered an enormous amount of the experimental effort starting in the eighties of the last century. Although today BECs of different atoms are readily produced in laboratories worldwide, the creation of quantum degenerate atomic gases took many years during which many experimental techniques at the forefront of technology were developed. In this subsection we give a basic description of today's typical experimental setup with a very brief historical overview. The main reference we rely on is Ref. [21].

Already in the early experimental phase of the quest for nanokelvin temperatures, possibility of storing atoms in any type of a vessel was ruled out. Instead, a proper configuration of magnetic, optical or combined magneto-optical potential is used as an external confining potential, usually called a trap. Atoms are trapped around the potential minimum due to interaction of their induced magnetic or electric dipole moments with external field. In most cases, harmonic potential

$$V(\vec{r}) = \frac{1}{2}M(\omega_x^2 x^2 + \omega_y^2 y^2 + \omega_z^2 z^2)\,, \tag{1.19}$$

is a reasonable approximation of the external trap potential. Different trap configurations have been experimentally realized: for instance, highly elongated traps (which can be considered as effectively one dimensional), or pancake shaped traps (effectively two-dimensional regime). Beside this common type of a harmonic confinement, periodic external potentials (optical lattices) are widely used in nowadays experiments. We will mainly consider an axially-symmetric harmonic trap potential, with the radial trap frequency $\omega_x = \omega_y = \omega$. The usual form of the potential is

$$V(\vec{r}) = \frac{1}{2}M\omega^2(\rho^2 + \lambda_z^2 z^2)\,, \tag{1.20}$$

where we introduce the trap aspect ratio $\lambda_z = \omega_z/\omega$. Typical values of the trap frequencies are of the order of $2\pi \times (10 - 100)$Hz, with a typical length scale of the order of several microns.

The initial attempts to realize a BEC, focused on the spin-polarized hydrogen. The hydrogen was singled out among other atom types since it remains in the gas phase even at very low temperatures. Correspondingly, many techniques were originally developed for the hydrogen samples. Yet, it turned out that alkali atoms, such as Rb, Li, Na, K, have several advantages over hydrogen. First, they can be cooled using laser cooling techniques [21, 22] by the commercially available lasers whose wavelengths correspond to the transitions between energy levels of alkali atoms. Second, stronger elastic collisions allow an improved cooling rate in the process of evaporative cooling [21, 23]. Evaporative cooling can be performed in several ways. Usually it is implemented by lowering the trap depth. In this way, atoms with more than average energy are removed from the trap, hence allowing the remaining atoms to equilibrate at lower temperature. Another way is to perform the radio frequency forced evaporation by transferring internal state of energetic atoms into the untrapped configuration. By varying the used frequency, the final value of the temperature can be controlled. One of the crucial steps that finally led to the achievement of the high phase-space density necessary for the observation of a BEC was precisely the combination of the laser cooling and evaporative cooling techniques.

Another vital experimental aspect is the characterization of a BEC once it has been produced. In typical experiments, the sample has the size from 10^3 to 10^6 bosonic alkali atoms, trapped in the external field in the space volume of $(100\mu\mathrm{m})^3$, with a density in the range $10^{18}-10^{21}\ \mathrm{m}^{-3}$, and the temperature of 100 nK. How the system can be probed to confirm that it really represents a BEC and has properties predicted theoretically? As usual, the probe has to be “gentle” enough not to perturb the system significantly, hence cold bosonic gases are mainly probed optically. There are several widely used techniques, and we mention the most important ones.

From early experiments until today, the absorption imaging remains the most used tool for characterization of a BEC. The sample is irradiated by a laser beam resonant with an internal atomic transition and the shadow of the sample is measured by a CCD camera. Such a procedure may not produce the desired results always, since the image can be blacked out by the high density of the sample. For this reason, once the BEC regime has been reached, the trap is usually turned off, the cloud is allowed to expand freely for several seconds, and then the absorption imaging is performed. The procedure is denoted as the time-of-flight (TOF) measurement. In general, the quantity which is measured in this way is the optical density of the sample (responsible for the absorption). It is proportional to the column particle density, which can be determined by this measurement technique.

In the first papers [3, 4], the TOF approach was used to prove the presence of the condensate in the sample based on the signatures discussed in subsection 1.2.1 for the noninteracting gas in the harmonic trap. Time-of-flight images revealed the emergence of density peaks on top of broad thermal distributions. Also, the peak in the density became more and more prominent as the temperature decreased further. In addition, the measured velocity distribution demonstrated stark contrast in the regimes above and below condensation temperature, being isotropic in the former case and highly anisotropic in the latter case, reflecting the anisotropy of the trap. From the measured density profiles, other quantities can be also estimated. Usually, noninteracting gas model is used for the extraction of the sample properties. For example, the temperature of the sample is determined by fitting a function (1.16) to the experimental data for the thermal cloud.

Obviously, the TOF measurements are destructive and make the observation of the condensate dynamics quite complicated. With this technique a real-time monitoring of a dynamical process requires many steps: initially, a BEC is produced, then in the certain interval time some dynamical process happens, and finally the BEC is destructively imaged. To obtain another piece of information on the dynamical evolution, for another value of the time of evolution, the whole procedure has to be repeated, starting from the production of a BEC. Another difficulty arises in the interpretation of experimental data. The noninteracting gas model for the harmonic trap is simple enough to enable quantitative explanation, however, the accurate description of the expanding interacting gas at finite temperature is far more complicated. Very early [16], dispersive imaging techniques were utilized for gathering in-situ information on the density profiles of cold gases in a nondestructive way. One of the techniques used successfully for an in-situ imaging of dense samples is a phase-contrast imaging. This procedure can be implemented through two different experimental protocols. In the first one, the light diffracted from the sample is recorded, while in the second one, the interference patterns of the phase-shifted incident light and the diffracted signal are measured. In this way, information on the complex phase acquired by the non-resonant light in the atomic sample is extracted [24]. Again, the quantity which is measured is the optical density along the line of sight, yet the measurement can be performed even for a very dense samples. This type of measurement allows multiple imaging of the same cloud, hence it is much more convenient for studying condensate dynamics.

Up to now we have only considered a noninteracting gas of particles, because this is the system that was originally used to derive the Bose-Einstein distribution. Of course, realistic systems require many-body approach including interactions and the noninteracting description is only an approximation. Now we discuss the type and strength of interactions in the dilute atomic systems, and later in the thesis we will explain how they modify the noninteracting picture.

A predominant interaction in dilute cold atom systems is a two-body interaction, typically in the form of scattering of atoms. In this thesis we consider only a short range van der Waals interaction between charge-neutral atoms. A dipole-dipole interaction is also present, but usually can be neglected in the case of alkali atoms. However, it plays prominent role in recent experiments with ^{52}Cr, where the effects of long-range dipolar interaction become measurable [25]. Due to diluteness of the system, a typical atom-atom distance is larger then the effective interaction range, and details of the short-range interaction potential are not so important. In the low-energy low-momentum limit, the potential can be parameterized by a single parameter a, representing the atomic s-wave scattering length. In the pseudopotential description, the van der Waals interaction is replaced by a contact potential

$$V_{\text{int}}(\vec{r}-\vec{r}\,') = g\delta(\vec{r}-\vec{r}\,')\,, \tag{1.21}$$

where the interaction strength is given by

$$g = \frac{4\pi\hbar^2 a}{M}\,. \tag{1.22}$$

The interaction is repulsive for $g > 0$ and attractive in the opposite case. It is known that a BEC with attractive interactions is unstable toward collapse if the particle density is high enough [5]. In this thesis, we confine the discussion to the repulsively interacting BECs.

In general, scattering properties of atoms depend on their internal states. This fact allows the adjustment of the s-wave scattering length by the control of the external parameters of the system. More specifically, several atomic species exhibit the so-called Feshbach resonance - dependence of the scattering length on the external magnetic field B, which is given by the expression

$$a(B) = a_{\text{BG}}\left(1 + \frac{\Delta_B}{B - B_\infty}\right)\,, \tag{1.23}$$

where a_{BG} is the off-resonant scattering length, B_∞ is the resonance position and Δ_B is the resonance width. Feshbach resonance is a very useful tool that allows fine and versatile tuning of the interaction strength in the cold atom systems over a range of several orders of magnitude from highly repulsive to highly attractive regime. A phenomenon is well known in atomic and nuclear physics as Feshbach-Fano resonance [26, 27]. Beside the original reference by Tiesinga et al. [28] which analyzed the benefits of using the resonance in the experiments with ultracold atoms, the underlying theory has been discussed in the review paper by Chin et al. [6] and in several textbooks [19, 29]. Here we give only a brief explanation, based on a fact that two atoms can interact via an energetically open or closed channel. These two channels are coupled and include Zeeman terms. By tuning the external magnetic field it is possible to make a bound state of a closed channel resonant with the income energy in the open channel. In that case the scattering length diverges, as given in Eq. (1.23) for $B = B_\infty$. The properties of Feshbach resonances are exploited in many experiments and one of the topics in this thesis will explore some related recent experimental results.

To summarize the subsection, the achievement of the BEC regime took a lot of effort and many techniques had to be developed for this purpose. However, once this has been achieved, the cold atomic systems have become the cleanest experimental setting for studying macroscopic quantum phenomena. All parameters of these systems are highly controllable and tunable: the geometry, temperature, density and even the type and the strength of interaction. For this reason the field of ultracold atoms is still in the process of strong expansion and cross-collaboration with other fields, and further new important insights are expected.

1.2.3 Interacting bosons at low temperatures

After discussing physical characteristics of cold bosonic atoms, we are ready to write down the Hamiltonian of the system:

$$\hat{H} = \int d\vec{r} \left(-\hat{\psi}^\dagger(\vec{r}) \frac{\hbar^2}{2M} \nabla^2 \hat{\psi}(\vec{r}) + V(\vec{r}) \hat{\psi}^\dagger(\vec{r}) \hat{\psi}(\vec{r}) + \frac{g}{2} \hat{\psi}^\dagger(\vec{r}) \hat{\psi}^\dagger(\vec{r}) \hat{\psi}(\vec{r}) \hat{\psi}(\vec{r}) \right) . \quad (1.24)$$

Here $\hat{\psi}^\dagger(\vec{r})$ and $\hat{\psi}(\vec{r})$ are bosonic field operators in the second quantized form, and satisfy commutation relations $[\hat{\psi}(\vec{r}), \hat{\psi}(\vec{r}\,')] = 0$, $[\hat{\psi}^\dagger(\vec{r}), \hat{\psi}^\dagger(\vec{r}\,')] = 0$, $[\hat{\psi}^\dagger(\vec{r}), \hat{\psi}(\vec{r'})] = \delta(\vec{r} - \vec{r}\,')$. On the right hand side of Eq. (1.24) we have the kinetic energy term, potential energy of particles in the external trap given by $V(\vec{r})$ and interaction term which stems from $\int d\vec{r}d\vec{r}\,'V_{\text{int}}(\vec{r}-\vec{r}\,')\hat{\psi}^{\dagger}(\vec{r})\hat{\psi}(\vec{r})\hat{\psi}^{\dagger}(\vec{r}\,')\hat{\psi}(\vec{r}\,') = g\int d\vec{r}\hat{\psi}^{\dagger}(\vec{r})\hat{\psi}^{\dagger}(\vec{r})\hat{\psi}(\vec{r})\hat{\psi}(\vec{r})$.

Hamiltonian given by Eq. (1.24) without the external trap potential was studied in the early work of Bogoliubov in relation to superfluidity observed in ^{4}He [30]. It represents the starting point in theoretical studies of a BEC. Here we give an elementary exposition of main ideas of the Bogoliubov and, in parallel, we introduce concepts important for the description of an interacting BEC.

In the homogenous case, a good quantum number of the system is the wavevector $\vec{k}$. Therefore, we use the decomposition

$$\hat{\psi}(\vec{r}) = \frac{1}{v^{1/2}}\sum_{\vec{k}} e^{i\vec{k}\vec{r}}\hat{a}_{\vec{k}}\,, \tag{1.25}$$

where $\hat{a}_{\vec{k}}$ are annihilation operators in the occupation number basis, with single-particle eigenfunctions in the form of plane waves. In the noninteracting limit, we expect macroscopic occupation N_0 of the ground state that we designate as $|N_0\rangle$. If we take into account the exact relations

$$\hat{a}_0|N_0>=\sqrt{N_0}|N_0-1>, \quad \hat{a}_0^{\dagger}|N_0>=\sqrt{N_0+1}|N_0+1>\,, \tag{1.26}$$

and the fact that $N_0+1\approx N_0-1\approx N_0$, we arrive at the following approximations which replace operators $\hat{a}_0$ and $a_0^{\dagger}$ with c-numbers: $\hat{a}_0\approx\sqrt{N_0}$ and $\hat{a}_0^{\dagger}\approx\sqrt{N_0}$. The error made by using this approximation is of the order of $[a_0, a_0^{\dagger}] = 1$, and can be neglected compared to the macroscopic value of N_0. Said another way, we have approximated the expression (1.25) by

$$\hat{\psi}(\vec{r}) \approx \psi + \delta\hat{\psi}(\vec{r})\,, \tag{1.27}$$

where $\psi = (N_0/v)^{1/2} = n_0^{1/2}$ is a classical field, and the operator $\delta\hat{\psi}(\vec{r})$ corresponds to quantum fluctuations around the classical value. The next step in the Bogoliubov approach is to consider quantum fluctuations as being small and to keep only terms up to the second order in $\delta\hat{\psi}$. With these simplifications we can find an appropriate transformation which converts the quadratic approximation of the Hamiltonian into the diagonal form. The final result is the Bogoliubov excitation spectrum of the system given by

$$\epsilon_{\mathrm{Bog}}\left(\vec{k}\right)=\sqrt{\frac{\hbar^2\vec{k}^2}{2M}\left(\frac{\hbar^2\vec{k}^2}{2M}+2gn_0\right)}\,. \tag{1.28}$$

In the limit of large $|\vec{k}|$, the spectrum yields excitations of a noninteracting gas. Collective phenomena appear in the long wavelength limit where the collective phonon mode is found [30]. The microscopic derivation of the excitation spectrum (1.28) fits well with the Landau's phenomenological description of the superfluid. Another relevant quantity that can be derived within the Bogoliubov framework is the condensate depletion due to interactions at $T=0$. The number of non-condensed particles is proportional to $\sqrt{na^3}$, which for the case of strongly interacting system such as liquid ^{4}He yields the depletion as high as 90%. For this reason, the superfluidity of ^{4}He is considered only as an indirect manifestation of the Bose-Einstein condensation.

In general, the relation between the condensation and superfluidity is a subtle one. It can be shown that the macroscopic occupation of the ground state (1.27) introduces the off-diagonal long range order (ODLRO) into the system [31]:

$$\lim_{|\vec{r}-\vec{r}\,'|\to\infty}\langle\hat{\psi}^\dagger(\vec{r})\hat{\psi}(\vec{r}\,')\rangle=n_0\,. \tag{1.29}$$

However, long range correlations that are the manifestation of a superfluidity may be present even without the condensation, as for instance in two-dimensional systems [7].

In order to put the phenomenon of Bose-Einstein condensation into a broader context, we emphasize that the decomposition (1.27) represents the spontaneous breaking of the U(1) symmetry related to the conservation of the number of particles in the system described by the Hamiltonian (1.24). Hence, ψ is the order parameter that acquires nonzero value in the condensed phase [31, 32].

Quantitative tests of the theoretical concepts introduced in this subsection became possible only with the experimental realization of Bose-Einstein condensation in dilute vapors of alkali atoms. However, the experiments introduced an important additional feature - the inhomogeneity of the system due to the trapping potential. The first theoretical study of a interacting bosonic system in a harmonic trap was presented in Ref. [33] in relation to the early experiments that were trying to produce hydrogen BEC. Since then, different approaches have been used to describe the condensation of interacting bosonic gas in an external trap potential. In this thesis we will work in the mean-field framework, with an order parameter introduced in a similar manner as in Eq. (1.27). The exposition of the mean-field framework for the trapped system is given in Chapter 4.

Throughout the years, a lot has been learned about the phenomenon of a BEC by a powerful combination of ingenious experiments and equally ingenious theoretical modeling. Yet, despite the intensive progress in the field, there are still many open questions related to the fundamental topics, as will be indicated throughout the thesis.

1.3 This thesis

The main objective of this thesis is a thorough analysis and understanding of two interesting physical scenarios for the manipulation of cold bosonic atoms that have recently came into the focus of the experimental research. Namely, we will first explore the details of the phase diagram of a rotating ideal bosonic gas in an anharmonic trap. As a second topic, we will investigate the nonlinear features of the excitation of collective oscillation modes by a modulation of the interaction strength.

On the way to accomplish this, in Chapter 2 we work out the details of the numerical method which is capable of providing us with a highly-accurate energy spectrum of a few-body system. As we already saw in the subsection 1.2.1, the accurate information on the energy spectrum of the system is required for the description of a BEC phase transition. The method that we elaborate on is based on the exact diagonalization of the short-time evolution operator and was introduced earlier in a simplified form [9]. To understand the benefits of the method, we first analyze the errors associated with space discretization of the time-evolution operator. Based on analytical and numerical analysis, we show that the discretization error vanishes exponentially with $1/\Delta^2$, where Δ is the discretization spacing. This nonperturbative behavior highly outperforms polynomial errors in discretization spacing Δ which arises in the common real-space discretization of the Hamiltonian. The key complexity of the method is the accurate calculation of the matrix elements which are given by transition amplitudes. To address this requirement, we apply recently introduced effective action approach [10, 11] for obtaining short-time expansion of the propagator to very high orders. We demonstrate high efficiency of the method on several one- and two-dimensional models.

Having the efficient numerical method at our disposal, in Chapter 3 we study properties of a rotating ideal gas. The introduction of the angular momentum into the system is one way of reaching the highly correlated regime in the cold atom setup. As will be explained, beside other effects, a rotation effectively introduces a deconfining component into the trap potential. Particularly, in the regime of a fast rotation, the gas may experience the complete deconfinement. Hence an additional quartic potential was used for the trapping in the experiments from Ref. [12], but the interesting regime of fast rotation has not been completely understood. Using the exact diagonalization of a time evolution operator, we study numerically Bose-Einstein condensation in the modified external potential which is a combination of the harmonic and quartic component. The shape of the potential changes from convex with a single minimum to the Mexican hat shape, depending on the rotation frequency. We explore how the change of the trapping potential influences the phase diagram properties. We also calculate the density profiles of the gas and time-of-flight pictures in different regimes and find that typical time-scales for free expansion are increased by an order of magnitude in the delicate regime of fast rotation.

In Chapter 4, we continue and expand a brief exposition of subsection 1.2.3, and discuss several different mean-field frameworks for the description of properties of a weakly interacting BECs. First we present the zero temperature mean-field description. We neglect quantum fluctuations and assume that all atoms are condensed at $T = 0$. In that case, we show that BEC properties are captured by the effective nonlinear equation, the famous Gross-Pitaevskii equation [34, 19, 13, 14]. Then we move to the study of finite-temperature mean-field models of BEC. The relevance of this aspect is two-fold: on one hand, mean-field models are widely used for the interpretation of experimental data, and on the other hand, from the conceptual point of view, it turns out that different models suffer from different unphysical drawbacks. We review and compare the existing models by calculating density profiles within different approximations. To illustrate the influence of weak interactions on the Bose-Einstein condensation, we re-derive the mean-field interaction-induced shift of the condensation temperature.

Chapter 5 deals with the collective excitations of BEC in the nonlinear regime. Characteristics of a BEC can be probed by monitoring its dynamical response to the external perturbation. Usually, the ground-state BEC is produced and then it is perturbed by a modulation of the external trap potential. A specific feature of the recent experiment [15] is the harmonic modulation of the s-wave scattering length via a Feshbach resonance, yielding a time-dependent interaction strength $g = g(t)$. An external driving frequency Ω is used for the modulation, and depending on its closeness to some of the condensate eigenfrequencies, either a resonant or non-resonant behavior can be observed. This is a new venue for studying nonlinear dynamical regime, since the equation governing the condensate dynamics on the mean-field level is nonlinear, and large amplitude oscillations are readily produced in the resonant regime. By combining different analytical and numerical methods we analyze how nonlinear effects influence the properties of the excited collective modes, with implications on the interpretation of the actual experimental data. Prominent nonlinear features, such as: mode coupling, higher harmonics generation, and significant shifts in the frequencies of collective modes are found and quantitatively explained using an analytic perturbative approach.

At the end of each chapter, we present possible future directions for extending the study of research topics of this thesis. Finally, we summarize all results in Chapter 6. Additional material and derivations are organized in Appendices.

Chapter 2 Properties of quantum systems via diagonalization of transition amplitudes

Deep in the condensate phase, features of cold atoms are determined by low-lying energy levels: ground state and few excited states corresponding to the thermal cloud. On the other hand, thermodynamic properties and details of the BEC phase transition are determined by the full energy spectrum. As we have seen in Chapter 1, the exact calculation of the condensation temperature, even for an ideal bosonic gas, requires a summation over the whole energy spectrum of the system. Due to its simplicity, the semiclassical approximation is widely used for this purpose. In this Chapter we work out details of a numerical method based on the exact diagonalization of a time-evolution operator that allows us access to a very large number of numerically exact energy levels of few-body systems. Afterwards, in Chapter 3, we use the method to find the condensation temperature of the fast-rotating ideal gas in an anharmonic trap.

In the standard operator formulation of quantum mechanics, the description of a physical system is based on constructing the Hamilton operator $\hat{H}$. Properties of quantum systems are then obtained by solving the corresponding time-independent Schrödinger equation,

$$\hat{H}|\psi\rangle = E|\psi\rangle \,. \tag{2.1}$$

Exact solutions can be found only for a very limited set of simple models. A wide variety of analytical approximation techniques has been developed in the past for treatment of such problems. In addition, the last two decades have seen a rapid growth in the application of different numerical methods for solving the Schrödinger equation. Approaches based on real-space discretization start from some given finite-difference prescription. Such methods have been extensively studied in the past, and the main difficulties follow from the finite-difference representations of the kinetic operator.

A numerical approach based on diagonalizing of the evolution operator, introduced in Ref. [9], does not suffer from problems with the representation of differential operators on real-space grids, and has substantial advantages in practical applications to few-body problems. Effectively, in this way the problem is transferred from that of representing the kinetic operator on a real-space grid to the calculating of corresponding transition amplitudes. Detailed analysis of the errors associated with the implementation of this approach is the main objective of this Chapter. It provides full understanding of the method and allows its optimal use, as well as further significant improvements within a generalized calculation scheme.

The advantages of the method discussed here [9, 35, 36, 37] follow from two key properties. First, the objects being diagonalized are transition amplitudes, which are well defined irrespective of discretization scheme, i.e. the exponential of the Hamiltonian effectively regularizes the kinetic operator, making possible representations of the evolution operator that do not depend on the space grid. Second, the successful diagonalization of the evolution operator $\exp(-t\hat{H})$ for any time of propagation t immediately gives the solution of the eigenproblem for the Hamiltonian. Thus, the time of propagation in this approach is just an auxiliary parameter. Said another way, we use the time-dependent evolution operator to extract time-independent information regarding the quantum system. If one could calculate transition amplitudes exactly, then the obtained results for the energy eigenproblem would not depend on the time of propagation. However, in practical applications one uses some approximation scheme to calculate the amplitudes, and in this case the precision of the obtained results for energy eigenvalues and eigenstates does depend on time t. The general applicability of the outlined method follows from the fact that one can use short-time propagation amplitudes to obtain highly accurate results.

In order to complete this numerical method and make it generally applicable, it is necessary to address the following key questions:

1. How to analytically estimate the effects of spatial discretization?
2. How to optimize the choice of evolution time t, so as to minimize errors?
3. How to accurately calculate transition amplitudes?

The authors in Ref. [9] have only briefly commented on the first two questions, and numerically determined the values of parameters that can be used for precise calculations of energy eigenvalues and eigenstates for several models. In this Chapter we address the above questions, which have not been fully answered before. First we present the method and notation, and identify the sources of the errors present in real-space discretization approaches. Then we analyze in detail the above questions 1 and 2, and discuss the effects of discretization on the numerically calculated values of the observables for a given physical system. We analytically derive estimates for errors stemming from space discretization coarseness, finite size effects, and choice of the evolution time parameter t. All the analytically derived results are numerically verified to hold on several instructive models.

Errors associated with the time of evolution parameter t (question 3 above) must be carefully taken into account and may substantially limit the precision of numerical calculation in the diagonalization method. This problem was not addressed at all in Ref. [9], but has been addressed recently [38, 39, 40, 41, 42] using various approaches. We significantly improve the method by applying the recently introduced effective action approach [43, 44, 10, 45, 46, 11] to completely resolve the problem formulated in question 3. We stress that use of higher-order effective actions represents an efficient and numerically inexpensive way to calculate transition amplitudes, and leads to many orders of magnitude increase in precision of calculated properties of the system. We will demonstrate on several lower-dimensional models how use of higher-order effective actions significantly reduces numerical errors and systematically improves the obtained energy eigenvalues and eigenstates.

This Chapter gives a complete analysis of the method based on the diagonalization of transition amplitudes, providing us with necessary analytical knowledge to estimate errors of all types associated with this method and to numerically very accurately calculate large numbers of energy eigenvalues and eigenstates. This invites various applications of the method to the study of few-body quantum systems, some of which are discussed throughout the thesis.

The expressions written throughout the second and third section are, for compactness of notation, for one particle in one dimension. Extension to more particles and dimensions is straightforward, just as with the above short-time transition amplitude. Note that we are working in imaginary time, which is well suited for numerical calculations and does not affect in any way calculated energy levels nor other time-independent properties of the system. We have also set $\hbar$ to unity in this Chapter.

2.1 Space-discretized Schrödinger equation

In the coordinate representation the time-independent Schrödinger's equation takes the form

$$\int dy\, \langle x|\hat{H}|y\rangle\, \langle y|\psi\rangle = E\, \langle x|\psi\rangle\, . \tag{2.2}$$

The standard way to numerically implement exact diagonalization is to go from continuous coordinates x to ones living on a discrete space grid $x_n = n\Delta$, where Δ is a given spacing and $n \in \mathbb{Z}$. Integrations in the above equation are performed using the simple rectangular quadrature rule, or some higher-order finite-difference formula. This completes the transition to the space-discretized counterpart of the continuous theory, however, to represent this on a computer we still have to restrict the integers n to a finite range. This is equivalent to introducing a space cutoff L, or putting the system in a infinitely high potential box. For example, the rectangular quadrature rule leads to the following space-discretized Schrödinger equation

$$\sum_{m=-N_{\rm cut}}^{N_{\rm cut}-1} H_{nm} \langle m\Delta|\psi\rangle = E(\Delta, L)\, \langle n\Delta|\psi\rangle\, , \tag{2.3}$$

where $H_{nm} = \Delta \cdot \langle n\Delta|\hat{H}|m\Delta\rangle$, $N_{\rm cut} = [L/\Delta]$, and square brackets represent the integer part of the argument. As a result, we have obtained a $2N_{\rm cut} \times 2N_{\rm cut}$ matrix that represents the Hamiltonian of the system. The eigenvalues of this matrix depend on the two parameters introduced in the above discretization process: cutoff L and discretization step Δ. Continuous physical quantities are recovered in the limit $L \to \infty$ and $\Delta \to 0$. The outlined procedure is very useful in dealing with spatially localized physical problems, such as electronic structure calculations in semiconductor and polymer physics [47].

The two approximations involved in the discretization procedure, characterized by parameters Δ and L, are common steps in solving eigenproblems of Hamiltonians in e.g. electronic structure calculations [47], and as such have been extensively analyzed. The imposed constraint on the values of spatial coordinates to the finite interval $(-L, L)$ is a valid approach for capturing information on localized eigenstates. In this approximation the system is effectively surrounded by an infinitely high wall, and as the cutoff L tends to infinity, we approach the exact energy levels always from above, which is a typical variational behavior. Therefore, we designate errors associated with the cutoff L as variational. The effects of the discretization step Δ are more complex, and follow from the fact that the kinetic energy operator cannot be exactly represented on finite real-space grids. For example, a typical naive discretization of the kinetic energy operator gives in our notation the following Hamiltonian matrix elements [48]

$$H_{nm} = \begin{cases} 1/\Delta^2 + V(n\Delta) & \text{if } n = m \\ -1/(2\Delta^2) & \text{if } |n-m| = 1 \\ 0 & \text{otherwise.} \end{cases} \tag{2.4}$$

Note that in the absence of a potential term V in the Hamiltonian, the above definition corresponds to a tight-binding model [48]. This prescription leads to numerical results for eigenvalues which in the $\Delta \to 0$ limit converge to the exact continuum values as Δ^2. The errors associated with this approach have non-variational behavior, i.e. the obtained results are not always upper bounds of the exact energy levels. Several papers discuss this issue and analyze the behavior of errors in the direct diagonalization approach (for more details, see Refs. [49, 50] and references therein). The state-of-the-art in this approach is a set of systematically improved prescriptions for discretization of the kinetic energy operator, which speeds up convergence to the continuum limit to higher powers of Δ^2. However, within this approach convergence is always polynomial in Δ. Some recent results [51] also exist on extensions of this approach that provide effective variational behavior of the discretized kinetic energy operator.

As outlined in the Introduction, we focus on an alternative approach, based on solving the eigenproblem of the corresponding transition amplitudes as proposed in [9]. The central equation is

$$e^{-t\hat{H}}|\psi\rangle = e^{-tE}|\psi\rangle\,, \tag{2.5}$$

or in the discretized form

$$\sum_{m=-N_{\text{cut}}}^{N_{\text{cut}}-1} A_{nm}(t)\,\langle m\Delta|\psi\rangle = e^{-t\,E(\Delta,L,t)}\,\langle n\Delta|\psi\rangle\,, \tag{2.6}$$

where $A_{nm}(t) = \Delta\cdot A(n\Delta, m\Delta; t) = \Delta\cdot\langle n\Delta|e^{-t\hat{H}}|m\Delta\rangle$. In this approach the time of evolution t plays the role of an auxiliary parameter. This parameter is not related to the discretization, and in a continuous theory it does not affect the obtained eigenvalues and eigenstates. However, in a discretized theory the numerically calcu-

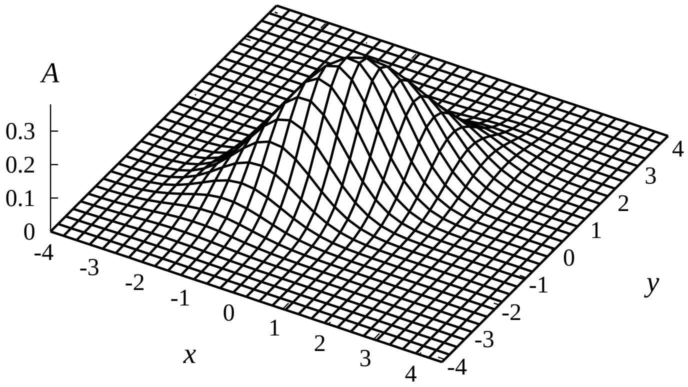

Figure 2.1: Harmonic oscillator transition amplitude as a function of coordinates x and y for $t = 1$.

lated eigenvalues and eigenstates will necessarily depend on this parameter as well, as emphasized by the right-hand size of Eq. (2.6). Therefore, the original problem is now transformed into the eigenproblem of the matrix $A_{nm}(t)$, whose indices take all integer values in the range $-N_{\text{cut}} \leq n, m < N_{\text{cut}}$, where $N_{\text{cut}} = [L/\Delta]$.

Fig. 2.1 shows how a typical transition amplitude, in this case that of a harmonic oscillator, depends on coordinates x and y. The transition amplitude of a harmonic oscillator with the Hamiltonian $\hat{H}_{\text{HO}} = \hat{p}^2/2 + \hat{x}^2/2$ can be calculated analytically and is given by explicit the expression:

$$A_{\text{HO}}(x, y; t) = \sqrt{\frac{1}{2\pi \sinh t}} \exp\left[-\frac{1}{2\sinh t}\left((x^2 + y^2)\cosh t - 2xy\right)\right] . \tag{2.7}$$

Note that the consideration is general since non-trivial mass and frequency of the harmonic oscillator can be easily taken into account by a simple rescaling of the coordinate and momentum. As can be seen from the figure, transition amplitudes are spatially well localized. This is particularly simple to understand for the short times of propagation that we consider for a general case in the external potential. For a very short propagation times, transition amplitudes can be roughly calculated as:

$$A(x, y; t) \approx \frac{1}{\sqrt{2\pi t}} e^{-\frac{(x-y)^2}{2t} - tV\left(\frac{x+y}{2}\right)} . \tag{2.8}$$

From the last expression, we see that the kinetic term exponentially localizes the transition amplitude matrix to the vicinity of the main diagonal. Similarly, the potential brings about exponential localization along the main diagonal around its minimum. The localization of dominant values of the transition amplitude to a small area in the $x-y$ plane gives practical justification for introduction of space cutoff L in this approach.

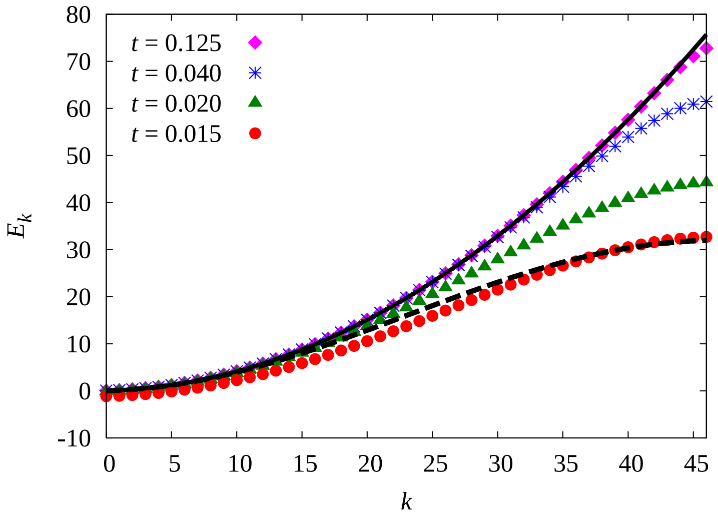

Figure 2.2: Eigenspectrum of a free particle in a box. Eigenvalues E_k are given as a function of level number k. The solid line gives the exact parabolic dispersion $E_k = \pi^2(k+1)^2/8L^2$, while the dashed line presents results calculated in the tight-binding approximation. The graph also shows numerical results obtained by the diagonalization of transition amplitudes for different values of time of evolution t. All the numerical calculations are for $L = 6$ and $\Delta = 0.25$, hence $N_{\text{cut}} = L/\Delta = 24$.

In the continuum theory, the transition amplitude eigenproblem is mathematically equivalent to the Schrödinger equation. It is important to stress, however, that the procedure of space discretization introduces important differences between eigenproblems (2.3) and (2.6). In particular, as we will show in the next section, the procedure based on the diagonalization of transition amplitudes leads to much faster (non-polynomial) convergence. An illustration of the relation of these two calculation schemes is shown in Fig. 2.2 which compares the exact parabolic dispersion of a free particle in a box with numerical calculations based on diagonalizations of the Hamiltonian and of the transition amplitudes. From the figure we see that the time parameter t in the transition amplitude approach plays an important role. Increase of the evolution time t gives better agreement with the exact dispersion relation.

2.2 Discretization effects

The free-particle transition amplitude

$$A^{\text{free}}(x,y;t)=\frac{1}{\sqrt{2\pi t}}\,e^{-\frac{(x-y)^2}{2t}} \tag{2.9}$$

satisfies the relation

$$\int dx\, A^{\text{free}}(x,y;t)=1\ . \tag{2.10}$$

The consequence of this is conservation of probability. In the space-discretized analogue of this model $x=n\Delta$, $y=m\Delta$, and the transition amplitude is $A^{\text{free}}_{nm}(t)=\Delta\, A^{\text{free}}(n\Delta,m\Delta;t)$. Using the Poisson summation formula

$$\sum_{n\in\mathbb{Z}} e^{-\alpha n^2}=\sqrt{\frac{\pi}{\alpha}}\sum_{n\in\mathbb{Z}} e^{-\frac{\pi^2}{\alpha}n^2}\ , \tag{2.11}$$

we find that the space discretized free particle amplitude satisfies

$$\sum_{n\in\mathbb{Z}} A^{\text{free}}_{nm}(t)=\sum_{n\in\mathbb{Z}} e^{-\frac{2\pi^2}{\Delta^2}n^2 t}\approx 1+2e^{-\frac{2\pi^2}{\Delta^2}t}\ . \tag{2.12}$$

Conservation of probability is thus obtained only in the continuum limit $\Delta\to 0$. Note that the effect of discretization is non-perturbative in discretization step Δ, i.e. it is smaller than any power of Δ. The effect of discretization is also universal in that it holds for all models, since the free particle transition amplitude is the dominant term in the short time expansion of the transition amplitude of a general theory.

To show this explicitly we use the short time expansion of the transition amplitude of a general theory [44] to show that

$$\int dx\, A(x,y;t)=\frac{1}{\sqrt{2\pi t}}\int dx\, e^{-\frac{1}{2t}x^2}\sum_l t^l f_l(x,y)\ , \tag{2.13}$$

where $f_0=1$ and the other functions f_l are determined by the potential and its derivatives. Writing the even part of $f_l(x,y)$ as $g(x^2,y)$ we find

$$\int dx\, A(x,y;t)=\frac{1}{\sqrt{t}}\sum_l t^l g_l(2t^2\partial_t,y)\sqrt{t}\ . \tag{2.14}$$

Similarly, using the above Poisson summation formula, we find

$$\sum_{n\in\mathbb{Z}} A_{nm}(t) - \int dx\, A(x,y;t) = \frac{2}{\sqrt{t}} \sum_l t^l g_l(2t^2\partial_t, y)\sqrt{t} e^{-\frac{2\pi^2}{\Delta^2}t} \; . \tag{2.15}$$

Performing the indicated differentiations the right hand side becomes $\exp(-\frac{2\pi^2}{\Delta^2}t) \cdot \sum_l h_l(y)t^l$. One could now calculate the functions h_l from the short time expansions of f_l. The p-level effective action gives a short time expansion, which is truncated at order t^p. As a result, $\sum_l h_l(y)t^l$ is a polynomial in time of order p. The dominant short time behavior is thus given by the universal exponential term. As a consequence, the transition of a general model to its space discretized form is given by

$$\sum_{n\in\mathbb{Z}} A_{nm}(t) - \int dx\, A(x,y;t) \sim e^{-\frac{2\pi^2}{\Delta^2}t} \; . \tag{2.16}$$

This universal and non-perturbatively small deviation from the continuum indicates that one should center numerical calculation schemes on transition amplitudes rather than the Hamiltonian. By diagonalizing the transition amplitude for any time of propagation t we obtain the energy eigenvalues and eigenfunctions

$$\int dy\, A(x,y;t)\psi_k(y) = e^{-tE_k}\psi_k(x) \; . \tag{2.17}$$

To solve this numerically we first discretize space with discretization step Δ, and second we introduce a spatial cut-off L such that $|x| < L$. Amplitudes are now $2N_{\text{cut}} \times 2N_{\text{cut}}$ matrices whose diagonalization leads to $2N_{\text{cut}}$ eigenstates ψ_k and eigenvalues $e^{-tE_k(\Delta,L,t)}$.

As we have seen, discretization introduces a non-perturbatively small error in transition amplitudes proportional to $\exp(-2\pi^2 t/\Delta^2)$. We should therefore expect the discretization error for energy eigenvalues to be

$$E_k(\Delta,L,t) - E_k \sim -\frac{1}{t}\, e^{-\frac{2\pi^2}{\Delta^2}t} \; . \tag{2.18}$$

We have numerically investigated this for a diverse set of models and have shown the above relation to hold in all cases. It is also illustrative to verify this for analytically tractable models. Using the known analytical expressions for transition amplitude and energy eigenstates for a free particle in a box [52, 53], as well as the Poisson summation formula in Eq. (2.11), we find that the energy eigenstates of the space discretized model satisfy

$$E_k(\Delta, L, t) - E_k = -\frac{2}{t}\, e^{-\frac{2\pi^2}{\Delta^2}t} \cosh \frac{\pi^2(k+1)t}{L\Delta}\ , \tag{2.19}$$

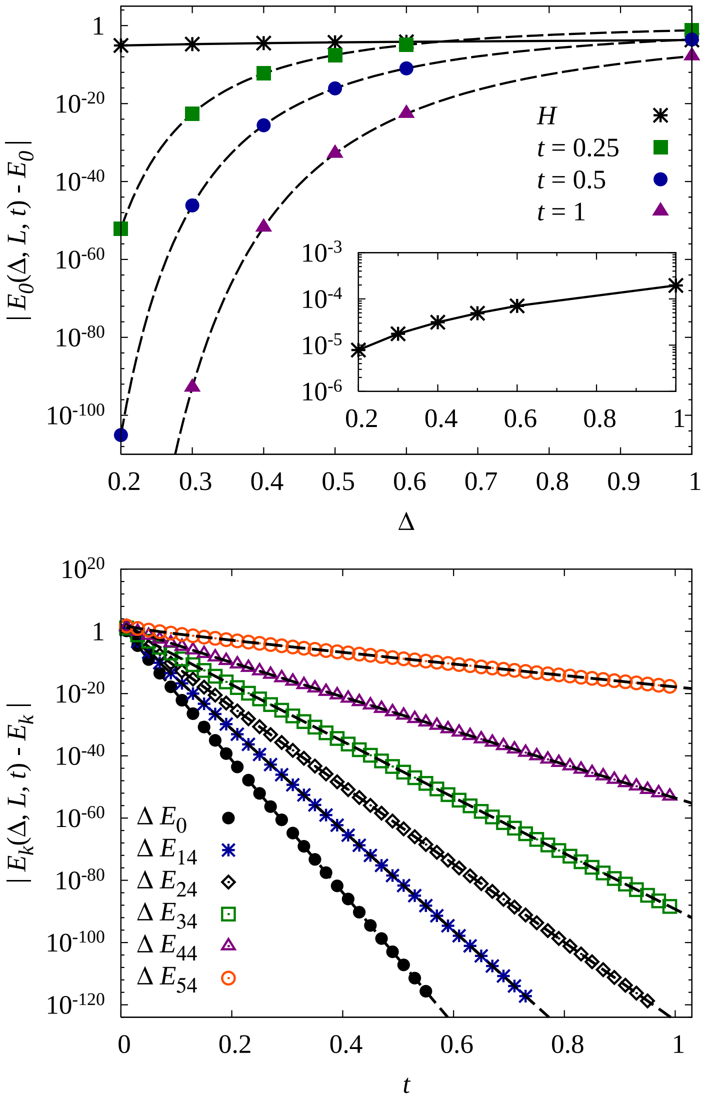

Figure 2.3: Top: Plot of $|E_0(\Delta, L, t) - E_0|$ for a free particle in a box as a function of Δ for different values of time of evolution t and $L = 6$. For comparison, we also plot the corresponding deviations of numerical results (designated by H) obtained using direct diagonalization of the space-discretized Hamiltonian, defined by Eq. (2.4). Bottom: This plot shows how the deviations $|E_k(\Delta, L, t) - E_k|$ depend on t for several energy levels k. The parameters used are $L = 6$, $\Delta = 0.2$. In both plots the dashed lines represent discretization error estimates given in Eq. (2.19).

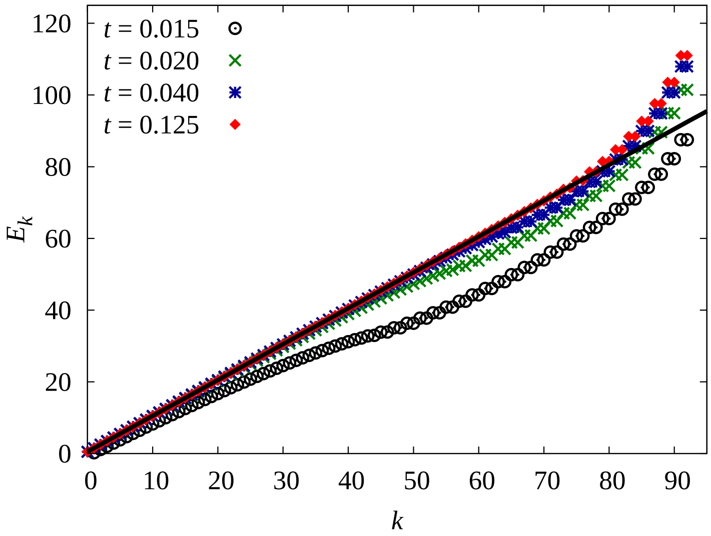

Figure 2.4: Harmonic oscillator dispersion relation. The solid line gives the exact linear dispersion $E_k = k + 1/2$. The points correspond to numerically calculated energy eigenvalues E_k as function of level k. We show the results of the diagonalization of transition amplitudes for several values of t. In this plot $L = 12$, $\Delta = 0.25$.

where $E_k = \frac{\pi^2(k+1)^2}{8L^2}$ and $k = 0, 1, 2, \ldots$ As expected, the universal term gives the dominant Δ dependence. One obtains similar analytical results for the case of the harmonic oscillator.

The non-perturbatively small effect of spatial discretization is the reason why the new method highly outperforms direct diagonalization of the Hamiltonian and leads to much smaller errors for the same size of discretization step Δ. In addition to this the free parameter associated with the method, the time of evolution t, can be used to further minimize errors. As illustrated in Fig. 2.2, while keeping Δ fixed, we can adjust time t to obtain much smaller errors and practically reproduce the exact spectrum of the theory. This is also evident in Fig. 2.3, where we see that by adjusting t, errors can be reduced by orders of magnitude for fixed value of discretization step Δ.

We next consider a harmonic oscillator. Fig 2.4 shows how the presented method may be used to obtain energy eigenvalues to high levels. The numerical calculations agree well with the well known linear dispersion of the harmonic oscillator. Figs. 2.5(top) and 2.5(bottom) display respectively the Δ and t dependence of the deviations $|E_k(\Delta, L, t) - E_k|$, showing agreement with the analytically derived estimate of the discretization error given in Eq. (2.18). In order to achieve such a

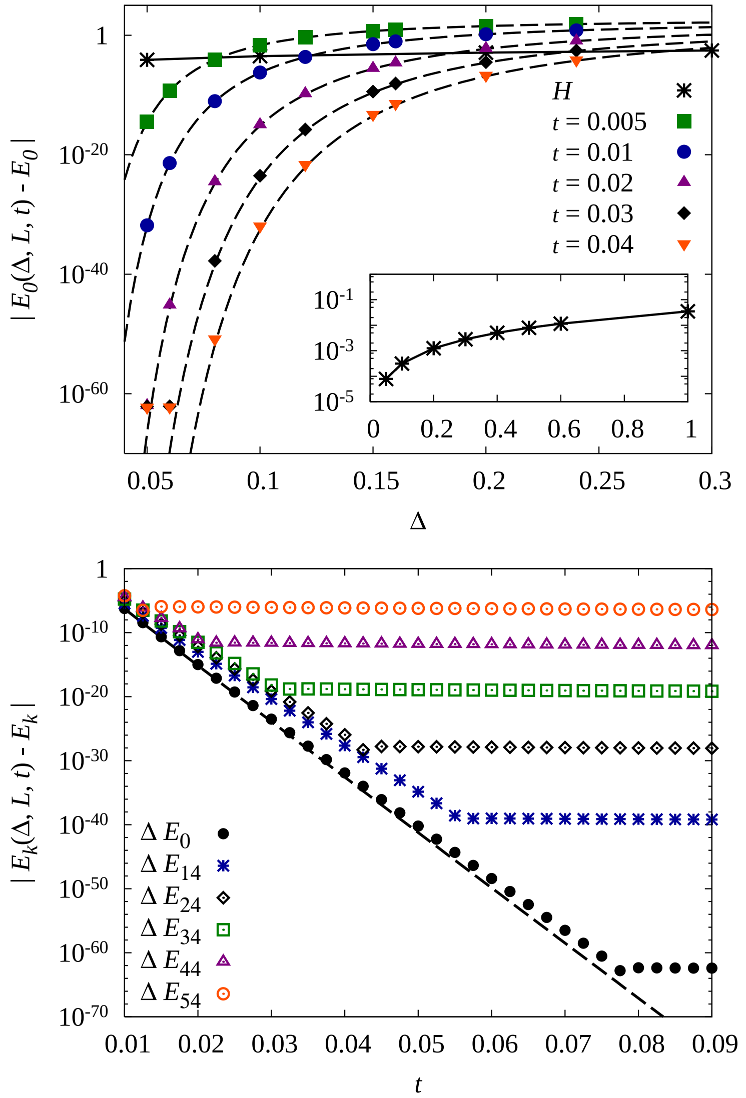

Figure 2.5: Top: Plot of $|E_0(\Delta, L, t) - E_0|$ for a harmonic oscillator as a function of discretization step Δ for different values of time of evolution t with $L = 12$. For a comparison, we also plot the corresponding results (designated by H) obtained using direct diagonalization of the space-discretized harmonic oscillator Hamiltonian. Bottom: Plot of the deviations $|E_k(\Delta, L, t) - E_k|$ given as a function of time t for several levels k. The parameters used are $L = 12$, $\Delta = 0.1$. In both plots the dashed lines correspond to the discretization error estimate for E_0 given in Eq. (2.19).

high accuracy of numerical results as presented on all graphs, we have used the MATHEMATICA software package [54].

Fig. 2.5(bottom) shows how the deviations $|E_k(\Delta, L, t) - E_k|$ depend on t for several levels k. The plot corresponds to the harmonic oscillator but is typical of a general theory. The saturation of errors for large t comes about when the discretization error, given by the universal estimate in Eq. (2.18), becomes smaller than the error due to space cutoff L. Analytical estimates for cutoff error are given at the end of this section. At this point we just mention that the finite size effects can already be seen in Fig. 2.4, where for high values of level number k numerical results start to move away from the linear dispersion characteristic of a harmonic oscillator to the parabolic dispersion characteristic of a box potential.

We end the section by looking at finite size effects, i.e. errors related to introduction of space cutoff L. For any theory with non-trivial potential, the cutoff L is artificially introduced and it affects the obtained energy eigenvalues, as we have already discussed. To estimate the effects of the cutoff, we first note that they are closely related to the spatial extent of the potential V, as well as the spatial extent of eigenfunctions of the system: errors in the corresponding energy eigenvalues can be considered small only if the eigenstates $\psi_k(x)$ are well localized in the interval $|x| < L$.

The effects of space cutoffs have been previously studied for continuous-space theories [55, 56]. The shift in energy level $E_k(L) - E_k$ is found to be positive in this case, and approximately given by the formula

$$E_k(L) - E_k = C_k(a) \left(\int_a^L \frac{dx}{|\psi_k(x)|^2} \right)^{-1} , \tag{2.20}$$

where a is an appropriately chosen value of coordinate x such that it is larger than and well away from the largest zero of $\psi_k(x)$ but smaller than and well away from the space cutoff L. The constant $C_k(a)$ depends on the normalization of eigenfunction and the choice of parameter a. For example, the ground state has no zeros, and we can always choose the value $a = 0$. In that case, constant $C_0(0)$ is given by

$$C_0(0) = \left(\int_{-L}^L dx\, |\psi_0(x)|^2 \right)^{-1} , \tag{2.21}$$

where we assume that the eigenfunction $\psi_0(x)$ is normalized, $\int_{-\infty}^{\infty} dx\, |\psi_0(x)|^2 = 1$.

In practical applications, when we use diagonalization of the discretized transition amplitudes, the errors in energy level will necessarily also depend on the parameter t and other discretization parameters. Here we give a simple estimate of ground energy errors that follows from the spectral decomposition of diagonal

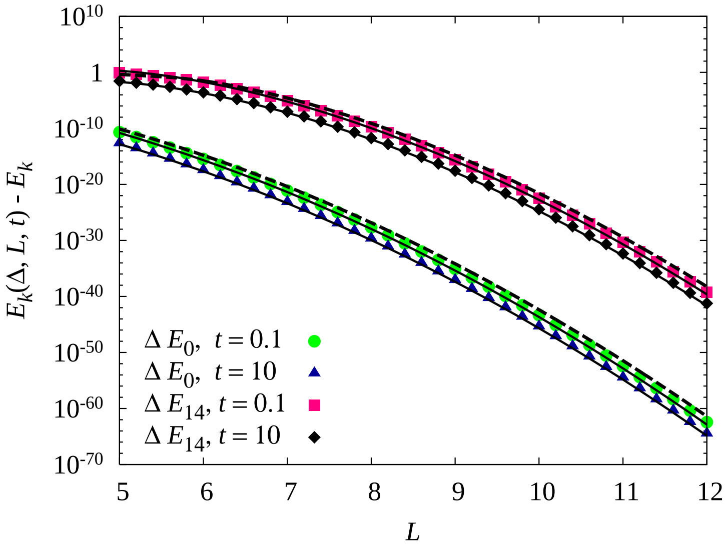

Figure 2.6: Deviations $E_k(\Delta, L, t) - E_k$ for a harmonic oscillator as a function of space cutoff L for different values of time of evolution t. The discretization step is $\Delta = 0.1$. Solid thin lines give the dominant behavior of Eq. (2.23). The dashed thick lines correspond to the error estimate in Eq. (2.20).

amplitudes. For large t we have $A(x, x; t) \approx |\psi_0(x)|^2 e^{-E_0 t}$. Integrating this we find an approximate result for the ground energy of a system with cutoff L

$$E_0(L, t) \approx -\frac{1}{t} \ln \int_{-L}^{L} dx\, A(x, x; t)\,, \tag{2.22}$$

In the $L \to \infty$ limit we recover the exact ground energy, so that a simple estimate of finite size effects on E_0 is given by

$$E_0(L, t) - E_0 \approx \frac{1}{t} \int_{|x|>L} dx\, |\psi_0(x)|^2\,. \tag{2.23}$$

Although the above equation is just a rough estimate of the errors introduced by a space cutoff L, Fig. 2.6 shows that it is in good agreement with numerical results for the harmonic oscillator. In order to clearly demonstrate L-dependence of errors in this graph, we have used small value of the discretization step Δ, such that discretization errors can be neglected. The dashed lines in the figure represent error estimates given by Eq. (2.20).

Using the data from Fig. 2.6 we can now fully explain the saturation of errors observed in Fig. 2.5(bottom). The value of the cutoff L used to obtain this data was $L = 12$. As can be seen from Fig. 2.6, this value of the cutoff parameter yields an error of the order 10^{-65} for the ground-state energy for $t \sim 0.1$, and of the order 10^{-40} for energy eigenlevel E_{14}. These values exactly correspond to the saturated errors in Fig. 2.5(bottom).

Although in the general case the eigenstates that come into Eqs. (2.20) and (2.23) are not known, we can still use them in conjunction with other approximation techniques to estimate finite size effects. We also see that, due to the larger spatial extent of higher energy eigenstates, the cutoff-related errors are minimal for the ground energy. Note however that one is not really interested in the precise calculation of finite size errors, but only needs to estimate the minimal size of the cutoff L for which finite size effects are negligible. For that purpose one can use either of the above approximate formulas.

2.3 Effective actions

So far we have considered only integrable models, i.e. models for which we know the exact transition amplitudes. As a result we have thus far encountered and analyzed only two sources of errors: those associated with discretization step Δ and cutoff L. The vast majority of models are not integrable. The outlined method is still applicable if one uses some approximation for calculating transition amplitudes.

As we can see, the precise calculation of transition amplitudes is essential for practical applications of this method. In Ref. [9] all calculations are based on the naive approximation for transition amplitudes

$$A^{(1)}(x, y; t) \approx \frac{1}{\sqrt{(2\pi t)^d}}\, e^{-\frac{(x-y)^2}{2t} - t\frac{V(x)+V(y)}{2}}\,, \tag{2.24}$$

which is correct only to order $O(t)$, and is for this reason designated by $A^{(1)}$. If one uses the naive approximation for transition amplitudes, then times of propagation must be very short for errors to be small enough. Practically, even for short times of propagation, such errors are always much larger than the errors due to discretization, and therefore significantly limit the applicability of the method. In addition to this, the results obtained in the previous section on exactly solvable models suggest that longer times of propagation generally give smaller errors in the diagonalization approach. The trade-off between these effects and its implications on numerical results have been documented in [9].

To address this, in principle one can use Monte Carlo simulations [57, 58] to calculate amplitudes A to high precision. Although this can effectively resolve the problem in many cases, it is often numerically very expensive. More importantly, resorting to the use of Monte Carlo practically limits further analytical approaches. We will instead use the recently introduced effective action approach [44, 10, 45, 46, 11] that gives closed-form analytic expressions $A^{(p)}(x, y; t)$ for transition amplitudes which converge much faster,

$$A^{(p)}(x, y; t) = A(x, y; t) + O(t^{p+1}/t^{d/2}) \,, \tag{2.25}$$

where p is an integer number corresponding to the order of the effective action used. For a general many-body theory effective actions up to $p = 10$ have been derived, while for a specific models much higher values can be obtained, e.g. for the anharmonic oscillator and other polynomial interactions, for which effective actions have been calculated up to $p = 144$. So, if p is high enough, it is sufficient that the time of evolution is less than the radius of convergence of the above series ($t < \tau_c \sim 1$) and errors in calculated values of transition amplitudes will be negligible. This is illustrated in Fig. 2.7 for the case of a quartic anharmonic oscillator. The use of high-order expansion in the time of propagation of amplitudes will allow us to use times of evolution up to τ_c, which are much longer than the typical times one can use with the naive ($p = 1$) amplitudes. At the same time, the expansion up to very high orders substantially decreases the errors associated with t, and may practically eliminate them.

The analytic expressions for higher-order approximations for transition amplitudes are based on the notion of effective actions, which are introduced by casting the solution of the time dependent Schrödinger equation for the transition amplitude in the form

$$A(x, y; t) = \frac{1}{\sqrt{(2\pi t)^d}} \, e^{-\frac{(x-y)^2}{2t} - tW\left(\frac{x+y}{2}, x-y; t\right)} \,, \tag{2.26}$$

where $W(x, \delta; t)$ is the effective potential, with the following boundary behavior:

$$\lim_{t\to 0} W(x, \delta; t) = V(x) \,. \tag{2.27}$$

As shown previously, the effective potential $W(x, \delta; t)$ is regular in the vicinity of $t = 0$, enabling us to represent it in the form of a power series in short time of propagation t. The coefficients in this series are functions of the potential and

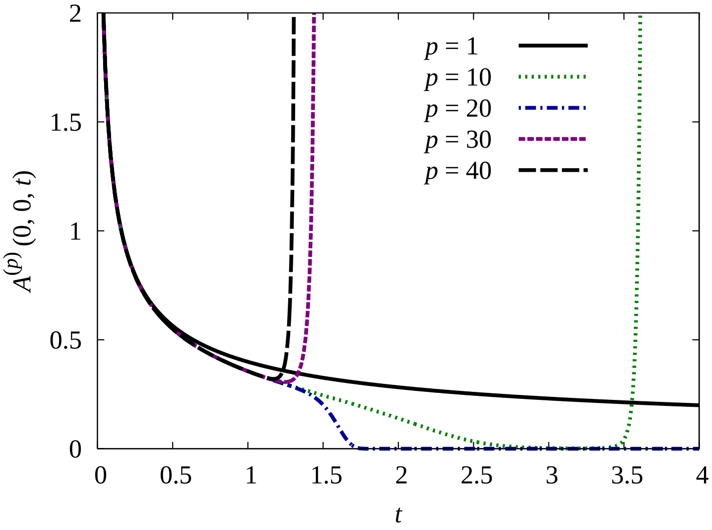

Figure 2.7: Transition amplitude $A^{(p)}(0,0;t)$ as a function of the time of propagation t, calculated analytically using different levels p of the effective action. The plot is for the quartic anharmonic potential $V(x) = \frac{k_2}{2}x^2 + \frac{k_4}{24}x^4$, with parameters $k_2 = 1$, $k_4 = 10$.

its derivatives. The truncation of the series for the effective potential up to order t^{p-1}, designated by $W^{(p-1)}(x,\delta;t)$, gives the expansion of the transition amplitude accurate to t^p,

$$A^{(p)}(x,y;t) = \frac{1}{\sqrt{(2\pi t)^d}} e^{-\frac{(x-y)^2}{2t} - tW^{(p-1)}\left(\frac{x+y}{2}, x-y; t\right)}. \tag{2.28}$$

The analytic expressions for higher-order effective actions therefore yield analytic approximations for amplitudes with the convergence behavior given by Eq. (2.25). We emphasize that although the structure of the effective action solution form (2.26) is motivated by the path integral formalism, the expression for amplitudes obtained in the above approach contain no integrals and can be used straightforwardly as long as the time of propagation is below the radius of convergence of the short-time series expansion.

For the exactly solvable case of a harmonic oscillator one finds that the radius of convergence is $\tau_c = \pi$. The radius of convergence is simply the distance in the complex time plain from the origin to the nearest singularity of the propagator. For the harmonic oscillator the singularities are located at $\pm ik\pi$, $k \in \mathbb{N}$. The consequence of these singularities is that the power series for the effective potential

$W(x, \delta; t)$ converges only for $t < \tau_c$. It is often difficult to analytically determine the radius of convergence of the short time expansion of the transition amplitude. However, numerically this is a very simple problem, since outside of the radius of convergence the calculated approximative amplitudes rapidly tend to infinity (for levels p for which the effective potential is not bounded from below; see Ref. [59]) or to zero with the increase of p. From Fig. 2.7 we easily estimate radius of convergence to be $\tau_c \approx 1$ for a quartic anharmonic potential $V(x) = \frac{k_2}{2}x^2 + \frac{k_4}{24}x^4$, with parameters $k_2 = 1$, $k_4 = 10$. Such numerical determination of the radius of convergence for a given level p is always done before practical use of the effective potential. Note that we are not interested in the precise value of τ_c, just in its rough estimate which will allow us to safely use times of propagation below τ_c.

To conclude the section, let us stress that the effective action approach can be used only for sufficiently smooth potentials, i.e. those that have derivatives of the required order, corresponding to the level p of effective action, as discussed in Ref. [44]. For potentials that do not fulfill this condition (e.g. stepwise potentials), the effective action approach cannot be directly used. However, one can replace the original potential with some of its smooth deformations, perform numerical calculations, and at the end take the limit of the deformation parameter in which the original potential is recovered. The numerical results obtained in such a way must be carefully cross-checked using other methods.

2.4 Numerical results for one-dimensional models

In this section we apply the approach outlined above to several $d = 1$ models and demonstrate its substantial advantages for numerical studies of eigenstates of various physical systems. We numerically analyze all sources of errors present in this approach due to discretization parameters L and Δ, as well as the time of propagation parameter t. We present the obtained numerical results for energy eigenvalues and eigenstates. We also assess the quality of the obtained energy spectra through comparison with the semiclassical approximation for the density of states, which should be accurate at least for the higher regions of the spectrum.

The first model we study is the quartic anharmonic oscillator with potential

$$V(x) = \frac{k_2}{2}x^2 + \frac{k_4}{24}x^4\,. \tag{2.29}$$

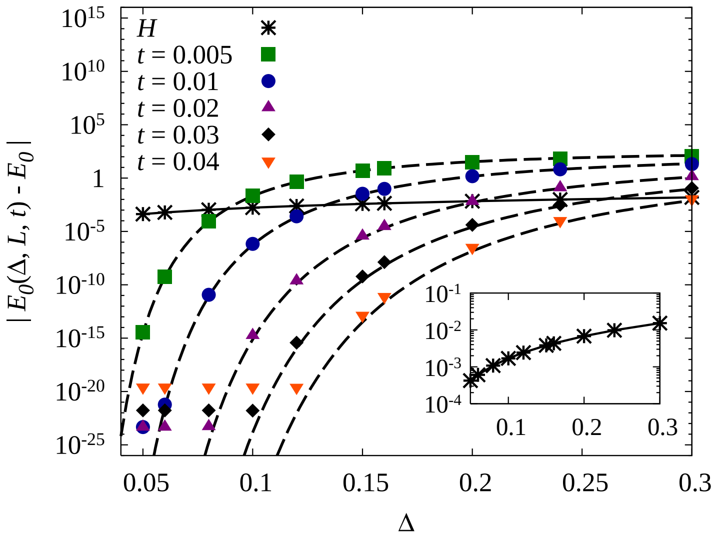

Figure 2.8: Plot of $|E_0(\Delta, L, t) - E_0|$ for an anharmonic oscillator (2.29) given as a function of Δ for different values of time of evolution t. The parameters used are $L = 6$, $k_2 = 1$, and anharmonicity $k_4 = 48$. Dashed lines correspond to the discretization error in Eq. (2.19). For comparison, we also plot the corresponding deviations of numerical results (designated by H) obtained using direct diagonalization of the corresponding space-discretized Hamiltonian.

For this potential the effective actions have been previously derived up to $p = 144$ [60], and here we will use various levels p to illustrate the dependence of errors on the level p used in calculations. We will study the interesting regime of the strong coupling k_4, since there are various other techniques that can be successfully used for small couplings.

Fig. 2.8 displays $|E_0(\Delta, L, t) - E_0|$ as a function of discretization step Δ for the case of an anharmonic oscillator with potential (2.29). The parameters used in the plot are $L = 6$, $k_2 = 1$, and anharmonicity $k_4 = 48$. The transition amplitude matrix elements were calculated using $p = 18$ effective actions [44]. The high precision value for the exact ground energy that we compare to was calculated in Ref. [61]. As we can see, even though we are dealing with a relatively strong anharmonicity, the numerically calculated values stay right on the dashed black lines corresponding to the universal discretization error just as in the case of the previously considered integrable models. This is in complete agreement with our analytical derivation of the discretization error.

As can be seen from Fig. 2.8 the numerical results clearly demonstrate that the

Δ-dependence of errors within our calculation scheme highly outperforms the polynomial dependence in Δ^2 obtained by the direct diagonalization of the Hamiltonian. This is true even for short times of propagation t. Although interaction terms in the potential affect the numerical values of errors, diagonalization of the transition amplitudes still substantially outperforms diagonalization of the Hamiltonian, and is the preferred method. This success is a consequence of the non-perturbative behavior of the spatial discretization error within this calculation scheme. This leads us to the key conclusion that discretization parameters can be always optimized so that presented approach of solving eigenvalue problem of space-discretized transition amplitudes highly outperforms direct diagonalization of the space-discretized Hamiltonian. The continuum limit $\Delta \to 0$ is far more easily approached in the first case and the corresponding discretization errors are substantially smaller for the same discretization coarseness. From the numerical point of view, as the value of parameter Δ directly determines the size of the matrix to be diagonalized, the computational cost for the same precision is significantly reduced.

Further analysis of various errors in the ground energy calculation for parameters $k_2 = 1$, $k_4 = 48$ of the anharmonic potential (2.29) is given in Fig. 2.9. The dependence of the error related to the introduction of the space cutoff L is illustrated in Fig. 2.9(top), while Fig. 2.9(bottom) gives the dependence of ground energy errors on the time of propagation parameter t for various values of the discretization step Δ. On both graphs we see the results obtained with effective actions of different levels p. Fig. 2.9(bottom) clearly shows that the errors due to the time of propagation are proportional to t^p, as expected when we use the effective action of the level p. The errors in eigenvalues are of the same order as errors in calculation of individual matrix elements, and for this reason we see the typical t^p behavior of ground and higher energy eigenvalues. It is already now evident that the use of higher-order effective actions increases the accuracy of numerically calculated energy eigenstates for many orders of magnitude.

The L-dependence of the error is analytically known [55, 56]. The saturation of errors on the top graph for a given level p corresponds to a maximal precision that can be achieved with that p, i.e. denotes the value of L for which errors introduced by other sources become larger than the error due to the finite value of the space cutoff. This can be easily seen if we combine the data from both graphs. For example, the level $p = 9$ effective action has the saturated value of the error of the order of 10^{-14}. For $t = 0.02$ we find that the error due to the time of propagation is of the same order if one uses sufficiently fine discretization ($\Delta = 0.05$). Therefore, the saturation of errors on the left-hand graph are caused by the errors due to the time of propagation. However, if one uses discretization which is not sufficiently fine, the saturation of errors can be also caused by the discretization effects. Such effects can

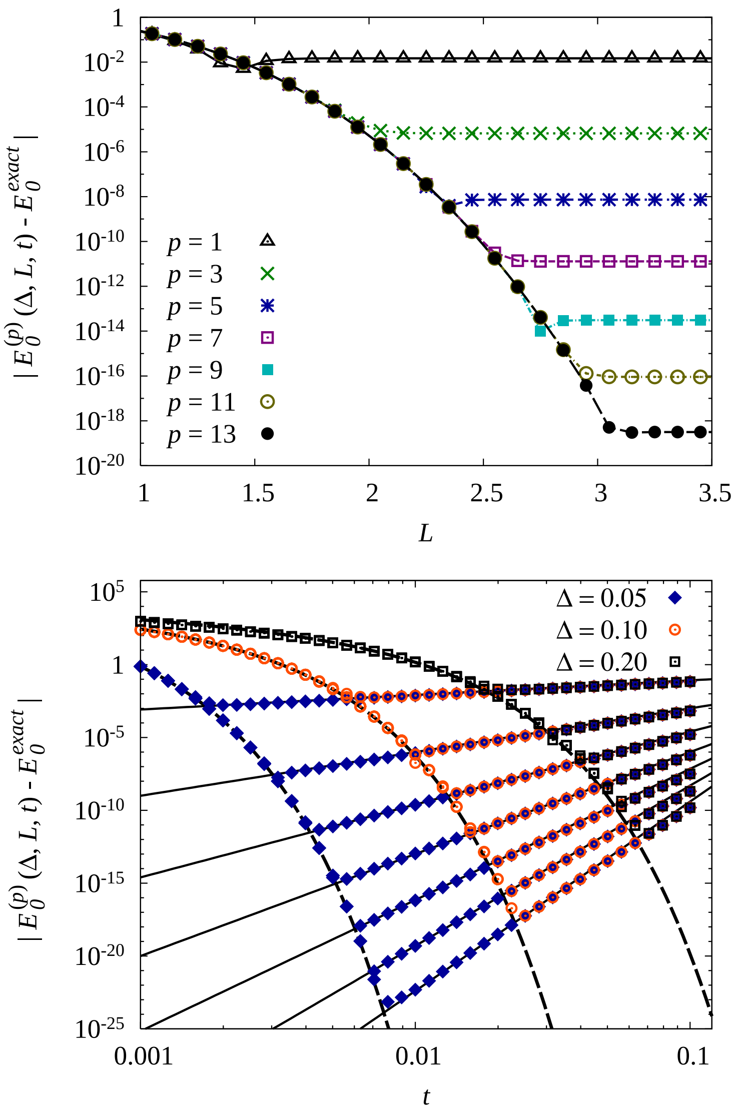

Figure 2.9: Deviations from the ground energy $|E_0^{(p)}(\Delta, L, t) - E_0^{\text{exact}}|$ as a function of the space cutoff L (top) and as a function of the time t (bottom). The ground energy is obtained using different levels $p = 1, 3, 5, 7, 9, 11, 13$ (top to bottom) of the effective action for the quartic anharmonic potential, with parameters $k_2 = 1$, $k_4 = 48$, $\Delta = 0.05$, $t = 0.02$ on top graph, and $L = 4$ on bottom graph. The exact ground energy $E_0^{\text{exact}} = 0.95156847272950001114693\ldots$ is taken from Ref. [61]. Dashed lines on the graph (b) correspond to the discretization error (2.19).

Table 2.1: Low-lying energy levels of the anharmonic quartic potential, obtained by diagonalization using level $p = 13$ effective action. The parameters are $k_2 = 1$, $k_4 = 48$, $L = 5$, $\Delta = 0.05$, $t = 0.01$. For higher energy eigenvalues, errors are estimated by comparison with the diagonalization results obtained from higher-order effective actions, finer discretizations, larger space cutoffs, and lower values of the propagation time t.

k	E_k	$\lvert\Delta E_k\rvert$	δE_k
0	0.9515684727295000111468(8)	5×10^{-23}	6×10^{-23}
1	3.292867821434465922691(67)	4×10^{-22}	2×10^{-22}
2	6.30388056744652609989(522)	2×10^{-21}	4×10^{-22}
3	9.72732317270370501553(448)	5×10^{-21}	5×10^{-22}
4	13.4812758360385893838(1489)	2×10^{-20}	2×10^{-21}
5	17.5141323992530709259(6206)	3×10^{-20}	2×10^{-21}
6	21.7909563917965158973(8744)	6×10^{-20}	3×10^{-21}
7	26.286125156056810490(92289)	2×10^{-19}	7×10^{-21}
8	30.979882837938369575(08213)	2×10^{-19}	8×10^{-21}
9	35.856438766665971146(24181)	3×10^{-19}	9×10^{-21}

be also analytically estimated to be proportional to $-2\exp(-2\pi^2 t/\Delta^2)\cosh(\pi^2(k+1)/L\Delta)/t$, as we have shown in the previous section.

Table 2.1 gives low-lying energy eigenvalues of the anharmonic oscillator for a particular choice of the parameters of the potential and discretization parameters. In principle, one can achieve arbitrary precision by the use of appropriately chosen discretization parameters. Of course, for arbitrary precision calculations one has to use one of the software packages able to support such calculations. For example, we have used MATHEMATICA [54] in order to be able to achieve high-precision results presented on the above graphs. The important conclusion is that even for very moderate values of discretization parameters, the use of higher-order effective actions leads to very small errors, which may be practically implemented with minimal computing resources.

The analysis of errors such as the one presented in Fig. 2.9 is sufficient to estimate optimal values of discretization parameters. In general, for a desired numerical precision of energy eigenvalues, the optimal values of parameters are chosen so that all types of errors are approximately the same. The overall error is always dominated by the largest of all errors, and therefore it is optimal to have all errors of the same order of magnitude.

For specific calculations one can have additional constraints. For example, if one is interested only in energy eigenvalues, then the optimal parameters are obtained by minimizing all errors and minimizing the ratio $N_{\mathrm{cut}} = L/\Delta$, which corresponds to the size of the transition operator matrix $S = 2N_{\mathrm{cut}}$ that needs to be numerically diagonalized. The minimization of N_{cut} is performed in order to minimize computation time needed for the diagonalization, which roughly scales as N_{cut}^3.

On the other hand, if one is interested in details of energy eigenfunctions, then it might be necessary to have a fixed small value for the discretization step Δ, which will allow all features of eigenstates to be visible. This is especially important for studies of higher energy eigenfunctions which e.g. have many nodes, and in order to study them it is necessary to have sufficient spatial resolution. In such case, the value of Δ is fixed and other parameters are chosen so as to minimize the errors to a desired value. For example, with the discretization step of the order $\Delta = 10^{-3}$ we have been able to accurately calculate several hundreds energy eigenfunction of the quartic anharmonic oscillator.

Table 2.2 gives eigenvalues of the double-well potential, obtained from the quartic anharmonic potential (2.29) by setting the constant k_2 to some negative value. As can be seen, numerically obtained energy eigenvalues have the precision similar to the previous case of the quartic potential without symmetry breaking. The double well behavior of the potential does not present any obstacle in its numerical treatment by this method.

Another situation in which one might be interested to keep the ratio $N_{\mathrm{cut}} = L/\Delta$, i.e. the size of the space-discretized evolution operator matrix as large as possible is when a large number of energy eigenlevels is needed. The number of energy eigenvalues that can be calculated by the diagonalization is limited by the size of the matrix $S = 2N_{\mathrm{cut}}$. Usually the highest energy levels cannot be used due to the accumulation of numerical errors, and therefore one needs to have a matrix of sufficient size in order to study energy spectra. In such cases it is necessary to use highly optimized libraries for numeric diagonalization. We have implemented the effective actions as a C programming language code [60] and used LAPACK [62] library for numeric diagonalization to calculate large number of energy eigenvalues and eigenfunctions.

Even when one uses such a sophisticated tool, the highest eigenvalues cannot be used due to accumulation of numerical errors. In order to assess the quality of the obtained results for higher energy eigenstates, it is necessary to compare the

Table 2.2: Low-lying energy levels of the double-well potential, obtained by diagonalization using level $p = 18$ effective action. The parameters used: $k_2 = -1$, $k_4 = 12$, $L = 16$, $\Delta = 0.1$, $t = 0.05$. The errors are estimated by comparison with the diagonalization results obtained from higher-order effective actions, finer discretizations, larger space cutoffs, and lower values of the propagation time t.

k	E_k	$\lvert\Delta E_k\rvert$	δE_k
0	0.328826502590357561530(2)	7×10^{-22}	2×10^{-21}
1	1.41726810105965210733(23)	5×10^{-21}	4×10^{-21}
2	3.0819506284815341204(849)	3×10^{-20}	1×10^{-20}
3	5.019323060355788021(7990)	2×10^{-19}	4×10^{-20}
4	7.186203252338934478(3958)	5×10^{-19}	8×10^{-20}
5	9.54285734251209386(72421)	2×10^{-18}	2×10^{-19}
6	12.06403774639116375(04211)	4×10^{-18}	4×10^{-19}
7	14.7314279571006902(462590)	1×10^{-17}	7×10^{-19}
8	17.5310745155383834(413592)	3×10^{-17}	2×10^{-18}
9	20.4519281359123716(968554)	5×10^{-17}	3×10^{-18}

numerical results with some known properties of the physical system. One such property is density of states, defined formally as

$$\rho(E) = \sum_{k=0}^{\infty} \delta(E - E_k)\,, \tag{2.30}$$

assuming that the system has a discrete spectrum. This highly relevant physical quantity can be directly calculated using the numerically obtained spectra. On the other hand, it can be also analytically calculated using semiclassical approximation. This approximation is valid at least in the high-energy region, and we can use it to assess the quality of our numerical results. In semiclassical approximation, the density of states in d spatial dimensions is calculated as

$$\rho_{\mathrm{sc}}(E) = \int \frac{d\vec{x}\, d\vec{p}}{(2\pi\hbar)^d}\, \delta(E - \mathcal{H}(\vec{x}, \vec{p}))\,. \tag{2.31}$$

replacing the discrete spectrum with a continuous distribution of energy defined by the classical Hamilton function $\mathcal{H}(\vec{x}, \vec{p})$. After integration over momenta, we obtain the well known result [52]

$$\rho_{\rm sc}(E) = \frac{\left(\frac{1}{2\pi\hbar^2}\right)^{d/2}}{\Gamma\left(d/2\right)} \int d\vec{x}\ \Theta(E - V(\vec{x}))\ (E - V(\vec{x}))^{d/2-1}\,, \tag{2.32}$$

where Θ is the Heaviside step-function and Γ is the Gamma function. For the quartic anharmonic potential (2.29) in $d = 1$ the density of states can be expressed in terms of the complete elliptic integral of the first kind $K(k) = F(\pi/2, k)$ [63],

$$\rho_{\rm sc}(E) = \frac{\sqrt{2/\pi^2\hbar^2}}{(k_2^2/4 + k_4 E/6)^{1/4}} K\left(\sqrt{\frac{1}{2} - \frac{k_2/4}{\sqrt{k_2^2/4 + k_4 E/6}}}\right)\,. \tag{2.33}$$

In practical applications, especially in $d = 1$, it might be difficult to compare directly semiclassical approximation for density of states and numerically obtained histogram for $\rho(E)$, since energy levels are usually not degenerated, so the spectrum is very sparse. In order to have sufficient statistics for a reasonable histogram, one has to use large value for bin size, and effectively the whole numerically available spectrum is reduced to just a few bins. For this reason, it is more instructive to study the cumulative density of states,

$$n(E) = \int_{V_{min}}^{E} dE'\ \rho(E')\,, \tag{2.34}$$

which counts the number of energy eigenstates smaller or equal to E. For quartic anharmonic oscillator the cumulative density of states is given by the above integral of the complete elliptic integral of the first kind, and can be calculated numerically. Fig. 2.10 gives comparison of cumulative density of states calculated from our numerical diagonalization results and semiclassical approximation $n_{\rm sc}(E)$. As expected, the agreement is excellent up to very high values of energies, where numerical diagonalization eventually fails due to the finite number of calculated energy eigenvalues and effects of discretization. Such behavior can be improved by using finer discretization (smaller spacing size), as illustrated by two different discretization steps for $k_4 = 48$, in Fig. 2.10. Such analysis can be used to assess the obtained spectrum and determine the number of reliable energy eigenvalues. Typically we can achieve up to 10^4 reliable energy eigenlevels with simulations on a single CPU.

In order to further demonstrate the applicability of the method, we also present

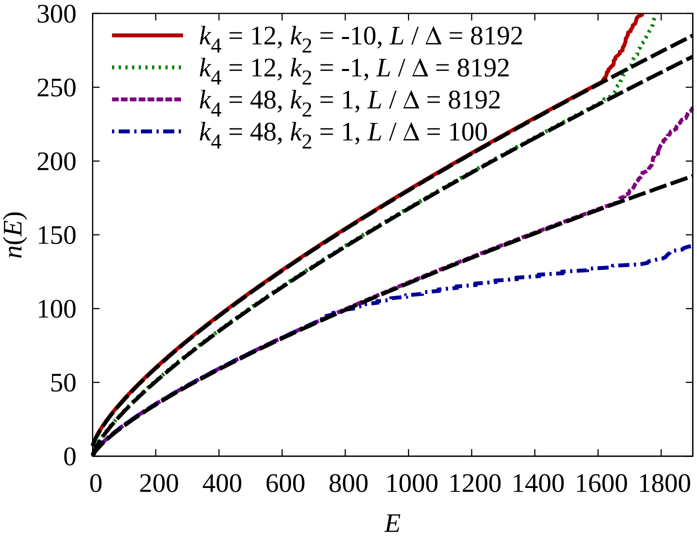

Figure 2.10: Cumulative distribution of the density of numerically obtained energy eigenstates for the quartic anharmonic ($k_2 = 1$) and double-well potential ($k_2 = -1$), for $t = 0.02$, $p = 21$ and the following values of diagonalization parameters: $L = 10$ for $k_4 = 12$ and $L = 8$ for $k_4 = 48$. The discretization step is given on the graph by the value of L/Δ, top to bottom. Long-dashed lines give corresponding semiclassical approximations for the cumulative density of states.

numerical results for the modified Pöschl-Teller model

$$V(x) = -\frac{\chi^2}{2}\,\frac{\lambda(\lambda-1)}{\cosh^2\chi x}\,, \tag{2.35}$$

which has only a finite set of discrete energy eigenlevels $E_k = -\chi^2(\lambda-1-k)^2/2$ for integer k from the interval $0 \le k \le \lambda - 1$. Energy eigenvalues and eigenfunctions of this model are analytically known, and we will use them to further test our method. Effective actions to very high order are available also for this potential [60], and we use them for numerical diagonalization of the evolution operator. Naturally, the diagonalization will give as many eigenvalues and eigenvectors as the size of the matrix S, but only the first few can be interpreted as bound states of the potential, according to the above condition $0 \le k \le \lambda - 1$.

Fig. 2.11(top) gives the analysis of errors in the ground energy due to the space cutoff, while Fig. 2.11(bottom) gives the corresponding analysis of L-errors for numerical calculation of the energy level E_5. As we can see, the behavior of errors is the same as for the case of anharmonic oscillator, and we are again able to obtain high

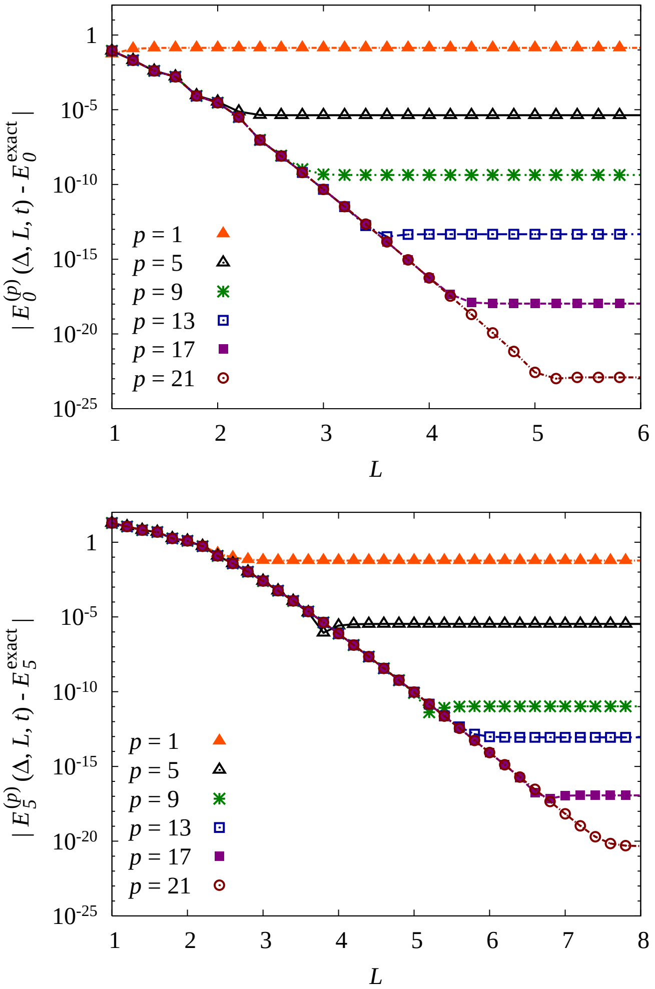

Figure 2.11: Deviations $|E_k^{(p)}(\Delta, L, t) - E_k^{\rm exact}|$ as a function of L for $k = 0$ (top) and $k = 5$ (bottom), for the modified Pöschl-Teller potential. Energy eigenvalues are obtained using effective action levels $p = 1, 5, 9, 13, 17, 21$ and $t = 0.1$, with the parameters $\chi = 0.5$, $\lambda = 15.5$, $\Delta = 0.02$.

accuracy results. Fig. 2.12 gives the time dependence of errors in ground energy obtained by numerical diagonalization using different levels p of effective actions. The scaling of errors proportional to t^p is evident from the graph, as well as the discretization errors due to the finite discretization step Δ. To ensure that the effective potential is bounded from below, in this case we have to remove higher-order powers of discretized velocity δ from the effective potential near $x = 0$, since such terms have non-vanishing negative coefficients in the vicinity of $x = 0$, due to a peculiar nature of the potential. In practical applications, one can use e.g. $p = 1$ effective

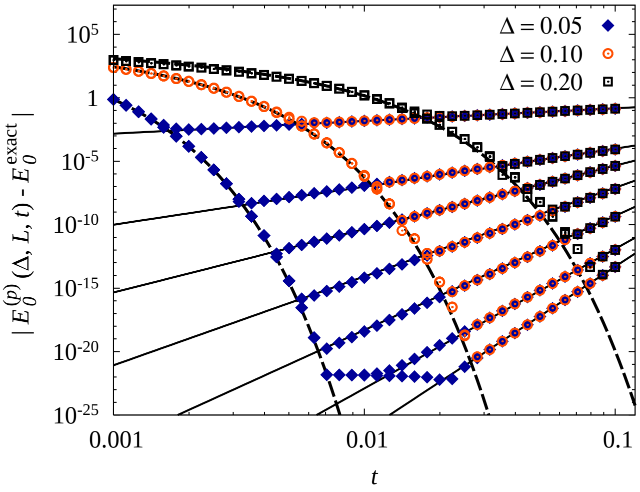

Figure 2.12: Deviations $|E_k^{(p)}(\Delta, L, t) - E_k^{\mathrm{exact}}|$ as a function of t for $k = 0$, for the modified Pöschl-Teller potential. Energy eigenvalues are obtained using effective action levels $p = 1, 3, 5, 7, 9, 11, 13$ and $L = 5$, with the parameters $\chi = 0.5$, $\lambda = 15.5$, $\Delta = 0.02$. Dashed lines in correspond to the discretization error (2.19).

action (which does not depend on δ) near $x = 0$. As can be seen, this does not affect the obtained numerical results.

Table 2.3(top) gives the obtained energy spectra for the modified Pöschl-Teller potential with the parameters $\chi = 0.5$, $\lambda = 15.5$. If necessary, the precision of obtained energy levels can be further increased by appropriately changing the discretization parameters. Contrary to the situation for anharmonic oscillator, where relative error of numerically calculated low-lying energy levels did not change significantly, here we see that the increase in the error is substantial. This is caused by the fact that this potential has only a small finite set of discrete bound states, so energy levels $k \sim 10$ correspond to the very top of the discrete spectrum. In practical applications such pathological situations are not encountered, but as we can see, even this can be dealt with by the proper choice of discretization parameters. The quality of numerically calculated eigenfunctions is assessed in Table 2.3(bottom), where we give a symmetric matrix of scalar products $\langle \psi_k | \psi_l^{\mathrm{exact}} \rangle$ of numerically calculated and analytic eigenfunctions. As we can see, the overlap between analytic and numeric eigenfunctions is excellent, and they are orthogonal with high precision, which is preserved even for higher energy levels. We have also verified that for parameters given in the caption of Table 2.3 and with the discretization step of the order $\Delta = 10^{-3}$ eigenfunctions of all bound states can be accurately reproduced.

Table 2.3: Top: Low-lying energy levels of the modified Pöschl-Teller potential, obtained by diagonalization using level $p = 21$ effective action. The parameters used: $\chi = 0.5$, $\lambda = 15.5$, $L = 5$, $\Delta = 0.02$, $t = 0.1$. Bottom: Symmetric table of scalar products $\langle \psi_k | \psi_l^{\mathrm{exact}} \rangle$ of numerically calculated and analytic eigenstates for $k, l = 0, 1, 2, 3, 4$.

k	E_k	E_k^{exact}	$\lvert E_k - E_k^{\mathrm{exact}} \rvert$	δE_k
0	$-26.28125000000000000000000(174)$	-26.28125	2×10^{-24}	7×10^{-26}
1	$-22.781250000000000000000(28812)$	-22.78125	3×10^{-22}	2×10^{-23}
2	$-19.53124999999999999999(736443)$	-19.53125	3×10^{-21}	2×10^{-22}
3	$-16.5312499999999999999(6571136)$	-16.53125	4×10^{-20}	2×10^{-21}
4	$-13.7812499999999999(8195897101)$	-13.78125	2×10^{-17}	2×10^{-18}
5	$-11.28124999999999(398393103608)$	-11.28125	6×10^{-15}	6×10^{-16}
6	$-9.0312499999(8602255352218206)$	-9.03125	2×10^{-12}	2×10^{-13}
7	$-7.031249999(773547728177905754)$	-7.03125	3×10^{-10}	4×10^{-11}
8	$-5.2812499(74811672590174261082)$	-5.28125	3×10^{-8}	5×10^{-9}

	0	1	2	3	4
0	$1 - 4 \cdot 10^{-12}$	$1.2 \cdot 10^{-13}$	$2.8 \cdot 10^{-6}$	$7.4 \cdot 10^{-14}$	$3.0 \cdot 10^{-7}$
1	$1.2 \cdot 10^{-13}$	$1 - 1 \cdot 10^{-11}$	$2.1 \cdot 10^{-13}$	$4.5 \cdot 10^{-6}$	$4.6 \cdot 10^{-14}$
2	$2.8 \cdot 10^{-6}$	$2.1 \cdot 10^{-13}$	$1 - 2 \cdot 10^{-11}$	$1.3 \cdot 10^{-13}$	$5.9 \cdot 10^{-6}$
3	$7.4 \cdot 10^{-14}$	$4.5 \cdot 10^{-6}$	$1.3 \cdot 10^{-13}$	$1 - 4 \cdot 10^{-11}$	$3.1 \cdot 10^{-13}$
4	$3.0 \cdot 10^{-7}$	$4.6 \cdot 10^{-14}$	$5.9 \cdot 10^{-6}$	$3.1 \cdot 10^{-13}$	$1 - 5 \cdot 10^{-11}$

2.5 Numerical results for two-dimensional models

In this section we illustrate the application of the numerical method based on the diagonalization of transition amplitudes on two models in $d = 2$ spatial dimensions. The first model is the anharmonic oscillator

$$V(x, y) = \frac{k_2}{2}(x^2 + y^2) + \frac{k_4}{24}(x^2 + y^2)^2 \,, \tag{2.36}$$

which is used for a description of the trapping potential used in a recent experiment with fast-rotating Bose-Einstein condensate of ^{87}Rb atoms [12, 64, 65].

The graphs in Fig. 2.13 are calculated for $k_2 = 0$, when the potential is reduced to a pure quartic interaction. The analysis of errors is very similar as in the one-dimensional cases we studied in the previous section. The dependence of ground energy errors on the space cutoff L is shown in Fig. 2.13(top), and we see the

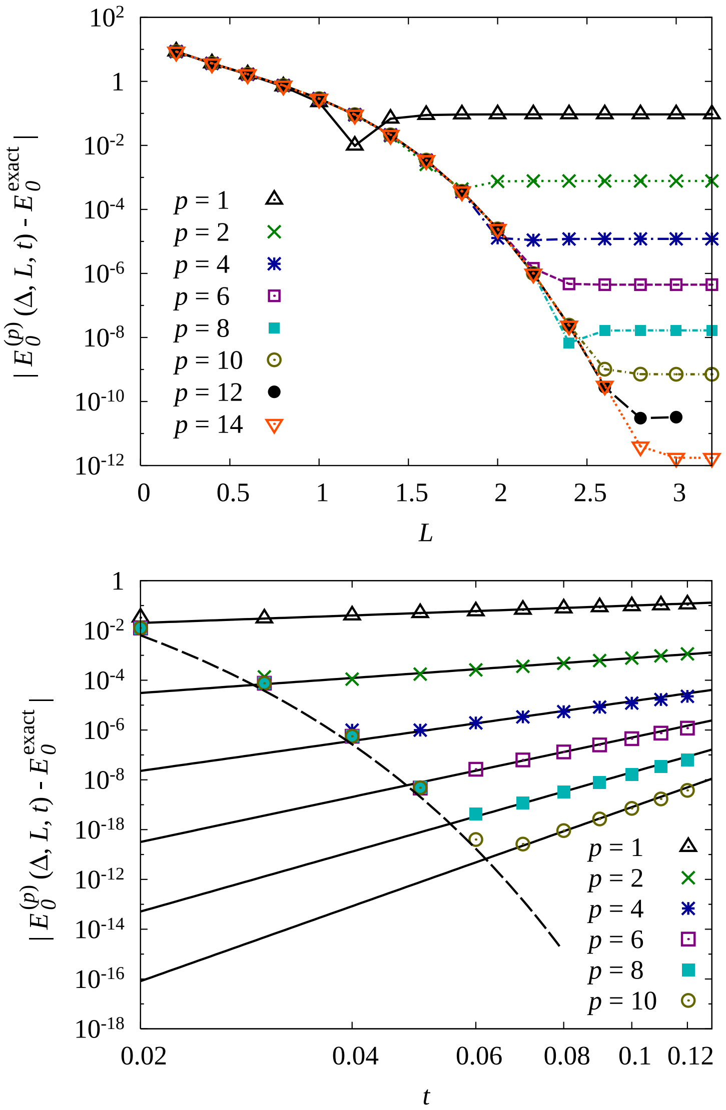

Figure 2.13: Deviations from the ground energy $|E_0^{(p)}(\Delta, L, t) - E_0|$ as a function of the space cutoff L (top) and as a function of the time t (bottom) for the potential (2.36) for $k_2 = 0$ and $k_4 = 24$. The discretization parameters are $\Delta = 0.2$, $t = 0.1$ on the top graph, and $L = 3$ on the bottom graph. Deviations are calculated using the ground energy $E_0 = 1.47714975357799(4)$ obtained with $p = 21$ effective action. The dashed line in the bottom graph corresponds to the discretization error (2.19).

usual saturation of errors for sufficiently large values of L. The saturated value rapidly decreases (by several orders of magnitude) as we increase the level p of the effective action used to calculate space-discretized matrix of the evolution operator. Fig. 2.13(bottom) shows the time dependence of ground energy errors, which are

Table 2.4: Low-lying energy levels of a $d = 2$ anharmonic potential (2.36), obtained using the level $p = 21$ effective action. The discretization parameters are $L = 14$, $\Delta = 0.14$, and $t = 0.2$.

k	E_k, $k_2 = -0.1025$, $k_4 = k_4^{exp}$	E_k, $k_2 = -0.1025$, $k_4 = 10^3\, k_4^{exp}$
0	-1.1279858856602	1.1287297831435
1	-1.1169327267787	2.6161348497834
2	-1.1169327267787	2.6161348497834
3	-1.0842518375067	4.3476515279810
4	-1.0842518374840	4.3476515279812
5	-1.0311383813261	4.6528451852013
6	-1.0311383813261	6.2704552903671
7	-0.95910186300510	6.2704552903671
8	-0.95910186300478	6.7589882491411
9	-0.86968170695135	6.7589882491412

found to fully agree with the scaling law t^p for sufficiently fine discretization. Again, the discretization errors conform to the universal dependence given in Eq. (2.19). Here there is an additional factor of 2 in the cosh term due to the dimensionality of the system.

Table 2.4 gives the numerically obtained energy eigenvalues for different sets of parameters of the potential (2.36). Motivated by the values of the experimental parameters [12, 64], we introduce and use the constant $k_4^{exp} = 1.95 \times 10^{-3}$. From the analysis of discretization errors and errors related to the use of a chosen effective action level p, we can estimate the errors in found energy eigenvalues to be of the order 10^{-15}. The results in the Table 2.4 are obtained by numerical diagonalization based on the C SPEEDUP code [60] and the use of the LAPACK [62] library. The estimated error in energy eigenvalues is smaller than the (relative) error which can be achieved in typical C simulations, which is of the order 10^{-14}. This is easily verified, since for several different values of discretization parameters we get the same stable results shown in the table. Therefore, this table gives certain digits in all energy eigenvalues, and the error can be cited as implicit (half of the last digit). This is good example for practical applications, where we have managed to eliminate all types of errors below the limit that can be seen due to inherent numerical errors of computer simulation. However, if such complete elimination of errors is not possible due to the limitations in computer memory or computation time, the analysis of errors presented in Fig. 2.13 allows us to reliably estimate numerical errors in energy eigenvalues.

Fig. 2.14 shows the numerically obtained ground state for this two-dimensional potential for the case of $k_2 < 0$. The ground state has the expected Mexican-hat shape. The figure gives a three-dimensional plot of the ground state on the left, and the corresponding density plot on the right, with values of the wave function mapped to colors. Fig. 2.15 gives density plots of $k = 1, 2, 3, 4$ eigenfunctions for the same values of parameters. The discretization is sufficiently fine ($\Delta = 0.25$) so that all features of calculated eigenfunctions are clearly visible.

As in the one-dimensional case, we will calculate the density of states $\rho_{\rm sc}(E)$ in semiclassical approximation, and use it as a criterion for the reliability of high-energy eigenstates. In $d = 2$, the density of states is given by a simple formula

$$\rho_{\rm sc}(E) = \frac{1}{2\pi} \int\!\!\int dx dy\ \Theta(E - V(x, y))\,. \tag{2.37}$$

For the quartic anharmonic potential (2.36) the density of states can be analytically calculated

$$\rho_{\rm sc}(E) = -\frac{3\,k_2}{k_4} + \sqrt{\frac{9\,k_2^2}{k_4^2} + \frac{6E}{k_4}}\,. \tag{2.38}$$

Fig. 2.16(top) shows the comparison of semiclassical approximation for the density of states, and the histogram for numerically obtained energy eigenvalues of the

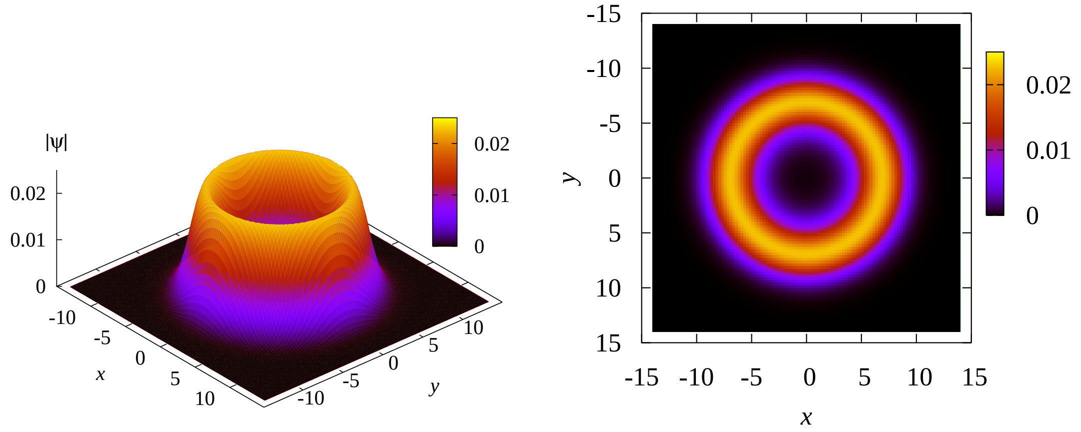

Figure 2.14: Ground state (as 3-D plot on the left, and as a density plot on the right) of a $d = 2$ anharmonic potential (2.36) obtained using $p = 21$ effective action. The parameters are $k_2 = -0.1025$, $k_4 = k_4^{exp}$, $L = 20$, $\Delta = 0.25$, $t = 0.2$.

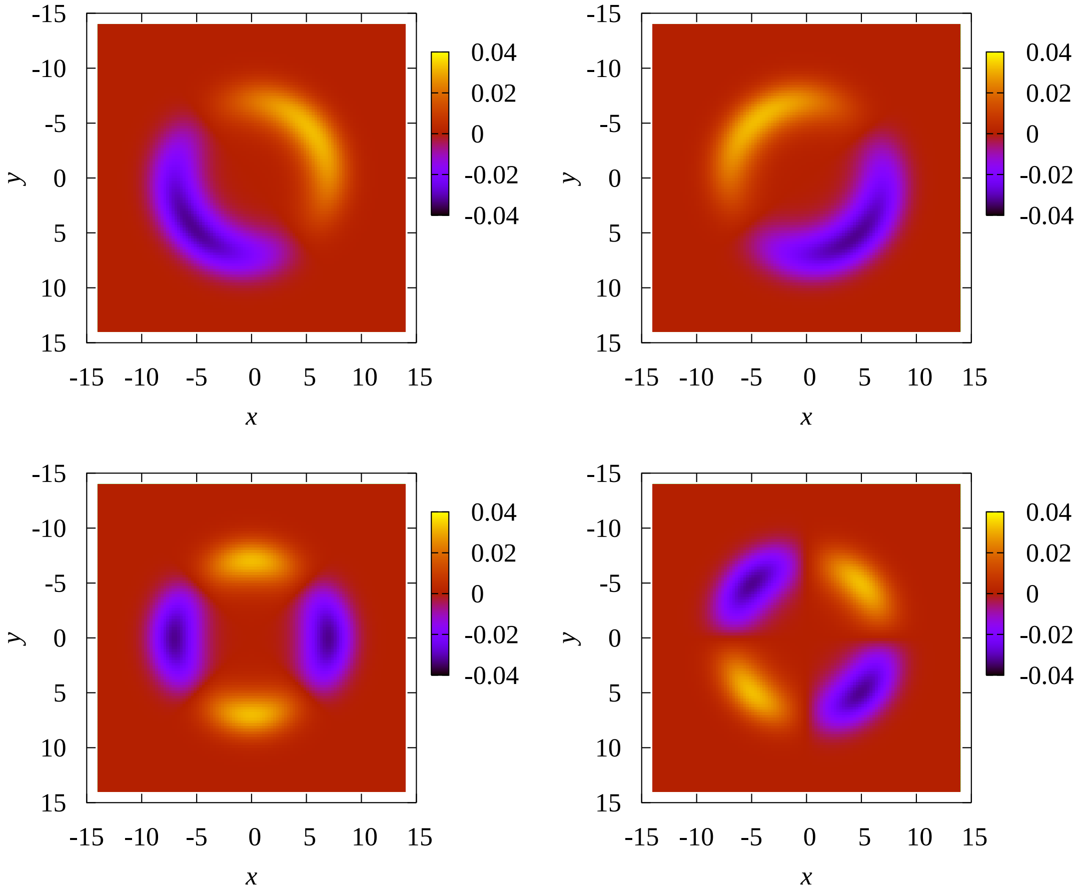

Figure 2.15: Density plots of level $k = 1, 2, 3, 4$ eigenstates of a $d = 2$ anharmonic potential (2.36) obtained using $p = 21$ effective action. The parameters are $k_2 = -0.1025$, $k_4 = k_4^{exp}$, $L = 20$, $\Delta = 0.25$, $t = 0.2$.

potential (2.36). Due to the high degeneracy of energy eigenstates in $d = 2$, the histogram of numerically found energy levels contains enough statistics over the whole region of energies, and therefore can be used for assessment of the quality of numerical spectra. As we see, the agreement is better and better when we use finer space discretization. Depending on the needed number of energy levels and maximal value of the energy considered to be relevant for the calculation we can choose appropriate values of discretization parameters that will provide reliable numerical results up to desired energy value. For example, for the choice of discretization parameters $L = 14$, $\Delta = 0.14$, we can reliably use energy levels up to $E \approx 120$.

Fig. 2.16(bottom) shows the comparison of cumulative density of states $n(E)$ calculated for numerically obtained results and in semiclassical approximation, by

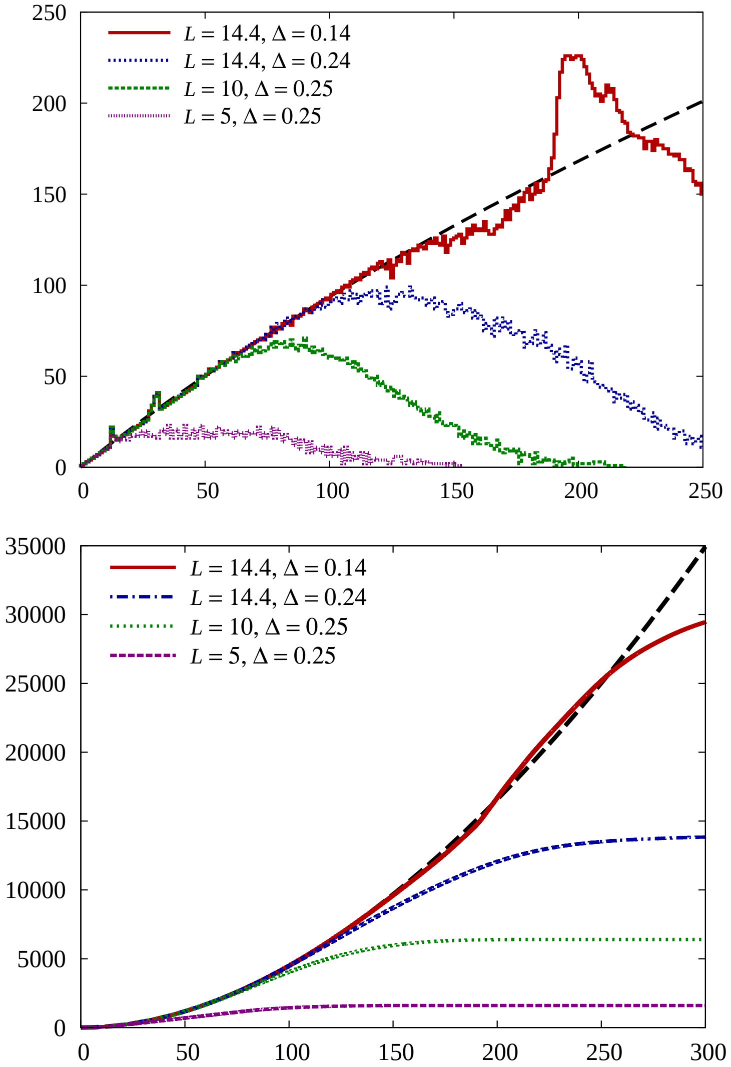

Figure 2.16: Distribution of the density of numerically obtained energy eigenstates (top) and cumulative distribution of the density of numerically obtained energy eigenstates (bottom) for a $d = 2$ anharmonic potential (2.36), calculated with the level $p = 21$ effective action. The parameters are $k_2 = 1$, $k_4 = k_4^{exp}$, $t = 0.2$, while discretization parameters are given on the graph, corresponding to the curves top to bottom. Long-dashed lines on both graphs give the corresponding semiclassical approximations.

integrating the expression (2.38), which can be calculated analytically. The comparison of numerical and semiclassical cumulative density of states in Fig. 2.16(bottom) verifies our conclusions from Fig. 2.16(top), and again sets the same limit of reliable energy levels for chosen discretization parameters.

The second two-dimensional model we have studied numerically is a sextic anharmonic oscillator,

$$V(x,y) = V_x(x) + V_y(y) + V_{xy}(x-y)\,, \tag{2.39}$$

where $V_i(x) = V_{i0}\,(a_i x^2 + b_i x^4 + c_i x^6)$. The values of the coefficients used are given in Table 2.5. The study of this potential is motivated by Ref. [66], where it has been used to investigate the transition from regular to chaotic classical motion. Fig. 2.17 shows the numerically obtained ground state for this two-dimensional potential, as a three-dimensional plot on the left, and as a density plot on the right. Fig. 2.18 gives density plots of $k = 1, 3, 7, 8$ eigenfunctions for the same values of parameters. The discretization is sufficiently fine ($\Delta = 0.04$) so that we can resolve all details in the presented eigenstates.

Table 2.5: Parameters of the sextic potential (2.39).

i	V_{i0}	a_i	b_i	c_i
x	100	1.56	-0.61	0.32
y	100	0.69	-0.12	0.03
xy	100	-1.00	0.25	0.08

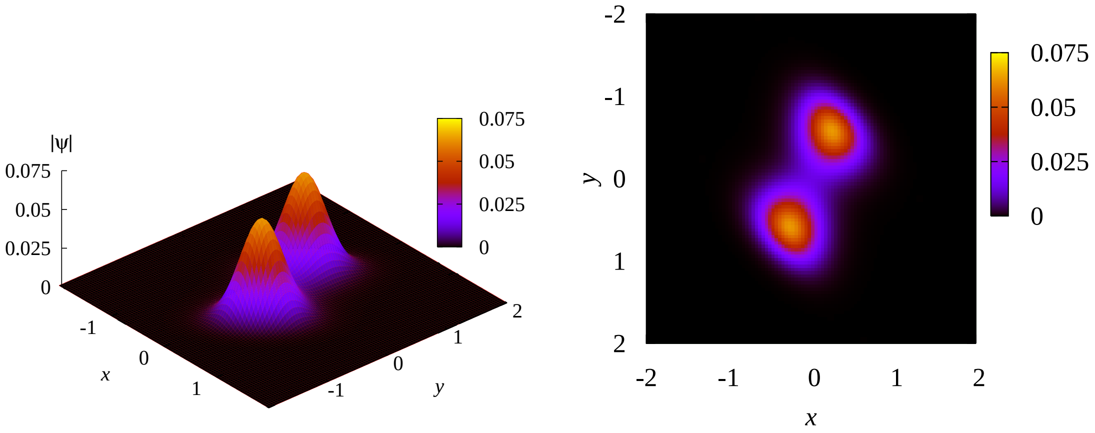

Figure 2.17: Ground state (as 3-D plot on the top, and as a density plot on the bottom) of a sextic anharmonic potential, obtained by diagonalization using the level $p = 21$ effective action. The parameters of the potential are given in the text. The diagonalization parameters: $L = 4$, $\Delta = 0.04$, $t = 0.01$.

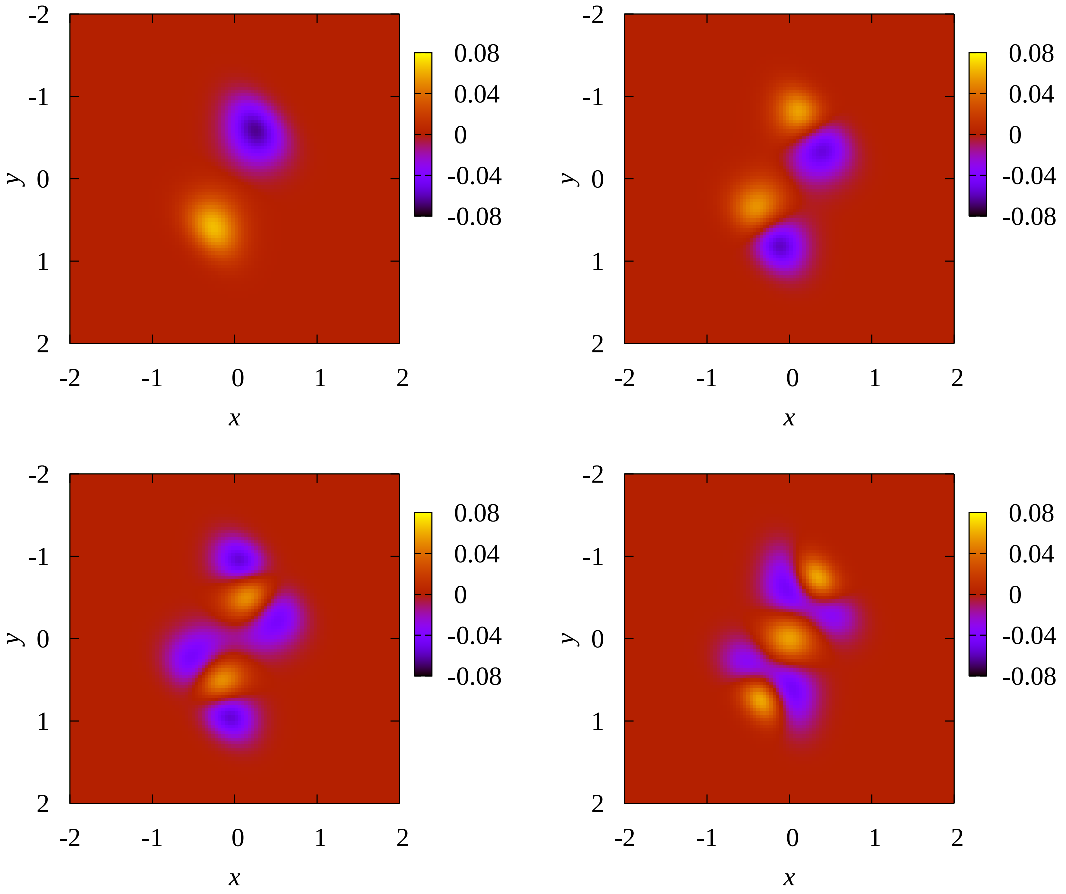

Figure 2.18: Density plots of level $k = 1, 3, 7, 8$ eigenstates of a sextic anharmonic potential, obtained by diagonalization using the level $p = 21$ effective action. The parameters of the potential are given in the text. The diagonalization parameters: $L = 4$, $\Delta = 0.04$, $t = 0.01$.

We have demonstrated that the presented approach can be successfully used for numerical studies of lower-dimensional models. Note that in $d = 3$ the complexity of the algorithm and sizes of matrices to be diagonalized may practically limit the applicability to the calculation of only low-lying energy levels. Also, in this case it might be difficult to numerically obtain three-dimensional eigenfunctions on finer grids, since even moderate grids with 50-100 points in one dimension would require exact diagonalization of extremely large matrices.

At the end, let us compare the complexity of the presented approach and direct diagonalization of the space-discretized Hamiltonian, as well as finite-element methods. The main difference in the complexity of algorithms is related to the exponential growth in the size of analytic expressions for the effective potential with the increase of the level p, as discussed in Ref. [44]. Therefore, the required CPU time for construction of the matrix to be diagonalized in the presented approach grows exponentially with the level p, while in other methods the construction of such a matrix does not require a significant amount of time. However, the time for exact diagonalization far outweighs the time needed for construction of even large matrices with moderate levels p of the order 10-20. The significant benefit of practically eliminating errors associated with the time of propagation therefore fully justifies the use of the effective action approach. Of course, in practical applications one has to study the complexity of the algorithm and to choose the optimal level p which will sufficiently reduce the errors, while keeping the complexity of the calculation on the acceptable level.

2.6 Conclusions and outlook

In this Chapter, we have dealt with the thorough understanding and optimization of the method of the calculation of the properties of quantum systems based on the diagonalization of transition amplitudes, previously introduced in Ref. [9]. First, we have focused on analyzing the errors associated with real-space discretization and finite size effects. In particular, we have shown that within this calculation scheme spatial discretization leads to a universal and non-perturbatively small discretization error. This highly outperforms the usual polynomial behavior of errors in approaches based on the diagonalization of space-discretized Hamiltonians. A key problem in practical applications of this approach - accurate calculation of transition amplitudes, matrix elements of the space-discretized evolution operator, has been resolved using recently introduced effective action approach [44], which gives systematic short-time expansion of the evolution operator.

The derived analytical estimates for all types of errors, including errors due to the approximative calculation of transition amplitudes, provide us with a way to choose optimal discretization parameters and to reduce overall errors in energy eigenvalues and eigenstates for many orders of magnitude, as was demonstrated for several one- and two-dimensional models. We have shown that numerical diagonalization of the space-discretized evolution operator can be successfully applied for studies of many interesting lower dimensional models. The approach allows exact numeric calculation of a large number of energy eigenvalues and eigenstates of the system. Due to the superior behavior of discretization and other errors in this method compared to methods based on diagonalization of the discretized Hamilton operator and related methods, the presented approach is a method of choice for numerical studies of lower-dimensional physical systems. An application of the approach for numerical investigation of properties of fast rotating Bose-Einstein condensates is given in Chapter 3. Further interesting line of research would be to combine the present method with the density matrix renormalization group (DMRG) approach [48, 67].

Chapter 3 Thermodynamics of a rotating ideal BEC

The behavior of a BEC under rotation is essential for understanding many fundamental phenomena [68, 7, 19]. The response of a quantum fluid to rotation represents one of the seminal hallmarks of superfluidity characterized by a nucleation of vortices with a quantized circulation. In the past, quantum vortices were studied experimentally in the superfluid helium and in type-II superconductors. An important advantage of the cold atomic gases for studying vortices is that the typical size of a vortex core is 3 orders of magnitude larger than in the superfluid Helium, and, even more importantly, it is large enough to be observed optically [69, 7]. Early experiments with rotating cold gases explored different regimes: for slow rotation a small number of vortices was observed [70, 69], while the triangular Abrikosov lattice [71] composed of about 100 vortices was detected in the case of a higher rotation frequency [72]. Eventually, in the case of a very rapid rotation it is expected that bosons would go from the superfluid phase into a strongly correlated phase that is related to the quantum Hall physics [73].

The equivalence of the rotation and the motion of a charged particle in a magnetic field can be easily understood by considering the Hamiltonian of a single particle in a harmonic trap in a rotating reference frame with the rotation frequency $\vec{\Omega} = \Omega\,\vec{e}_z$ [68]:

$$\begin{aligned}
\hat{H}_{\mathrm{rot}} &= \hat{H} - \vec{\Omega}\cdot\hat{\vec{\mathcal{L}}} \\
&= \frac{1}{2M}(\hat{p}_x^2 + \hat{p}_y^2 + \hat{p}_z^2) + \frac{1}{2}M\omega^2(\hat{x}^2 + \hat{y}^2 + \lambda_z^2\hat{z}^2) - \Omega\,\vec{e}_z\cdot(\hat{\vec{r}}\times\hat{\vec{p}}) \\
&= \frac{1}{2M}(\hat{p}_x + M\Omega\hat{y})^2 + \frac{1}{2M}(\hat{p}_y - M\Omega\hat{x})^2 \\
&\quad + \frac{1}{2}M(\omega^2 - \Omega^2)(\hat{x}^2 + \hat{y}^2) + \frac{1}{2M}\hat{p}_z^2 + \frac{1}{2}M\lambda_z^2\omega^2\hat{z}^2, \qquad (3.1)
\end{aligned}$$

where $\hat{\vec{\mathcal{L}}}$ is the angular momentum and all the variables in the last expression are given in the rotating reference frame. From Eq. (3.1), we see that in the limit $\Omega \to \omega$, the Hamiltonian becomes formally equivalent to the one describing particles in the magnetic field $\vec{B} = 2M\vec{\Omega}$.

However, once harmonically trapped Bose-Einstein condensate is rotated critically, i.e. the rotation frequency becomes so large that it fully compensates the radially confining harmonic trapping, the system turns out to be radially no longer confined. In the absence of additional potential terms, the condensate would start to expand in directions perpendicular to the rotation axis. For an overcritical rotation, this expansion would even be accelerated by the presence of a residual centrifugal force. This poses a severe problem to the experimental achievement of strongly correlated bosonic states. In order to reach experimentally this delicate regime, Fetter suggested in Ref. [74] a small quartic term to be added to the harmonic trap potential, which would provide a confinement in the radial direction in the case of a critical and overcritical rotation.

The proposal has been experimentally realized in Paris by the Dalibard group for a BEC of ^{87}Rb atoms [12, 7], by superimposing to the magnetic trap an additional Gaussian laser beam propagating in the z-direction,

$$U(x,y) = U_0 e^{-\frac{2(x^2+y^2)}{w^2}} \,. \tag{3.2}$$

In the previous equation, w denotes the laser beam waist and U_0 is the intensity of the beam. Within the laser beam waist, the potential can be approximated by:

$$U(x,y) \approx U_0 - 2\,U_0 \frac{x^2+y^2}{w^2} + 2\,U_0 \frac{(x^2+y^2)^2}{w^4}, \tag{3.3}$$

and this is how the quartic term is brought about. An additional laser beam that creates a small anisotropic potential in the $x-y$ plane is used for stirring the pure BEC at the rotation frequency Ω. After the angular momentum has been introduced into the system, the rotation is stopped and the condensate is allowed to equilibrate. Taking into account Eqs. (3.1) and (3.3), the resulting axially-symmetric trap with a small quartic anharmonicity in the $x-y$ plane, seen by individual atoms, has the form

$$V_{\rm BEC} = \frac{M}{2}(\omega^2 - \Omega^2)(x^2+y^2) + \frac{M}{2}\omega_z^2 z^2 + \frac{\kappa}{4}(x^2+y^2)^2 \,, \tag{3.4}$$

with the trap frequencies $\omega = 2\pi \times 64.8$ Hz, $\omega_z = 2\pi \times 11.0$ Hz, and the trap anharmonicity $\kappa = \kappa_{\rm BEC} = 2.6 \times 10^{-11}$ Jm^{-4}. The rotation frequency Ω, measured in units of ω and expressed by the ratio $\eta = \Omega/\omega$, represents the tunable control parameter, which could be experimentally varied in the range between 0 and 1.04.

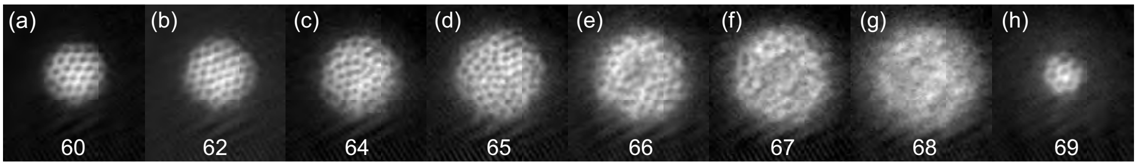

Figure 3.1: Images of a rotating BEC along the rotation direction for different rotation frequencies $\Omega/2\pi$. The linear size of each image is $306\,\mu$m. The results are taken from Ref. [12].

To probe the system, the TOF absorption imaging is performed. Typical results of the measurements for different rotation frequencies are presented in Fig. 3.1. It is obvious that up to $\Omega = 2\pi \times 68$ Hz the radius of a trapped cloud increases with increase in Ω. For $\Omega = 2\pi \times 66$ Hz and $\Omega = 2\pi \times 67$ Hz the radial density profile of the cloud follows the Mexican-hat shape of the potential, however number of observed vortices in this case is smaller than expected for such a large rotation frequency. Several possible schemes are discussed as a possible explanation of the observed features.

In order to contribute to the understanding of the experimental results, we study the BEC phase transition of an ideal Bose gas in the trapping potential (3.4), modified by the presence of a quartic term and a rotation with respect to the common harmonic trap (1.6). Depending on the value of the rotation frequency, the shape of the potential changes from convex with a single minimum to the Mexican-hat shape, which significantly influences the properties of a condensate. To study these effects, in the rest of this Chapter we calculate the condensation temperature, condensate fraction and density profiles of the cloud in the trap (3.4) and also simulate a free expansion of the condensate, corresponding to the TOF imaging.

As long as we approximately describe the system with the ideal Bose gas, all of its many-body properties in the grand-canonical ensemble can be derived purely from single-particle states. When considering the thermodynamic limit, usually the semiclassical approximation is applied, where the single-particle ground state E_0 is retained and treated quantum mechanically, while all other excited states are treated as a continuum [19, 65]. The validity of the semiclassical approximation can be rigorously justified in some regimes of the relevant parameters. As briefly mentioned in Chapter 1, the semiclassical approximation is justified in the high-temperature limit, when the thermal energy is larger than the typical spacing of energy levels, $k_B T \geq (E_{n+1} - E_n)$. Also, it remains reasonable good irrespective of the rotation frequency Ω once the total particle number N is large enough and the trap anharmonicity κ is small enough. The latter condition implies that the underlying potential (3.4) has a small curvature around its minimum, and hence the corresponding density of energy levels is sufficiently high. However, in this context the question arises how accurate the semiclassical approximation is, for which system parameters it is not anymore sufficient for a precise description of BEC phenomena, as well as when it finally breaks down, requiring a full quantum-mechanical treatment of the system.

In order to analyze the problem more quantitatively, it is mandatory to determine the single-particle energy eigenvalues and eigenfunctions fully quantum mechanically. In this Chapter we show how the exact diagonalization of a time-evolution operator, presented in Chapter 2, is applied for studying both global and local properties of fast-rotating Bose-Einstein condensates. To this end we proceed as follows: first we calculate a large number of energy eigenvalues and eigenfunctions for the anharmonic potential (3.4). Afterwards, we discuss how a finite number of numerically available energy eigenvalues affects the results and how they can be improved by introducing systematic semiclassical corrections. On the basis of this precise numerical single-particle information, we study global properties of a rotating condensate. Finally, we calculate local properties of the condensate, such as density profiles and TOF absorption pictures.

To begin with, we rewrite Eq. (1.3) for the total number of particles in a more convenient form in terms of the single-particle partition function $Z_1(\beta)$, defined as

$$Z_1(\beta) = \sum_{n=0}^{\infty} e^{-\beta E_n} \,. \tag{3.5}$$

To do this, we single out the contribution of the ground state and use the Taylor's expansion $1/(1-x) = \sum_{n=0}^{\infty} x^n$ (valid for $|x| < 1$), to derive the following expression:

$$N \;=\; \sum_{n=0}^{\infty} \frac{1}{e^{\beta(E_n-\mu)} - 1} = \mathcal{B}_0(\mu, T) + \sum_{n=1}^{\infty}\sum_{j=1}^{\infty} e^{-j\beta(E_n-\mu)} \,. \tag{3.6}$$

By rearranging the summation order in the previous equation, we finally obtain:

$$\begin{aligned} N &= \mathcal{B}_0(\mu,T) + \sum_{j=1}^{\infty} e^{j\beta\mu} \sum_{n=1}^{\infty} e^{-j\beta E_n} \,, \\ &= \mathcal{B}_0(\mu,T) + \sum_{j=1}^{\infty} e^{j\beta\mu} \left(Z_1(j\beta) - e^{-j\beta E_0} \right) \,, \end{aligned} \tag{3.7}$$

where the summation on the right-hand side of the previous equation corresponds to the cumulant expansion. In order to avoid any double-counting, we have subtracted the contribution of the ground state within the single-particle partition function because a possible macroscopic occupation of the ground state is separately taken into account.

The BEC phase transition is achieved only in the thermodynamic limit of an infinite number of atoms, thus making numerical studies of the condensation increasingly difficult. Usually, the problem is solved by fixing the chemical potential μ at the low temperatures of the condensate phase to the ground-state energy, i.e. by setting $\mu = E_0$. This requires that the ground state is treated separately by associating a macroscopic value N_0 to the ground-state occupation number $\mathcal{B}_0(\mu,T)$, for $T < T_c$. Thus, from Eq. (3.7), the total number of particles in the condensate phase follows to be:

$$N = N_0 + \sum_{j=1}^{\infty} \left(e^{j\beta E_0} Z_1(j\beta) - 1 \right) \,. \tag{3.8}$$

The equation (3.8) yields the temperature dependence of N_0. Within the gas phase, where the macroscopic occupation of the ground state vanishes, i.e. we have $N_0 = 0$, Eq. (3.7) determines the temperature dependence of the chemical potential μ. Therefore, the value of $\beta_c = 1/k_B T_c$, which characterizes the boundary between both phases, follows from Eq. (3.8) by setting $N_0 = 0$ and $\mu = E_0$:

$$N = \sum_{j=1}^{\infty} \left[e^{j\beta_c E_0} Z_1(j\beta_c) - 1 \right] \,. \tag{3.9}$$

We conclude that, for a given number N of ideal bosons, the condensation temperature can be exactly calculated only if both the single-particle ground-state energy E_0 and the full temperature dependence of the one-particle partition function (3.5) are known.

3.1 Numerical calculation of energy eigenvalues and eigenstates

A very efficient method for calculating properties of few-body quantum systems, that we use, is the direct diagonalization of the space-discretized propagator in imaginary time. The approach is able to give very accurate energy eigenvalues even for moderate values of the propagation time t of the order 0.1, as shown in detail in Chapter 2. Note that throughout this Chapter we use dimensionless units, in which all energies are expressed in terms of $\hbar\omega$, while the length unit is the corresponding harmonic oscillator length $\sqrt{\hbar/M\omega}$.

Table 3.1 presents the first several energy eigenvalues for the two-dimensional $(x-y)$ part of the BEC potential (3.4) for the non-rotating case ($\eta = 0$), as well as for the critically-rotating condensate ($\eta = 1$). The table on the left gives the energy spectrum of the potential with the anharmonicity $\kappa = \kappa_{\rm BEC}$ used in the experiment [12], while the right table shows the spectrum for the much larger anharmonicity $\kappa = 10^3\ \kappa_{\rm BEC}$. The degeneracies of numerically obtained eigenstates in all cases

Table 3.1: Lowest energy levels of the xy-part of the BEC potential (3.4) for non-rotating ($\eta = 0$) and critically rotating ($\eta = 1$) condensate with the quartic anharmonicity $\kappa = \kappa_{\rm BEC}$ (left) and $\kappa = 10^3\ \kappa_{\rm BEC}$ (right). They are obtained by using level $p = 21$ effective action with the discretization parameters of Table 3.3. The spacing Δ was always chosen so that $L/\Delta = 100$, and the propagation time was $t = 0.2$ for $\kappa = \kappa_{\rm BEC}$ and $t = 0.05$ for $\kappa = 10^3\ \kappa_{\rm BEC}$. Errors are given by the precision of the last digit, typically 10^{-12} to 10^{-13}, and are estimated by comparing the numerical results obtained with different discretization parameters.

	$E_n/\hbar\omega$, $\kappa = \kappa_{\rm BEC}$	
n	$\eta = 0$	$\eta = 1$
0	1.0009731351803	0.1162667164134
1	2.0029165834022	0.2674689968905
2	2.0029165834022	0.2674689968905
3	3.0058275442161	0.4426927375269
4	3.0058275442161	0.4426927375270
5	3.0067964582067	0.4725275724941
6	4.0097032385903	0.6368178804983
7	4.0097032385903	0.6368178804984
8	4.0116368851078	0.6848142470356
9	4.0116368851078	0.6848142470357

	$E_n/\hbar\omega$, $\kappa = 10^3\ \kappa_{\rm BEC}$	
n	$\eta = 0$	$\eta = 1$
0	1.468486725893	1.162667164134
1	3.213056378201	2.674689968905
2	3.213056378201	2.674689968905
3	5.163819069871	4.426927375269
4	5.163819069871	4.426927375270
5	5.406908088225	4.725275724941
6	7.282930987460	6.368178804982
7	7.282930987460	6.368178804982
8	7.690584058915	6.848142470357
9	7.690584058915	6.848142470357

Table 3.2: Lowest energy levels of the xy-part of the BEC potential (3.4) for over-critically rotating ($\eta = 1.04$) condensate with the quartic anharmonicity $\kappa = \kappa_{\mathrm{BEC}}$ and $\kappa = 10^3\ \kappa_{\mathrm{BEC}}$ according to the same numerical procedure as in Table 3.1.

	$E_n/\hbar\omega$, $\eta = 1.04$	
n	κ_{BEC}	$10^3\ \kappa_{\mathrm{BEC}}$
0	-0.6617041825660	1.135693826206
1	-0.6465857464220	2.628129903790
2	-0.6465857464220	2.628129903790
3	-0.6032113415949	4.363876633929
4	-0.6032113415948	4.363876633929
5	-0.5349860004310	4.667653582963
6	-0.5349860004309	6.290444734007
7	-0.4451224795419	6.290444734007
8	-0.4451224795419	6.777210773169
9	-0.3362724309903	6.777210773169

correspond to the expected structure of the spectrum, which can be deduced from the symmetry of the problem. In addition to this, the interesting case of critical rotation ($\eta = 1$) allows a further verification of the numerical results. To this end we recall that the energy eigenvalues of a pure quartic oscillator, to which V_{BEC} reduces in this case, are proportional to $\kappa^{1/3}$ due to a spatial rescaling in the underlying Schrödinger equation. Therefore, we expect that the energy eigenvalues for $\kappa = 10^3\ \kappa_{\mathrm{BEC}}$ are precisely 10 times larger than the corresponding eigenvalues for $\kappa = \kappa_{\mathrm{BEC}}$. Comparing the rightmost columns in Table 3.1 we see exactly this scaling. This demonstrates conclusively that the presented method can be successfully applied also in this deeply non-perturbative parameter regime. Furthermore, Table 3.2 gives the energy spectrum of an over-critically rotating ($\eta = 1.04$) condensate, illustrating that the same approach can be used in this delicate regime as well.

With these results single-particle partition functions $Z_1(\beta)$ can now be calculated according to Eq. (3.5). This is especially suitable for the low-temperature regime, when higher energy levels give a negligible contribution. Although the above described approach is able to accurately give several thousands of energy eigenvalues, their number is always necessarily limited. This is easily seen from Fig. 3.2, where we compare the density of states for a critically rotating condensate with the corre-

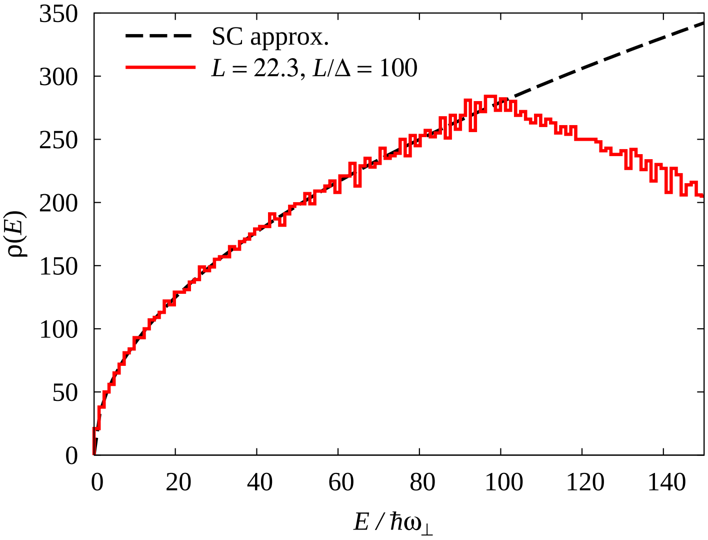

Figure 3.2: Numerically calculated density of states for xy-part of the BEC potential with $\kappa = \kappa_{\mathrm{BEC}}$ for a critically rotating condensate, obtained by using level $p = 21$ effective action. The discretization parameters are $L = 22.3$, $L/\Delta = 100$, and $t = 0.2$. The dashed line is the corresponding semiclassical approximation for the density of states.

sponding semiclassical approximation for the density of states (2.38). This comparison allows us to estimate the maximal reliable two-dimensional energy eigenvalue E_{max} which can be obtained numerically for a given set of discretization parameters. For example, from Fig. 3.2 we can estimate $E_{\mathrm{max}} \approx 90$ for $\eta = 1$ with the discretization parameters $L = 22.3$, $L/\Delta = 100$, and $t = 0.2$. Table 3.3 gives estimates for the maximal reliable energy eigenvalue for the anharmonicities $\kappa = \kappa_{\mathrm{BEC}}$ and $\kappa = 10^3\ \kappa_{\mathrm{BEC}}$ for several values of rotation frequencies. These results are obtained from numerical calculations using the SPEEDUP codes [60]. This table gives also an overview over those discretization parameters which were used for a numerical diagonalization of the BEC potential (3.4) in order to calculate both global and local properties of the condensate throughout this Chapter.

In the low-temperature limit the finiteness of the number of known energy eigenstates does not present a problem. In fact, a precise knowledge of a large number of energy eigenvalues makes this approach a preferred method for a numerically exact treatment of low-temperature phenomena. On the other hand, the high-temperature regime, where thermal contributions of higher energy states play a significant role, is not treatable in the same way. This regime is usually not relevant for studies of

Table 3.3: Maximal reliable numerically calculated energy eigenvalue E_{max} of the xy-part of the BEC potential (3.4) for different values of $\eta = \Omega/\omega$, estimated from comparing the numerically obtained density of states $\rho(E)$ with the semiclassical approximation. The numerical diagonalization was done using level $p = 21$ effective action. The spacing Δ was always chosen so that $L/\Delta = 100$, and the propagation time was $t = 0.2$ for $\kappa = \kappa_{\mathrm{BEC}}$ and $t = 0.05$ for $\kappa = 10^3\ \kappa_{\mathrm{BEC}}$. The total number of reliable energy eigenstates is in all cases of the order of 10^4.

	$\kappa = \kappa_{\mathrm{BEC}}$		$\kappa = 10^3\ \kappa_{\mathrm{BEC}}$	
η	$E_{\mathrm{max}}/\hbar\omega$	L	$E_{\mathrm{max}}/\hbar\omega$	L
0.0	140	14.2	190	3.90
0.2	140	14.4	190	3.90
0.4	140	15.0	180	3.91
0.6	140	16.3	180	3.92
0.8	130	18.6	180	3.94
1.0	90	22.3	170	3.96
1.04	90	23.2	170	3.96

BEC experiments, but we consider it for the sake of completeness. When the temperature is sufficiently high, so that effects of higher energy eigenstates cannot be neglected, the inverse temperature β becomes a small parameter. Thus, it becomes possible to calculate numerically the single-particle partition function as a sum of diagonal amplitudes, i.e.

$$Z_1(\beta) = \mathrm{Tr}\, e^{-\beta \hat{H}} \approx \sum_{\mathbf{j}} A(\mathbf{j}\Delta, \mathbf{j}\Delta; \beta)\Delta^d\,, \tag{3.10}$$

where Δ represents the spatial spacing, as before, the values of $\mathbf{j}$ are defined by $\mathbf{j} \in [-L/\Delta, L/\Delta]^d$, with the spatial cutoff L chosen in such a way as to ensure the localization of the evolution matrix within the interval $[-L, L]^d$, and transition amplitudes for small β can be calculated directly using the effective action approach [10, 44].

3.2 Finite number of energy eigenvalues and semiclassical corrections

In the previous section we have described a numerical approach that is capable of providing a large number of accurate energy eigenvalues for a general quantum system. For instance, we are able to calculate typically 10^4 energy eigenvalues for the considered BEC potential (3.4). In this section we discuss in more detail how the finiteness of numerically available energy eigenstates affects the calculation of thermodynamic properties of Bose-Einstein condensates.

As outlined at the beginning of this Chapter, the information on single-particle eigenvalues is sufficient for calculating the condensation temperature according to Eq. (3.9). Below the condensation temperature, the ground-state occupancy follows from solving Eq. (3.8). In practical calculations, however, one is inevitably forced to restrict the sum over j in the cumulant expansion (3.8) to some finite cutoff J, resulting in the following approximation for the number of thermal atoms

$$N - N_0 \approx \sum_{j=1}^{J} \sum_{n=1}^{\infty} e^{-j\beta(E_n - E_0)} \,. \tag{3.11}$$

Thus, the ground-state occupancy N_0 depends not only on the particle number N and the temperature T, but also on the cumulant cutoff J. In particular, when we solve Eq. (3.11) for the (inverse) condensation temperature β_c, obtained from the condition $N_0 = 0$, we will get the solution in the form $\beta_c(J)$, with an explicit dependence on J. The exact condensation temperature β_c is only obtained in the limit $J \to \infty$.

Fig. 3.3 illustrates the J-dependence resulting from Eq. (3.11) for both a non-rotating and a critically rotating condensate. As expected, the sum saturates for high values of J to some finite number $N - N_0$. By tuning the temperature in such a way that the sum saturates at the desired value of the total number of atoms N in the system, which corresponds to $N_0 = 0$, one is, in principle, able to extract the value of the condensation temperature T_c.

Although the results in Fig. 3.3 suggest that this approach can be applied straightforwardly, a closer look at the results for numerically calculated values of $N - N_0$ reveals several problems that have to be addressed. At first we have to investigate how the results depend on the number of energy eigenstates used in the

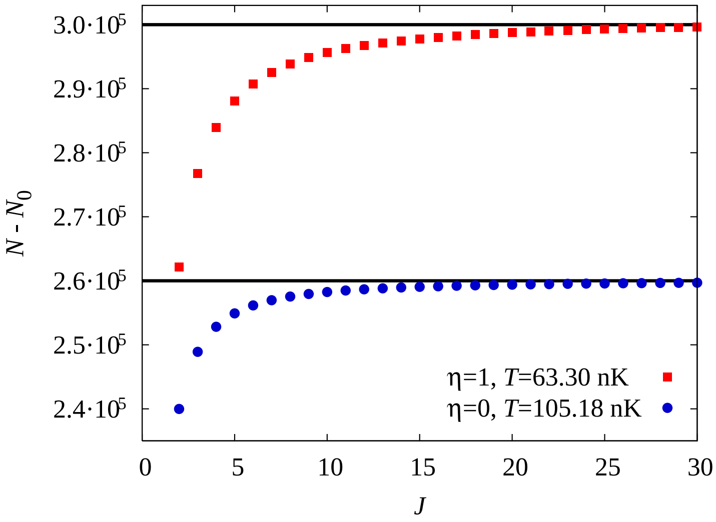

Figure 3.3: Number of thermally excited atoms $N - N_0$ as a function of the cutoff J in the cumulant expansion (3.11). The results are given for a non-rotating condensate at $T = 105.18$ nK and for a critically rotating condensate at $T = 63.30$ nK. The results are obtained by level $p = 21$ effective action, and all available numerical eigenstates are used to calculate $N - N_0$. The discretization parameters were $L = 14.2$ for $\eta = 0$ and $L = 22.3$ for $\eta = 1$. In both cases the spacing was chosen according to $L/\Delta = 100$, and the propagation time was $t = 0.2$.

numerical calculation. Fig. 3.4 gives this dependence for a critically rotating condensate at its critical temperature $T_c = 63.30$ nK. We can see that the dependence on the maximal available two-dimensional energy eigenvalue $E_{\max}$ is quite significant. The inset of this figure reveals another problem: the value to which number $N_0 - N$ saturates depends in addition on the cumulant cutoff J, as explained earlier. While the J-dependence can be dealt with by using a very large value of the cumulant cutoff in numerical calculations, the dependence on the maximal energy eigenvalue $E_{\max}$ must be eliminated by taking into account a proper semiclassical correction to the single-particle partition functions.

Namely, the finite number of energy eigenstates implies that the single-particle partition functions are only estimated by

$$Z_1(\beta) \approx \sum_{n=0}^{n_{\max}} e^{-\beta E_n}\,, \tag{3.12}$$

where $n_{\max}$ corresponds to the value $E_{\max}$ of the numerically available maximal en-

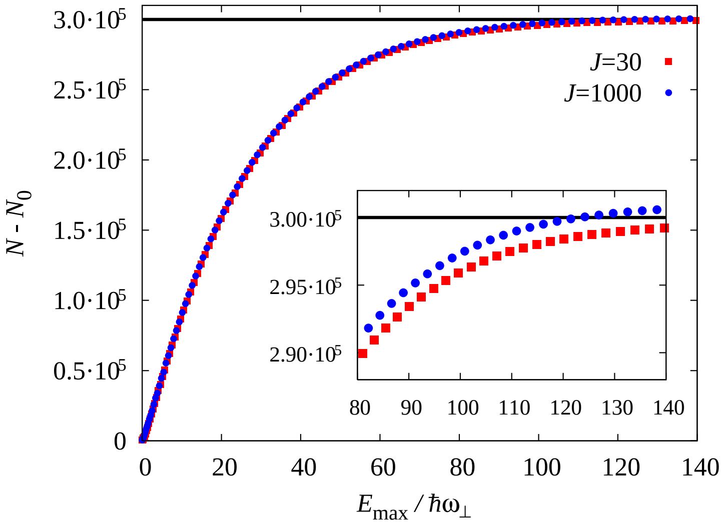

Figure 3.4: Number of thermally excited atoms $N - N_0$ calculated as a function of the maximal available two-dimensional energy eigenvalue $E_{\rm max}$ at $T = 63.30$ nK. The results are given for two different values of the cumulant cutoff J for a critically rotating condensate, with the same parameters as in Fig. 3.3. The horizontal line corresponds to the number of atoms $N = 3 \cdot 10^5$ in the experiment [12].

ergy eigenvalue. A semiclassical correction to this value, can be calculated according to Ref. [65] as

$$\Delta Z_1(\beta, E_{\rm max}) = \int \frac{d\vec{r}\, d\vec{p}}{(2\pi\hbar)^3}\, e^{-\beta \mathcal{H}(\vec{r},\vec{p})}\, \Theta(\mathcal{H}(\vec{r},\vec{p}) - E_{\rm max})\,, \tag{3.13}$$

where $\mathcal{H}(\vec{r},\vec{p})$ as before represents the classical Hamiltonian of the system, while Θ denotes the Heaviside step-function.

For the trap potential (3.4), in z-direction we have a pure harmonic potential, which can be treated exactly. Therefore, we focus only on the two-dimensional problem in the $x-y$ plane. In this case, the semiclassical correction for the single-particle partition function (3.13) can be expressed in terms of the complementary error function:

$$\begin{aligned} \Delta Z_1^{(2)}(\beta, E_{\rm max}) &= \frac{1}{2\beta} \left\{ \frac{e^{-\beta E_{\rm max}}}{\kappa} \left[-(1-\eta^2)\sqrt{(1-\eta^2)^2 + 4\kappa E_{\rm max}} \right] \right. \\ &\quad \left. + \sqrt{\frac{\pi}{\kappa\beta}}\, e^{\frac{\beta(1-\eta^2)^2}{4\kappa}} \times \mathrm{Erfc}\left(\sqrt{\beta E_{\rm max} + \frac{\beta(1-\eta^2)^2}{4\kappa}} \right) \right\}, \end{aligned} \tag{3.14}$$

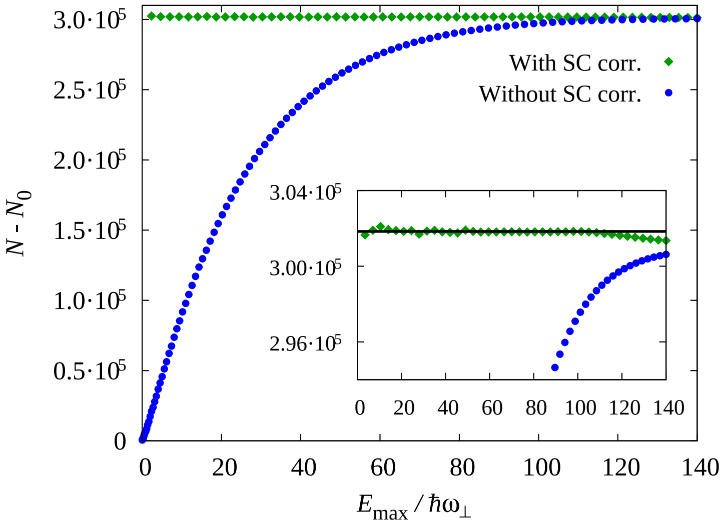

Figure 3.5: Number of thermally excited atoms $N - N_0$ calculated as a function of $E_{\max}$ with and without semiclassical corrections, calculated with a large cumulant cutoff $J = 10^4$ to eliminate the J-dependence. The results correspond to a critically rotating condensate with the same parameters as in Fig. 3.3. The horizontal line corresponds to $N = 301834$ which represents the exact value at $T_c = 63.30$ nK.

where the superscript denotes that only the $x - y$ part of the potential is considered.

When this semiclassical correction is taken into account, the numerical results show almost no dependence on $E_{\max}$, as can be seen from Fig. 3.5. Here we have used an excessively large value of the cumulant cutoff $J = 10^4$ in order to completely eliminate any J dependence. From the inset in this graph we also see that $E_{\max}$ must be chosen in accordance with the value estimated in the previous section for the maximal reliable energy eigenvalue obtained by numerical diagonalization. If we use a value $E_{\max}$ larger than this, we will be underestimating the higher part of the energy spectra, and obtain incorrect results. For a critically rotating condensate with the anharmonicity $\kappa = \kappa_{\mathrm{BEC}}$ the estimated value of $E_{\max}$ from Table 3.3 is around 90 $\hbar\omega$, which agrees with the results from the inset of Fig. 3.5. If we use this value for $E_{\max}$ and calculate properties of the condensate using numerically obtained eigenstates below $E_{\max}$ with semiclassical corrections according to Eq. (3.14), we will obtain the exact results with very high accuracy.

3.3 Global properties of rotating BECs

In this section we will apply the presented approach to calculate different global properties of rotating BECs. First, we will calculate condensation temperature, and then, we will present phase diagrams defined in terms of condensate-fraction dependence on the temperature for different trap parameters. Additionally, we will compare numerical results with semiclassical values and identify when the full numerical treatment becomes necessary.

3.3.1 Condensation temperature

If we take into account semiclassical corrections, as explained in the previous section, we can calculate, for instance, the condensation temperature of the condensate for different rotation frequencies. This implies that we have to find the temperature for which the number of thermal atoms saturates precisely at the total number of atoms N. In practice, this works the other way around: for a given condensation temperature T_{c} we numerically calculate the particle number in the system using Eq. (3.11), which gives the number of atoms in the system required for a condensation temperature to be equal to T_{c}. This procedure is implemented in Fig. 3.6 for several values of the rotation frequency Ω in units of $\eta = \Omega/\omega$. For example, for $T_{\mathrm{c}} = 63.14$ nK we see that the corresponding number of particles is $N = 3 \cdot 10^5$, which coincides with the value for a critically rotating condensate in the experiment of Dalibard and collaborators [12].

In principle, such a procedure is only applicable for low-accuracy calculations of the critical temperature, since otherwise one has to use very large values of the cutoff J which would practically slow-down numerical calculations. If one is interested in more precise results, a suitable J-dependence must be properly taken into account. In order to be able to efficiently extract the correct value of β_{c}, we will derive an analytical estimate of the asymptotic error $\Delta\beta_{\mathrm{c}} = \beta_{\mathrm{c}} - \beta_{\mathrm{c}}(J)$, which is introduced by the presence of the cutoff J. Note that always $\Delta\beta_{\mathrm{c}} > 0$, since $\beta_{\mathrm{c}}(J) < \beta_{\mathrm{c}}$ has to compensate the missing terms in the sum (3.11).

If we insert $\beta_{\mathrm{c}} = \beta_{\mathrm{c}}(J) + \Delta\beta_{\mathrm{c}}$ into Eq. (3.11), the error $\Delta\beta_{\mathrm{c}}$ can considered to be small for sufficiently large value of the cutoff J. By comparing Eq. (3.11) with

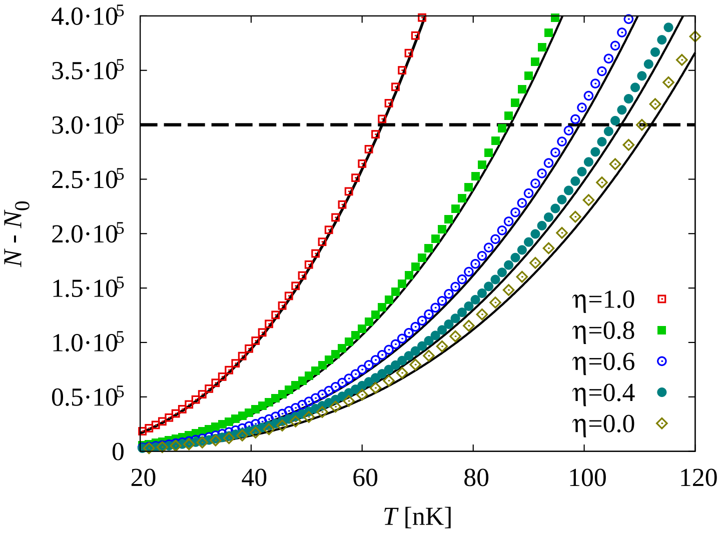

Figure 3.6: Number of thermally excited atoms $N - N_0$ as a function of the temperature T for different values of the rotation frequency and the quartic anharmonicity $\kappa = \kappa_{\text{BEC}}$. The discretization parameters are given in Table 3.3, and the results are calculated by taking into account semiclassical corrections. The dashed line corresponds to the number of atoms $N = 3 \cdot 10^5$ in the experiment [12]. For comparison, the full lines depict the semiclassical results from Ref. [65].

the exact expression (3.9) we obtain

$$\sum_{j=J+1}^{\infty} \sum_{n=1}^{\infty} e^{-j\beta_{\text{c}}(E_n - E_0)} \approx \Delta\beta_{\text{c}} \sum_{j=1}^{J} \sum_{n=1}^{\infty} j(E_n - E_0)\, e^{-j\beta_{\text{c}}(E_n - E_0)} \,. \tag{3.15}$$

The term $j(E_n - E_0)$ within the sum can be obtained by setting $N_0 = 0$ and applying the partial derivative $\partial/\partial\beta_{\text{c}}$ to Eq. (3.11):

$$-\Delta\beta_{\text{c}} \frac{\partial N}{\partial \beta_{\text{c}}} \approx \left[1 - \Delta\beta_{\text{c}} \frac{\partial}{\partial \beta_{\text{c}}}\right] \sum_{j=J+1}^{\infty} \sum_{n=1}^{\infty} e^{-j\beta_{\text{c}}(E_n - E_0)} \,. \tag{3.16}$$

Note that the derivative of the particle number N with respect to β_{c} is not equal to zero, since N is here effectively defined by the sum (3.9). Therefore, we have instead

$$\frac{\partial N}{\partial \beta_{\text{c}}} = -\sum_{j=1}^{\infty} \sum_{n=1}^{\infty} j\,(E_n - E_0)\, e^{-j\beta_{\text{c}}(E_n - E_0)} \,. \tag{3.17}$$

Clearly, the right-hand side is a negative quantity that does not depend on J. However, it does depend on β_c, as well as on the energy spectrum of the system.

If the system is close to a d-dimensional harmonic oscillator, which is the case for the potential (3.4) with the small anharmonicity relevant for the experiment, for large values of J we have approximately

$$\sum_{j=J+1}^{\infty} \sum_{n=1}^{\infty} e^{-j\beta_\mathrm{c}(E_n - E_0)} \approx d\, \frac{e^{-(J+1)\beta_\mathrm{c}\hbar\omega}}{1 - e^{-\beta_\mathrm{c}\hbar\omega}}\,, \tag{3.18}$$

where ω denotes an effective harmonic frequency and d is the dimensionality of the corresponding system. In our case, we apply the semi-classical correction only to the $x - y$ part of the potential and for this reason $d = 2$. For the case of a large anharmonicity, the effective frequency ω would depend on κ, representing the harmonic expansion of the potential around its minimum. With such an estimate, Eq. (3.16) reduces to

$$\Delta\beta_\mathrm{c} \approx -\frac{d}{1 - e^{-\beta_\mathrm{c}\hbar\omega}} \times \frac{e^{-(J+1)\beta_\mathrm{c}\hbar\omega}}{\partial N/\partial\beta_\mathrm{c} + (J+1)\, e^{-(J+1)\beta_\mathrm{c}\hbar\omega} \frac{d\hbar\omega}{1-e^{-\beta_\mathrm{c}\hbar\omega}}}\,. \tag{3.19}$$

The term $(J+1)\, e^{-(J+1)\beta_\mathrm{c}\hbar\omega}$ in the denominator of the second factor can be neglected for large enough values of the cutoff J, yielding as a simplified version of the above expression:

$$\Delta\beta_\mathrm{c} \approx -\frac{d\, e^{-(J+1)\beta_\mathrm{c}\hbar\omega}}{\partial N/\partial\beta_\mathrm{c}\, (1 - e^{-\beta_\mathrm{c}\hbar\omega})}\,. \tag{3.20}$$

In order to use the derived estimates for $\Delta\beta_\mathrm{c}$, apparently one would already have to know the sought-after value of β_c as well as the difficult derivative $\partial N/\partial\beta_\mathrm{c}$. However, in practical applications this obstacle can be circumvented as follows. The expressions (3.19) and (3.20) can be used for fitting the numerical data for $\beta_\mathrm{c}(J) = \beta_\mathrm{c} - \Delta\beta_\mathrm{c}$, as is illustrated in Fig. 3.7. In this standard approach, all unknown values are fit parameters, obtained numerically by the least-square method. Note that not only β_c is obtained by such a fitting procedure, but also other parameters, such as $\partial N/\partial\beta_\mathrm{c}$, or the effective harmonic frequency ω. The important point here is to capture the correct J-dependence, while all other parameters do not depend on it, so that they can be extracted by fitting. For example, in Fig. 3.7 we have used

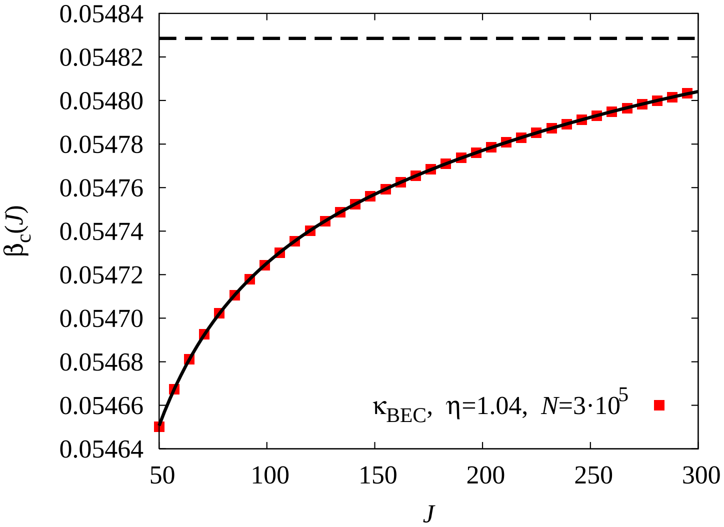

Figure 3.7: Dependence of β_c on the cumulant cutoff J for an over-critically ($\eta = 1.04$) rotating condensate of $N = 3{\cdot}10^5$ atoms of ^{87}Rb with the quartic anharmonicity of the trap $\kappa = \kappa_{\rm BEC}$. The discretization parameters are given in Table 3.3. The dashed line corresponds to a value of β_c obtained by fitting the numerical results to the function (3.21), while the full line gives the fitted function $f(J)$.

the fitting function

$$f(J) = \beta_c - \frac{c_1 e^{-c_2(J+1)}}{1 + c_3(J+1)\, e^{-c_4(J+1)}}\,, \tag{3.21}$$

which reproduces the numerical data quite accurately and gives high-precision results for the condensation temperature T_c. The virtue of the derived estimates lies in the fact that they can be used to extract the information on the condensation temperature even for moderate values of J, when a saturation is not yet achieved. This substantially speeds up the numerical calculation of condensation temperatures, especially when it has to be done for different values of potential parameters, such as the frequency ratio $\eta = \Omega/\omega$.

Fig. 3.8 summarizes the numerical results for the condensation temperature T_c for the anharmonicity $\kappa = \kappa_{\rm BEC}$ as well as the particle numbers $N = 3 \cdot 10^5$ and $N = 1 \cdot 10^4$. If we compare the obtained numerical results with the semiclassical approximation from Ref. [65], we see that the agreement turns out to be relatively good for the undercritical regime, but it becomes worse for an overcritical rotation of the condensate. After presenting results for the ground-state occupancy, which were

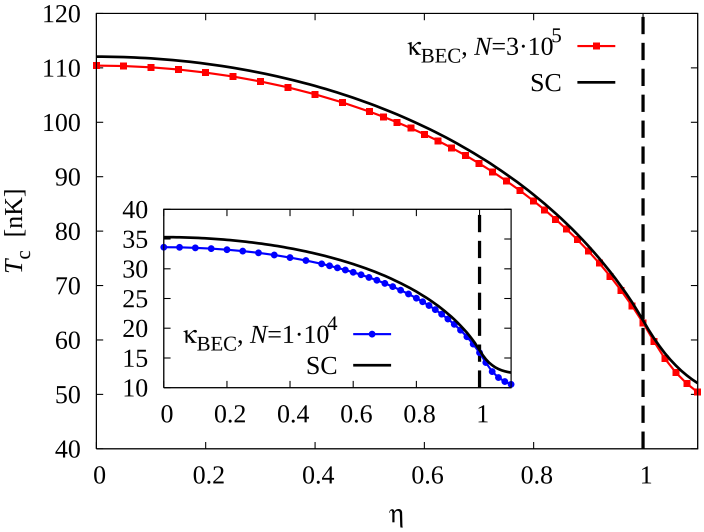

Figure 3.8: The condensation temperature as a function of the rotation frequency for the condensate of $N = 3 \cdot 10^5$ and $N = 1 \cdot 10^4$ atoms of ^{87}Rb, with the quartic anharmonicity of the trap $\kappa = \kappa_{\mathrm{BEC}}$. The discretization parameters are given in Table 3.3. The full lines correspond to the semiclassical approximation for T_{c} from Ref. [65].

obtained from this approach in the next section, we will compare our numerically exact results with the semiclassical approximation in more detail, and identify the parameter ranges where a full numerical treatment becomes necessary.

3.3.2 Ground-state occupancy

The ground-state occupancy is the next important global property of Bose-Einstein condensates we will look into. Below the condensation temperature a non-trivial fraction of atoms is in the ground state, thus yielding a macroscopic value of the occupancy ratio N_0/N.

Using the same approach as above, we can calculate the ground-state occupancy from Eq. (3.8). After determining the ground-state energy E_0 from an exact diagonalization of the evolution operator, we obtain the occupancy as

$$\frac{N_0}{N} = 1 - \frac{1}{N} \sum_{j=1}^{\infty} \left[e^{j\beta E_0} Z_1(j\beta) - 1 \right] . \tag{3.22}$$

In order to calculate N_0/N, we need the full single-particle energy spectrum. For

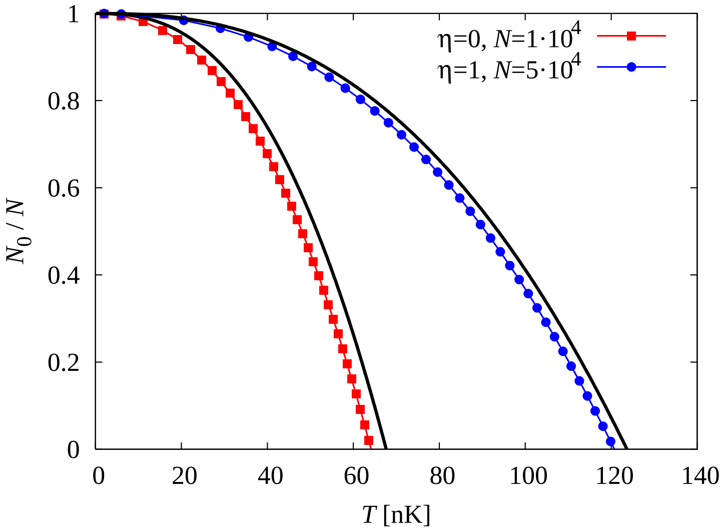

Figure 3.9: Ground-state occupancy N_0/N as a function of the temperature T for non-rotating and critically rotating condensate for different values of the total number of atoms. The quartic anharmonicity is $\kappa = 10^3\ \kappa_{\mathrm{BEC}}$, and the discretization parameters are given in Table 3.3. The full lines depict the semiclassical results from Ref. [65].

low temperatures, the large number of energy eigenstates obtained within the exact diagonalization is sufficient. In the sum of Eq. (3.22) we have again to introduce a cutoff J and to eliminate it by applying the methods described in previous sections. To this end one uses either a very large value for the cutoff or one derives the appropriate finite correction term, and fits the results to the derived function.

Fig. 3.9 presents numerical results for the ground-state occupancy of the condensate. The quartic anharmonicity of the trap is chosen to be $\kappa = 10^3\ \kappa_{\mathrm{BEC}}$, and the results are given for the non-rotating case with the total number of atoms $N = 1 \cdot 10^4$ and for critically rotating condensate with $N = 5 \cdot 10^4$ atoms. A comparison with the semiclassical results derived in Ref. [65] shows that the deviations increase with larger temperatures and smaller particle numbers.

3.3.3 Comparison with semiclassical approximation

In order to access the applicability and quality of the semiclassical approximation, we now make a quantitative comparison of the semiclassical results and full numerical results obtained in previous sections. Fig. 3.10 depicts the relative errors of the semiclassically calculated condensation temperature. As we can see, the agreement is

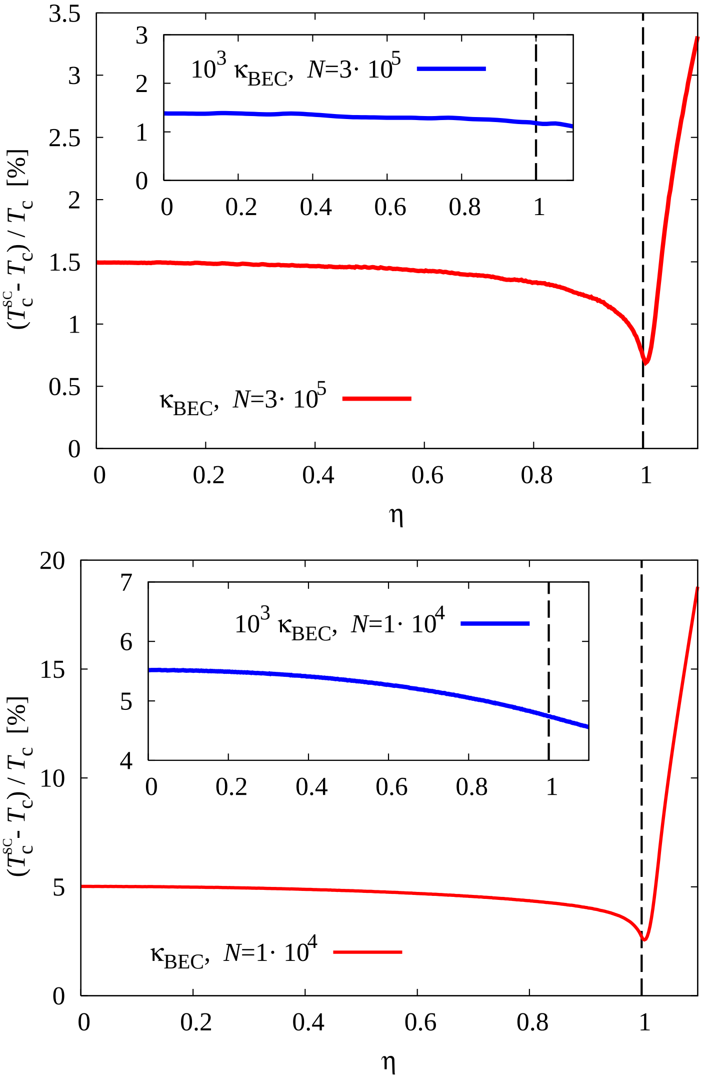

Figure 3.10: Relative error of semiclassical results for the condensation temperature [65] as a function of the rotation frequency Ω in units of $\eta = \Omega/\omega$ for $N = 3 \cdot 10^5$ (top) and $N = 1 \cdot 10^4$ (bottom). The quartic anharmonicity is $\kappa = \kappa_{\mathrm{BEC}}$, and the discretization parameters are given in Table 3.3. The insets in both plots give the corresponding results for the large anharmonicity $\kappa = 10^3\ \kappa_{\mathrm{BEC}}$.

relatively good for large particle numbers and small anharmonicity if the condensate rotates under-critically. The error in this case is of the order of 1 % to 1.5 %, and turns out to be minimal for a critical rotation. However, the error significantly increases for an overcritical rotation up to almost 3.5 % for $\eta = 1.1$. Therefore, while the semiclassical approximation is acceptable for undercritical rotation, in the overcritical regime a numerical treatment becomes necessary. This is even more pronounced if we decrease the particle number to 10^4, which is quite typical for many BEC experiments. In that case, semiclassical results already have an error of the order of 20 %. For large anharmonicity the rotation effect is not so important, as we can see from insets on both graphs in Fig. 3.10. However, for the particle number 10^4 a numerical treatment is indispensable, since the errors of the semiclassical results amount up to 5 %.

3.4 Local properties of rotating BECs

Local properties of ultra-cold quantum gases are ubiquitously used to observe and study the phenomenon of Bose-Einstein condensation. The prominent peak in TOF absorption pictures, which appears suddenly when the temperature is decreased below $T_{\rm c}$, is a clear signature for the occurrence of a BEC phase transition. It is experimentally used to measure the thermodynamic properties of the condensate. In this section we will show how the presented numerical approach can be applied to calculate both the density profiles and the TOF absorption imaging profiles.

3.4.1 Density profiles

For the ideal Bose gas, the density profiles of the condensate and of the gas phase are given by Eqs. (1.11) and (1.12), respectively. Having at our disposal numerically calculated energy eigenvalues and eigenfunctions, we can calculate the density profile of the condensate. In order to do so, we first have to obtain the ground-state occupancy number N_0 using the approach described in the previous section. Once this is done, Eq. (1.12) allows to calculate the density profile. In view of a comparison with absorption imaging, which always produces two-dimensional profiles, we have to integrate our numerically determined three-dimensional particle density $n(\vec{r})$ along the imaging axis. Fig. 3.11 presents typical results for the resulting density profiles of Bose-Einstein condensates for both the non-rotating and the critically-rotating case. Obviously, a rotation of the condensate leads to an effective spreading due to the appearance of a centrifugal potential.

Although this approach is sufficient for treating the low-temperature regime, where the condensate is present, we emphasize that the same method can also be used to deal with the thermal regime, when the temperature is increased above $T_{\rm c}$. For even higher temperatures, when the number of energy eigenstates, that need to

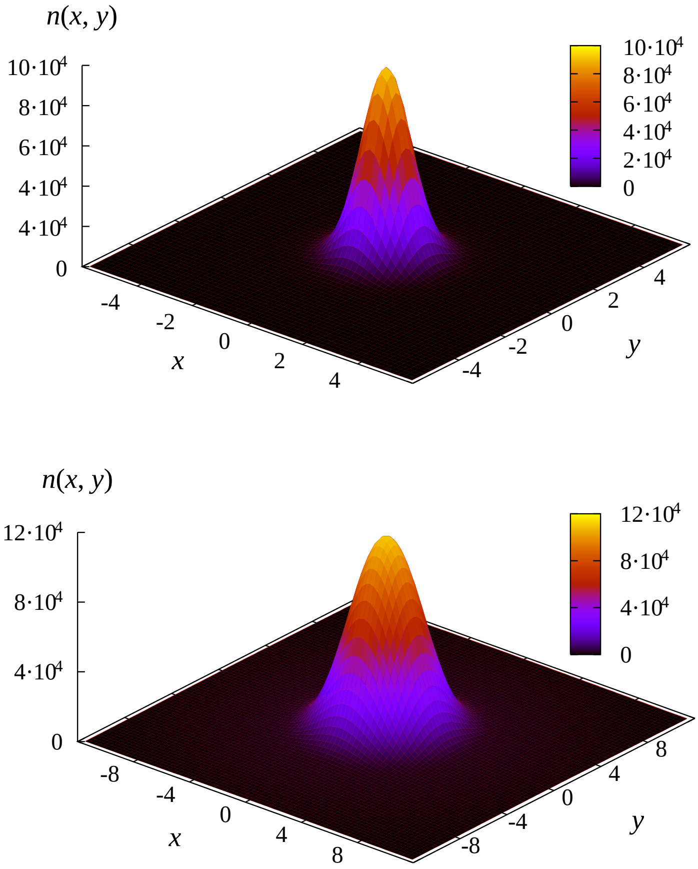

Figure 3.11: Density profile in xy-plane for a non-rotating (top) and a critically rotating (bottom) condensate of $N = 3 \cdot 10^5$ atoms of ^{87}Rb with the anharmonicity $\kappa = \kappa_{\mathrm{BEC}}$ at $T = 30$ nK. The dimensionless unit length on both graphs corresponds to 1.34 μm, i.e. the linear size of the profile is approximately 16.1 μm (top) and 32.2 μm (bottom). The discretization parameters are given in Table 3.3.

be taken into account, exceeds the number of numerically accessible eigenstates, the presented approach can be extended in a similar way as the partition function was calculated previously as a sum of diagonal transition amplitudes. Using the cumulant expansion of occupancies and the spectral decomposition of thermal transition amplitudes, the density profile can be written for high enough temperatures as

$$n(\vec{r}) = N_0 |\psi_0(\vec{r})|^2 + \sum_{j \geq 1} \left[e^{j\beta E_0} A(\vec{r}, \vec{r}; j\beta\hbar) - |\psi_0(\vec{r})|^2 \right] . \tag{3.23}$$

Here $A(\vec{r}, \vec{r}; j\beta\hbar)$ represents the imaginary-time amplitude for a single-particle transition from the position $\vec{r}$ to the position $\vec{r}$ for the imaginary time $t = j\beta\hbar$.

While both definitions (1.12) and (3.23) are mathematically equivalent when one is able to exactly calculate infinitely many energy eigenstates and required transition amplitudes for an arbitrary propagation time, the first definition is more suitable for low temperatures, when the number of relevant energy eigenstates is moderate, and the second one is suitable for high temperatures, when the imaginary propagation time $\hbar\beta$ is small, and the short-time expansion can be successfully applied.

3.4.2 Time-of-flight graphs for BECs

In typical BEC experiments, a trapping potential is switched off and the gas is allowed to expand freely during a short flight time t which is of the order of several tens of milliseconds. Afterwards an absorption picture is taken which maps the density profile to the plane perpendicular to the laser beam. For the ideal Bose condensate, the density profile after time t is given by

$$n(\vec{r}, t) = N_0 |\psi_0(\vec{r}, t)|^2 + \sum_{n\geq 1} \mathcal{B}_n(E_0, T) |\psi_n(\vec{r}, t)|^2 \,, \tag{3.24}$$

where the density profile has to be integrated along the imaging axis, and the eigenstates $\psi_n(\vec{r}, t)$ are propagated according to the free Hamiltonian, containing only the kinetic term, since the trapping potential is switched off. If the energy eigenstates are available exactly, either analytically or numerically, their propagation in time can be calculated by performing two consecutive Fourier transformations:

$$\psi_n(\vec{r}, t) = \int \frac{d\vec{k}\, d\vec{R}}{(2\pi)^3}\, e^{i[\vec{k}\cdot(\vec{r}-\vec{R}) - \omega_{\vec{k}} t]}\, \psi_n(\vec{R}) \,, \tag{3.25}$$

where the term $e^{-i\omega_{\vec{k}} t}$ accounts for a free-particle propagation in $\vec{k}$-space, $\omega_{\vec{k}} = \hbar^2 k^2/(2M)$. In practical applications, when the energy eigenstates are calculated by a numerical diagonalization of space-discretized transition amplitudes, the natural way to calculate the above free-particle time evolution is to use Fast Fourier Transform (FFT) numerical libraries.

For high temperatures we can use a mathematically equivalent definition of the density profile which is derived again from using the cumulant expansion of occupancy numbers and the spectral decomposition of transition amplitudes:

$$\begin{aligned} n(\vec{r},t) \;=\; & N_0|\psi_0(\vec{r},t)|^2 + \sum_{j\geq 1}\left[e^{j\beta E_0} \int \frac{d^3\vec{k}_1\, d^3\vec{k}_2\, d^3\vec{X}_1\, d^3\vec{X}_2}{(2\pi)^6} \right. \\ & \left. \times e^{i[(\vec{k}_1-\vec{k}_2)\cdot\vec{r}-\vec{k}_1\cdot\vec{X}_1+\vec{k}_2\cdot\vec{X}_2-(\omega_{\vec{k}_1}-\omega_{\vec{k}_2})t]} \times A(\vec{X}_1,\vec{X}_2;j\beta\hbar) - |\psi_0(\vec{r},t)|^2 \right] . \end{aligned} \tag{3.26}$$

In both approaches it is first necessary to calculate the ground-state energy E_0 and the eigenfunction $\psi_0(\vec{r})$, as well as the ground-state occupancy N_0. If we rely on Eqs. (3.24) and (3.25) to calculate TOF graphs, we have to calculate as many eigenstates as possible by numerical diagonalization. Conversely, if it is possible to use directly Eq. (3.26), we can apply the effective action short-time expansion of thermal transition amplitudes. In both cases FFT is ideally suited for calculating TOF graphs.

3.4.3 Overcritical rotation

The case of critical and overcritical rotation $\eta \geq 1$ is realized in the Paris experiment by introducing the anharmonic part of the potential (3.4), so that the condensate is confined even when the harmonic part of the trapping potential is completely compensated or overcompensated by the rotation. The experimental realization of this delicate balance was difficult to achieve, but nevertheless when the condensate was successfully confined while rotating over-critically, the measurements of its properties can be done using the standard techniques, including absorption imaging. Within the semiclassical approach one has to carefully consider this situation, since the chemical potential is defined by the minimum of the potential, Eq. (1.14), and now cannot be simply set to zero anymore [65]. In our numerical approach, however, the implementation of the methods described in previous sections is straightforward even for overcritical rotation. First one calculates energy eigenvalues and eigenstates using exact diagonalization, yielding negative values for the first several eigenstates. Table 3.2 shows the resulting energy spectrum of an overcritically rotating condensate ($\eta = 1.04$) for the experimental value of the anharmonicity κ_{BEC}, as well as for the case of large anharmonicity $10^3\ \kappa_{\mathrm{BEC}}$.

Condensation temperature and other global properties as well as local properties of overcritically rotating condensates can also be calculated as before. Fig. 3.12 gives

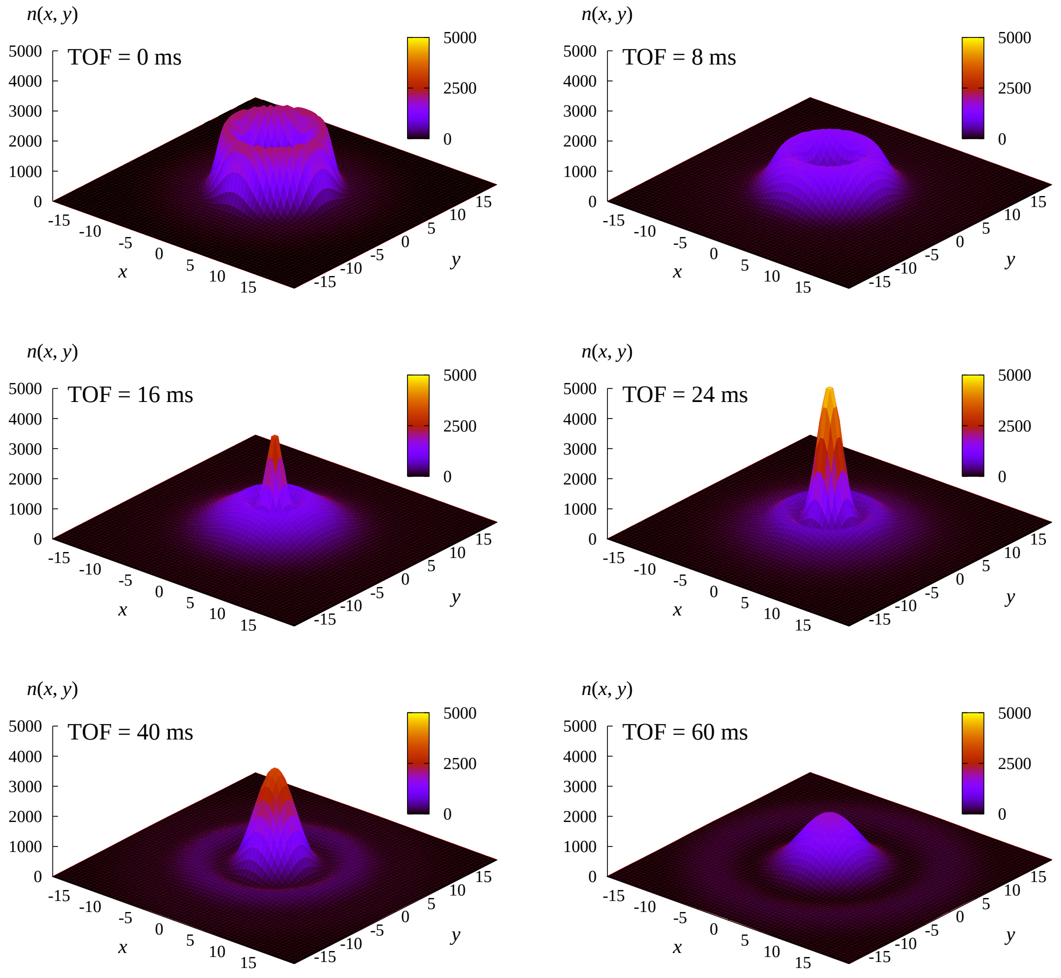
TOF = 0 ms
TOF = 8 ms
TOF = 16 ms
TOF = 24 ms
TOF = 40 ms
TOF = 60 ms

Figure 3.12: Time-of-flight absorption density profiles in xy-plane for an overcritically rotating ($\eta = 1.04$) condensate of $N = 3 \cdot 10^5$ atoms of ^{87}Rb with the anharmonicity $\kappa = \kappa_{\text{BEC}}$ at $T = 30$ nK. The flight time, is given at each plot. The dimensionless unit length on all graphs corresponds to 1.34 μm and the linear size of profiles is approximately 53.6 μm. The discretization parameters are given in Table 3.3.

the TOF absorption imaging sequence in the xy-plane for an overcritically ($\eta = 1.04$) rotating Bose-Einstein condensate with the anharmonicity $\kappa = \kappa_{\text{BEC}}$ and the particle number $N = 3 \cdot 10^5$ at $T = 30$ nK, exhibiting an interesting behavior. The initial density profile has a minimum at the origin, due to the shape of the anharmonic potential. The free expansion of the condensate leads to an increase in the particle density at the origin, and only afterwards the condensate density profile expands monotonically. Fig. 3.13 presents the time dependence of the particle density at

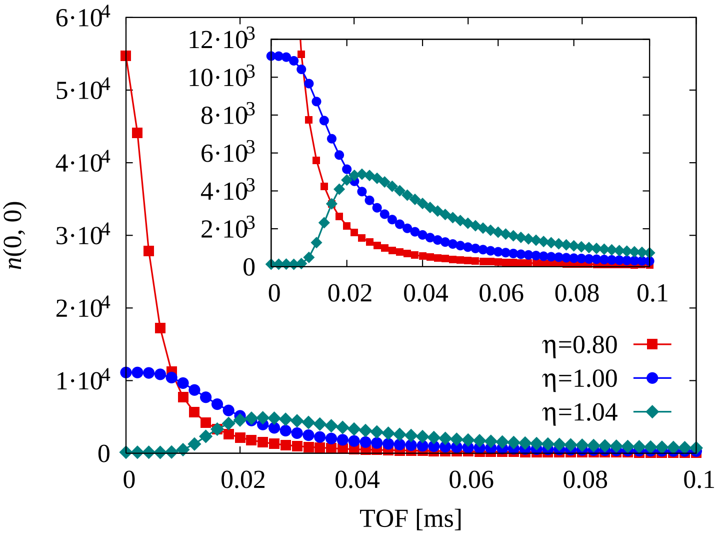

Figure 3.13: Condensate density at the origin of $x - y$ plane as a function of the time of flight (TOF) for the condensate of $N = 3 \cdot 10^5$ atoms of ^{87}Rb at $T = 30$ nK for several rotation frequencies Ω in units of $\eta = \Omega/\omega$. The quartic anharmonicity is $\kappa = \kappa_{\mathrm{BEC}}$ and the discretization parameters are given in Table 3.3.

the origin for varying rotation frequencies, parameterized by the ratio $\eta = \Omega/\omega$. We read off that approaching the critical rotation slows down the expansion of the condensate. For overcritical rotation this is even more pronounced, due to the appearance of the peak in the particle density for the expansion time $t > 0$. This leads to an expansion that is typically an order of magnitude slower for the rotation with $\eta > 1$.

3.5 Conclusions and outlook

In this Chapter the exact diagonalization of a time evolution operator is applied to the study of ideal Bose gases in the anharmonic trap. Earlier derived higher-order effective actions are used for an efficient numerical calculation of both global and local properties of fast-rotating Bose-Einstein condensates. To this end we have calculated large numbers of single-particle eigenvalues and eigenstates and using this information, we have obtained the condensation temperature and the ground-state occupancy of the condensate, as well as density profiles and TOF absorption graphs. We have have focused on a critical and an overcritical rotation and have found a substantial increase in the time scale for the expansion of the condensate after the trapping potential is switched off compared to the undercritical case. Further study should incorporate the effects of weak interactions on the Bose-Einstein condensation in the external potential (3.4), either in the mean-field framework or by the full numerical treatment. Finally, we note that approach presented here can also be used for numerical studies of properties of rotating ultra-cold Fermi gases [75].

Chapter 4 Mean-field description of an interacting BEC

In the previous Chapter we have considered BEC of an ideal Bose gas, and, despite neglecting the interactions, we had to apply sophisticated numerical methods for characterization of the BEC phase transition and properties of the condensate. Now we extend the description of a Bose gas to include interactions. For an exact microscopic description of an interacting Bose gas, we need to consider a full many-body Hamiltonian. For systems with a dominant two-body contact interaction, the Hamiltonian has the form (1.24):

$$\hat{H} = \int d\vec{r} \left(-\hat{\psi}^\dagger(\vec{r}) \frac{\hbar^2}{2M} \nabla^2 \hat{\psi}(\vec{r}) + V(\vec{r}) \hat{\psi}^\dagger(\vec{r}) \hat{\psi}(\vec{r}) + \frac{g}{2} \hat{\psi}^\dagger(\vec{r}) \hat{\psi}^\dagger(\vec{r}) \hat{\psi}(\vec{r}) \hat{\psi}(\vec{r}) \right) . \quad (4.1)$$

In the case of ultra-cold atomic gases, the bosons are alkali atoms, which are not elementary particles. However, due to very low temperatures, the atoms can be considered to be always in their ground states and their internal structure can be neglected. The exact treatment of the system described by the Hamiltonian (4.1) is possible only by numerical simulations based on Monte Carlo approach [76, 77]. Such simulations are ubiquitously time-consuming and significantly limit the scope of problems that can be addressed. For this reason, a number of approximative methods have been developed. Simplified approximative approaches are much easier for the numerical implementation and sometimes even provide analytical insights into the studied problem. Furthermore, very often, information on the parameters of the system, such as the temperature or condensate fraction, are extracted from experimental data indirectly, by fitting to expressions derived within one of simplified schemes.

In this Chapter we review the mean-field Hartree-Fock (HF) approximation for a many-body Hamiltonian (4.1). The HF approximation is the most-widely used approach to study finite-temperature properties of weakly interacting BECs [78, 5]. We will show within this mean-field scheme how the presence of the interaction influences properties of the condensate, both in the zero-temperature limit, and in the vicinity of the BEC phase transition. We focus on harmonically trapped bosons for two reasons: the trapping is always present in the experiments, and also the calculation of the condensation temperature of the homogenous system turned out to be a notorious problem, debated in many ways for several decades [79]. We scrutiny and compare several widely used implementations of the HF approximation with the emphasis on their advantages and drawbacks. The interest in the topic increases as new experiments have reported the observation of beyond mean-field effects [80, 81], which should be incorporated into the existing models.

The partition function of the system in the grand canonical ensemble is given by

$$\mathcal{Z}(\beta) = \mathrm{Tr}\, e^{-\beta(\hat{H}-\mu\hat{N})}, \tag{4.2}$$

and can be rewritten as a bosonic functional integral in the imaginary time [32]:

$$\mathcal{Z}(\beta) = \oint \mathcal{D}\Psi \oint \mathcal{D}\Psi^* e^{-\mathcal{A}_{\mathrm{E}}[\Psi(\vec{r},\tau),\Psi^*(\vec{r},\tau)]/\hbar}, \tag{4.3}$$

where $\Psi(\vec{r},\tau)$ and $\Psi^*(\vec{r},\tau)$ are periodic functions, with the period $\hbar\beta$:

$$\Psi(\vec{r},\tau) = \Psi(\vec{r},\tau+\hbar\beta)\,,\, \Psi^*(\vec{r},\tau) = \Psi^*(\vec{r},\tau+\hbar\beta)\,. \tag{4.4}$$

For the Hamiltonian (4.1) the Euclidean action $\mathcal{A}_{\mathrm{E}}$ is given by

$$\begin{aligned} \mathcal{A}_{\mathrm{E}}[\Psi(\vec{r},\tau),\Psi^*(\vec{r},\tau)] \;=\; & \int_0^{\hbar\beta} d\tau \int d\vec{r}\, \Psi^*(\vec{r},\tau) \left(\hbar\frac{\partial}{\partial\tau} - \frac{\hbar^2}{2M}\triangle + V(\vec{r}) - \mu\right)\Psi(\vec{r},\tau) \\ & + \frac{g}{2}\int_0^{\hbar\beta} d\tau \int d\vec{r}\, \Psi^*(\vec{r},\tau)\Psi(\vec{r},\tau)\Psi^*(\vec{r},\tau)\Psi(\vec{r},\tau)\,. \end{aligned} \tag{4.5}$$

A presence of the interacting Ψ^4 term in the action makes the calculation of the partition function analytically intractable, and to proceed further we apply the standard mean-field approach. In order to study Bose-Einstein condensation, according to the Bogoliubov prescription (1.27), we first decompose the field Ψ into the order parameter $\psi(\vec{r},\tau)$, which corresponds to the macroscopic condensate wave-function, and fluctuations $\delta\psi(\vec{r},\tau)$:

$$\Psi(\vec{r},\tau) = \psi(\vec{r},\tau) + \delta\psi(\vec{r},\tau)\,. \tag{4.6}$$

In the functional formalism this represents a change of variables, and the action now contains terms up to the 4th order in $\delta\psi$ that we should integrate over. Without further approximations, however, this problem is equivalent to the original functional integral. Numerous approximation techniques were developed to treat terms of the 3rd and 4th order in different approximative ways [19, 82]. In the Hartree-Fock-Bogoliubov approach, we approximate the 4th order term as

$$\begin{aligned}\delta\psi^*\delta\psi\,\delta\psi^*\delta\psi \;\approx\; & 4\langle\delta\psi^*\delta\psi\rangle\delta\psi^*\delta\psi+\langle\delta\psi^*\delta\psi^*\rangle\delta\psi\delta\psi+\langle\delta\psi\delta\psi\rangle\delta\psi^*\delta\psi^* \\ & -2\langle\delta\psi^*\delta\psi\rangle\langle\delta\psi^*\delta\psi\rangle-\langle\delta\psi\delta\psi\rangle\langle\delta\psi^*\delta\psi^*\rangle . \end{aligned} \tag{4.7}$$

In accordance with the previous decomposition, we introduce auxiliary functions

$$\begin{aligned} h(\vec r,\tau;\vec r,\tau) &= \langle\delta\psi^*(\vec r,\tau)\delta\psi(\vec r,\tau)\rangle\,, \\ f(\vec r,\tau;\vec r\,',\tau') &= \langle\delta\psi^*(\vec r,\tau)\delta\psi(\vec r\,',\tau')\rangle\,, \\ b(\vec r,\tau;\vec r\,',\tau') &= \langle\delta\psi(\vec r,\tau)\delta\psi(\vec r\,',\tau')\rangle\,, \end{aligned}$$

which are denoted as Hartree, Fock and Bogoliubov term, respectively. At the moment, the introduced average values are purely formal, but can be later defined so as to make the complete procedure self-consistent. In the case of the contact interaction (1.21), the Hartree and Fock terms yield equal contributions, hence a factor of 4 in front of the corresponding term in Eq. (4.7).

After applying the mean-field approximation (4.7), the action $\mathcal{A}_{\mathrm{E}}$ becomes quadratic in $\delta\psi$, and now the functional integrations of the Gaussian integrals can be explicitly performed. The final result for the partition function can be written in the form

$$\mathcal{Z}(\beta)=e^{-\beta\,\Gamma_{\mathrm{eff}}[\psi,\psi^*,h,f,b]}\,, \tag{4.8}$$

where Γ_{eff} is the effective action, defined as a functional of five arguments: $\psi(\vec r,\tau)$, $\psi^*(\vec r,\tau)$, $h(\vec r,\tau;\vec r,\tau)$, $f(\vec r,\tau;\vec r\,',\tau')$ and $b(\vec r,\tau;\vec r\,',\tau')$. They are determined by extremizing the effective action $\Gamma_{\mathrm{eff}}[\psi,\psi^*,h,f,b]$ with respect to each of them:

$$\frac{\delta\Gamma_{\mathrm{eff}}}{\delta\psi}=0,\ \frac{\delta\Gamma_{\mathrm{eff}}}{\delta\psi^*}=0,\ \frac{\delta\Gamma_{\mathrm{eff}}}{\delta h}=0,\ \frac{\delta\Gamma_{\mathrm{eff}}}{\delta f}=0,\ \frac{\delta\Gamma_{\mathrm{eff}}}{\delta b}=0.$$

In the quest for the simplest mean-field description of an inhomogeneous BEC, we will make another simplification by neglecting Bogoliubov terms, i.e. anomalous correlations $b(\vec r,\tau;\vec r\,',\tau')$, as discussed in Ref. [83]. This assumption is justified in the limit $T \to 0$, however it is very often used for all temperatures. The topic is explored in detail in Ref. [84] where the consequences of the approximation are thoroughly discussed. Additionally, we neglect the possible depletion of the condensate at the zero temperature, i.e. the depletion that arises due to interactions, which is a reasonable approximation in the case of a weakly interacting gas.

Finally, after implementing all the described steps, we arrive at the finite-temperature HF description of a bosonic gas, which is given by the following system of equations:

$$\left[\hbar\frac{\partial}{\partial\tau} - \frac{\hbar^2}{2M}\triangle + V(\vec{r}) + g|\psi(\vec{r},\tau)|^2 + 2\,gh(\vec{r},\tau;\vec{r},\tau)\right]\psi(\vec{r},\tau) = \mu\psi(\vec{r},\tau)\,, \quad (4.9)$$

$$h(\vec{r},\tau;\vec{r},\tau) = \sum_{\vec{k}} \psi_{\vec{k}}(\vec{r})\psi^*_{\vec{k}}(\vec{r})\frac{1}{e^{\hbar\beta(E_{\vec{k}}-\mu)} - 1}\,, \quad (4.10)$$

$$\left[-\frac{\hbar^2}{2M}\triangle + V(\vec{r}) + 2\,g|\psi(\vec{r},\tau)|^2 + 2\,gh(\vec{r},\tau;\vec{r},\tau)\right]\psi_{\vec{k}}(\vec{r}) = E_{\vec{k}}\psi_{\vec{k}}(\vec{r})\,, \quad (4.11)$$

where $\psi_{\vec{k}}(\vec{r})$ are effective single-particle wave-functions, and $E_{\vec{k}}$ are the corresponding eigenvalues. More details on the derivation can be found in Ref. [78]. Although formally the HF equations depend on the imaginary time τ, physically is only relevant the equilibrium case, when the macroscopic wave-function of the condensate $\psi(\vec{r},\tau)$ does not depend on τ anymore ($\partial\psi(\vec{r},\tau)/\partial\tau = 0$), but only on the position $\vec{r}$. The above set of equations has to be solved self-consistently, taking into account that the total number of particles is fixed to N, and leads to the solution that consists of the effective single-particle eigenfunctions $\psi_{\vec{k}}$ and eigenvalues $E_{\vec{k}}$, the Hartree function h, and the condensate wave-function ψ. From Eq. (4.10) we immediately see the physical interpretation of the Hartree function h, which represents the density of the thermal cloud, $n_{\mathrm{th}}(\vec{r})$. Effectively, within the mean-field description, the gas of bosons is split into the condensate and thermal component. We note the close analogy with the noninteracting gas description presented in Chapter 1, with the important exception that the two components now mutually interact. By varying the total number of particles N and the temperature T, a complete $N-T$ phase diagram can be explored. Before considering a BEC phase transition in the mean-field approximation, we first present the zero-temperature limit of the HF approximation.

4.1 Gross-Pitaevskii equation

In the zero-temperature limit, we can neglect the thermal cloud, and set

$$\lim_{\beta\to\infty} n_{\mathrm{th}}(\vec{r}) = 0\,, \tag{4.12}$$

which stems directly from Eq. (4.10). In this case, Eq. (4.11) becomes irelevant, while from Eq. (4.9) we find the time-independent Gross-Pitaevskii (GP) equation [13, 14, 34] for the order parameter:

$$\left[-\frac{\hbar^2}{2M}\triangle + V(\vec{r}) + g|\psi(\vec{r})|^2\right]\psi(\vec{r}) = \mu\psi(\vec{r})\,. \tag{4.13}$$

Effectively, in the mean-field approximation at zero temperature, we assume that all atoms occupy the same state $\psi(\vec{r})$, which we denote as the condensate wavefunction. Note that already by neglecting anomalous averages we have disregarded a depletion of the condensate at zero temperature that arises due to interactions. However, it turns out that this is a reasonable approximation in the wide range of experimental parameters for a weakly interacting gas. On the left-hand side of the GP equation (4.13) we have a kinetic energy term, an external trap potential $V(\vec{r})$, and a nonlinear term originating from the mean-field interaction between the atoms. The GP equation belongs to the class of nonlinear Schrödinger equations, which are extensively studied also in the field of nonlinear optics [85, 86].

Now, let us analyze solutions of the GP equation. To begin with, we note that the noninteracting limit is straightforwardly reproduced: for $g \to 0$, the condensate wavefunction is the ground state of the external potential $V(\vec{r})$, and the value of the chemical potential is equal to the ground-state energy. In the limit of strong repulsive interactions (for a large number of atoms, for example), the term corresponding to the kinetic energy can be safely neglected. In that case we find an algebraic stationary solution

$$|\psi(\vec{r})|^2 = \frac{1}{g}(\mu - V(\vec{r}))\,\theta(\mu - V(\vec{r})), \tag{4.14}$$

which is the well-known Thomas-Fermi (TF) solution [19]. The value of the chemical potential μ is determined as usual, by fixing the total number of atoms in the system to N. In particular, for the harmonic trap, the solution for the noninteracting case is a Gaussian, while the TF solution yields a parabolic profile. It is easy to understand

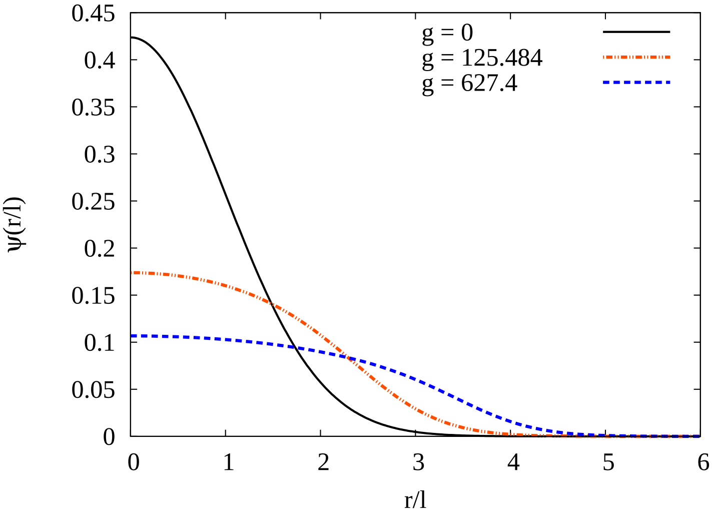

Figure 4.1: Wave functions of the condensate for different interaction strengths. We assume a spherically symmetric harmonic trap $V(\vec{r}) = M\omega^2 r^2/2$. Radial coordinate is expressed in units of $l = \sqrt{\hbar/M\omega}$, while the interaction strength is given in the dimensionless units $g \equiv 4\pi a N/l$.

that the repulsive interaction leads to the broadening of the density profile compared to the noninteracting Gaussian. This is illustrated in Fig. 4.1, where we show wave functions of the condensate obtained by numerically solving the GP equation for different interaction strengths. To find the condensate ground state, we perform the imaginary-time propagation of the GP equation [87]. More details on the numerical algorithms are given in Appendix A. Due to its simplicity, TF approximation is widely used for the interpretation of experimental data obtained for systems with a large number of atoms.

In a similar manner, starting from the real-time formalism and neglecting the condensate depletion, in the mean-field framework we obtain the time-dependent GP equation:

$$i\hbar\frac{\partial\psi(\vec{r},t)}{\partial t} = \left[-\frac{\hbar^2}{2M}\Delta + V(\vec{r}) + g|\psi(\vec{r},t))|^2\right]\psi(\vec{r},t), \tag{4.15}$$

which describes the condensate dynamics at $T = 0$. This equation also allows the study of the condensate excitation spectra, which is essential information for probing system's properties.

The time-dependent GP equation can be also derived variationally, from the action principle [19] based on the Lagrangian

$$L_{\text{GP}} = \int d\vec{r}\, \mathcal{L}_{\text{GP}}(\vec{r})\,, \tag{4.16}$$

where the Lagrangian density is given by

$$\mathcal{L}_{\text{GP}}(\vec{r}) = \frac{i\hbar}{2}\left(\psi\frac{\partial\psi^*}{\partial t} - \psi^*\frac{\partial\psi}{\partial t}\right) + \frac{\hbar^2}{2M}|\nabla\psi|^2 + V(\vec{r})|\psi|^2 + \frac{g}{2}|\psi|^4\,. \tag{4.17}$$

By performing the extremization of the action with respect to $\psi(\vec{r},t)$,

$$\frac{\delta\int_{t_1}^{t_2} dt L_{\text{GP}}}{\delta\psi^*(\vec{r},t)} = 0, \tag{4.18}$$

we again arrive at the GP Eq. (4.15). This is an important observation, since it represents the basis of the time-dependent variational analysis. We exploit this approach later in Chapter 5.

4.2 Finite-temperature properties of a BEC

After briefly exploring the properties of a weakly interacting BEC in the zero-temperature limit, we now continue the study of its finite-temperature properties in the HF approximation, Eqs. (4.9)-(4.11). To facilitate an almost analytical approach, we abolish Eq. (4.11) and treat excited states within a semiclassical approximation, while keeping the generalized GP equation (4.9) for the condensate phase. To apply the semiclassical approximation, similarly to derivation of Eq. (1.13), we use the classical Hamiltonian $\mathcal{H}(\vec{r},\vec{p}) = \vec{p}^{\,2}/2M + 2g(n_0(\vec{r}) + n_{\text{th}}(\vec{r}))$, in accordance with Eq. (4.11), and replace a summation over the discrete eigenstates in Eq. (4.10) by an integration over momentum $\vec{p}$. We assume a spherically symmetric trap, i.e. $V(\vec{r}) = V(r)$, and search for the equilibrium configuration $(\partial\psi(\vec{r},\tau)/\partial\tau = 0)$, when $\psi(\vec{r},\tau) \equiv \psi(r)$. Eqs. (4.10) and (4.11) are now reduced to a single equation, and, together with the equation for a total number of particles, we have the following system of equations:

$$\left[-\frac{\hbar^2}{2M}\triangle + V(r) + g\,n_0(r) + 2\,g\,n_{\rm th}(r)\right]\psi(r) = \mu\,\psi(r)\,, \tag{4.19}$$

$$n_{\rm th}(r) \;=\; \frac{1}{\lambda_T^3}\zeta_{3/2}\left(e^{\beta(\mu-2g(n_{\rm th}(r)+n_0(r))-V(r))}\right)\,, \tag{4.20}$$

$$N \;=\; N_0 + N_{\rm th} = \int d\vec{r}\,n_0(r) + \int d\vec{r}\,n_{\rm th}(r)\,. \tag{4.21}$$

Here, as before, the condensate density is given by $n_0(r) = |\psi(r)|^2$. We denote the above system of equations as GPSC model.

Before considering the full GPSC model of a BEC, we will first consider a series of simpler models: the almost-ideal model (widely used in the analysis of the experimental data), the semi-ideal model [88, 89], and the Thomas-Fermi-semiclassical model (TFSC), in which Eq. (4.19) is solved in the TF approximation. These models gradually add more details to the description of a BEC and become more complex, while at the same time they allow us to study properties of a BEC in a systematic way and to build new knowledge based on the previously obtained one.

In the rest of this Chapter, we assume an isotropic harmonic trap $V(r) = M\omega^2 r^2/2$, with a typical length scale $l = \sqrt{\hbar/M\omega}$. For ^{87}Rb we use the value of the scattering length of $a = 5.4\,\mathrm{nm}$ in all presented numerical results.

4.2.1 Almost-ideal model

The crudest finite-temperature approximation of an interacting BEC takes into account only the effect of interactions on the condensate cloud, while it considers thermal atoms as an ideal gas. This is justified by the fact that, due to a spatial compression of the condensate in the external trap, the density of this component is high and effects of interaction play a prominent role. On the other hand, thermal cloud is more spread, with a lower density, which allows us to consider it as an ideal gas. To simplify the model further, we describe the condensate within the TF approximation. Thus, using Eqs. (4.14) and (1.13), we obtain:

$$n_0(r) \;=\; \frac{1}{g}\left(\mu - V(r)\right)\theta(\mu - V(r))\,, \tag{4.22}$$

$$n_{\rm th}(r) \;=\; \frac{1}{\lambda_T^3}\zeta_{3/2}\left(e^{\beta(\mu-V(r))}\right)\,. \tag{4.23}$$

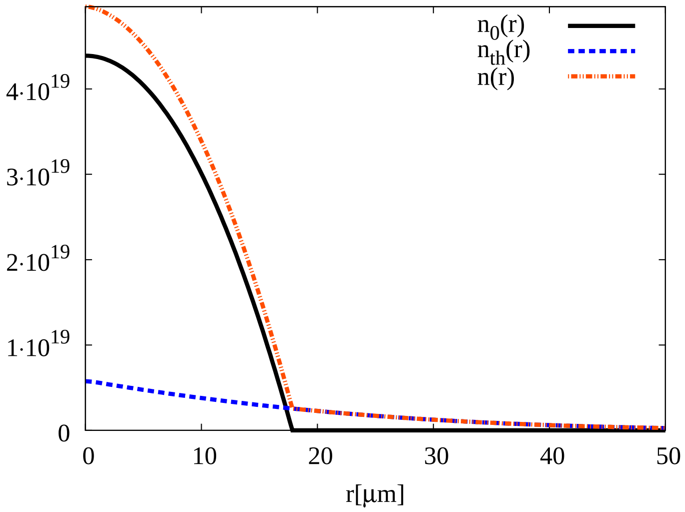

Figure 4.2: Density profiles of different components (m^{-3}) versus the radial coordinate r within the almost-ideal model for the parameters $N = 10^6$, $T = 60\,\mathrm{nK}$, $\omega = 100\,\mathrm{Hz}$.

Obviously, in order to have a well-behaved value of $n_{\mathrm{th}}(0)$, we have to use the approximation $\mu = 0$ for the thermal gas in the condensate phase. A typical density profiles are shown in Fig. 4.2. Within this framework, the two components do not interact mutually and their density profiles are monotonously decreasing functions of the radial coordinate. Although the model is oversimplified and the thermodynamic properties of a BEC it provides correspond to the noninteracting gas, it has been widely used since the first observation of a BEC until the present state-of-the-art experiments.

4.2.2 Semi-ideal model

A basic premise of this model is to treat thermal atoms as an ideal gas within the effective potential, which is a combination of the external trap potential and the mean-field repulsive interaction of the condensate: $V_{\mathrm{eff}}(r) = V(r) + 2gn_0(r)$ [88, 89]. Additionally, we neglect the influence of the thermal component on the condensate, and describe the BEC ground-state within the TF approximation. With this set of simplifications, from Eqs. (1.13) and (4.14), we obtain the following system of equations:

$$n_0(r) = \frac{1}{g}(\mu - V(r))\,\theta(\mu - V(r)), \tag{4.24}$$

$$n_{\rm th}(r) = \frac{1}{\lambda_T^3}\zeta_{3/2}\left(e^{-\beta|\mu - V(r)|}\right). \tag{4.25}$$

In the condensed phase, the value of the chemical potential is given by $\mu = \frac{\hbar\omega}{2}(\frac{15N_0 a}{l})^{\frac{2}{5}}$, which is obtained by fixing the number of atoms in BEC to N_0. Typical density profiles obtained by solving Eqs. (4.24) and (4.25) are shown in Fig. 4.3. We observe a spatial separation of the condensate and the thermal cloud - condensate resides in the trap center, while thermal atoms are more spread. Additionally, due to a repulsive effect of the condensate to the thermal component, the density profile of the thermal cloud is not a monotonous function of the radial coordinate r, unlike in the case of the almost-ideal model. This is far more realistic from the experimental point of view.

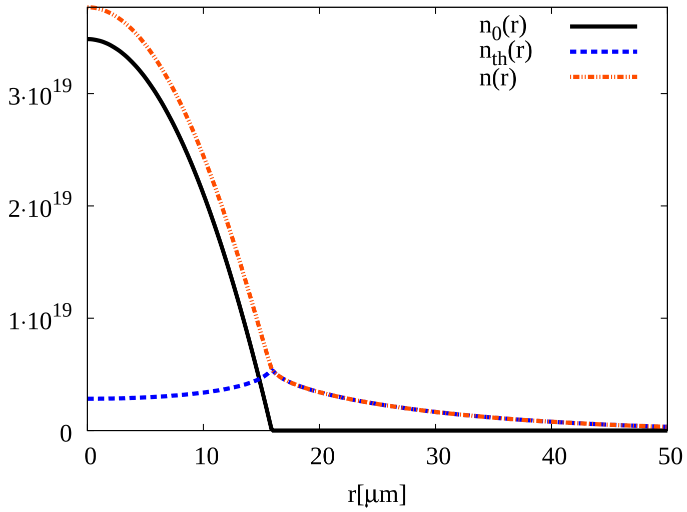

Figure 4.3: Density profiles of different components (m^{-3}) versus the radial coordinate r within the semi-ideal model for the parameters $N = 10^6$, $T = 60\,\mathrm{nK}$, $\omega = 100\,\mathrm{Hz}$.

The semi-ideal model defined by Eqs. (4.24) and (4.25) is simple enough to even allow an analytic calculation of thermodynamic properties of a BEC. It was shown that it yields a lower condensate fraction with respect to the noninteracting case (1.10) for the same temperature [88, 89]. However, it turns out that the condensation temperature within the semi-ideal approach is the same as for the ideal gas model.

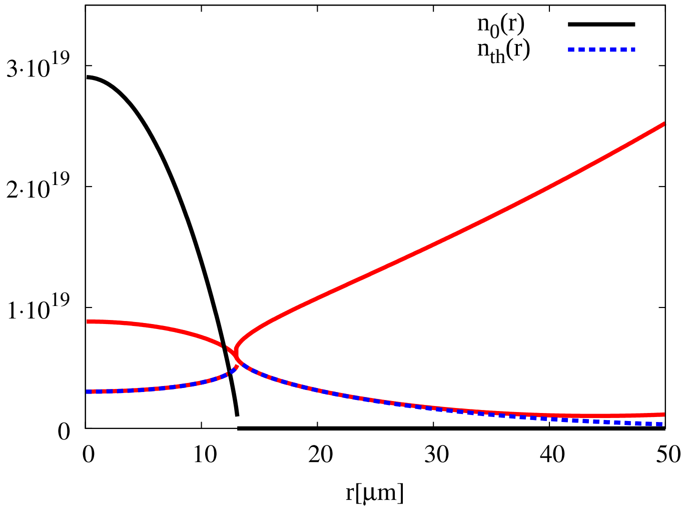

Figure 4.4: Density profiles of different components (m^{-3}) versus the radial coordinate r within the TFSC model for the parameters $N = 874403$, $T = 60\,\mathrm{nK}$, $\omega = 100\,\mathrm{Hz}$. Red solid curves are analytic solutions obtained using the Robinson formula.

This is too crude approximation from the experimental point of view and, in order to understand how the properties of a BEC phase transition are modified in the presence of interactions, we need to develop a better approximation.

4.2.3 TFSC model

In this model, we describe the ground state using the TF approximation, while excited states are treated within the semiclassical approximation (4.20), without further simplifications. Hence, we arrive at the following system of equations:

$$n_0(r) = \frac{1}{g}\left(\mu - V(r) - 2g n_{\mathrm{th}}(r)\right), \tag{4.26}$$

$$n_{\mathrm{th}}(r) = \frac{1}{\lambda_T^3}\zeta_{3/2}\left(e^{-\beta|\mu - V(r) - 2g n_{\mathrm{th}}(r)|}\right), \tag{4.27}$$

which we call the Thomas-Fermi-semiclassical model (TFSC). A typical numerical solution of Eqs. (4.26) and (4.27) is given in Fig. 4.4. The obtained density profiles are similar to those of the semi-ideal model. However, in this model certain unphysical discontinuities appear close to the condensate boundary, where we observe jumps both in the density of the thermal cloud and of the condensate component.

In order to verify the obtained numerical results, we will use an analytic approximation of the TFSC model. To this end, we rewrite the semiclassical expression (4.27) using the Robinson formula [63]:

$$\zeta_\nu(e^z) = \Gamma(1-\nu)(-z)^{\nu-1} + \sum_{k=0}^{\infty} \frac{z^k}{k!}\zeta_{\nu-k}, \tag{4.28}$$

where, as before, $\Gamma(z)$ is the Gamma function, and ζ_ν is the Riemann zeta function. Close to the condensate boundary, the value of $\mu - V(r) - 2gn_{\text{th}}(r)$ is small and we can rely on the approximation

$$\zeta_{3/2}(e^z) \approx \Gamma(-1/2)(-z)^{1/2} + \zeta_{3/2} + z\zeta_{1/2}\,, \tag{4.29}$$

to obtain an implicit equation for $n_{\text{th}}(r)$:

$$\begin{aligned} n_{\text{th}}(r) \quad \approx \quad & \frac{1}{\lambda_T^3}\Big[\Gamma(-1/2)\,\beta^{1/2}\,|\mu - V(r) - 2gn_{\text{th}}(r)|^{1/2} \\ & +\zeta_{3/2} - \zeta_{1/2}\,\beta\,|\mu - V(r) - 2gn_{\text{th}}(r)|\Big]\,. \end{aligned} \tag{4.30}$$

When solving Eq. (4.30), we encounter four different possible branches for $n_{\text{th}}(r)$, due to the two quadratic equations. However, only two branches are physically meaningful and can be identified easily. Results for the density of the thermal component obtained in this way are also shown in Fig. 4.4 by red solid lines. We see good agreement of the approximation (4.30) with numerically calculated values based on the full TFSC model. Furthermore, this analytical approach confirms the presence of discontinuities in the density profiles close to the condensate boundary. Therefore, the discontinuities are not an artifact of numerical simulations, but the problem of the model itself. This issue was noticed already in the early Ref. [33], and it is a consequence of the TF approximation. However, the model is able to predict an approximate phase diagram of a BEC, which is in a very good agreement with experimental data, as we discuss later in this Chapter.

4.2.4 GPSC model

Finally, we consider the full set of Eqs. (4.19)-(4.21), i.e. the GPSC model. We solve the equations for a fixed number of particles N using an iterative method. One way to start the iterations is to assume that all atoms are in the condensate and to solve Eq. (4.19) without the thermal cloud. In the next step, the previous solution

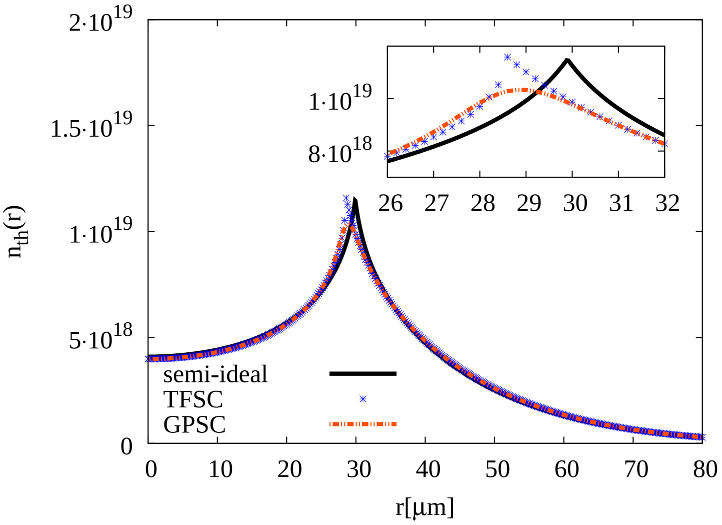

Figure 4.5: The density profile of thermal atoms $n_{\text{th}}(\text{m}^{-3})$ versus the radial coordinate r, calculated using the three different approximations for the values of parameters $N = 10^7$, $T = 100\,\text{nK}$, $\omega = 100\,\text{Hz}$. We see a good agreement between the TFSC and GPSC calculations, due to a large numbers of atoms in the trap.

for the condensate cloud is inserted into the algebraic Eq. (4.20), which is then solved for $n_{\text{th}}(r)$. After integration of $n_{\text{th}}(r)$ over r, a new value of the number of atoms in the condensate N_0 is calculated as $N - N_{\text{th}}$, and the procedure is repeated by solving Eq. (4.19), but with the new values of N_0 and $n_{\text{th}}(r)$, calculated in the previous step. This procedure is repeated until the desired convergence of the results is achieved. Of course, many modifications of the described procedure are possible, and practically one would like to identify the iteration procedure which leads to the fastest convergence toward the final result. The obtained density profiles are shown in Fig. 4.5. We stress that the discontinuities present in the TFSC model are absent in the GPSC model. Obviously, the presence of the kinetic energy term in Eq. (4.19) leads to smooth density distributions and cures the discontinuities problem of the TFSC model. For a large number of particles, TFSC and GPSC solutions are very close to each other, while for the smaller number of particles the TFSC solution is closer to the semi-ideal model result.

To study onset of Bose-Einstein condensation, let us consider the following scenario: we fix the temperature T, and then change the total number of particles N in the trap. As the number of particles increases, the occupation of the ground state becomes higher and higher, and, above a certain threshold, condensation sets in. Illustrative numerical results are given in Fig. 4.6. A normalized density $4\pi n(r) r^2/N$

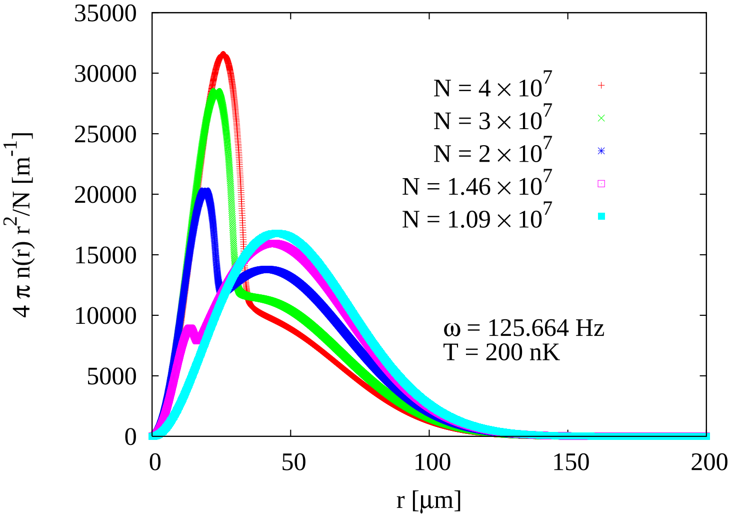

Figure 4.6: Plot of $4\pi n(r) r^2/N$ versus the radial coordinate r within the GPSC model for the parameters $T = 200\,\text{nK}$, $\omega = 125.664\,\text{Hz}$.

versus the radial coordinate r within the GPSC model is shown in the graph. For a very large number of atoms we see a single dominant peak corresponding to the condensate. As the number of atoms decreases, the thermal component becomes visible, and another broader peak emerges. Finally, below the critical value of the total number of atoms, the condensate component disappears completely.

High accuracy of the GPSC model is confirmed by direct comparison with the numerical results obtained from Monte Carlo simulations [76]. However, GPSC model fails precisely in describing the phase transition properly. It turns out that the system of Eqs. (4.19)-(4.21) does not admit a solution in the vicinity of the phase transition, when it is approached from the condensate side. For all physical quantities to be well-behaved, it is crucial that the value of the chemical potential is lower than the value of the classical energy of excited states, $\mu < \mathcal{H}(\vec{r}, \vec{p})$. Unfortunately, for small values of $n_0(r)$, this condition is not satisfied. The inconsistency arises since we treat the ground state quantum-mechanically and all the other states semiclassically. For this reason, in the next subsection, we calculate thermodynamic properties of interacting bosons within the TFSC model.

4.2.5 Calculation of the condensation temperature

A representative phase diagram of ultra-cold gas of bosons in the harmonic trap is displayed in Fig. 4.7. Calculations are performed within the TFSC model. We

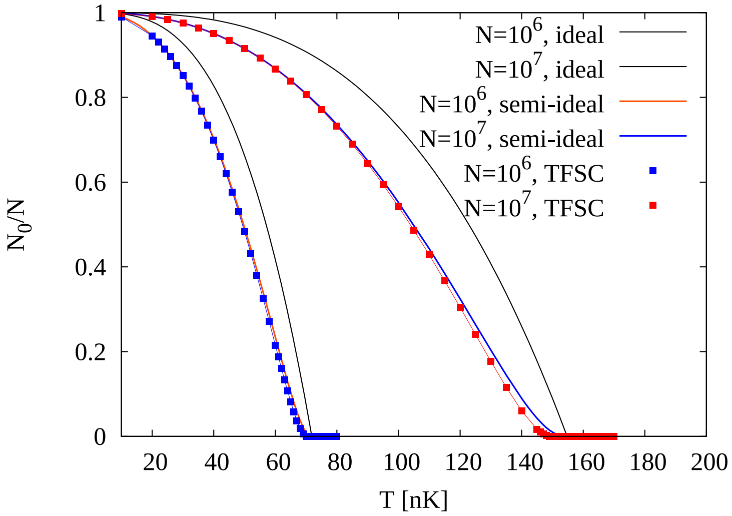

Figure 4.7: Condensate fraction N_0/N versus the temperature T for $\omega = 100\,\mathrm{Hz}$.

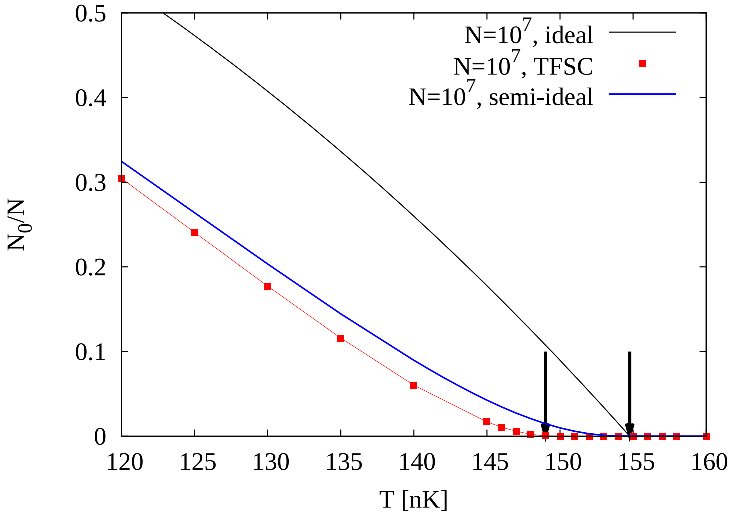

Figure 4.8: Condensate fraction N_0/N versus the temperature T for $\omega = 100\,\mathrm{Hz}$. In the semi-ideal model the condensation temperature is the same as in the ideal case $T_c^0 = 154.77\,\mathrm{nK}$, while the TFSC approximation yields a lower condensation temperature $T_c = 149.5\,\mathrm{nK}$, in agreement with the analytical calculation.

have solved Eqs. (4.26) and (4.27) for the fixed number of particles in the given temperature range and calculated the corresponding condensate fractions N_0/N. From Fig. 4.8, we clearly see the decrease in the condensation temperature due to interaction effects.

We now focus on the analytical calculation of the shift in the condensation temperature with respect to the noninteracting case [90]. To study effects of interaction within the TFSC model, we start from the gas phase. In that case the condensate is absent, and $n_0(r) = 0$. If we insert this into Eq. (4.27), we get

$$n_{\mathrm{th}}(r) = \frac{1}{\lambda_T^3}\zeta_{3/2}\left(e^{\beta(\mu - 2gn_{\mathrm{th}}(r) - V(r))}\right). \tag{4.31}$$

The condensation first appears in the center of the trap, where the following relation holds:

$$n_{\mathrm{th}}(0) = \frac{1}{\lambda_T^3}\zeta_{3/2}\left(e^{\beta(\mu - 2gn_{\mathrm{th}}(0))}\right).$$

Therefore, at the onset of a BEC phase transition, we have $\mu_{\mathrm{c}} = 2gn^{\mathrm{c}}_{\mathrm{th}}(0)$ and $n^{\mathrm{c}}_{\mathrm{th}}(0) = \frac{1}{\lambda_T^3}\zeta_{3/2}$, which yields the critical value of the chemical potential is $\mu_{\mathrm{c}} = 2g\zeta_{3/2}/\lambda_T^3$. Now we calculate the critical number of atoms in the trap as

$$N_{\mathrm{c}} = 4\pi \int_0^\infty dr\, r^2 \frac{1}{\lambda_T^3}\zeta_{3/2}\left(e^{\beta(\mu_{\mathrm{c}} - 2gn_{\mathrm{th}}(r) - V(r))}\right). \tag{4.32}$$

To calculate the above integral, we use the perturbative approach and expand the zeta function to power series in the interaction constant g to linear terms. This means that we consider the term $\mu_{\mathrm{c}} - 2gn_{\mathrm{th}}(r)$ as a small quantity. In this way we obtain

$$\begin{aligned} N_{\mathrm{c}} &\approx \frac{4\pi}{\lambda_T^3}\int_0^\infty dr\, r^2 \left[\zeta_{3/2}\left(e^{-\beta V(r)}\right) + \beta\zeta_{1/2}\left(e^{-\beta V(r)}\right)\left(\mu_{\mathrm{c}} - 2gn_{\mathrm{th}}(r)\right)\right] \\ &\approx \frac{4\pi}{\lambda_T^3}\int_0^\infty dr\, r^2 \left[\zeta_{3/2}\left(e^{-\beta V(r)}\right) + \beta\zeta_{1/2}\left(e^{-\beta V(r)}\right)\right. \\ &\quad \left.\times\left(2\frac{g}{\lambda_T^3}\zeta_{3/2} - 2\frac{g}{\lambda_T^3}\zeta_{3/2}\left(e^{-\beta V(r)}\right)\right)\right] \\ &= \frac{1}{\lambda_T^3}\left[\frac{2\pi}{\beta M\omega^2}\right]^{3/2}\left[\zeta_3 + 2g\beta\frac{1}{\lambda_T^3}\zeta_{3/2}\zeta_2 - 2g\beta\frac{1}{\lambda_T^3}\zeta\left(\frac{1}{2},\frac{3}{2};\frac{3}{2}\right)\right], \end{aligned} \tag{4.33}$$

where $\zeta(i,j;k) = \sum_{m,n=1}^{\infty} 1/m^i n^j (m+n)^k$. From the above expression we immediately find the shift of the condensation temperature [90]:

$$\delta T_{\mathrm{c}} = \frac{T_{\mathrm{c}}^{\mathrm{int}} - T_{\mathrm{c}}^0}{T_{\mathrm{c}}^0} = -1.33\frac{a}{l}N^{1/6}, \tag{4.34}$$

and conclude that repulsive interactions lead to the lower condensation temperature compared to the noninteracting case. The result (4.34) is derived by assuming that

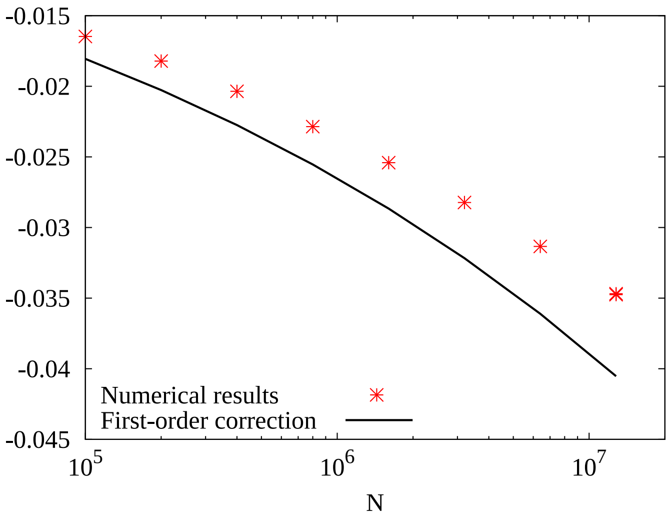

Figure 4.9: A relative shift in the condensation temperature $\delta T_{\rm c}$ as a function of the number of particles in the trap N for $\omega = 100\,\mathrm{Hz}$.

we approach the BEC phase transition from the gas phase. We stress that the same result can be obtained by considering condensate phase in the vicinity of the phase transition within the TFSC model. It is important to note that we only obtain the interaction-induced shift in the condensation temperature. Finite-size effects [91, 92] are beyond our consideration, because we rely on the TF and semiclassical approximation. A comparison of the analytical expression (4.34), which gives a first-order correction to $T_{\rm c}$ in the interaction strength, and numerical results based on Eqs. (4.26) and (4.27), is shown in Fig. 4.9. In this graph, $\delta T_{\rm c}$ is given as a function of the number of particles in the trap. We observe a reasonable agreement of the TFSC result (4.34) with the numerical data.

4.3 Experimental assessment of different models

Density profile of a BEC cloud is experimentally measurable quantity, using either the absorption TOF imaging or in-situ techniques described in Chapter 1. The values of other physical quantities are then extracted from the experimental data in a roundabout way.

Early experimental efforts [93, 94] to measure the occupation of the ground state as a function of the temperature have usually employed the absorption TOF imaging. Thermometry was then performed by fitting the semiclassical result (1.17) to the wings of the measured velocity distribution of a thermal cloud. The condensate component was identified as a characteristic narrow central peak, and the condensate fraction was obtained by fitting either an additional Gaussian profile or a parabolic TF profile to that part of the distribution, in accordance with the previously described almost-ideal model. These early experimental studies were only able to validate that the phase diagram of the system is quite accurately described by the noninteracting result from Eq. (1.10). The inherent statistical and systematic errors prevented real quantitative tests of the mean-field models.

The first clear experimental demonstration, which measured values of condensate fractions different from the corresponding ideal values of Eq. (1.10), was reported in Ref. [89]. The experimental procedure included TOF absorption imaging and an additional technique, a coherent Brag scattering. The advantage of the latter technique is its ability to provide a complete spatial separation of the condensate and thermal cloud during the TOF expansion. The condensate fraction was determined with a high certainty by counting the scattered atoms. However, once again a ballistic expansion of the thermal cloud was assumed, and the temperature was determined by fitting the semiclassical density profile of the expanded noninteracting gas (1.13) to the measured density profile of the thermal cloud. Despite this, the obtained phase diagram clearly demonstrated a reduced condensate fraction compared to the noninteracting result (1.10). A good agreement of experimental values with the results obtained within the semi-ideal model was found, while the agreement was even better with the predictions of the TFSC model. The main focus of Ref. [89] was a precise measurement of the interaction-induced shift of the condensation temperature and its comparison with Eq. (4.34). One of the main conclusions was that improved models are necessary for a good quantitative description of the expansion of finite-temperature BECs and reliable analysis of experimental data.

In order to avoid intricacies of the accurate modeling of the TOF expansion, Ref. [24] has exploited the in-situ phase-contrast imaging to investigate the BEC phase diagram experimentally. The values of the chemical potential μ and the temperature T were determined by fitting to functions that stem from the interacting finite-temperature models to the in-situ measured data. Most reliable fits were obtained in the case of the Popov model [78], which is very similar to the presented TFSC model. We stress that authors of Ref. [24] have used the consistent procedure: the same mean-field model was used for the extraction of all relevant quantities (μ, T, N_0, N) from the experimental results, as well as for the analysis of the phase diagram.

As one of the chief outcomes of that study, the mean-field interaction-induced shift in the condensation temperature, Eq. (4.34), was experimentally confirmed.

Finally, a new series of experiments [80, 81] in 2011 addressed the same topic by utilizing the Feshbach resonance technique of ^{39}K in combination with absorption TOF imaging. Several advantageous aspects of a Feshbach resonance were used. First of all, a wide range of interaction strengths was covered. Also, reference measurements for the same number of atoms and different interaction strengths were performed. Furthermore, a ballistic expansion was carefully engineered by tuning the value of the scattering length to zero during the TOF expansion. For the weakly interacting gas, the mean-field correction result (4.34) was found to be in good agreement with the experimental data. In addition, for the case of stronger interactions, beyond-mean-field effects were clearly observed for the first time.

4.4 Conclusions and outlook

In this Chapter we have reviewed the mean-field description of harmonically trapped BECs. In the zero-temperature limit we have presented widely used Gross-Pitaevskii equation, which we will further exploit in Chapter 5. The relevance of the finite-temperature mean-field models stems from the fact that they are regularly used in the interpretation of experimental data and extraction of density profiles for the condensate and for the thermal cloud. We have considered four different finite-temperature mean-field models. By comparing the predictions of all the considered models, we have concluded that the TFSC model provides the most appropriate and consistent choice from the practical point of view. It is quite easy for numerical implementation, and is capable to reasonably describe the BEC phase transition. Within this approach we have derived the interaction-induced shift of the condensation temperature. The model, however, has a major drawback in that it leads to the unphysical discontinuities in the density profiles. The semi-ideal and GPSC model yield continuous density profiles, but do not capture thermodynamic properties of the system properly. Some of the mentioned issues are even more serious in the case of a more complex trap geometry or in the rotating systems [95]. The results obtained so far point to the necessity of using improved semiclassical approximations for the thermal atoms, which are better suited to the quantum-mechanical description of the ground-state. Now that experiments have succeeded in achieving the clear observation of beyond-mean-field effects, the improvements in widely used approximations become a demand.

Chapter 5 Nonlinear BEC dynamics by harmonic modulation of s-wave scattering length

A thorough knowledge of the excitation spectra of a quantum system is quite important since the properties of its excitations characterize the phase of the matter in a very precise way. The excitation spectra capture information on the system's correlations and define the response of the system to external perturbations. Experimentally, they are determined by exposing the system to a weak perturbation and by measuring the induced dynamics. Thus, the dynamics of the system and its excitation spectra are closely related concepts.

First microscopic derivation of the excitation spectrum of a superfluid, given by Eq. (1.28), was published in the seminal paper of Bogoliubov in 1947 [30]. The obtained spectrum contains a collective phonon mode in the limit of a vanishing wave number, and single-particle excitations in the limit of a large wave number. The original aim of Bogoliubov was the explanation of the superfluidity in ^{4}He and the collective motion of bosonic particles was identified as the underlying mechanism that leads to the phenomenon. Yet, the Bogoliubov approach assumes weak interactions, while ^{4}He is a strongly interacting system and the agreement between the theoretical and experimental results is only qualitative. The dilute vapors of alkali atoms were the first proper experimental realization of a weakly interacting bosonic system that allowed quantitative tests of the theoretical concepts introduced in the early papers of Landau [96] and Bogoliubov [30]. For this reason, the experiments studying the collective bosonic modes were initiated soon after the first achievement of an atomic BEC.

A basic underlying idea of the early experiments was a clear demonstration of the distinction between the collective response of the condensed cloud and the response of thermal atoms to external perturbations. A common scenario in the majority of experiments is to start with the ground-state condensate at very low temperature, where the condensate depletion is negligible, and to induce collective oscillation modes by a temporary modulation of the external trapping potential

[97, 98, 99, 100, 101]. For instance, in the early experiment reported in Ref. [97] collective modes were excited by applying a small time-dependent perturbation of a given frequency to the transversal component of the trap-potential and the real-time dynamics in terms of shape oscillations of the condensate was observed. Based on these measurements, two low-lying eigenmodes of different symmetry were identified. The same procedure was repeated at higher temperatures, when the condensate is not present, and, as expected, the thermal cloud has produced only a response corresponding to the excitations of a normal noninteracting gas. In the experimental study published in the same year Ref. [98], the condensate was excited by the time-dependent modulation of the trapping potential, which additionally included a spatial displacement of the potential minimum. In this case, shape oscillations coupled with the center of mass motion were observed. A typical experimental observation is given in Fig. 5.1. In order to make a detailed comparison with theoretical models, the eigenmode frequencies were measured for different numbers of trapped atoms and for different trap strengths.

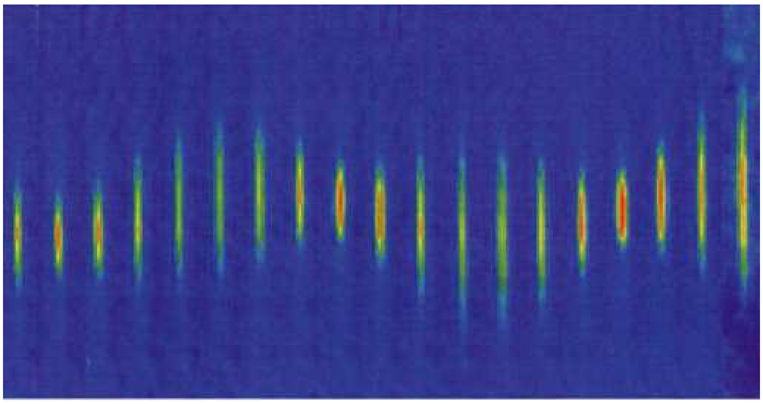

Figure 5.1: An experimental measurement of the collective BEC modes. A figure obtained by Stamper-Kurn and Ketterle, taken from Ref. [5]. The time evolution of a BEC cloud is presented by a series of density profiles. Shape oscillations are coupled with the center of mass motion. The field of view in the vertical direction is about 620 μm and time step is 5 ms per frame.

The original derivation of the Bogoliubov excitation spectrum was performed for a translationally invariant system. However, in cold-atom experiments, bosons are always confined by the external trap and we have to deal with an inhomogeneous system. In order to be able to keep up with the experimental advances, new theoretical approaches for the description of collective modes of a trapped system were developed. In the mean-field framework, linearization of the GP equation (4.15) around the ground-state [102] is analogous to the Bogoliubov approach for the inhomogeneous case. Of course, the procedure is not analytically tractable and has to be implemented numerically. Most widespreadly used analytical approximative results, which also exploit GP equation as a starting point, are Stringari's results obtained in the Thomas-Fermi limit [103], and variational results presented in Refs. [104, 105]. A very good agreement between the experimental values of the frequencies of low-lying modes and theoretical results based on the linearized mean-field equations was established [102, 103, 104] and validity of the mean-field description, given by the GP equation (4.15), was fully confirmed.

All results mentioned until now have assumed small-amplitude oscillations and thus rely on a linearized regime of the initial GP equation. Once this regime was explored to some extent, more complex, physically content-rich, and more interesting dynamical features became the focus of experimental studies. We will mention the most prominent examples. As a first notable example of nonlinear collective BEC excitations we mention localized solutions, usually called solitons [19, 85, 86]. As already pointed out, the main equation that describes the dynamics of a BEC at $T = 0$, the GP equation (4.15), is a nonlinear Schrödinger equation. This type of equations is studied extensively in the field of nonlinear optics and from this context it is well-known that it admits nonlinear localized solutions. Several recent experiments [106, 107] have studied creation and interaction of solitons in the atomic BEC. Another subject of wide interest is pattern formation in a driven system, in particular formation of Faraday patterns [108, 109, 110]. An observation of this type of dynamics in a BEC was given in Ref. [111], where a density wave in the axial direction was produced by a strong modulation of the strength of the radial trapping potential. A further experimental research includes study of a quantum turbulent regime in a BEC [112] by a combination of rotation, strong modulation of a trap strength and a trap displacement. In essence, quantum turbulence is a superfluid turbulence characterized by the presence of tangled vortices. It was initially studied in the superfluid Helium, but now it can be studied in a more controlled way in a BEC setup, as shown in Ref. [112].

In addition to already mentioned research avenues, an exciting possibility for reaching a non-trivial nonlinear dynamical regime in a BEC cloud is given by a real-time tuning of the interaction strength via a Feshbach resonance mechanism introduced in Chapter 1. Harmonic modulation of the s-wave scattering length as a method for excitation of collective oscillation modes was proposed in Refs. [113, 114, 115, 116], but it was experimentally realized only recently in Ref. [15]. In the mean-field approximation at $T = 0$, the time-dependent interaction leads to a time-dependent nonlinearity $g(t)$ in the GP equation. Depending on the closeness of the external modulation frequency Ω to one of condensate's eigenmodes, a qualitatively different dynamical behaviors emerge. In the non-resonant case, we have small-amplitude oscillations of the condensate size around the equilibrium widths, and we are in the regime of linear response. However, as Ω approaches an eigenmode, we expect a resonant behavior which is characterized by large amplitude oscillations. In this case it is clear that a linear response analysis does not provide a qualitatively good description of the system dynamics.

Motivated by the experimental study, described in Ref. [15], in this Chapter we consider dynamical features induced by harmonic modulation of the s-wave scattering length. Our study is a step beyond the linear regime, toward the resonant behavior, and it is suited for the parametric region where low-lying collective modes can still be defined as in the linear regime, but their properties are modified by nonlinear effects. Obtained results are relevant for the proper interpretation of experimental data, and for understanding of near-resonant properties of nonlinear systems.

In the following, we first review variational description of low-lying modes in the linear regime. Then, we turn to the recent experiment, published in Ref. [15], that has achieved harmonic modulation of the s-wave scattering length and briefly explain experimental procedure and results. Finally, we study the nonlinear dynamical regime induced by harmonic modulation of the s-wave scattering length, first for a spherically symmetric BEC, and afterwards for an axially-symmetric BEC. In both cases, we obtain excitation spectra as Fourier transforms of the time-dependent condensate sizes and from here we identify nonlinear features. In addition, we develop perturbation theory based on the Poincaré-Lindstedt method which successfully explains the observed nonlinear effects.

5.1 Variational description of low-lying modes

Our analytical method of choice for studying nonlinear BEC dynamics is variational approach introduced in Refs. [104, 105]. For completeness and for instructive reasons, we first present the method and main results on low-lying collective BEC modes obtained previously in the linear regime. As explained in Chapter 4, the time-dependent GP equation can be obtained by extremizing the functional (4.16) with respect to $\psi(\vec{r},t)$. In the core of the variational description is the idea to plug in an Ansatz for the condensate wave function into Eq. (4.16) and to derive the corresponding Euler-Lagrange equations of the system with respect to the parameters present in the Ansatz. In this way, instead of the partial differential GP equation, we reduce the description of a system to ordinary differential equations, which is far simpler. Naturally, this presents an approximation, and careful examination of its validity and associated errors is necessary.

To this end, we closely follow derivations presented originally in Refs. [104, 105]. We assume that the condensate wave function has the same Gaussian form in the interacting case as in the noninteracting one, just with renormalized parameters. Thus, we use a time-dependent variational method based on a Gaussian Ansatz, which for the anisotropic harmonic trap (1.19) reads

$$\psi^G(x,y,z,t) = \mathcal{N}(t) \prod_{\sigma=x,y,z} \exp\left[-\frac{1}{2}\frac{(\sigma-\sigma_0(t))^2}{u_\sigma(t)^2} + i\,\sigma\varphi_\sigma(t) + i\sigma^2\phi_\sigma(t)\right] , \qquad (5.1)$$

where $\mathcal{N}(t) = \pi^{-\frac{3}{4}} u_x(t)^{-\frac{1}{2}} u_y(t)^{-\frac{1}{2}} u_z(t)^{-\frac{1}{2}}$ is a time-dependent normalization, while $u_\sigma(t)$, $\phi_\sigma(t)$, σ_0 and φ_σ are variational parameters. For convenience, throughout this Chapter, we normalize the wave function to unity and for consistency we include the total number of atoms into the corresponding interaction strength. Thus, we modify the notation introduced earlier by performing the following transformation: $\psi(\vec{r},t) \to \psi(\vec{r},t)/\sqrt{N}$, $g \to g \times N$. The introduced variational parameters have straightforward interpretation: $u_\sigma(t)$ parameters correspond to the condensate widths in different directions and are roughly proportional to the root-mean-square widths of the exact condensate wave function $\psi(x,y,z,t)$; $\phi_\sigma(t)$ and $\varphi_\sigma(t)$ parameters represent the corresponding phases of the wave function and are essential for the proper description of dynamical features; a possible center-of-mass motion is captured by the parameters σ_0.

Following Ref. [104], we insert Ansatz (5.1) into the Lagrangian (4.16) yielding the GP equation, and extremize it with respect to variational parameters. All the details of the derivation are given in Appendix B and here we give only a brief explanation. By extremizing the functional, we first obtain a coupled system of differential equations of the first order for all variational parameters. The equations for the phases ϕ_σ and φ_σ can be solved explicitly in terms of the widths u_σ and the center of mass coordinates σ_0. In this way we obtain two sets of ordinary second-order differential equations that govern the condensate dynamics. A center-of-mass motion is decoupled from the shape oscillations and is determined by simple harmonic oscillator equations, which are independent of interatomic interactions:

$$\ddot{\sigma}_0(t) + \lambda_\sigma^2 \sigma_0(t) = 0,\ \sigma \in \{x, y, z\}\,. \tag{5.2}$$

On the other hand, the widths of the condensate exhibit non-trivial dynamics given by a set of coupled nonlinear differential equations:

$$\ddot{u}_\sigma(t) + \lambda_\sigma^2 u_\sigma(t) - \frac{1}{u_\sigma(t)^3} - \frac{\mathcal{P}}{u_\sigma(t) u_x(t) u_y(t) u_z(t)} = 0,\ \sigma \in \{x, y, z\}\,. \tag{5.3}$$

In the previous equations and from now on, we use dimensionless notation: we choose a convenient frequency scale ω (for example, the external trap frequency in one of the spatial directions) and express all lengths in the units of the characteristic harmonic oscillator length $l = \sqrt{\hbar/M\omega}$, time in units of ω^{-1} and external frequencies in units of ω: $\lambda_\sigma = \omega_\sigma/\omega$, $\sigma \in \{x, y, z\}$. The dimensionless interaction parameter $\mathcal{P}$ is given by $\mathcal{P} = g/((2\pi)^{3/2}\hbar\omega l^3) = \sqrt{2/\pi} Na/l$.

In this approach, the initial partial differential equation (4.15) is approximated with the two sets of ordinary differential equations, given by Eqs. (5.2) and (5.3), which allow analytical considerations. The first properties of the condensate that can be calculated are the equilibrium widths u_{x0}, u_{y0} and u_{z0}. They are found by solving an algebraic system of equations:

$$\lambda_\sigma^2 u_{\sigma 0} - \frac{1}{u_{\sigma 0}} - \frac{\mathcal{P}}{u_{\sigma 0} u_{x0} u_{y0} u_{z0}} = 0,\ \sigma \in \{x, y, z\}\,. \tag{5.4}$$

The equilibrium widths represent stationary solutions of Eqs. (5.3).

Now we turn to the calculation of the frequencies of low-lying modes. To begin with, from Eqs.(5.2) we read off frequencies that correspond to the center-of-mass motion. These are dipole modes and their frequencies are equal to the external trap frequencies (for the case of a harmonic trap). Most often, this type of excitations is created by shifting the trap in space. Actually, the well established experimental procedure for the precise determination of the trap parameters is based on the measurement of the dipole mode frequencies [21].

Next, by linearizing the Eqs. (5.3) around the equilibrium widths (5.4), we can obtain information on collective modes related to the BEC shape oscillations. We will consider experimentally relevant case of an axially symmetric trap, such that $\lambda_x = \lambda_y = 1$, $u_{x0} = u_{y0} \equiv u_{\rho 0}$. Due to the axial symmetry of the considered system, the projection of the angular momentum along the z-axis, $\mathcal{L}_z$, is a good quantum number and we use it for the classification of the modes. By solving the corresponding eigenproblem, we find three different modes depicted in Fig. 5.2. According to their symmetry properties, we designate the modes as the $|\mathcal{L}_z| = 2$ quadrupole mode, the $\mathcal{L}_z = 0$ quadrupole mode, and the breathing mode (which also corresponds to $\mathcal{L}_z = 0$). Eigenvalues of the linearized system of equations yield the frequencies of the collective modes. Frequencies of the $\mathcal{L}_z = 0$ quadrupole mode ω_{Q0}, and the breathing mode ω_{B0} are given by:

$$\omega_{B0,Q0} = \sqrt{2}\left[\left(1+\lambda_z^2-\frac{\mathcal{P}}{4u_{\rho 0}^2 u_{z0}^3}\right) \pm \sqrt{\left(1-\lambda_z^2+\frac{\mathcal{P}}{4u_{\rho 0}^2 u_{z0}^3}\right)^2 + 8\left(\frac{\mathcal{P}}{4u_{\rho 0}^3 u_{z0}^2}\right)^2}\,\right]^{1/2}, \tag{5.5}$$

while the frequency of the $|\mathcal{L}_z| = 2$ quadrupole mode is given by:

$$\omega_{Q0}^{|\mathcal{L}_z|=2} = \sqrt{4 - 2\frac{\mathcal{P}}{u_{\rho 0}^4 u_{z0}}}\,. \tag{5.6}$$

As shown in Fig. 5.2, the $|\mathcal{L}_z| = 2$ quadrupole mode is characterized by out-of-phase oscillations in x and y directions, the $|\mathcal{L}_z| = 0$ quadrupole mode exhibits out-of-phase radial and axial oscillations, while in-phase radial and axial oscillations correspond to the breathing mode.

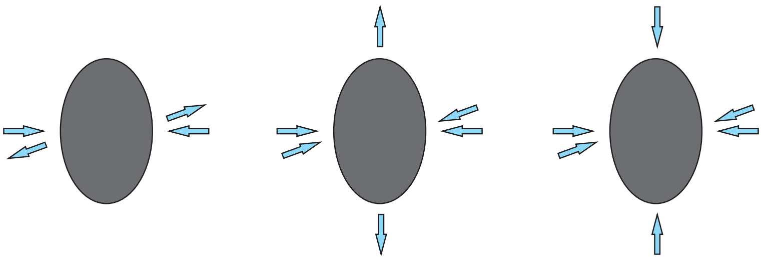

Figure 5.2: A schematic illustration of the condensate eigenmodes: $|\mathcal{L}_z| = 2$ quadrupole mode (left), $|\mathcal{L}_z| = 0$ quadrupole mode (middle) and $|\mathcal{L}_z| = 0$ breathing mode (right).

The main result obtained by using the Gaussian approximation is an analytical estimate for the frequencies of the low-lying collective modes, expressed by Eqs. (5.5) and (5.6) [104, 105]. We emphasize that, although based on the Gaussian Ansatz, the variational approximation reproduces exactly the frequencies of collective modes not only for the weakly interacting BEC, but also for the strongly interacting BEC in the Thomas-Fermi regime [103, 104]. Therefore, it represents a solid analytical description of BEC dynamics. Most importantly, a reasonable quantitative agreement was obtained between the linear response theoretical results (5.5) and (5.6) and experimental results for BEC excited using the trap modulation. In general, a detailed experimental information on collective modes allows us to test our theoretical understanding of the properties of an atomic BEC. The essential merit of testing theoretical predictions using collective oscillation modes stems from the possibility to measure frequencies of collective modes with a high accuracy on the order of less than 1% [100, 99, 101].

We point out that the early theoretical studies of collective modes of BEC [102, 103, 104] focused on the exploration of dynamical properties in the linear regime of small amplitude oscillations. Certain nonlinear aspects of condensate dynamics induced by a trap modulation are given in Refs. [117, 118, 119], whereas two-component BECs are dealt with in Refs. [120, 121]. In the next section we turn to the recent experimental study in which nonlinear effects arise from the modulation of the interaction strength and study how nonlinear dynamical features are reflected on the properties of the excitation spectrum.

5.2 Harmonic modulation of the s-wave scattering length: experiment

Details of the Feshbach resonance of a ^{7}Li BEC were explored by the R. Hulet's group from the Rice University in Ref. [122], and an extreme tunability of interactions was experimentally demonstrated. In the mentioned experiment, atoms were trapped by the optical trap, while the bias magnetic field was used for tuning the scattering length via the Feshbach resonance. For the range of values of magnetic field B, a ground-state condensate was produced and the corresponding density profiles were observed. By measuring the width of the condensate distribution and comparing these values with the corresponding numerical data based on the GP equation (4.15), information on the scattering length spanning seven orders of magnitude was extracted, as can be seen in Fig. 5.3. In this way, precise values of the parameters of the Feshbach resonance (1.23) were obtained:

$$a_{\mathrm{BG}} = -24.5 a_0, \quad \Delta_B = 19.23(3)\,\mathrm{mT}, \quad B_\infty = 73.68(2)\,\mathrm{mT},$$

where a_0 represents the Bohr radius.

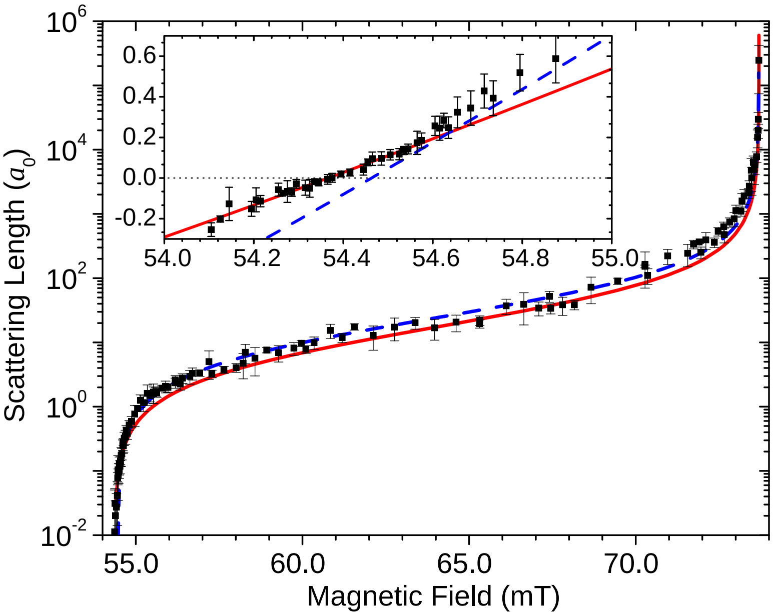

Figure 5.3: Feshbach resonance of a ^{7}Li BEC: Dependence of the scattering length on the external magnetic field. Results are taken from Ref. [122].

In the follow-up paper, Ref. [15], the same group in collaboration with the group of V. Bagnato from Sao Pãulo University, has experimentally realized an alternative way of a ^{7}Li condensate excitation, based on using the Feshbach resonance. By periodically changing an external magnetic field as $B(t) = B_{\mathrm{av}} + \delta B \cos \Omega t$, they were able to obtain harmonic modulation of the s-wave scattering length in the form

$$a(t) \simeq a_{\mathrm{av}} + \delta_a \cos \Omega t\,, \tag{5.7}$$

where $a_{\mathrm{av}} = a(B_{\mathrm{av}}) \approx 3a_0 > \delta_a = -\frac{a_{\mathrm{BG}}\Delta_B \delta B}{(B_{\mathrm{av}}-B_\infty)^2} \approx 2a_0$. In this way, a time-dependent interaction among atoms was realized, which is expressed in terms of the dimensionless parameter $\mathcal{P}(t)$ as

$$\mathcal{P}(t) = \mathcal{P} + \mathcal{Q} \cos \Omega t\,, \tag{5.8}$$

where $\mathcal{P} = \sqrt{2/\pi} N a_{\rm av}/l$ denotes the average interaction strength, $\mathcal{Q} = \sqrt{2/\pi} N \delta_a / l$ is a modulation amplitude, and Ω represents the modulation or driving frequency. The dimensionless experimental parameters from Ref. [15] have the values

$$\mathcal{P} = 15, \quad \mathcal{Q} = 10, \quad \lambda_z = 0.021\,, \tag{5.9}$$

corresponding to the highly elongated trap with the modulated but always positive (repelling) interaction. In the experiment, the oscillations of the condensate size were observed by in-situ phase-contrast imaging, presented in Fig. 5.4.

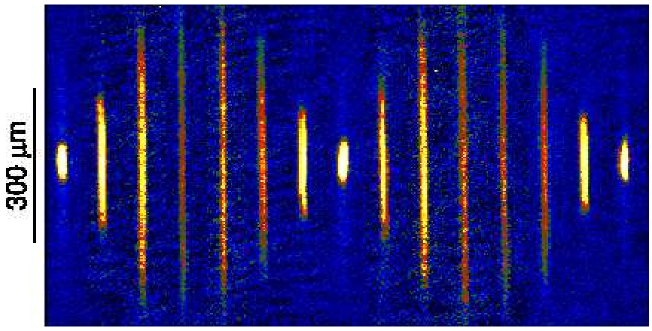

Figure 5.4: Oscillations of the BEC cloud, presented by a series of density profiles taken at equidistant time step of 15 ms. Results are taken from Ref. [15].

The interpretation of the experimental data was based on the analytical results for the frequencies of the low-lying collective modes obtained from the linearized form of the Gaussian approximation. For experimental data, Eq. (5.5) yields the following values for the frequencies of the quadrupole and the breathing mode:

$$\omega_{Q0} = 0.035375\,, \quad \omega_{B0} = 2.00002\,. \tag{5.10}$$

The external trap was stationary, thus preventing excitations of the dipole (Kohn) mode, corresponding to the center-of-mass motion. For the specific set of experimental parameters basically only the quadrupole oscillation mode was excited in this way and resonances located at the quadrupole frequency and its second harmonic were observed.

There are several advantages of such an experimental scheme: for instance, in future experiments with multi-species BEC, a single component could be individually excited in this way, while the excitation of other components would occur only indirectly.

However, due to the nonlinear form of the underlying GP equation, we expect nonlinearity-induced shifts in the frequencies of low-lying modes compared to the values obtained from Eq. (5.5), calculated using the linear stability analysis. In particular, in the case of a close matching of the driving frequency Ω and one of the BEC eigenmodes, we expect resonances, i.e. large amplitude oscillations of the condensate size. When this happens, the role of the nonlinear terms becomes crucial and nonlinear phenomena become dominant. Furthermore, we emphasize that oscillations with very small amplitudes, which occur in the linear regime, are experimentally hard to observe. On the other hand, very large amplitude oscillations lead to a fragmentation of the condensate [15, 123]. Thus, the case in between is of the main experimental interest and represents our main objective, as we discuss in the next section.

5.3 Harmonic modulation of the s-wave scattering length: theoretical framework

To study nonlinear BEC dynamics, we use an approach that is complementary to the recent theoretical considerations [113, 114, 115, 116] of a BEC with harmonically modulated interaction. In Ref. [114] the real-time dynamics of a spherically symmetric BEC was numerically studied and analytically explained using the resonant Bogoliubov-Mitropolsky method [124]. On the other hand, in our approach in order to discern induced dynamical features, we look directly at the excitation spectrum obtained from a Fourier transform of the time-dependent condensate width. From this type of numerical analysis we find characteristic nonlinear properties: higher harmonic generation, nonlinear mode coupling, and significant shifts in the frequencies of collective modes with respect to their linear response counterparts. In addition, we work out an analytic perturbative theory with respect to the modulation amplitude, capable of capturing many of the mentioned nonlinear effects obtained numerically.

Nonlinearity-induced frequency shifts were considered previously in Ref. [117] for the case of bosonic collective modes excited by modulation of the trapping potential, and also in Ref. [125] for the case of a superfluid Fermi gas in the BCS-BEC crossover. Our analytical approach is based on the Poincaré-Lindstedt method [126, 127, 128, 124], in the same spirit as presented in Refs. [117, 125, 126]. However, the harmonic modulation of the interaction strength introduces additional features that require a separate treatment.

In Ref. [116] it was predicted that a harmonic modulation of the scattering length leads to the creation of Faraday patterns in BEC, i.e. density waves. Up to now, Faraday patterns have been experimentally induced by harmonic modulation of the transverse confinement strength [111], which is studied analytically and numerically in Ref. [129]. Here we focus only on the nonlinear properties of low-lying collective modes and do not consider possible excitations of Faraday patterns.

In order to obtain analytical insight into the condensate dynamics induced by the harmonic modulation of the s-wave scattering length described by Eq. (5.7), we use the Gaussian variational approximation approximation. We consider an axially symmetric BEC, ($\lambda_x = \lambda_y = 1$, $u_x = u_y \equiv u_\rho$), excited by modulation of the interaction strength, which preserves the axial symmetry of the condensate during its time evolution. For this reason, we use a simplified axially-symmetric form of Eqs. (5.3):

$$\ddot{u}_\rho(t) + u_\rho(t) - \frac{1}{u_\rho(t)^3} - \frac{\mathcal{P}(t)}{u_\rho(t)^3 u_z(t)} = 0\,, \tag{5.11}$$

$$\ddot{u}_z(t) + \lambda_z^2 u_z(t) - \frac{1}{u_z(t)^3} - \frac{\mathcal{P}(t)}{u_\rho(t)^2 u_z(t)^2} = 0\,, \tag{5.12}$$

which we will refer to as a Gaussian approximation.

To estimate the accuracy of the Gaussian approximation for describing the dynamics induced by the harmonic modulation of the interaction strength, we compare its solution with an exact numerical solution of the GP equation. In Fig. 5.5, we plot the resulting time-dependent axial and radial condensate widths $\rho_{\mathrm{rms}}(t)$ and $z_{\mathrm{rms}}(t)$, calculated as root mean square values

$$\rho_{\mathrm{rms}}(t) = \sqrt{2\pi \int_{-\infty}^{\infty} dz \int_0^{\infty} \rho\, d\rho\, |\psi(\rho,z,t)|^2\, \rho^2}\,, \tag{5.13}$$

$$z_{\mathrm{rms}}(t) = \sqrt{2\pi \int_{-\infty}^{\infty} dz \int_0^{\infty} \rho\, d\rho\, |\psi(\rho,z,t)|^2\, z^2}\,, \tag{5.14}$$

of the solution of the GP equation, as well as numerical solutions of Eqs. (5.11) and (5.12). We assume that initially the condensate is in the ground state. In the variational description, this translates into initial conditions $u_\rho(0) = u_{\rho 0}$, $\dot{u}_\rho(0) = 0$, $u_z(0) = u_{z0}$, $\dot{u}_z(0) = 0$, where $u_{\rho 0}$ and u_{z0} are the time-independent solutions

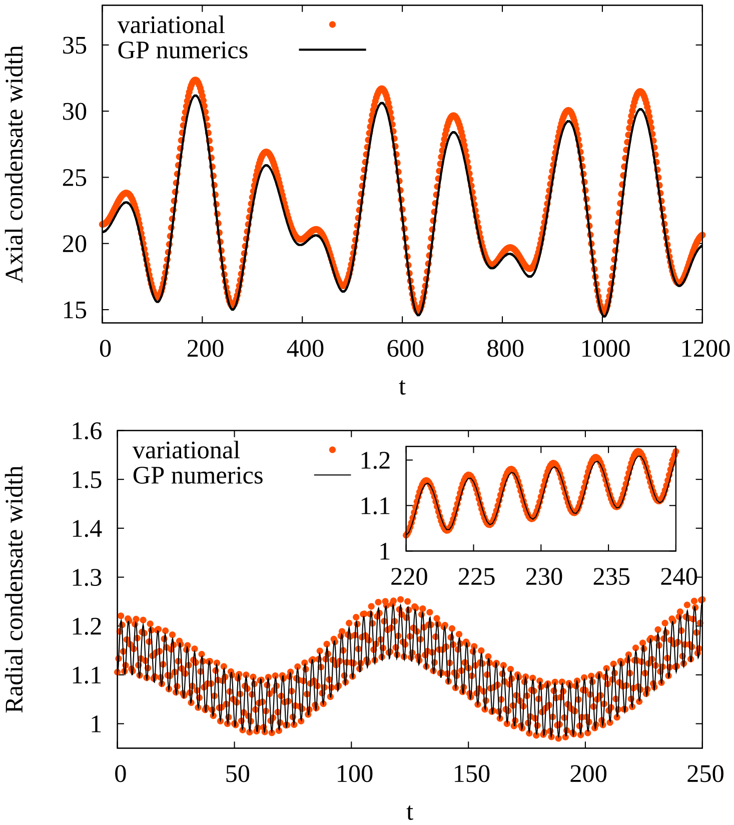

Figure 5.5: Time-dependent axial and radial condensate widths calculated as root mean square averages. Comparison of the numerical solution of the time-dependent GP equation with a solution obtained by using the Gaussian approximation for the actual experimental parameters in Eq. (5.9) and $\Omega = 0.05$.

of Eqs. (5.11) and (5.12), while in GP simulations we reach the ground state by performing an imaginary-time propagation until convergence to the ground state is achieved [87]. For solving the GP equation (4.15), we use the split-step Crank-Nicolson method [87] explained in detail in Appendix A. From the typical results presented in Fig. 5.5, which correspond to the actual experimental parameters, it is evident that we have a good qualitative agreement between the two approaches, even for long times of the dynamical evolution.

5.4 Spherically-symmetric BEC

Using a simple symmetry-based reasoning, we immediately conclude that harmonic modulation of the interaction strength in the case of a spherically symmetric BEC, ($\lambda_z = 1$), leads to the excitation of the breathing mode only, so that $u_\rho(t) = u_z(t) \equiv u(t)$. This fact simplifies numerical and analytical calculations and this is why we first consider this case before we embark to the study of a more complex, axially-symmetric BEC.

The system of ordinary differential Eqs. (5.11) and (5.12) in this case reduces to a single equation:

$$\ddot{u}(t) + u(t) - \frac{1}{u(t)^3} - \frac{\mathcal{P}(t)}{u(t)^4} = 0\,. \tag{5.15}$$

The equilibrium condensate width u_0 satisfies the equation

$$u_0 - \frac{1}{u_0^3} - \frac{\mathcal{P}}{u_0^4} = 0\,, \tag{5.16}$$

and a linear stability analysis yields the breathing mode frequency

$$\omega_0 = \sqrt{1 + \frac{3}{u_0^4} + \frac{4\mathcal{P}}{u_0^5}}\,. \tag{5.17}$$

Note that the above result for the breathing mode can be also obtained from Eq. (5.5) if we set $\lambda_z = 1$, $u_{\rho 0} = u_{z0} \equiv u_0$, and take into account Eq. (5.16).

The main feature of the modulation-induced dynamics is that it strongly depends on the value of the driving frequency Ω. To illustrate this, we set $\mathcal{P} = 0.4$, $\mathcal{Q} = 0.1$ and solve Eq. (5.15) for different values of the driving Ω. From the linear response theory, we have $u_0 = 1.08183$, $\omega_0 = 2.06638$ and we assume that the condensate is initially in equilibrium, i.e. $u(0) = u_0, \dot{u}(0) = 0$. Numerical results are presented in Fig. 5.6. Large amplitude oscillations and beating phenomena are observed for both $\Omega \approx \omega_0$ and for $\Omega \approx 2\omega_0$.

The phenomenology based on Eq. (5.15) is more systematically shown in Fig. 5.7, where we plot the oscillation amplitude, defined as $(u_{\mathrm{max}} - u_{\mathrm{min}})/2$, versus the driving frequency Ω. A resonant behavior becomes apparent for both $\Omega \approx \omega_0$ and $\Omega \approx 2\omega_0$. In the same figure we also show the expected positions of resonances calculated using the linear stability analysis. Clearly, the prominent peaks exhibit shifts with respect to the solid vertical lines, representing ω_0 and $2\omega_0$. As expected, a stronger

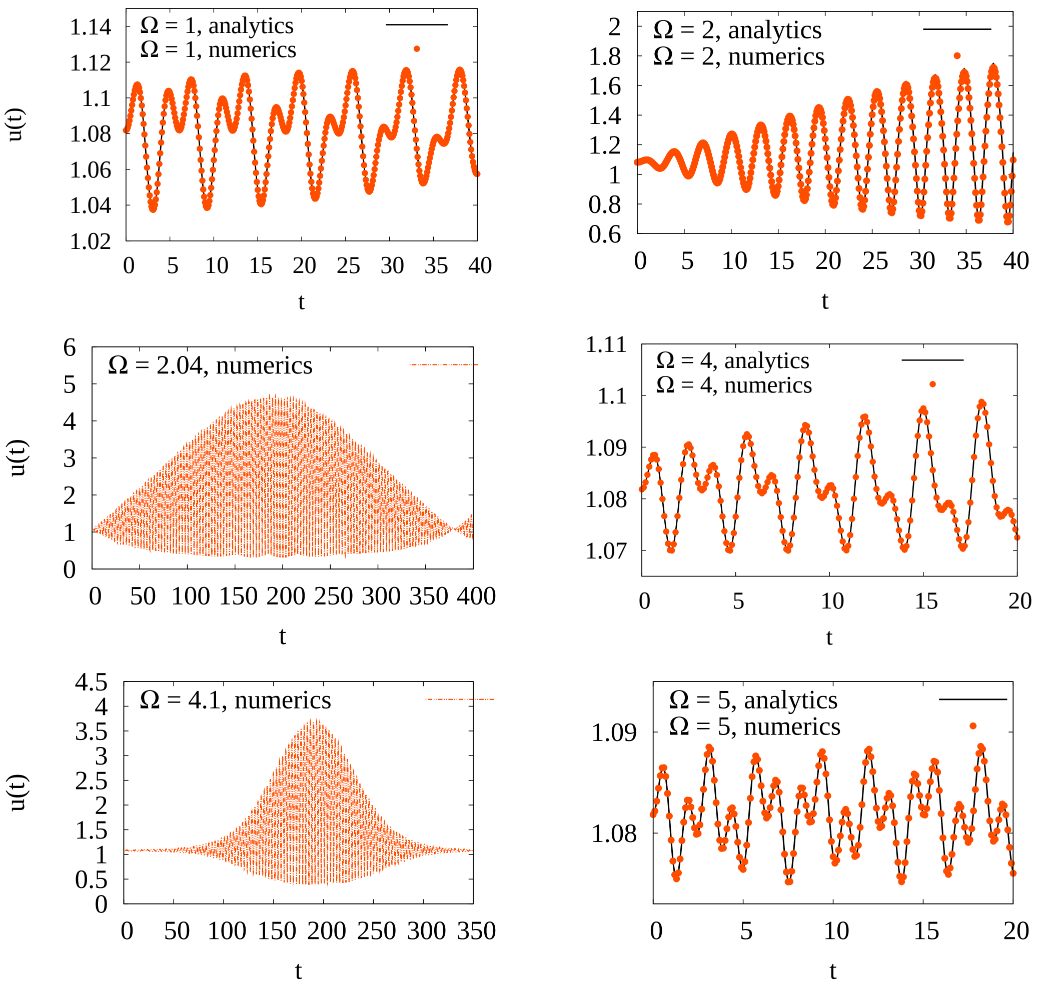

Figure 5.6: Condensate width dynamics $u(t)$ versus t within the Gaussian approximation for $\mathcal{P} = 0.4$, $\mathcal{Q} = 0.1$ and several different driving frequencies Ω. We plot the exact numerical solution of Eq. (5.15). For off-resonant driving frequencies Ω, we also show our analytical third-order perturbative result (designated 'analytics'), as explained in section III.B.

modulation amplitude leads to a larger frequency shift, as can be seen from the inset.

The curves presented in Fig. 5.7 are obtained by an equidistant sampling of the external driving frequency Ω. In addition to the expected resonances close to ω_0 and $2\omega_0$, a more thorough exploration of solutions of the variational equation (5.15) shows that other "resonances" are present, such as, e.g. $\Omega \approx \omega_0/2$ and $\Omega \approx 2\omega_0/3$. This is further demonstrated in Fig. 5.8. These "resonances" are harder to observe

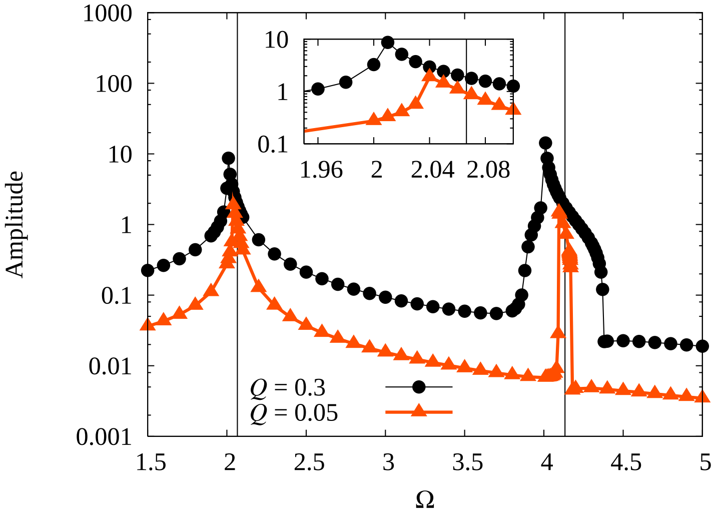

Figure 5.7: Oscillation amplitude $(u_{\max} - u_{\min})/2$ versus driving frequency Ω for $\mathcal{P} = 0.4$. In the inset, we zoom to the first peak to emphasize that both the shape and the value of a resonance depend on the modulation amplitude $\mathcal{Q}$ and that resonances occur at a driving frequency Ω, which differs from ω_0. The solid vertical lines correspond to ω_0 and $2\omega_0$.

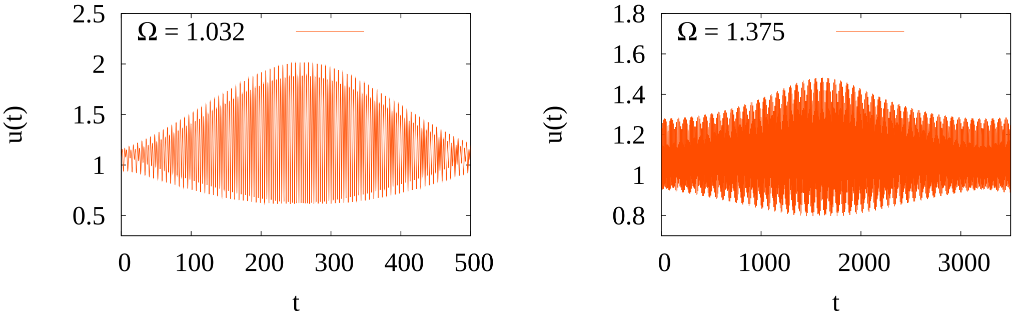

Figure 5.8: Exact numerical solution of Eq. (5.15) for the condensate width $u(t)$ versus t for $\mathcal{P} = 0.4$, $\mathcal{Q} = 0.3$, corresponding to $\omega_0 = 2.06638$. We observe large amplitude oscillations for $\Omega \approx \omega_0/2$ in the left panel, while in the right panel the "resonant" behavior is present for $\Omega \approx 2\omega_0/3$.

numerically, since it is necessary to perform a fine tuning of the external frequency. However, they clearly demonstrate nonlinear BEC properties and an experimental observation of these phenomena is certainly of high interest. We note that the observed resonance pattern of the form $\Omega \approx 2\omega_0/n$ (where n is an integer) arises also in the case of a parametrically driven system described by the Mathieu equation,

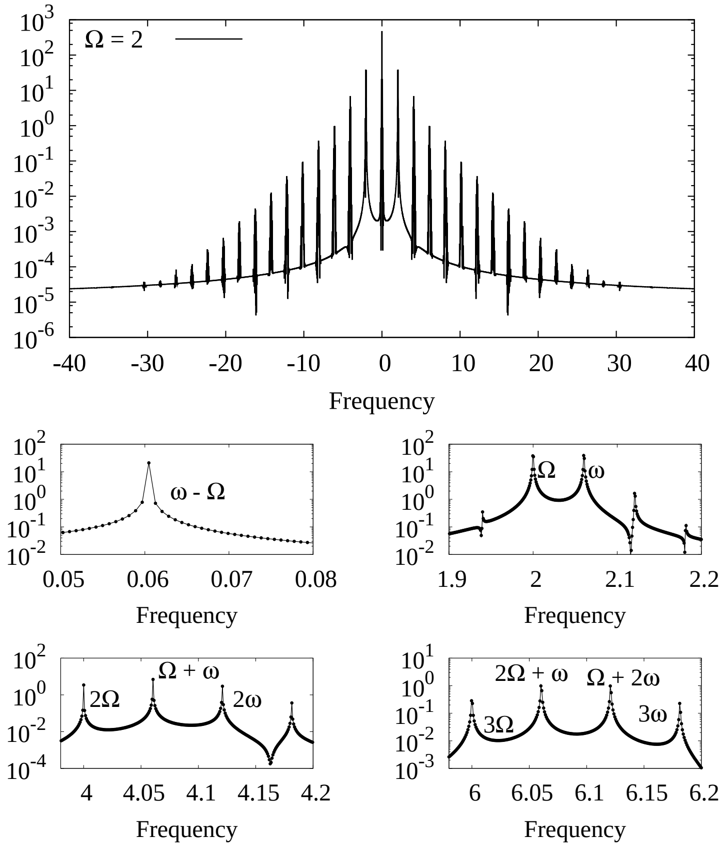

Figure 5.9: Fourier transform of $u(t)$ for $\mathcal{P} = 0.4$, $\mathcal{Q} = 0.1$, and $\Omega = 2$. First plot presents the complete spectrum on a semi-log scale, while the subsequent plots focus on regions of interest in the spectrum.

for instance, in the context of the Paul trap [130].

To examine such excited modes directly, we look at the Fourier transform of the condensate width $u(t)$. To this end, we numerically solve Eq. (5.15) and find the Fourier transform of its solution using the MATHEMATICA software package [54]. An example of such an excitation spectrum for $\mathcal{P} = 0.4$, $\mathcal{Q} = 0.1$, and $\Omega = 2$ is given in Fig. 5.9. The spectrum contains two prominent modes: a breathing mode of frequency ω (close, but not equal to ω_0), and a mode that corresponds to the driving frequency Ω, along with many higher-order harmonics of the general form $m\Omega + n\omega$, where m and n are integers.

In Fig. 5.10 we juxtapose two zoomed-in Fourier spectra for two different driving frequencies for $\mathcal{P} = 0.4$ and $\mathcal{Q} = 0.2$. On the left plot, we show a spectrum for $\Omega = 1$. The vertical solid line corresponds to ω_0 and we find the peak in the

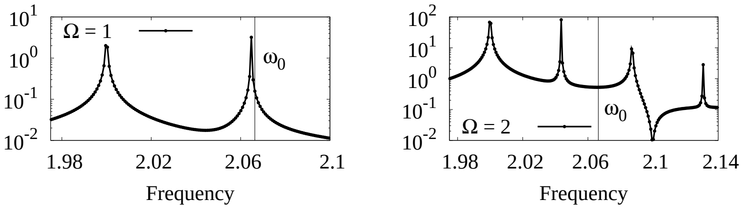

Figure 5.10: Parts of the Fourier spectra for $\mathcal{P} = 0.4$, $\mathcal{Q} = 0.2$, and two different driving frequencies: $\Omega = 1$ (left) and $\Omega = 2$ (right). Position of a linear response result ω_0 is given by a vertical solid line.

spectrum that lies almost precisely at this position. On the contrary, from the right plot of Fig. 5.10, which corresponds almost to the resonant excitation at $\Omega = 2$, we see that the prominent peak is displaced from the vertical line. This is the most clear-cut illustration of the shifted eigenfrequency arising due to the nonlinearity of the underlying dynamical equations. Our objective is to develop an analytical approach capable of taking into account these nonlinear effects.

5.4.1 Poincaré-Lindstedt method

In its essence, our analytical approach represents the standard Poincaré-Lindstedt method [127, 128, 124, 126]. Linearizing the variational equation (5.15) around the time-independent solution u_0 for a vanishing driving $\mathcal{Q} = 0$, we obtain the zeroth-order approximation for the collective mode $\omega = \omega_0$, expressed by Eq. (5.17). To calculate the collective mode to higher orders, we explicitly introduce the sought-after eigenfrequency ω into the calculation by rescaling the time from t to $s = \omega t$, yielding the equation:

$$\omega^2\, \ddot{u}(s) + u(s) - \frac{1}{u(s)^3} - \frac{\mathcal{P}}{u(s)^4} - \frac{\mathcal{Q}}{u(s)^4} \cos\frac{\Omega s}{\omega} = 0\,. \tag{5.18}$$

In the next step, we assume the following perturbative expansions in the modulation amplitude $\mathcal{Q}$:

$$u(s) = u_0 + \mathcal{Q}\, u_1(s) + \mathcal{Q}^2\, u_2(s) + \mathcal{Q}^3\, u_3(s) + \ldots\,, \tag{5.19}$$

$$\omega = \omega_0 + \mathcal{Q}\, \omega_1 + \mathcal{Q}^2\, \omega_2 + \mathcal{Q}^3\, \omega_3 + \ldots\,, \tag{5.20}$$

where we expand ω around ω_0 and introduce the frequency shifts ω_1, $\omega_2, \ldots$, for each order in the expansion in $\mathcal{Q}$. By inserting the above expansions into the Eq. (5.18) and collecting terms of the same order in $\mathcal{Q}$, we obtain a hierarchical system of linear differential equations. To the third order, we find:

$$\begin{aligned}
\omega_0^2 \ddot{u}_1(s) + \omega_0^2 u_1(s) &= \frac{1}{u_0^4} \cos \frac{\Omega s}{\omega}\,, \\
\omega_0^2 \ddot{u}_2(s) + \omega_0^2 u_2(s) &= -2\omega_0\omega_1 \ddot{u}_1(s) - \frac{4}{u_0^5} u_1(s) \cos \frac{\Omega s}{\omega} + \alpha u_1(s)^2, \\
\omega_0^2 \ddot{u}_3(s) + \omega_0^2 u_3(s) &= -2\omega_0\omega_2 \ddot{u}_1(s) - 2\beta u_1(s)^3 + 2\alpha u_1(s) u_2(s) - \omega_1^2 \ddot{u}_1(s) \\
&\quad + \frac{10}{u_0^6}\, u_1(s)^2 \, \cos \frac{\Omega s}{\omega} - \frac{4}{u_0^5}\, u_2(s) \, \cos \frac{\Omega s}{\omega} - 2\omega_0\, \omega_1\, \ddot{u}_2(s),
\end{aligned}$$

where $\alpha = 10\,\mathcal{P}/u_0^6 + 6/u_0^5$ and $\beta = 10\,\mathcal{P}/u_0^7 + 5/u_0^6$.

These equations disentangle in a natural way: we solve the first one for $u_1(s)$, and use that solution to solve the second one for $u_2(s)$, and so on. At the n-th level of the perturbative expansion ($n \geq 1$) we use the initial conditions $u_n(0) = 0, \dot{u}_n(0) = 0$. As is well known, the presence of the term $\cos s$ on the right-hand side of some of the previous equations would yield a solution that contains the secular term $s \sin s$. Such a secular term grows linearly in time, which makes it the dominant term in the expansion (5.19) that otherwise contains only periodic functions in s. In order to ensure a regular behavior of the perturbative expansion, the respective frequency shifts ω_1, $\omega_2, \ldots$ are determined by imposing the cancellation of secular terms.

This analytical procedure is implemented up to the third order in the modulation amplitude $\mathcal{Q}$ by using the software package MATHEMATICA [54]. Although the calculation is straightforward, it easily becomes tedious for higher orders of perturbation theory. Note that it is necessary to perform the calculation to at least third order since it turns out to be the lowest-order solution where secular terms appear and where the nontrivial frequency shift can be calculated. We have solved explicitly equations for $u_1(s)$, $u_2(s)$, and $u_3(s)$ and in Fig. 5.6 we show an excellent agreement of our analytical solutions with a respective numerical solution of Eq. (5.15). From the first-order solution $u_1(t)$ we read off only the two basic modes ω_0 and Ω, while the second-order harmonics $2\omega_0$, $\omega_0 - \Omega$, $\omega_0 + \Omega$ and 2Ω appear in $u_2(t)$. In the third order of perturbation theory, higher-order harmonics $\omega - 2\Omega$, $2\omega - \Omega$, $2\omega + \Omega$, $\omega + 2\Omega$, 3ω, and 3Ω are also present. Concerning the cancellation of secular terms, the first-order correction ω_1 vanishes, leading to a frequency shift which is quadratic in $\mathcal{Q}$:

$$\omega = \omega_0 + \frac{\mathcal{Q}^2}{12 u_0^{20} \omega_0^3} \frac{\mathrm{P}(\Omega)}{(\Omega^2 - \omega_0^2)^2\,(\Omega^2 - 4\omega_0^2)} + \ldots\,, \tag{5.21}$$

where the polynomial $\mathrm{P}(\Omega)$ is given by

$$\begin{aligned} \mathrm{P}(\Omega) = {} & \Omega^4 \left[-240\mathcal{P}u_0^5 + 36u_0^6(-4 + 3u_0^4\omega_0^2)\right] \\ & + \Omega^2 \left[-1100\mathcal{P}^2 - 30\mathcal{P}u_0(44 - 65u_0^4\omega_0^2) + 9u_0^2(-44 + 127u_0^4\omega_0^2 - 44u_0^8\omega_0^4)\right] \\ & + 5600\mathcal{P}^2\omega_0^2 + 840\mathcal{P}u_0\omega_0^2(8 - 3u_0^4\omega_0^2) + 36u_0^2\omega_0^2(56 - 39u_0^4\omega_0^2 + 8u_0^8\omega_0^4). \end{aligned} \tag{5.22}$$

MATHEMATICA notebook which implements this analytical calculation is available at our web site [60].

5.4.2 Results and discussion

The result given by Eq. (5.21) is the main achievement of our analytical analysis in the previous section. It is obtained within a second-order perturbative approach in $\mathcal{Q}$ and it describes the breathing mode frequency dependence on the driving Ω and the modulation amplitude $\mathcal{Q}$ as a result of nonlinear effects. Due to the underlying perturbative expansion, we do not expect Eq. (5.21) to be meaningful at the precise position of the resonances. However, by comparison with numerical results based on the variational equation, we find that Eq. (5.21) represents quite a reasonable approximation even close to the resonant region.

To illustrate this, in Fig. 5.11 we show two such comparisons. In the upper panel we consider the parameter set $\mathcal{P} = 0.4$ and $\mathcal{Q} = 0.1$, and observe significant frequency shifts only in the narrow resonant regions. We notice an excellent agreement of numerical values with the analytical result given by Eq. (5.21). In the lower panel we consider the parameter set $\mathcal{P} = 1$ and $\mathcal{Q} = 0.8$, with much stronger modulation amplitude. In this case we observe significant frequency shifts for the broader range of modulation frequencies Ω. In spite of a strong modulation, we still see a qualitatively good agreement of numerical results with the analytical prediction given by Eq. (5.21). In principle, better agreement can be achieved using higher-order perturbative approximation. The dashed line on both figures represents $\Omega/2$, given as a guide to the eye. It also serves as a crude description of what we observe numerically in the range $\Omega \approx 2\omega_0$.

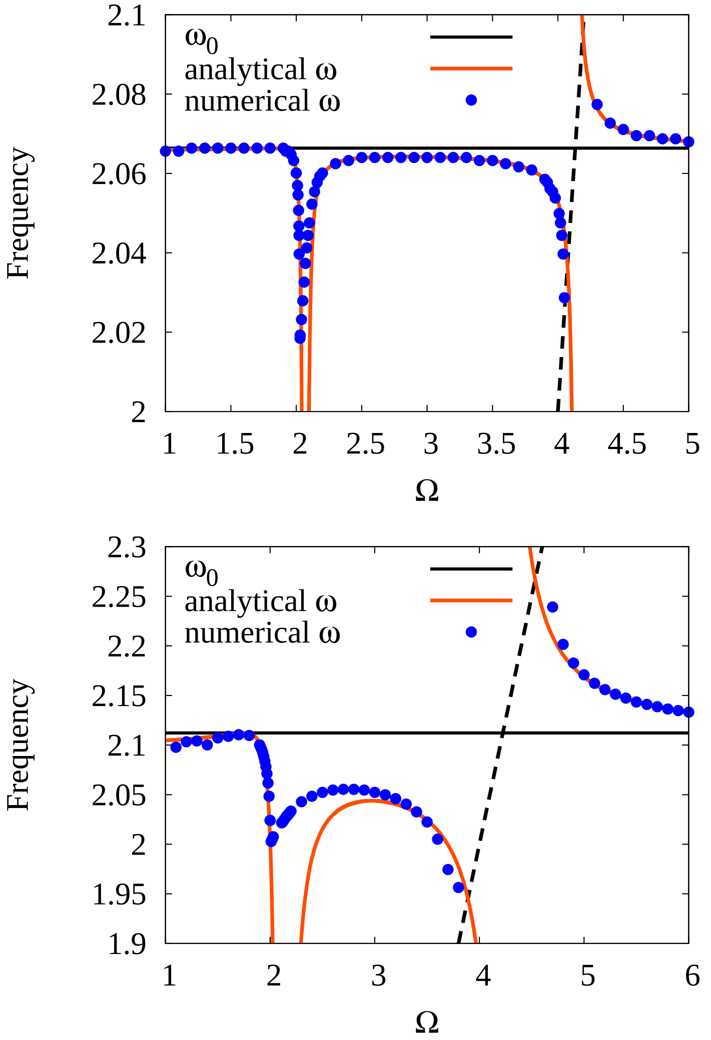

Figure 5.11: Frequency of the breathing mode versus the driving frequency Ω for $\mathcal{P} = 0.4$ and $\mathcal{Q} = 0.1$ (top), and $\mathcal{P} = 1$ and $\mathcal{Q} = 0.8$ (bottom). The dashed line represents $\Omega/2$ and is given to guide the eye.

The presence of two poles at $\Omega = \omega_0$ and $\Omega = 2\omega_0$ in Eq. (5.21) implies the possible existence of real resonances in the BEC with a harmonically modulated interaction. A perturbative expansion to higher orders would introduce some additional poles, responsible for higher-order "resonant" behavior observed at $\Omega \approx 2\omega_0/n$ ($n \geq 3$). Still, the poles seem to be only an artifact of our approximative perturbative scheme, not present in the exact description. For example, a simple resummation performed using the second-order perturbative result removes these effects, although this is only an ad-hoc approximation. We stress that this issue concerning the true resonant behavior can not be settled either by relying on a numerical calculation due to inherent numerical artifacts related to finite numerical precision and finite computational time. To resolve it, one should rely on an analytical consideration along the lines of Ref. [118] or use some analytical tool applicable at resonances, such as the resonant Bogoliubov-Mitropolsky method [124].

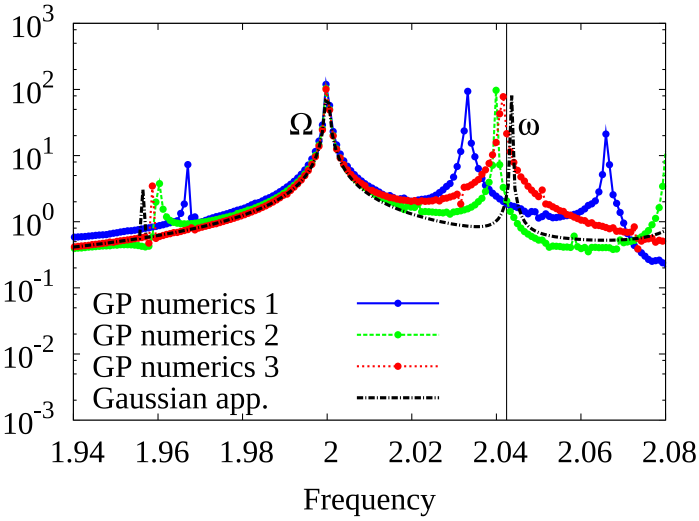

Figure 5.12: Part of the Fourier spectrum of the time-dependent condensate width for $\mathcal{P} = 0.4$, $\mathcal{Q} = 0.2$, $\Omega = 2$. For numerical solution of GP equation we use several discretization schemes: GP numerics 1 (time step $\varepsilon = 10^{-3}$, spacing $h = 4 \times 10^{-2}$), GP numerics 2 ($\varepsilon = 5 \times 10^{-4}$, $h = 2 \times 10^{-2}$), GP numerics 3 ($\varepsilon = 5 \times 10^{-5}$, $h = 5 \times 10^{-3}$). Details of the used numerical algorithms are given in Appendix A. For comparison we also show the corresponding spectrum obtained from the Gaussian approximation (dotted-dashed line) and analytical result (5.21) for the position of breathing mode (solid vertical line).

In addition to comparison of our analytical results with numerical solutions based on the Gaussian variational approximation, we present a comparison with the full numerical solution of the GP equation. In order to be able to perform Fourier analysis with sufficient resolution, it is necessary to obtain an accurate solution for long evolution times. We do this by using the split-step method in combination with the semi-implicit Crank-Nicolson method [87]. As we refine the GP numerics by using finer space and time discretization parameters, our numerical results become stable as shown in Fig. 5.12. From the same figure, we observe quantitatively good agreement between GP numerics and Gaussian approximation, reflected in close values obtained for the breathing mode frequency. In addition, numerical values for the breathing mode approach closely the analytical result of Eq. (5.21), shown by a solid vertical line in Fig. 5.12.

It is well known that for a corresponding two-dimensional axially-symmetric system with a constant interaction and trapping frequency, the breathing mode oscillations can be described by an exact linear equation [131, 132]. However, in the case of a time-dependent trapping frequency, the exact equation of motion is nonlinear [118]. To the best of our knowledge, for a time-dependent interaction strength the corresponding exact equation does not exist in the literature, but one can reasonably expect that nonlinear effects will remain in such systems, due to the inherent time dependence of the interaction.

5.5 Axially-symmetric BEC

To obtain results relevant for a comparison with the experiment reported in Ref. [15], we now study an axially-symmetric BEC. An illustration of the condensate dynamics is shown in Fig. 5.13 for $\mathcal{P} = 1$, $\mathcal{Q} = 0.2$, $\lambda_z = 0.3$. We plot numerical solutions of Eqs. (5.11) and (5.12) obtained for the equilibrium initial conditions $u_\rho(0) = u_{\rho 0}$, $\dot{u}_\rho(0) = 0$, $u_z(0) = u_{z0}$, and $\dot{u}_z(0) = 0$. For the specified parameters, the equilibrium widths are found to be $u_{\rho 0} = 1.09073$, $u_{z0} = 2.40754$, and from the linear stability analysis we find both the quadrupole mode frequency $\omega_{Q0} = 0.538735$ and the breathing mode frequency $\omega_{B0} = 2.00238$. For a driving frequency Ω close to ω_{Q0}, we observe large amplitude oscillations in the axial direction. An example of excitation spectra is shown in Fig. 5.14. Here, we have the three basic modes ω_Q, ω_B, Ω, and many higher-order harmonics.

5.5.1 Poincaré-Lindstedt method

In order to extract information on the frequencies of the collective modes beyond the linear stability analysis, we apply the perturbative expansion in the modulation amplitude $\mathcal{Q}$:

$$u_\rho(t) = u_{\rho 0} + \mathcal{Q}\, u_{\rho 1}(t) + \mathcal{Q}^2\, u_{\rho 2}(t) + \mathcal{Q}^3\, u_{\rho 3}(t) + \ldots, \tag{5.23}$$

$$u_z(t) = u_{z0} + \mathcal{Q}\, u_{z1}(t) + \mathcal{Q}^2\, u_{z2}(t) + \mathcal{Q}^3\, u_{z3}(t) + \ldots. \tag{5.24}$$

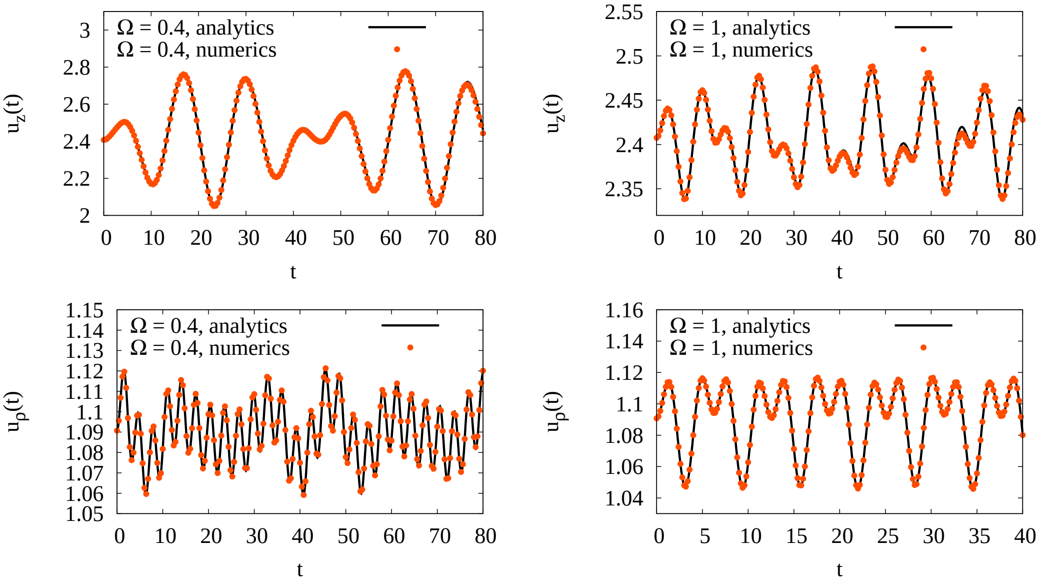

Figure 5.13: Condensate dynamics within the Gaussian approximation for $\mathcal{P} = 1$, $\mathcal{Q} = 0.2$, $\lambda_z = 0.3$ and two different driving frequencies $\Omega = 0.4$ (left plot) and $\Omega = 1$ (right plot). We plot exact numerical solution of Eqs. (5.11) and (5.12) together with the analytical second-order perturbative result, as explained in section IV.A.

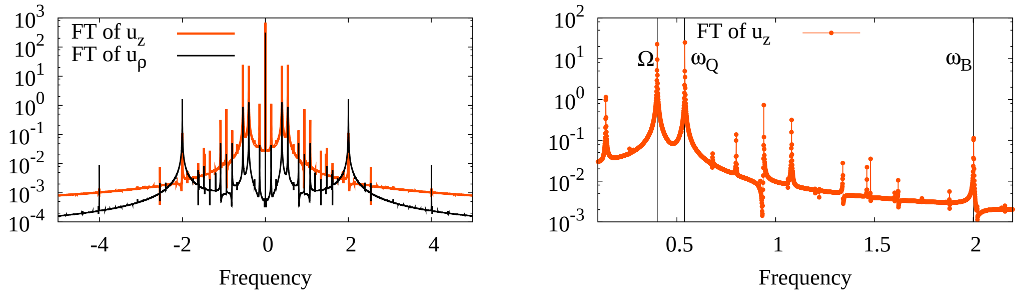

Figure 5.14: Fourier transformed $u_\rho(t)$ and $u_z(t)$ for $\mathcal{P} = 1$, $\mathcal{Q} = 0.2$, $\lambda_z = 0.3$, and $\Omega = 0.4$. Left plot gives complete spectrum, while on the right plot we show part of the spectrum together with positions of prominent peaks.

By inserting these expansions in Eqs. (5.11) and (5.12), and by performing additional expansions in $\mathcal{Q}$, we obtain a system of linear differential equations of the general form:

$$\ddot{u}_{\rho n}(t) + m_{11} u_{\rho n}(t) + m_{12} u_{zn}(t) + f_{\rho n}(t) = 0, \tag{5.25}$$

$$m_{21} u_{\rho n}(t) + \ddot{u}_{zn}(t) + m_{22} u_{zn}(t) + f_{zn}(t) = 0, \tag{5.26}$$

where $n = 1, 2, 3, \ldots$ is an integer, and

$$m_{11} = 4, \quad m_{12} = \mathcal{P}/u_{\rho 0}^3 u_{z0}^2, \quad m_{21} = 2\,\mathcal{P}/u_{\rho 0}^3 u_{z0}^2, \quad m_{22} = \lambda_z^2 + 3/u_{z0}^4 + 2\,\mathcal{P}/u_{\rho 0}^2 u_{z0}^3.$$

The n-th order functions $f_{\rho n}(t)$ and $f_{zn}(t)$ depend only on the solutions $u_{\rho i}(t)$ and $u_{zi}(t)$ of lower orders, $i < n$. For $n = 1$ we have

$$f_{\rho 1}(t) = -\frac{\cos \Omega t}{u_{\rho 0}^3 u_{z0}}, \quad f_{z1}(t) = -\frac{\cos \Omega t}{u_{\rho 0}^2 u_{z0}^2},$$

and for $n = 2$ we get correspondingly

$$\begin{aligned} f_{\rho 2}(t) &= \frac{3}{u_{\rho 0}^4 u_{z0}} \cos \Omega t \, u_{\rho 1}(t) - \frac{6}{u_{\rho 0}^5} u_{\rho 1}(t)^2 - \frac{6\mathcal{P}}{u_{\rho 0}^5 u_{z0}} u_{\rho 1}(t)^2 \\ &\quad + \frac{1}{u_{\rho 0}^3 u_{z0}^2} \cos \Omega t \, u_{z1}(t) - \frac{3\mathcal{P}}{u_{\rho 0}^4 u_{z0}^2} u_{\rho 1}(t) u_{z1}(t) - \frac{\mathcal{P}}{u_{\rho 0}^3 u_{z0}^3} u_{z1}(t)^2, \\ f_{z2}(t) &= \frac{2}{u_{\rho 0}^3 u_{z0}^2} \cos \Omega t \, u_{\rho 1}(t) - \frac{3\mathcal{P}}{u_{\rho 0}^4 u_{z0}^2} u_{\rho 1}(t)^2 - \frac{3\mathcal{P}}{u_{\rho 0}^2 u_{z0}^4} u_{z1}(t)^2 \\ &\quad + \frac{2}{u_{\rho 0}^2 u_{z0}^3} \cos \Omega t \, u_{z1}(t) - \frac{6}{u_{z0}^5} u_{z1}(t)^2 - \frac{4\mathcal{P}}{u_{\rho 0}^3 u_{z0}^3} u_{\rho 1}(t) u_{z1}(t). \end{aligned}$$

The linear transformation

$$u_{\rho n}(t) = x_n(t) + y_n(t), \tag{5.27}$$

$$u_{zn}(t) = c_1 \, x_n(t) + c_2 \, y_n(t), \tag{5.28}$$

with the coefficients

$$c_{1,2} = \frac{m_{22} - m_{11} \pm \sqrt{(m_{22} - m_{11})^2 + 4 m_{12} m_{21}}}{2 m_{12}},$$

decouples the system at the n-th level and leads to the equations of the form:

$$\ddot{x}_n(t) + \omega_{Q0}^2 x_n(t) + \frac{c_2 \, f_{\rho n}(t) - f_{zn}(t)}{c_2 - c_1} = 0, \tag{5.29}$$

$$\ddot{y}_n(t) + \omega_{B0}^2 y_n(t) + \frac{c_1 \, f_{\rho n}(t) - f_{zn}(t)}{c_1 - c_2} = 0. \tag{5.30}$$

Now it is clear how to proceed: we first solve Eqs. (5.29) and (5.30) for $x_1(t)$ and $y_1(t)$, and then using Eqs. (5.27) and (5.28) we obtain $u_{\rho 1}(t)$ and $u_{z1}(t)$. In the next step, we use these solutions and solve for $x_2(t)$ and $y_2(t)$ and so on. At each level $n \geq 1$ we impose the initial conditions $u_{\rho n}(0) = 0$, $\dot{u}_{\rho n}(0) = 0$, $u_{zn}(0) = 0$, and $\dot{u}_{zn}(0) = 0$. At the first level of perturbation theory, equations for x and y are decoupled, i.e. $x_1(t)$ and $y_1(t)$ are normal modes: $x_1(t)$ describes quadrupole oscillations, while $y_1(t)$ describes breathing oscillations. However, at the second order of perturbation theory $y_1(t)$ enters the equation for $x_2(t)$ and also $x_1(t)$ appears in equation for $y_2(t)$, i.e. we have a nonlinear mode coupling.

We have performed the explicit calculation to the second order by using the software package MATHEMATICA [54]. We have obtained an excellent agreement of second-order analytical results and numerical results, as can be seen in Fig. 5.13 for a moderate value of a modulation amplitude $\mathcal{Q}$. The first secular terms appear at the level $n = 3$. The expressions are cumbersome, but the relevant behavior is obtained from the following terms in the equation for $x_3(t)$:

$$\ddot{x}_3(t) + \omega_{Q0}^2 x_3(t) + C_Q \cos\omega_{Q0} t + \ldots = 0, \tag{5.31}$$

which leads to

$$x_3(t) = -\frac{C_Q}{2\omega_{Q0}} t \sin\omega_{Q0} t + \ldots \tag{5.32}$$

The last term can be absorbed into the first-order solution

$$\begin{aligned} u_\rho(t) &= A_Q \cos\omega_{Q0} t - \frac{C_Q \mathcal{Q}^2}{2\omega_{Q0}} t \sin\omega_{Q0} t + \ldots \\ &\approx A_Q \cos\left[(\omega_{Q0} + \Delta\omega_{Q0})t\right], \end{aligned} \tag{5.33}$$

and can be interpreted as a frequency shift of the quadrupole mode, quadratic in $\mathcal{Q}$:

$$\omega_Q = \omega_{Q0} + \Delta\omega_{Q0} = \omega_{Q0} + \mathcal{Q}^2 \frac{C_Q}{2\omega_{Q0} A_Q} + \ldots \tag{5.34}$$

The coefficients A_Q and C_Q are calculated using the MATHEMATICA code available at our site [60], and their explicit form is too long to be presented here. Along the same lines we have also calculated the frequency shift of the breathing mode.

5.5.2 Results and discussion

The main results of our calculation in this section are shown in Figs. 5.15 and 5.16. In Fig. 5.15 we plot the analytically obtained frequency of the quadrupole

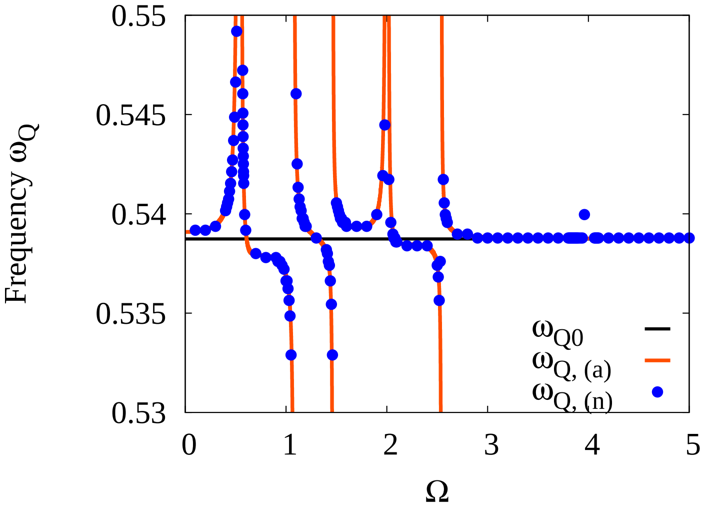

Figure 5.15: Frequency of the quadrupole mode ω_Q versus driving frequency Ω for $\mathcal{P} = 1$, $\mathcal{Q} = 0.2$, and $\lambda_z = 0.3$. We plot linear response result ω_{Q0}, second-order analytical result $\omega_{Q,(\mathrm{a})}$ and numerical values $\omega_{Q,(\mathrm{n})}$.

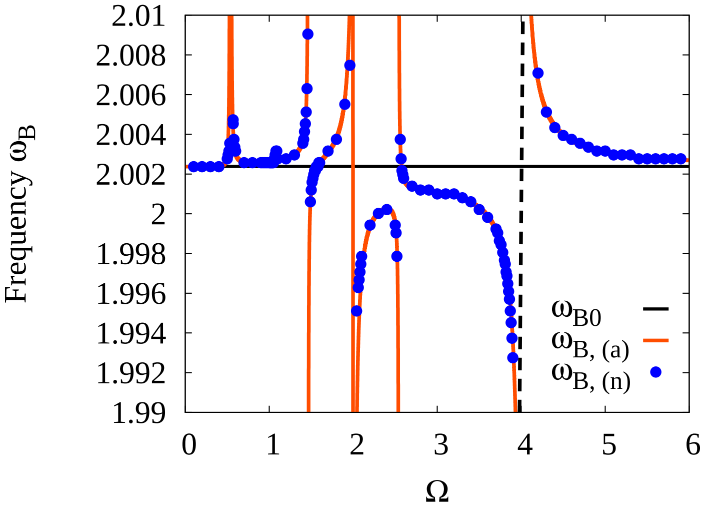

Figure 5.16: Frequency of the breathing mode ω_B versus driving frequency Ω for $\mathcal{P} = 1$, $\mathcal{Q} = 0.2$, and $\lambda_z = 0.3$. We plot linear response result ω_{B0}, second-order analytical result $\omega_{B,(a)}$ and numerical values $\omega_{B,(n)}$.

mode versus the driving Ω, using the second order perturbation theory together with the corresponding numerical result based on the Fourier analysis of solutions of Eqs. (5.11) and (5.12). An analogous plot for the frequency of the breathing mode is given in Fig. 5.16. Our analytical perturbative result for the shifted quadrupole mode frequency contains poles at ω_{Q0}, $2\omega_{Q0}$, $\omega_{B0}-\omega_{Q0}$, $\omega_{Q0}+\omega_{B0}$ and ω_{B0}. Similarly, for the shifted frequency of the breathing mode poles in the perturbative solution are found at ω_{Q0}, ω_{B0}, $2\omega_{B0}$, $\omega_{B0} - \omega_{Q0}$ and $\omega_{Q0} + \omega_{B0}$. In both figures we see excellent agreement of the perturbatively obtained results with the exact numerics.

In the experiment from Ref. [15], excitations of a highly elongated and strongly repulsive BEC were considered with the system parameters given in Eq. (5.9). For that case, according to Eq. (5.10) we get $\omega_{Q0} \ll \omega_{B0}$, and the driving frequency was chosen in the range $(0, 3\omega_{Q0})$. Good agreement of real-time dynamics obtained from the variational approximation with the exact solution of the time-dependent GP simulation occurs even for long propagation times, as can be seen in Fig. 5.5, which implies a good accuracy of the Gaussian approximation for calculating the frequencies of the excited modes. From the real-time dynamics shown in Fig. 5.5, we observe the excitation of the slow quadrupole mode as an out-of phase oscillation in the axial and in the radial direction. In addition, in the radial direction we observe fast breathing mode oscillations. This is typical for highly elongated condensates [133] and our analysis for the experimental parameters shows a strong excitation of the quadrupole mode, but also a significant excitation of the breathing mode in the radial direction. Due to the large modulation amplitude $\mathcal{Q}$, many higher order harmonics are excited, and, most importantly, we find frequency shifts of the quadrupole mode of about 10% in Fig 5.17. From the same figure we notice that, due to the chosen frequency range for Ω, only resonances located at ω_Q and $2\omega_Q$ are observed. The presence of nonlinear effects is already mentioned in Ref. [15]. However, we conclude that frequency shifts calculated here have to be taken into account for extracting the resonance curves from the underlying experimental data.

To achieve more clear-cut experimental observation of the nonlinearity-induced frequency shifts calculated in this paper, we suggest a different trap geometry from the one used in Ref. [15]. Measurements of stable BEC modes can be performed for about 1 s, and in order to extract precise values of the excited frequencies in the Fourier analysis, several oscillation periods should be captured within this time interval. A higher frequency of the quadrupole mode, that can be realized by using a larger trap aspect ratio λ_z, in combination with a higher modulation frequency would fulfill this condition. According to the results presented in Ref. [15], resonant driving may lead to condensate fragmentation. However, our numerical results indicate frequency shifts of 10 % even outside the resonant regions according to

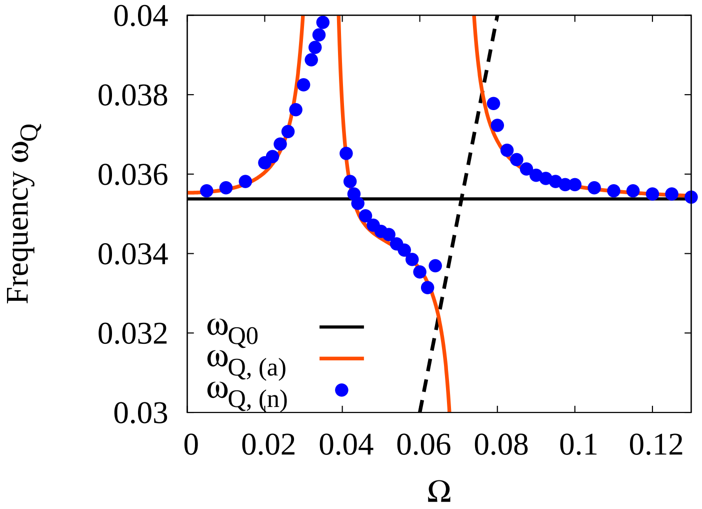

Figure 5.17: Frequency of the quadrupole mode ω_Q versus driving frequency Ω for the experimental parameters from Eq. (5.9). We plot linear response result ω_{Q0}, second-order analytical result $\omega_{Q,(a)}$, and numerical values $\omega_{Q,(n)}$.

Figs. 5.11 and 5.17, and this is where experimental measurements should be performed. Although an increase in λ_z leads to a more pronounced nonlinear mixing of quadrupole and breathing mode and may complicate condensate dynamics further, it may be possible to perform a Fourier analysis of experimental data, analogous to Ref. [101], and to compare it with the excitation spectra presented here. To achieve a complete matching of experimental data and our calculations, it may turn out that higher-order corrections to Eq. (5.7), which arise due to the nonlinear dependence of scattering length on the external magnetic field, have to be taken into account.

5.6 Conclusions and outlook

Motivated by recent experimental results, in this Chapter, we have studied nonlinear BEC dynamics induced by a harmonically modulated interaction at zero temperature. We have used a combination of an analytic perturbative approach, numerical analysis based on Gaussian approximation, and numerical simulations of a full time-dependent Gross-Pitaevskii equation. We have presented numerically calculated relevant excitation spectra and found prominent nonlinear features: mode coupling, higher harmonics generation, and significant shifts in the frequencies of collective modes. In addition, we have provided an analytical perturbative framework that captures most of the observed phenomena. The main results are analytic formulae describing the dependence of collective mode frequencies on the modulation amplitude and on the external driving frequency for different trap geometries. We believe that the study presented in this Chapter is a step toward understanding resonant processes in a nonlinear system. To extend the applicability of our analytical approach, a perturbative expansion to higher order has to be performed, or an appropriate resummation of the perturbative series could be applied.

The presented results could contribute to future experimental designs that may include mixtures of cold gases and their dynamical response to harmonically modulated interactions, such as pattern formation induced by the modulation of different time dependence of the scattering length. In addition, our results could contribute to resolving beyond-mean-field effects in the collective mode frequencies, as proposed in Refs. [134, 135], and for dipolar BEC in [136]. Nonlinearity-induced shifts of collective modes have to be properly taken into account to clearly delineate them from beyond-mean-field effects.

Chapter 6 Summary

Since the first experimental observation of Bose-Einstein condensation in the dilute vapors of alkali atoms in 1995, the field of ultracold atoms constantly expands. The experimental advances in the manipulation of quantum gases pave a way to the development of new technologies, and allow exploration of the quantum world with previously unseen precision and flexibility, uncovering at the same time new variety of far reaching physical phenomena. In this thesis we have studied two particular phenomena that give new insights into the properties of cold quantum gases and have been recently addressed experimentally.

To begin with, in Chapter 1 we have introduced the aspects of the research in the field of ultracold atoms, main concepts, and its position within the wide forefront of modern physics. In Chapter 2 we have developed an efficient numerical method for calculation of the eigenspectrum and eigenvectors of a system in an arbitrary trapping potential. The devised approach is based on the exact diagonalization of the time-evolution operator and can be applied for numerical studies of general few-body systems. We have carefully explored different types of systematic errors that arise in the process of the spatial discretization of the time-evolution operator. We have shown analytically and numerically that the discretization error vanishes as the exponential of $1/\Delta^2$, where Δ represents the discretization spacing. Thus, the method highly outperforms in efficiency the approaches based on the real- space discretization of the Hamiltonian, which exhibit polynomial error in Δ. For the highly accurate calculation of matrix elements of the evolution operator, necessary for the application of the method, we use the short-time expansion of transition amplitudes in the propagation time to high-orders. The chief ingredients of this part of the procedure are higher-order effective actions, that were derived previously. We have demonstrated the advantages of this method by calculating highly accurate energy spectra in a numerically efficient way for several one- and two-dimensional models.

Motivated by experimental studies of rotating ultra-cold quantum gases, in Chapter 3 we have studied the effects of the shape of trapping potentials to the properties of a Bose-Einstein condensate of an ideal gas. A rotation gives rise to the appearance of a deconfining harmonic potential. Particularly, in the interesting fast-rotating regime, when the rotation frequency approaches the confining frequency of the harmonic trap, the gas becomes unconfined and the condensate would disperse. One way to mitigate the deconfining effect is to use an additional, quartic term in the potential. As a result, the total external potential in the co-rotating frame acquires different shapes, depending on the rotation frequency. It is important to understand how this affects the properties of a BEC for the interpretation of data obtained in experiments with fast rotating BECs. By employing the method of exact diagonalization of the time-evolution operator from Chapter 2, we have obtained numerically exact energy spectra of the harmonic plus quartic trapping potential for different values of the rotation frequency. Using this, we have calculated the condensation temperature and found that it decreases with an increase of the rotation frequency. We have also presented density profiles of the condensate and thermal cloud at different temperatures and have simulated the time-of-flight imaging procedure for this setup. Interesting expansion dynamics has been found for the external potential in the shape of a Mexican hat, in the over-critical rotation regime. In the initial stage of the expansion the gas expands inwards, into the previously unoccupied inner space, and only after that the common free expansion starts. This leads to an increase in the typical time scales for the expansion of about one order of magnitude.

Chapter 4 is dedicated to the review of the mean-field description of a weakly interacting BEC. We have presented several widely used approximation techniques. In the zero temperature limit, we have introduced nonlinear mean-field Gross-Pitaevskii equation. In order to study BEC at finite temperature and to explore the BEC phase diagram, we have used Hartree-Fock framework in the form in which higher, thermally excited states are treated within the semiclassical approximation. Within this mean-field picture, a two-component model of a BEC naturally arises. In an approximative way, the condensate and thermal component are introduced enabling us to keep the intuition built on a noninteracting model. Depending on whether the interaction within each component is taken into account and how their mutual interaction is considered, several approximation schemes come into play. We have compared their properties, and emphasized the identified drawbacks. The interaction-induced shift of the condensation temperature has been re-derived. With these results, we have shown how the noninteracting BEC picture is modified in the presence of weak short-range interactions.

The excitation of collective oscillation modes is a direct way to probe the properties of a system, since frequencies of collective modes can be measured very accurately, with errors of below 1%. In Chapter 5 we have studied properties of collective modes subject to the harmonic modulation of the s-wave scattering length, i.e. contact interaction strength. We have used time-dependent Gross-Pitaevskii equation and the variational approach based on a Gaussian Ansatz to describe condensate dynamics numerically. In the non-resonant regime, when the driving frequency does not match any of the eigenfrequencies of the condensate, we have found small amplitude oscillations that correspond to the quadrupole and breathing mode, as expected for an axially-symmetric condensate. As the resonant regime is approached, nonlinear dynamical features emerge in the excitation spectra: nonlinear mode coupling, higher-harmonics generation and shifts in the frequencies of excited modes. We have developed a perturbative approach in the modulation amplitude, based on the Poincaré-Lindstedt method, and have obtained analytical results for the mentioned effects.

At the end of each chapter, we have indicated a possible future research direction to further extend the study of the topics presented in this thesis.

Appendix A Numerical solution of the GP equation

For the numerical solution of the GP equation, we use algorithms described in Ref. [87]. Original codes are written using the Fortran programming language, while we implemented the numerical procedure in the C programming language. For completeness, in this Appendix we outline the main steps of the applied numerical method for the simplest, spherically-symmetric case.

In general, there are two different type of questions that we want to answer by solving the GP equation: either we are interested in the equilibrium configurations, i.e. stationary solutions, or we simulate real-time dynamics of the system. It turns out that both situations can be treated on an equal footing by using propagation in real and imaginary time, t and τ respectively, which are connected by the expression:

$$i\,t = \tau\,. \tag{A.1}$$

The imaginary-time propagation is very useful and efficient technique for obtaining stationary states of both linear and nonlinear systems. Essentially, it is equivalent to the minimization of the energy functional, and here we explain its basics for the case of a linear system. The main underlying identity is given by

$$|\psi_0\rangle = \lim_{\tau\to\infty} e^{-\tau\hat{H}}|\psi_{\mathrm{initial}}\rangle\,, \tag{A.2}$$

where $|\psi_{\mathrm{initial}}\rangle$ is an arbitrary initial state, which has a nonzero overlap with the ground-state $|\psi_0\rangle$ of a system. Eq. (A.2) states that after long enough propagation in the imaginary time, we will obtain the ground state of the system. This can be easily understood by decomposing the initial state into the eigenvectors of the Hamiltonian $\hat{H}$,

$$e^{-\tau\hat{H}}|\psi_{\mathrm{initial}}\rangle = \sum_{k=0}^{\infty}\langle\psi_k|\psi_{\mathrm{initial}}\rangle e^{-\tau E_k}|\psi_k\rangle\,, \tag{A.3}$$

by noting that the coefficients in front of all eigenstates decay exponentially in the imaginary time τ, and that the slowest decaying coefficient is the one in front of the ground state. Imaginary-time propagation does not preserve the norm of the state, and we have to renormalize the state manually after each iteration step. Therefore, it is obvious that after certain time τ, the contribution of higher states will be negligible, and thus we will arrive at the result given by Eq. (A.2). A similar reasoning is valid also for nonlinear systems, hence in the case of the GP equation we apply the transformation (A.1) and use imaginary-time propagation to find the stationary states. From the numerical side, imaginary-time and real-time propagation can be implemented in a very similar manner, and we briefly present only the details of numerical implementation of the real-time propagation.

To simplify the expression for the Laplacian in a spherically-symmetric case, we first apply a commonly used rescaling:

$$\phi(r,t) = \frac{\psi(r,t)}{r}\,, \tag{A.4}$$

and transform the spherically-symmetric GP equation into its simplified form:

$$i\frac{\partial\phi(r,t)}{\partial t} = \left[-\frac{1}{2}\frac{\partial^2}{\partial r^2} + \frac{1}{2}r^2 + g\left|\frac{\phi(r,t)}{r}\right|^2\right]\phi(r,t)\,. \tag{A.5}$$

Next, we split the propagation into two steps, which correspond to the two parts of Eq. (A.5):

$$i\frac{\partial\phi(r,t)}{\partial t} = \left[\frac{1}{2}r^2 + g\left|\frac{\phi(r,t)}{r}\right|^2\right]\phi(r,t)\,, \tag{A.6}$$

$$i\frac{\partial\phi(r,t)}{\partial t} = -\frac{1}{2}\frac{\partial^2}{\partial r^2}\phi(r,t)\,. \tag{A.7}$$

This is the split-step approximation, valid for the short propagation time. It is motivated by a possibility to treat each of the two previous equations in a specially suited way: the first equation deals with the part of the Hamiltonian which is diagonal in the coordinate space, while the second equation considers the kinetic term. To perform the time discretization, we introduce the index n, which counts the time slices $\phi(r,t) \equiv \phi^n(r)$, where $t = n\varepsilon$, and ε is a discrete time-step of the propagation. According to Eqs. (A.6) and (A.7), there are two different steps to be performed for one time-step, in the propagation from t to $t+\varepsilon$. Correspondingly, we introduce the notation $\phi^{n+1/2}(r)$, which is the value of the wavefunction after the first part of the propagation according to Eq. (A.6), while after the additional step according to Eq. (A.7), the propagation to $t+\epsilon$ is finished, and a new wave function $\phi^{n+1}(r)$ is calculated. Finally, we rewrite Eqs. (A.6) and (A.7) in the approximate discretized form:

$$\phi^{n+1/2}(r) = e^{-i\varepsilon\left(\frac{1}{2}r^2+g\left|\frac{\phi^n(r)}{r}\right|^2\right)}\phi^n(r), \tag{A.8}$$

$$i\frac{1}{\varepsilon}\left(\phi^{n+1}(r)-\phi^{n+1/2}(r)\right) = -\frac{1}{4}\frac{\partial^2\phi^{n+1/2}}{\partial r^2} - \frac{1}{4}\frac{\partial^2\phi^{n+1}}{\partial r^2}\,. \tag{A.9}$$

In the last equation, we have used the semi-implicit Crank-Nicolson method [137], which is highly accurate, robust and inexpensive method for solving general diffusion equations. The accuracy of the approximation is ε^2.

To reduce the obtained differential equations to the algebraic form, we additionally perform space discretization with the discretization step h. To this end, we introduce index i, which takes values from 0 to $i_{\max}-1$, and approximate the second-order spatial derivative in the standard way:

$$\frac{\partial^2\phi^n}{\partial r^2} \to \frac{1}{4h^2}\left(\phi^n_{i+1}-2\phi^n_i+\phi^n_{i-1}\right)\,, \tag{A.10}$$

with the error of the order of h^2. As a result, we obtain a tridiagonal system of equations:

$$-A\phi^{n+1}_{i+1}+B\phi^{n+1}_i-A\phi^{n+1}_{i-1}=\delta_i\,, \tag{A.11}$$

where

$$\delta_i=(\varepsilon/4h^2)\phi^{n+1/2}_{i+1}+\left(1-\varepsilon/2h^2\right)\phi^{n+1/2}_i+(\varepsilon/4h^2)\phi^{n+1/2}_{i-1},\ A=\varepsilon/4h^2\,, B=1+\varepsilon/2h^2\,.$$

A solution of a tridiagonal system of equations can be cast in the form:

$$\phi^{n+1}_{i+1}=\alpha_i\phi^{n+1}_i+\beta_i\,, \tag{A.12}$$

and from this Ansatz we find the recursive relations for the solution:

$$\alpha_{i-1}=\frac{A}{B-A\alpha_i}\,,\quad \beta_{i-1}=\frac{\delta_i+A\beta_i}{B-A\alpha_i}\,. \tag{A.13}$$

From the boundary condition $\phi^n_{i_{\max}}=\phi^{n+1/2}_{i_{\max}}$, we derive initial values for α and β: $\alpha_{i_{\max}-1}=0$ and $\beta_{i_{\max}-1}=\phi^{n+1/2}_{i_{\max}}$, which we use to solve the recursive equations

(A.13). With another boundary condition $\phi_0^n = 0$, we finally solve Eq. (A.12). Due to the tridiagonal form of the above system of equations, the complexity of the algorithm is proportional to the number of discretization points.

Once the ground-state solution $\phi(r)$ is calculated using the imaginary-time version of the above algorithm, the corresponding values of the chemical potential μ and the energy E of the system can be calculated as:

$$\begin{aligned}\mu &= 4\pi \int_0^\infty dr \left[\phi^2(r)\left(\frac{r^2}{2} + g\phi^2(r)\right) + \frac{1}{2}\left(\frac{\partial\phi(r)}{\partial r}\right)^2\right], \\ E &= 4\pi \int_0^\infty dr \left[\phi^2(r)\left(\frac{r^2}{2} + \frac{g}{2}\phi^2(r)\right) + \frac{1}{2}\left(\frac{\partial\phi(r)}{\partial r}\right)^2\right].\end{aligned}$$

An example of the convergence of the value of the chemical potential as a function of a propagated imaginary-time is shown in Fig. A.1. We see the saturation of the chemical-potential value for a long time of propagation.

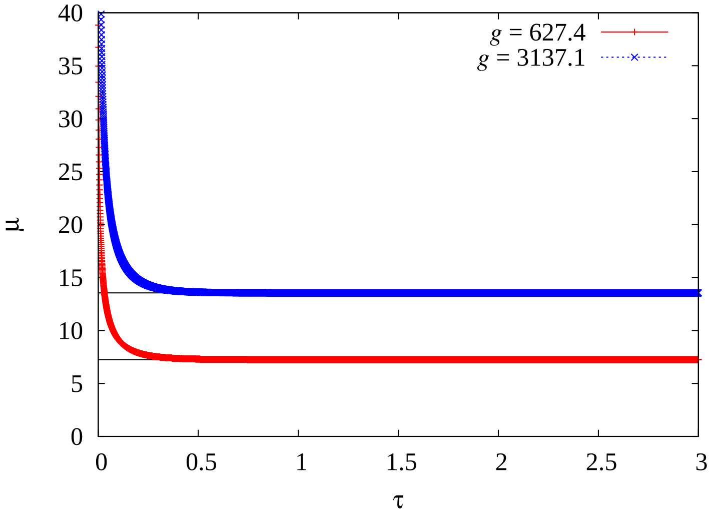

Figure A.1: The value of the chemical potential in units of $\hbar\omega$ as a function of the imaginary time of propagation τ, in units of ω^{-1}, for two different dimensionless interaction strengths $g = 4\pi Na/l$, calculated with the discretization parameters $\epsilon = 10^{-4}$ and $h = 10^{-2}$. We perform the calculation for the spherically symmetric trap $M\omega^2/2$, with the characteristic length scale $l = \sqrt{\hbar/M\omega}$. We see that for long times of propagation, the value of the chemical potential has converged toward the final result $\mu \approx 7.24836$, for $g = 627.4$, and $\mu \approx 13.5534$ for $g = 3137.1$.

This algorithm can be straightforwardly extended to higher-dimensional cases, as explained in detail in Ref. [87].

Appendix B Time-dependent variational analysis

For completeness, here we present details of the time-dependent variational analysis used in Chapter 5, which was originally introduced in Refs. [104, 105].

We start from the Lagrangian (4.16), assuming a time-dependent interaction $g(t)$. For the Gaussian variational Ansatz (5.1), we calculate

$$\psi^G \frac{\partial \psi^{G*}}{\partial t} - \psi^{G*} \frac{\partial \psi^G}{\partial t} = -2\, i\, \mathcal{N}(t)^2 \sum_{\sigma=x,y,z} \left(\sigma \dot{\varphi}_\sigma + \sigma^2 \dot{\phi}_\sigma \right) \exp\left(- \sum_{\sigma=x,y,z} \frac{(\sigma-\sigma_0)^2}{u_\sigma^2} \right),$$

$$\frac{\partial \psi^G}{\partial \sigma} \frac{\partial \psi^{G*}}{\partial \sigma} = \mathcal{N}(t)^2 \left(\frac{(\sigma - \sigma_0^2)}{u_\sigma^4} + (\varphi_\sigma + 2\sigma\phi_\sigma)^2 \right) \exp\left(- \sum_{\sigma=x,y,z} \frac{(\sigma-\sigma_0)^2}{u_\sigma^2} \right),$$

where we have introduced the notation $\mathcal{N}(t)^2 = (\pi^{3/2} u_x(t) u_y(t) u_z(t))^{-1}$, and $\sigma \in \{x, y, z\}$. Using the following Gaussian integrals

$$\begin{aligned}
\mathcal{N}(t)^2 \int d\vec{r}\, \sigma \exp\left(- \sum_{\sigma=x,y,z} \frac{(\sigma-\sigma_0)^2}{u_\sigma^2} \right) &= u_\sigma, \\
\mathcal{N}(t)^2 \int d\vec{r}\, \sigma^2 \exp\left(- \sum_{\sigma=x,y,z} \frac{(\sigma-\sigma_0)^2}{u_\sigma^2} \right) &= \frac{1}{2}\left(u_\sigma^2 + 2\sigma_0^2 \right), \\
\mathcal{N}(t)^4 \int d\vec{r}\, \exp\left(- \sum_{\sigma=x,y,z} \frac{2(\sigma-\sigma_0)^2}{u_\sigma^2} \right) &= \frac{1}{(2\pi)^{3/2} u_x u_y u_z},
\end{aligned}$$

we calculate the GP Lagrangian

$$\begin{aligned}
L_{\mathrm{GP}} = {} & \hbar \sum_{\sigma=x,y,z} \left(\sigma_0 \dot{\varphi}_\sigma + \frac{1}{2}\left(u_\sigma^2 + 2\sigma_0^2 \right) \dot{\phi}_\sigma \right) \\
& + \frac{\hbar^2}{2M} \sum_{\sigma=x,y,z} \left(\frac{1}{2u_\sigma^2} + \varphi_\sigma^2 + 4\varphi_\sigma \phi_\sigma \sigma_0 + 2\phi_\sigma^2 u_\sigma^2 + 4\phi_\sigma^2 \sigma_0^2 \right) \\
& + \sum_{\sigma=x,y,z} \frac{M\omega_\sigma^2}{2} \left(\frac{u_\sigma^2}{2} + \sigma_0^2 \right) + \frac{g(t)}{2} \frac{1}{(2\pi)^{3/2} u_x u_y u_z}.
\end{aligned}$$

Euler-Lagrange equations of motion for variational parameters $q \in \{\varphi_\sigma, \sigma_0, \phi_\sigma, u_\sigma\}$ have the form

$$\frac{d}{dt}\frac{\partial L}{\partial \dot{q}} - \frac{\partial L}{\partial q} = 0\,,$$

and for the above Lagrangian read:

$$\begin{aligned}
\varphi_\sigma - \frac{M}{\hbar}\dot{\sigma}_0 + 2\phi_\sigma\sigma_0 &= 0, && \text{(B.1)}\\
\hbar\dot{\varphi}_\sigma + 2\hbar\sigma_0\dot{\phi}_\sigma + \frac{2\hbar^2}{M}\varphi_\sigma\phi_\sigma + \frac{4\hbar^2}{M}\phi_\sigma^2\sigma_0 + M\omega_\sigma^2\sigma_0 &= 0 && \text{(B.2)}\\
\phi_\sigma - \frac{M}{2\hbar}\frac{\dot{u}_\sigma}{u_\sigma} &= 0, && \text{(B.3)}\\
\hbar\dot{\phi}_\sigma u_\sigma - \frac{\hbar^2}{2M}\frac{1}{u_\sigma^3} + \frac{2\hbar^2}{M}\phi_\sigma^2 u_\sigma + \frac{M\omega_\sigma^2}{2}u_\sigma - \frac{g(t)}{2(2\pi)^{3/2}}\frac{1}{u_x u_y u_z u_\sigma} &= 0. && \text{(B.4)}
\end{aligned}$$

Eqs. (B.1) and (B.3) give the explicit relation between φ_σ and σ_0, and between ϕ_σ and u_σ. By inserting Eqs. (B.1) and (B.3) into Eqs. (B.2) and (B.4), we obtain variational equations which we will refer to as a Gaussian approximation:

$$\begin{aligned}
\ddot{\sigma}_0(t) + \lambda_\sigma^2\sigma_0 &= 0\,, && \text{(B.5)}\\
\ddot{u}_\sigma(t) + \lambda_\sigma^2 u_\sigma(t) - \frac{1}{u_\sigma(t)^3} - \frac{\mathcal{P}(t)}{u_\sigma(t)u_x(t)u_y(t)u_z(t)} &= 0\,. && \text{(B.6)}
\end{aligned}$$

We also note that solutions of Eqs. (B.5) and (B.6) for $\sigma_0(t)$ and $u_\sigma(t)$ can be afterwards inserted into Eqs. (B.1) and (B.3) to obtain time-evolution of the phase parameters φ_σ and ϕ_σ. The last two equations are given in the dimensionless form: we choose a convenient frequency scale ω (for example, the external trap frequency in one of the spatial directions) and express all lengths in the units of the characteristic harmonic oscillator length $l = \sqrt{\hbar/M\omega}$, time in units of ω^{-1}, and external frequencies in units of ω: $\lambda_\sigma = \omega_\sigma/\omega$, $\sigma \in \{x, y, z\}$. The dimensionless interaction parameter $\mathcal{P}(t)$ is given by

$$\mathcal{P}(t) = \frac{g(t)}{(2\pi)^{3/2}\hbar\omega l^3} = \sqrt{\frac{2}{\pi}}N\frac{a(t)}{l}.$$

List of papers by Ivana Vidanović

This thesis is based on the following publications:

1. I. Vidanović, A. Balaž, H. Al-Jibbouri, and A. Pelster, Nonlinear Bose-Einstein-condensate Dynamics Induced by a Harmonic Modulation of the s-wave Scattering Length, *Phys. Rev. A* **84**, 013618 (2011), [**Chapter 5**]
2. A. Balaž, I. Vidanović, A. Bogojević, and A. Pelster, Ultra-fast converging path-integral approach for rotating ideal Bose-Einstein condensates, *Phys. Lett. A* **374**, 1539 (2010), [**Chapter 3**]
3. I. Vidanović, A. Bogojević, A. Balaž, and A. Belić, Properties of Quantum Systems Via Diagonalization of Transition Amplitudes. II. Systematic Improvements of Short-time Propagation, *Phys. Rev. E* **80**, 066706 (2009), [**Chapter 2**]
4. I. Vidanović, A. Bogojević, and A. Belić, Properties of Quantum Systems Via Diagonalization of Transition Amplitudes. I. Discretization Effects, *Phys. Rev. E* **80**, 066705 (2009), [**Chapter 2**]

Publications not included in the thesis:

1. A. Balaž, I. Vidanović, D. Stojiljković, D. Vudragović, A. Belić, and A. Bogojević, SPEEDUP Code for Calculation of Transition Amplitudes Via the Effective Action Approach, *Commun. Comput. Phys.* **11**, 739 (2012).
2. I. Vidanović, S. Arsenijević, and S. Elezović-Hadzić, Force-induced Desorption of Self-avoiding Walks on Sierpinski Gasket Fractals, *Eur. Phys. J. B.* **81**, 291 (2011).
3. A. Balaž, I. Vidanović, A. Bogojević, A. Belić, and A. Pelster, Fast Converging Path Integrals for Time-Dependent Potentials: II. Generalization to Many-Body Systems and Real-Time Formalism, *J. Stat. Mech.* P03005 (2011).

4. A. Balaž, I. Vidanović, A. Bogojević, A. Belić, and A. Pelster, Fast Converging Path Integrals for Time-Dependent Potentials: Recursive Calculation of Short-Time Expansion of the Propagator, *J. Stat. Mech.* P03004 (2011).
5. M. V. Milovanović, Th. Jolicoeur, and I. Vidanović, Modified Coulomb Gas Construction of Quantum Hall States from Nonunitary Conformal Field Theories, *Phys. Rev. B* **80**, 155324 (2009).
6. A. Balaž, A. Bogojević, I. Vidanović, and A. Pelster, Recursive Schrödinger Equation Approach to Faster Converging Path Integrals, *Phys. Rev. E* **79**, 036701 (2009).
7. A. Bogojević, I. Vidanović, A. Balaž, and A. Belić, Fast Convergence of Path Integrals for Many-Body Systems, *Phys. Lett. A* **372**, 3341 (2008).

References

[1] S. N. Bose, Plancks gesetz und lichtquantenhypothese, *Z. Phys.* **26**, 178 (1924). v, x, 1

[2] A. Einstein, Quantentheorie des einatomigen idealen gases, *Sitzungsber. Preuss. Akad. Wiss.* p. 261 (1924). v, x, 1

[3] M. H. Anderson, J. R. Ensher, M. R. Matthews, C. E. Wieman, and E. A. Cornell, Observation of Bose-Einstein condensation in a dilute atomic vapor, *Science* **269**, 198 (1995). vi, xi, 2, 7, 11

[4] K. B. Davis, M. O. Mewes, M. R. Andrews, N. J. van Druten, D. S. Durfee, D. M. Kurn, and W. Ketterle, Bose-Einstein condensation in a gas of sodium atoms, *Phys. Rev. Lett.* **75**, 3969 (1995). vi, xi, 2, 11

[5] F. Dalfovo, S. Giorgini, L. P. Pitaevskii, and S. Stringari, Theory of Bose-Einstein condensation in trapped gases, *Rev. Mod. Phys.* **71**, 463 (1999). vi, xi, 5, 7, 12, 84, 105

[6] C. Chin, R. Grimm, P. Julienne, and E. Tiesinga, Feshbach resonances in ultracold gases, *Rev. Mod. Phys.* **82**, 1225 (2010). vi, xi, 13

[7] I. Bloch, J. Dalibard, and W. Zwerger, Many-body physics with ultracold gases, *Rev. Mod. Phys.* **80**, 885 (2008). vi, vii, xi, xii, 15, 57, 58

[8] R. Feynman, Simulating physics with computers, *Int. J. Theor. Phys.* **21**, 467 (1982). vi, xi, 3

[9] A. Sethia, S. Sanyal, and Y. Singh, Discretized path integral method and properties of a quantum system, *J. Chem. Phys.* **93**, 7268 (1990). vii, xii, 16, 20, 21, 23, 33, 55

[10] A. Bogojević, A. Balaž, and A. Belić, Systematically accelerated convergence of path integrals, *Phys. Rev. Lett.* **94**, 180403 (2005). vii, xii, 16, 21, 34, 65

[11] A. Bogojević, I. Vidanović, A. Balaž, and A. Belić, Fast convergence of path integrals for many-body systems, *Phys. Lett. A* **372**, 3341 (2008). vii, xii, 16, 21, 34

[12] V. Bretin, S. Stock, Y. Seurin, and J. Dalibard, Fast rotation of a Bose-Einstein condensate, *Phys. Rev. Lett.* **92**, 050403 (2004). vii, xii, 17, 47, 49, 58, 59, 62, 68, 70, 71

[13] Gross E. P., Structure of a quantized vortex in boson systems, *Nuovo Cimento* **20**, 454 (1961). viii, xiii, 17, 88

[14] Pitaevskii L. P., Vortex lines in an imperfect Bose gas, *Sov. Phys. JETP* **13**, 451 (1961). viii, xiii, 17, 88

[15] S. E. Pollack, D. Dries, R. G. Hulet, K. M. F. Magalhães, E. A. L. Henn, E. R. F. Ramos, M. A. Caracanhas, and V. S. Bagnato, Collective excitation of a Bose-Einstein condensate by modulation of the atomic scattering length, *Phys. Rev. A* **81**, 053627 (2010). viii, xiii, 17, 107, 112, 113, 114, 126, 131

[16] M. R. Andrews, M.-O. Mewes, N. J. van Druten, D. S. Durfee, D. M. Kurn, and W. Ketterle, Direct, nondestructive observation of a Bose condensate, *Science* **273**, 84 (1996). 2, 11

[17] J. Klaers, J. Schmitt, F. Vewinger, and M. Weitz, Bose-Einstein condensation of photons in an optical microcavity, *Nature (London)* **468**, 545 (2010). 3

[18] V. Bagnato, D. E. Pritchard, and D. Kleppner, Bose-Einstein condensation in an external potential, *Phys. Rev. A* **35**, 4354 (1987). 3

[19] C. Pethick and H. Smith, *Bose-Einstein Condensation in Dilute Gases*, Cambridge University Press, Cambridge (2008). 3, 5, 6, 8, 13, 17, 57, 59, 86, 88, 90, 106

[20] W. Ketterle and N. J. van Druten, Bose-Einstein condensation of a finite number of particles trapped in one or three dimensions, *Phys. Rev. A* **54**, 656 (1996). 5

[21] W. Ketterle, D. S. Durfee, and D. M. Stamper-Kurn, Making, probing and understanding Bose-Einstein condensates, *arXiv:cond-mat/9904034* (1999). 8, 9, 10, 109

[22] H. Metcalf and P. van der Straten, Cooling and trapping of neutral atoms, *Phys. Rep.* **244**, 203 (1994). 10

[23] K. B. Davis, M.-O. Mewes, M. A. Joffe, M. R. Andrews, and W. Ketterle, Evaporative cooling of sodium atoms, *Phys. Rev. Lett.* **74**, 5202 (1995). 10

[24] R. Meppelink, R. A. Rozendaal, S. B. Koller, J. M. Vogels, and P. van der Straten, Thermodynamics of Bose-Einstein-condensed clouds using phase-contrast imaging, *Phys. Rev. A* **81**, 053632 (2010). 11, 101

[25] T. Lahaye, T. Koch, B. Frohlich, M. Fattori, J. Metz, A. Griesmaier, S. Giovanazzi, and T. Pfau, Strong dipolar effects in a quantum ferrofluid, *Nature (London)* **448**, 672 (2007). 12

[26] H. Feshbach, Unified theory of nuclear reactions, *Ann. Phys. (NY)* **5**, 357 (1958). 13

[27] U. Fano, Effects of configuration interaction on intensities and phase shifts, *Phys. Rev.* **124**, 1866 (1961). 13

[28] E. Tiesinga, B. J. Verhaar, and H. T. C. Stoof, Threshold and resonance phenomena in ultracold ground-state collisions, *Phys. Rev. A* **47**, 4114 (1993). 13

[29] J.T.M. Walraven, Elements of Quantum Gases: Thermodynamic and Collisional Properties of Trapped Atomic Gases, *Les Houches - predoc lectures 2010, (unpublished)*. 13

[30] N. N. Bogoliubov, On the theory of superfluidity, *J. Phys. (USSR)* **11**, 23 (1947). 14, 15, 104

[31] M. Stone, *The Physics of Quantum Fields*, Springer-Verlag, New York (2000). 15

[32] A. Altland and B. Simons, *Condensed Matter Field Theory*, Cambridge University Press, Cambridge (2006). 15, 85

[33] D. A. Huse and E. D. Siggia, The density distribution of a weakly interacting bose gas in an external potential, *J. Low Temp. Phys.* **46**, 137 (1982). 15, 95

[34] L. Pitaevskii and S. Stringari, *Bose-Einstein Condensation*, Clarendon Press, Oxford (2004). 17, 88

[35] A. Sethia, S. Sanyal, and F. Hirata, Eigenstates from the discretized path integral, *Chem. Phys. Lett.* **315**, 299 (1999). 20

[36] A. Sethia, S. Sanyal, and F. Hirata, Quantum dynamics: Path integral approach to time correlation functions in finite temperature, *J. Chem. Phys.* **114**, 5097 (2001). 20

[37] S. Sanyal and A. Sethia, Quantum properties of many boson system: Path integral approach, *Chem. Phys. Lett.* **404**, 192 (2005). 20

[38] H. Ishikawa, An accurate method for numerical calculations in quantum mechanics, *J. Phys. A* **35**, 4453 (2002). 21

[39] H. Shao and Z. Wang, Numerical solutions of the time-dependent Schrödinger equation: Reduction of the error due to space discretization, *Phys. Rev. E* **79**, 056705 (2009). 21

[40] S. A. Chin, S. Janecek, and E. Krotscheck, An arbitrary order diffusion algorithm for solving Schrödinger equations, *Comput. Phys. Commun.* **180**, 1700 (2009). 21

[41] S. Janecek and E. Krotscheck, A fast and simple program for solving local Schrödinger equations in two and three dimensions, *Comput. Phys. Commun.* **178**, 835 (2008). 21

[42] M. Aichinger, S.A. Chin, and E. Krotscheck, Fourth-order algorithms for solving local Schrödinger equations in a strong magnetic field, *Comput. Phys. Commun.* **171**, 197 (2005). 21

[43] A. Balaž, *O ubrzavanju konvergencije funkcionalnih integrala*, PhD thesis, Faculty of Physics, University of Belgrade (2008). 21

[44] A. Balaž, A. Bogojević, I. Vidanović, and A. Pelster, Recursive Schrödinger equation approach to faster converging path integrals, *Phys. Rev. E* **79**, 036701 (2009). 21, 26, 34, 36, 37, 55, 65

[45] A. Bogojević, A. Balaž, and A. Belić, Systematic speedup of path integrals of a generic N -fold discretized theory, *Phys. Rev. B* **72**, 064302 (2005). 21, 34

[46] A. Bogojević, A. Balaž, and A. Belić, Generalization of Euler's summation formula to path integrals, *Phys. Lett. A* **344**, 84 (2005). 21, 34

[47] T. L. Beck, Real-space mesh techniques in density-functional theory, *Rev. Mod. Phys.* **72**, 1041 (2000). 22

[48] M. A. Martin-Delgado, G. Sierra, and R. M. Noack, The density matrix renormalization group applied to single-particle quantum mechanics, *J. Phys. A* **32**, 6079 (1999). 23, 56

[49] J. R. Chelikowsky, N. Troullier, K. Wu, and Y. Saad, Higher-order finite-difference pseudopotential method: An application to diatomic molecules, *Phys. Rev. B* **50**, 11355 (1994). 23

[50] P. Maragakis, J. Soler, and E. Kaxiras, Variational finite-difference representation of the kinetic energy operator, *Phys. Rev. B* **64**, 193101 (2001). 23

[51] C.-K. Skylaris, A. A. Mostofi, P. D. Haynes, O. Diéguez, and M. C. Payne, Nonorthogonal generalized Wannier function pseudopotential plane-wave method, *Phys. Rev. B* **66**, 035119 (2002). 23

[52] H. Kleinert, *Path Integrals in Quantum Mechanics, Statistics, Polymer Physics, and Financial Markets*, World Scientific, Singapore (2006). 27, 43

[53] W. Janke and H. Kleinert, Summing paths for a particle in a box, *Lett. Nuovo Cimento* **25**, 297 (1979). 27

[54] Mathematica symbolic calculation software package `http://www.wolfram.com/mathematica`. 30, 40, 120, 122, 129

[55] G. Barton, A. J. Bray, and A. J. McKane, The influence of distant boundaries on quantum mechanical energy levels, *Am. J. Phys.* **58**, 751 (1990). 31, 38

[56] D. H. Berman, Boundary effects in quantum mechanics, *Am. J. Phys.* **59**, 937 (1991). 31, 38

[57] D. M. Ceperley, Path integrals in the theory of condensed helium, *Rev. Mod. Phys.* **67**, 279 (1995). 34

[58] M. Boninsegni, N. Prokof'ev, and B. Svistunov, Worm algorithm for continuous-space path integral Monte Carlo simulations, *Phys. Rev. Lett.* **96**, 070601 (2006). 34

[59] A. Bogojević, A. Balaž, and A. Belić, Asymptotic properties of path integral ideals, *Phys. Rev. E* **72**, 036128 (2005). 36

[60] SPEEDUP C and SCL BEC Mathematica codes, `http://www.scl.rs/speedup/`. 37, 41, 44, 49, 64, 123, 129

[61] W. Janke and H. Kleinert, Convergent strong-coupling expansions from divergent weak-coupling perturbation theory, *Phys. Rev. Lett.* **75**, 2787 (1995). 37, 39

[62] LAPACK – Linear Algebra PACKage, `http://www.netlib.org/lapack/`. 41, 49

[63] I. S. Gradshteyn and I. M. Ryzhik, *Table of integrals, series, and products*, Academic Press, San Diego (2000). 43, 95

[64] S. Stock, B. Battelier, V. Bretin, Z. Hadžibabić, and J. Dalibard, Bose-Einstein condensates in fast rotation, *Las. Phys. Lett.* **2**, 275 (2005). 47, 49

[65] S. Kling and A. Pelster, Thermodynamical properties of a rotating ideal Bose gas, *Phys. Rev. A* **76**, 023609 (2007). 47, 59, 68, 71, 73, 74, 75, 76, 80

[66] T. H. Seligman, J. J. M. Verbaarschot, and M. R. Zirnbauer, Quantum spectra and transition from regular to chaotic classical motion, *Phys. Rev. Lett.* **53**, 215 (1984). 53

[67] U. Schollwöck, The density-matrix renormalization group, *Rev. Mod. Phys.* **77**, 259 (2005). 56

[68] A. L. Fetter, Rotating trapped Bose-Einstein condensates, *Rev. Mod. Phys.* **81**, 647 (2009). 57

[69] K. W. Madison, F. Chevy, W. Wohlleben, and J. Dalibard, Vortex formation in a stirred Bose-Einstein condensate, *Phys. Rev. Lett.* **84**, 806 (2000). 57

[70] M. R. Matthews, B. P. Anderson, P. C. Haljan, D. S. Hall, C. E. Wieman, and E. A. Cornell, Vortices in a Bose-Einstein condensate, *Phys. Rev. Lett.* **83**, 2498 (1999). 57

[71] A. A. Abrikosov, On the magnetic properties of superconductors of the second group, *Sov. Phys. JETP* **5**, 1174 (1957). 57

[72] J. R. Abo-Shaeer, C. Raman, J. M. Vogels, and W. Ketterle, Observation of vortex lattices in Bose-Einstein condensates, *Science* **292**, 476 (2001). 57

[73] S. Viefers, Quantum Hall physics in rotating BoseEinstein condensates, *J. Phys.- Condens. Matter* **20**, 123202 (2008). 57

[74] A. L. Fetter, Rotating vortex lattice in a Bose-Einstein condensate trapped in combined quadratic and quartic radial potentials, *Phys. Rev. A* **64**, 063608 (2001). 58

[75] K. Howe, A. R. P. Lima, and A. Pelster, Rotating Fermi gases in an anharmonic trap, *Eur. Phys. J. D* **54**, 667 (2009). 83

[76] M. Holzmann, W. Krauth, and M. Naraschewski, Precision Monte Carlo test of the Hartree-Fock approximation for a trapped Bose gas, *Phys. Rev. A* **59**, 2956 (1999). 84, 97

[77] W. Krauth, Quantum Monte Carlo calculations for a large number of bosons in a harmonic trap, *Phys. Rev. Lett.* **77**, 3695 (1996). 84

[78] S. Giorgini, L. Pitaevskii, and S. Stringari, Thermodynamics of a trapped Bose-condensed gas, *J. Low Temp. Phys.* **109**, 309 (1997). 84, 87, 101

[79] V. I. Yukalov, Principal problems in Bose-Einstein condensation of dilute gases, *Las. Phys. Lett.* **1**, 435 (2004). 85

[80] N. Tammuz, R. P. Smith, R. L. D. Campbell, S. Beattie, S. Moulder, J. Dalibard, and Z. Hadžibabić, Can a Bose gas be saturated?, *Phys. Rev. Lett.* **106**, 230401 (2011). 85, 102

[81] R. P. Smith, R. L. D. Campbell, N. Tammuz, and Z. Hadžibabić, Effects of interactions on the critical temperature of a trapped Bose gas, *Phys. Rev. Lett.* **106**, 250403 (2011). 85, 102

[82] N. P. Proukakis and B. Jackson, Finite-temperature models of BoseEinstein condensation, *J. Phys. B* **41**, 203002 (2008). 86

[83] A. Griffin, Conserving and gapless approximations for an inhomogeneous Bose gas at finite temperatures, *Phys. Rev. B* **53**, 9341 (1996). 86

[84] V. I. Yukalov and H. Kleinert, Gapless Hartree-Fock-Bogoliubov approximation for Bose gases, *Phys. Rev. A* **73**, 063612 (2006). 87

[85] Y. S. Kivshar and B. A. Malomed, Dynamics of solitons in nearly integrable systems, *Rev. Mod. Phys.* **61**, 763 (1989). 88, 106

[86] M. Belić, N. Petrović, W.-P. Zhong, R.-H. Xie, and G. Chen, Analytical light bullet solutions to the generalized $(3+1)$-dimensional nonlinear Schrödinger equation, *Phys. Rev. Lett.* **101**, 123904 (2008). 88, 106

[87] P. Muruganandam and S. K. Adhikari, Fortran programs for the time-dependent GrossPitaevskii equation in a fully anisotropic trap, *Comput. Phys. Commun.* **180**, 1888 (2009). 89, 116, 125, 137, 141

[88] M. Naraschewski and D. M. Stamper-Kurn, Analytical description of a trapped semi-ideal Bose gas at finite temperature, *Phys. Rev. A* **58**, 2423 (1998). 91, 92, 93

[89] F. Gerbier, J. H. Thywissen, S. Richard, M. Hugbart, P. Bouyer, and A. Aspect, Experimental study of the thermodynamics of an interacting trapped Bose-Einstein condensed gas, *Phys. Rev. A* **70**, 013607 (2004). 91, 92, 93, 101

[90] S. Giorgini, L. P. Pitaevskii, and S. Stringari, Condensate fraction and critical temperature of a trapped interacting Bose gas, *Phys. Rev. A* **54**, R4633 (1996). 99

[91] S. Grossmann and M. Holthaus, On Bose-Einstein condensation in harmonic traps, *Phys. Lett. A* **208**, 188 (1995). 100

[92] T. Haugset, H. Haugerud, and J. O. Andersen, Bose-Einstein condensation in anisotropic harmonic traps, *Phys. Rev. A* **55**, 2922 (1997). 100

[93] J. R. Ensher, D. S. Jin, M. R. Matthews, C. E. Wieman, and E. A. Cornell, Bose-Einstein condensation in a dilute gas: Measurement of energy and ground-state occupation, *Phys. Rev. Lett.* **77**, 4984 (1996). 100

[94] M.-O. Mewes, M. R. Andrews, N. J. van Druten, D. M. Kurn, D. S. Durfee, and W. Ketterle, Bose-Einstein condensation in a tightly confining dc magnetic trap, *Phys. Rev. Lett.* **77**, 416 (1996). 100

[95] A. Griffin, T. Nikuni, and E. Zaremba, *Bose-Condensed Gases at Finite Temperatures*, Cambridge University Press, Cambridge (2009). 102

[96] L. D. Landau and E. M. Lifshitz, *Course of Theoretical Physics, Statistical physics*, Pergamon press, Oxford (1980). 104

[97] D. S. Jin, J. R. Ensher, M. R. Matthews, C. E. Wieman, and E. A. Cornell, Collective excitations of a Bose-Einstein condensate in a dilute gas, *Phys. Rev. Lett.* **77**, 420 (1996). 105

[98] M.-O. Mewes, M. R. Andrews, N. J. van Druten, D. M. Kurn, D. S. Durfee, C. G. Townsend, and W. Ketterle, Collective excitations of a Bose-Einstein condensate in a magnetic trap, *Phys. Rev. Lett.* **77**, 988 (1996). 105

[99] F. Chevy, V. Bretin, P. Rosenbusch, K. W. Madison, and J. Dalibard, Transverse breathing mode of an elongated Bose-Einstein condensate, *Phys. Rev. Lett.* **88**, 250402 (2002). 105, 111

[100] D. M. Stamper-Kurn, H.-J. Miesner, S. Inouye, M. R. Andrews, and W. Ketterle, Collisionless and hydrodynamic excitations of a Bose-Einstein condensate, *Phys. Rev. Lett.* **81**, 500 (1998). 105, 111

[101] H. Ott, J. Fortágh, S. Kraft, A. Günther, D. Komma, and C. Zimmermann, Nonlinear dynamics of a Bose-Einstein condensate in a magnetic waveguide, *Phys. Rev. Lett.* **91**, 040402 (2003). 105, 111, 132

[102] M. Edwards, P. A. Ruprecht, K. Burnett, R. J. Dodd, and C. W. Clark, Collective excitations of atomic Bose-Einstein condensates, *Phys. Rev. Lett.* **77**, 1671 (1996). 106, 111

[103] S. Stringari, Collective excitations of a trapped Bose-condensed gas, *Phys. Rev. Lett.* **77**, 2360 (1996). 106, 111

[104] V. M. Pérez-García, H. Michinel, J. I. Cirac, M. Lewenstein, and P. Zoller, Low energy excitations of a Bose-Einstein condensate: A time-dependent variational analysis, *Phys. Rev. Lett.* **77**, 5320 (1996). 106, 107, 108, 111, 142

[105] V. M. Pérez-García, H. Michinel, J. I. Cirac, M. Lewenstein, and P. Zoller, Dynamics of Bose-Einstein condensates: Variational solutions of the Gross-Pitaevskii equations, *Phys. Rev. A* **56**, 1424 (1997). 106, 107, 108, 111, 142

[106] C. Becker, S. Stellmer, P. Soltan-Panahi, S. Dorscher, M. Baumert, E.-M. Richter, J. Kronjager, K. Bongs, and K. Sengstock, Oscillations and interactions of dark and dark-bright solitons in Bose-Einstein condensates, *Nat. Phys.* **4**, 496 (2008). 106

[107] C. Hamner, J. J. Chang, P. Engels, and M. A. Hoefer, Generation of dark-bright soliton trains in superfluid-superfluid counterflow, *Phys. Rev. Lett.* **106**, 065302 (2011). 106

[108] M. Faraday, On a peculiar class of acoustical figures; and on certain forms assumed by a group of particles upon vibrating elastic surfaces, *Philos. Trans. R. Soc. London* **121**, 299 (1831). 106

[109] M. C. Cross and P. C. Hohenberg, Pattern formation outside of equilibrium, *Rev. Mod. Phys.* **65**, 851 (1993). 106

[110] J. P. Gollub and J. S. Langer, Pattern formation in nonequilibrium physics, *Rev. Mod. Phys.* **71**, S396 (1999). 106

[111] P. Engels, C. Atherton, and M. A. Hoefer, Observation of Faraday waves in a Bose-Einstein wondensate, *Phys. Rev. Lett.* **98**, 095301 (2007). 106, 115

[112] E. A. L. Henn, J. A. Seman, G. Roati, K. M. F. Magalhães, and V. S. Bagnato, Emergence of turbulence in an oscillating Bose-Einstein condensate, *Phys. Rev. Lett.* **103**, 045301 (2009). 106

[113] S. K. Adhikari, Resonance in BoseEinstein condensate oscillation from a periodic variation in scattering length, *J. Phys. B* **36**, 1109 (2003). 107, 114

[114] F. K. Abdullaev, R. M. Galimzyanov, M. Brtka, and R. A. Kraenkel, Resonances in a trapped 3D BoseEinstein condensate under periodically varying atomic scattering length, *J. Phys. B* **37**, 3535 (2004). 107, 114

[115] F. K. Abdullaev and J. Garnier, Collective oscillations of one-dimensional Bose-Einstein gas in a time-varying trap potential and atomic scattering length, *Phys. Rev. A* **70**, 053604 (2004). 107, 114

[116] K. Staliunas, S. Longhi, and G. J. de Valcárcel, Faraday patterns in Bose-Einstein condensates, *Phys. Rev. Lett.* **89**, 210406 (2002). 107, 114, 115

[117] F. Dalfovo, C. Minniti, and L. P. Pitaevskii, Frequency shift and mode coupling in the nonlinear dynamics of a Bose-condensed gas, *Phys. Rev. A* **56**, 4855 (1997). 111, 114

[118] J. J. García-Ripoll, V. M. Pérez-García, and P. Torres, Extended parametric resonances in nonlinear Schrödinger systems, *Phys. Rev. Lett.* **83**, 1715 (1999). 111, 125, 126

[119] J. J. G. Ripoll and V. M. Pérez-García, Barrier resonances in Bose-Einstein condensation, *Phys. Rev. A* **59**, 2220 (1999). 111

[120] J.-K. Xue, G.-Q. Li, A.-X. Zhang, and P. Peng, Nonlinear mode coupling and resonant excitations in two-component Bose-Einstein condensates, *Phys. Rev. E* **77**, 016606 (2008). 111

[121] H. Pu and N. P. Bigelow, Collective excitations, metastability, and nonlinear response of a trapped two-species Bose-Einstein condensate, *Phys. Rev. Lett.* **80**, 1134 (1998). 111

[122] S. E. Pollack, D. Dries, M. Junker, Y. P. Chen, T. A. Corcovilos, and R. G. Hulet, Extreme tunability of interactions in a ^{7}Li Bose-Einstein condensate, *Phys. Rev. Lett.* **102**, 090402 (2009). 111, 112

[123] V. I. Yukalov, E. P. Yukalova, and V. S. Bagnato, Bose systems in spatially random or time-varying potentials, *Las. Phys.* **19**, 686 (2009). 114

[124] N. N. Bogoliubov and Y. A. Mitropolsky, *Asymptotic Methods in the Theory of Non-Linear Oscillations*, Gordon&Breach, New York (1961). 114, 121, 125

[125] Y. Zhou, W. Wen, and G. Huang, Frequency shift and mode coupling of the collective modes of superfluid Fermi gases in the BCS-BEC crossover, *Phys. Rev. B* **77**, 104527 (2008). 114

[126] A. Pelster, H. Kleinert, and M. Schanz, High-order variational calculation for the frequency of time-periodic solutions, *Phys. Rev. E* **67**, 016604 (2003). 114, 121

[127] R. Mickens, *Introduction to Nonlinear Oscillations*, Cambridge University Press, Cambridge (1981). 114, 121

[128] N. Minorsky, *Nonlinear Oscillation*, Van Nostrand, Princeton (1962). 114, 121

[129] A. I. Nicolin, R. Carretero-González, and P. G. Kevrekidis, Faraday waves in Bose-Einstein condensates, *Phys. Rev. A* **76**, 063609 (2007). 115

[130] D. Leibfried, R. Blatt, C. Monroe, and D. Wineland, Quantum dynamics of single trapped ions, *Rev. Mod. Phys.* **75**, 281 (2003). 120

[131] L. P. Pitaevskii, Dynamics of collapse of a confined Bose gas, *Phys. Lett. A* **221**, 14 (1996). 126

[132] L. P. Pitaevskii and A. Rosch, Breathing modes and hidden symmetry of trapped atoms in two dimensions, *Phys. Rev. A* **55**, R853 (1997). 126

[133] L. Salasnich, A. Parola, and L. Reatto, Dimensional reduction in Bose-Einstein-condensed alkali-metal vapors, *Phys. Rev. A* **69**, 045601 (2004). 131

[134] L. Pitaevskii and S. Stringari, Elementary excitations in trapped Bose-Einstein condensed gases beyond the mean-field approximation, *Phys. Rev. Lett.* **81**, 4541 (1998). 133

[135] E. Braaten and J. Pearson, Semiclassical corrections to the oscillation frequencies of a trapped Bose-Einstein condensate, *Phys. Rev. Lett.* **82**, 255 (1999). 133

[136] A. R. P. Lima and A. Pelster, Quantum fluctuations in dipolar bose gases, *Phys. Rev. A* **84**, 041604 (2011). 133

[137] W. H. Press, S. A. Teukolsky, W. T. Vetterling, and B. P. Flannery, *Numerical Recipes in C*, Cambridge University Press, Cambridge (1997). 139

CURRICULUM VITAE - Ivana Vidanović

EDUCATION

- **(2007-2011)** PhD in Condensed Matter Physics, Faculty of Physics, University of Belgrade
- (**2001-2006)** BSc in Physics, Faculty of Physics, University of Belgrade
  Major: Theoretical Physics
- (**1997-2001)** Mathematical High School, Belgrade, Serbia

EMPLOYMENT AND RESEARCH PROJECTS

- **(2011-2012)** Serbian-German bilateral research project “Numerical and Analytical Investigation of Ultracold Bose Gases in Disordered Potentials”, funded by the Serbian Ministry of Education and Science and DAAD
- **(2011-2014)** National research project ON171017 “Modeling and Numerical Simulations of Complex Physical Systems”, funded by the Serbian Ministry of Education and Science
- **(2009-2010)** Serbian-German bilateral research project “Fast Converging Path Integral Approach to Bose-Einstein Condensation”, funded by the Serbian Ministry of Science and DAAD
- **(2008-present)** Employed at the Scientific Computing Laboratory of the Institute of Physics Belgrade, Serbia
- **(2007-2010)** National research project OI141035 “Modeling and numerical simulations of complex physical systems” funded by the Serbian Ministry of Science
- **(2006-2009)** FP6 project of the European Commission “CX-CMCS: EU Centre of Excellence for Computer Modeling of Complex Systems”

COLLABORATION WITH OTHER INSTITUTIONS

- **(May 2011)** Visit to Condensed Matter Group, MPI-PKS, Dresden, Germany, host Dr. Masud Haque
- **(2009-2010)** Several visits to Dr. Axel Pelster at the Free University of Berlin, University of Duisburg-Essen, and Potsdam University
- **(June-September 2005)** Summer student at the Paul Drude Institute, Berlin, Germany

ATTENDED WORKSHOPS AND CONFERENCES

- **March 2011** DPG-2011 Conference, Dresden, Germany
- **August 2010** Quo Vadis BEC? conference, MPI-PKS Dresden, Germany
- **July 2010** Many-Body Physics with Ultracold Gases, Les-Houches, France
- **September 2009** Arnold Sommerfeld Summer School on Condensed Matter Physics with Ultracold Quantum Gases, LMU Munich, Germany
- **September 2009** PreDoc school on Ultracold Quantum Gases of Atoms and Molecules, Les-Houches, France
- **November 2008** Tutor at the ICTP/Democritos Advanced School in High Performance and GRID Computing, Trieste, Italy
- **October 2008** Quo Vadis BEC? conference, Bad Honnef, Germany
- **September 2007** Path Integrals – New Trends and Perspectives, PI07 Conference, Dresden, Germany
- **August 2007** V International Student Conference of the Balkan Physical Union, Bodrum, Turkey
- **July 2007** QTS-5 Conference, Valladolid, Spain
- **March 2007** ICTP/Democritos Advanced School in High Performance Computing Tools for e-Science, Trieste, Italy